Rapid Solidification of Ni-Si-Fe Intermetallics in Drop Tube

Leigang Cao

Submitted in accordance with the requirements for the degree of

Doctor of Philosophy

University of Leeds

School of Chemical and Process Engineering

June, 2014

The candidate confirms that the work submitted is his own, except where work which has formed part of jointly-authored publications has been included. The contribution of the candidate and the other authors to this work has been explicitly indicated below. The candidate confirms that appropriate credit has been given within the thesis where reference has been made to the work of others.

1. Section 5.3 of this thesis is based on a jointly-authored journal paper: Cao, L., Cochrane, R. F. and Mullis, A. M., "Lamella structure formation in drop-tube processed Ni-25.3 at.% Si alloy." Journal of Alloys and Compounds, 2013, In Press. The candidate completed the experiments and analysed the results. Professor Andrew Mullis and Dr Robert Cochrane contributed ideas and valuable discussion of the paper.

Acknowledgements

I would like to give my deepest gratitude to my supervisors, Prof Andy Mullis and Dr Bob Cochrane for their constant supervision, guidance and encouragement throughout this work.

Thanks to China Scholarship Council and University of Leeds for the financial support to my study.

I would like to thank Diane Cochrane and Rob Simpson not only for their help on training me using the equipments but also for their patients on equipments maintenance and repairs. I would also like to give my thanks to Ellie Castle and Caroline Clopet for their friendly assistance on my project.

It is very important to analyze the experimental samples using different characteristic techniques in my project, like XRD, SEM and TEM. So here to Dr Tim Comyn, Mr John Harrington, Dr Michael Ward and Dr Richard Walshaw, thank you very much for your help.

Closer to home I would like to thanks my friends, Dr Mingfu Guan, Zhengyang Ling, Dr Wei Jiang, Dr Yue Zhang, Qian Fu and Xijin Hua's family, who made my stay so enjoyable and unforgettable.

Finally, I would like to thank my parents, my sisters, brother and relatives and particularly my girlfriend Jing Wu and her parents. Thank you very much for your unwavering support through the whole adventure. I could not have done it without you.

Thank you.

Leigang Cao

Abstract

The rapid solidification of the $Ni_{74.7-x}Fe_xSi_{25.3}$ (x = 0, 10 and 15 at.%) alloys was studied by the drop tube technique aiming to investigate the formation of intermetallic compounds and microstructural evolution at high cooling rates. The particles of different diameters were obtained, with 75-850 μm particles for the Ni-25 at.% Si alloy and 53-850 μm particles for the $Ni_{74.7-x}Fe_xSi_{25.3}$ (x = 10 and 15 at.%) alloys. Several characteristic techniques were used to analyze the as-solidified samples, including optical microscopy, SEM, TEM, DTA and XRD.

For the Ni-25.3 at.% Si alloys, the metastable phase $Ni_{25}Si_9$ formed as the dominant phase in all size ranges of the particles, with γ-$Ni_{31}Si_{12}$ and β_1-Ni_3Si also being present. Three typical microstructures were observed: (1) regular lamellar and (2) anomalous eutectic structures comprising the $Ni_{25}Si_9$ and β_1-Ni_3Si phases; (3) heteroclite structure with the matrix of $Ni_{25}Si_9$. The formation of the eutectic structures indicates that there is a possible eutectic reaction for the $Ni_{25}Si_9$ and β_1-Ni_3Si phases. With increasing cooling rate, an increasing fraction of the droplets formed the entire heteroclite structure.

The solidified phases and microstructures of the Ni-Fe-Si alloys were deeply influenced by the cooling rate. At low cooling rates, only γ-$Ni_{31}Si_{12}$ and a compound with the same structure as β_1 were obtained, while the additional metastable phase $Ni_{25}Si_9$ formed in the small particles (53-212 μm). Three typical microstructures were observed with increasing cooling rate: (1) regular structure comprising the single-phase γ-$Ni_{31}Si_{12}$ and eutectic structure of γ-$Ni_{31}Si_{12}$ and β_1-Ni_3Si; (2) refined lamellar structure with the wide band of γ-$Ni_{31}Si_{12}$; (3) anomalous structure with the matrix of $Ni_{25}Si_9$. It is suggested that there is an extended $Ni_{25}Si_9$ stability field in the Ni-rich part of Ni-Fe-Si ternary system. With increasing cooling rate, an increasing fraction of small droplets experience high undercoolings and, therefore, can be undercooled into the $Ni_{25}Si_9$ stability field forming the entire anomalous structure.

Table of Contents

List of Figures

List of Tables

List of Symbols

Symbol	Definition	Unit
C_0	Initial solute composition	at%
C_e	Eutectic compostion	at%
C_i	Fraction of occupied sites in layer *i*	-
C_l	Liquid composition	at%
C_p	Specific heat capacity	$J\ kg^{-1}\ K^{-1}$
C_s	Solid composition	at%
c_g	Heat capacity of nitrogen	$J\ kg^{-1}\ K^{-1}$
d_1	distance	m
D	diameter	m
D_i	Interfacial diffusion coefficient	$m^2\ s^{-1}$
E	Molar internal energy	$J\ mol^{-1}$
f	Volume fraction	-
f_a	Atom scattering factor	-
F	Structure factor of crystal	-
G	Molar gibbs free energy	$J\ mol^{-1}$
G_t	Thermal gradient	$K\ m^{-1}$
G_L	Molar gibbs free energy of the liquid state	$J\ mol^{-1}$
G_S	Molar gibbs free energy of the solid state	$J\ mol^{-1}$
H	Molar enthalpy	$J\ mol^{-1}$
I_0	Pre-exponatial factor	$m^{-3}\ s^{-1}$
I	Nucleation rate	$m^{-3}\ s^{-1}$
k_e	Equilibrium distribution coefficient	-
k_v	Non-equilibrium distribution coefficient	-
K	Curvature	m^{-1}
K_1	Materials-dependent constant	$K\ s\ m^{-2}$
K_2	Materials-dependent constant	K m
k_B	Boltzmann constant	$m^2\ kg\ s^{-2}\ K^{-1}$
L	Liquid	-
L_0	Camera length	-
L_V	Latent heat of fusion per unit volume	$J\ m^{-3}$

m	Slope	-
m_g	Mass of nitrogen	kg
M	Mole mass	g mol^{-1}
P	Pressure	Pa
P_e	Peclet number	-
Q_{rev}	Molar heat	J mol^{-1}
r	Radius	m
r_1	Distance	m
r^*	Critical radius	m
R	Gas constant	J mol^{-1} K^{-1}
R_0	Distance	m
R_{wp}	Weighted profile factor	-
R_{exp}	Expected weighted profile	-
S	Molar entropy	J mol^{-1} K^{-1}
S_m	Entropy	J mol^{-1} K^{-1}
$S(\theta)$	Shape factor	-
t_f	Local solidification time	s
T	Temperature	K
T_0	Critical temperature of diffusionless solidification	K
$T_0(c)$	Curve of diffusionless solidification	-
T_a	Room temperature	K
T_e	Eutectic temperature	K
T_{hyp}	Hypercooling temperature	K
T_L	Liquidus temperature	K
$T_L(C_0)$	Liquidus temperature at C_0	K
T_m	Melting temperature	K
T^*	Interface temperature	K
$T_m(r)$	Equilibrium melting temperature of the particle (radius r)	K
T_q	Temperature distribution in front of the S/L interface	K m^{-1}
T_S	Solidus temperature	K
$T_S(C_0)$	Solidus temperature at C_0	K
T_∞	Temperature far away from the S/L interface	K
V	Volume	m^3

V_g	Grow velocity	m s^{-1}
V_r	Relative velocity	m s^{-1}
W	The frequency of occurrence of a macrostate	-
X_E	Eutectic composition	at%
ΔC_0	Composition difference	at%
ΔG	Free energy difference	J mol^{-1}
ΔG_d	Activation energy of atom transformation	J
ΔG_{het}	Energy difference of heterogeneous nucleation	J
ΔG_r	Energy difference during the formation of a cluster	J
ΔG_V	energy change of the volume transformation	J mol^{-1} m^{-3}
ΔG^{ls}	Energy different of the solid and liquid	J
ΔG_{het}^*	Maximum excess free energy of heterogeneous nucleation	J
ΔG_{hom}^*	Maximum excess free energy of homogeneous nucleation	J
ΔG_n^*	Free energy of the critical nucleus containing n atoms	J mol^{-1}
ΔH_f	Latent heat of fusion	J kg^{-1}
ΔS_f	Entropy of fusion	J mol^{-1} K^{-1}
ΔS_v	Entropy per volume	J m^{-3} K^{-1}
ΔT	Undercooling	K
ΔT_c	Constitutional undercooling	K
ΔT_e	Extremum undercooling	K
ΔT_k	Kinetic undercooling	K
ΔT_r	Curvature undercooling	K
ΔT_T	Thermal undercooling	K
ΔT^*	Critical undercooling	K
α_f	Factor related to surface energy	-
γ_{SL}	Free energy of the solid/liquid interface	J m^{-2}
γ_{ML}	Free energy of the mould/liquid interface	J m^{-2}
γ_{SM}	Free energy of the solid/mould interface	J m^{-2}
δ_i	Diffusion length	m
δ_s	Secondary electron coefficient	-
ε	Surface emissivity	-
η_g	Dynamic viscosity of nitrogen	Kg m^{-1} s^{-1}
η_s	Backscatterd electron coefficient	-

θ	Angle	-
λ	Interlamellar spacing	m
λ_1	Primary dendrite arm spacing	m
λ_2	Secondary dendrite arm spacing	M
λ_w	Wavelength	m
λ_e	Extremum lamellar spacing	m
λ_g	Thermal conductivity of nitrogen	J cm^{-1} s^{-1} K^{-1}
μ	Refractive index of the medium	-
μ_i	Chemical potential of the component '*i*'	J mol^{-1}
ρ	Density of metal	kg m^{-3}
ρ_g	Density of nitrogen	kg m^{-3}
ρ_s	Density of the solid	kg m^{-3}
σ	Stefan-Boltzmann constant	W cm^{-2} K^{-4}
φ	Included angle	-
Γ	Gibbs-Thomson coefficient	K m

1 Introduction

Intermetallic materials have been paid great attention for their potential application as high temperature structural and non-structural materials, due to the possibility of combining the ductility of metals and the strength and oxidation resistance of ceramics. One such is the βNi_3Si compound for its high melting point (1443 K), excellent oxidation resistance [1] and great hardness (789HV) [2] at elevated temperatures. However, like many other intermetallics, it is also brittle at room temperature, which restricts its application owing to fabricating difficulties [3-7]. One potential route to overcome this difficulty is to form intermetallic-metal matrix composites by incorporating a ductile phase into the brittle matrix or solidifying a ductile phase from original melts, like in situ composites due to eutectic transformation [2, 8, 9]. Another potential route to improve this weakness is non-equilibrium processing via rapid solidification, with the resulting fine grain structure [10-12] and the presence of anti-phase domains and disorder-order structures increasing room temperature ductility [13, 14].

Rapid solidification can be achieved at slow cooling rates by the reduction of heterogeneous nucleation, e.g. melt fluxing and levitation techniques, wherein slowly-cooled but deeply-undercooled melt can be obtained. These experimental designs provide the possibility for detailed fundamental investigations of the processes occurring during the early stage of crystallization and direct observation of the microstructures at different levels of undercooling and measurement of the crystal growth-velocities. Another way to achieve rapid solidification is involving rapid cooling methods directly, like melt spinning, rapid quenching and drop tube techniques, wherein the non-equilibrium phases can be formed and retained. These experimental designs provide a good way to develop new materials and study the phase formation and microstructural development with increasing cooling rate.

The direct study of the solidification properties of β-Ni_3Si was firstly carried out by Ahmad et al. [15], who performed the undercooling experiments on Ni-25.3 at% Si alloy using a melt-fluxing technique. However, despite obtaining the required undercooling (the maximum value being 160 K) they were unable to obtain the single-phase β-Ni_3Si. Instead, at all undercoolings, the solidification was always to a lamellar eutectic structure of the single-phase γ-$Ni_{31}Si_{12}$ and supersaturated α-Ni lamellae with the suppression of βNi_3Si. The observed β_1 phase was from the decomposition of the metastable α-Ni phase in the post solidification process. Meanwhile, the growth velocities detected were extremely low, with a maximum of 0.018 m s^{-1} at maximum undercooling, 160 K, which is consistent with the general trend revealed by previous studies on the Ni-Si alloys that the solidification velocity drops with increasing Si concentration [16, 17]. In addition, small amounts of the metastable phase, $Ni_{25}Si_9$ and β_3, were retained in which a cooling rate of <10 K s^{-1} would be expected. Recently, extension studies on Ni-29.8 at.% Si eutectic alloy were carried out by Lu et al. [18], who obtained a small amount of amorphous phase at an undercooling in excess of 240 K with a low cooling rate of > 1 K s^{-1}, which gave a significant low cooling rate for amorphous phase formation in a binary alloy. The formation of the amorphous phase here might also be because of the high viscosity of the Ni-29.8 at.% Si melt, which has higher Si concentration in comparison with the Ni-25.3 at.% melt [15, 19].

Meanwhile, from the Ni-Fe phase diagram, it is clear that the elements Fe and Ni can form a continuous solid solution phase in some temperature regions [84]. Chemically, Ni and Fe are very similar, so direct substitution of Fe for Ni would be expected with small amount of Fe alloyed. Experimentally, the stability of the $L1_2$ ordered phase has been studied by Himuro et al. [20, 21] on the Ni_3Fe-Ni_3Si pseudo-binary system, wherein they observed the $L1_2$ precipitate from the alloy which enters the α-Ni stability field.

In the present work, the drop tube technique was used to solidify droplets of the Ni-25.3 at.% Si and $Ni_{74.7-x}Fe_xSi_{25.3}$ alloys at high cooling rates. A new solidification pathway at high cooling rates and the influence of the cooling rate on the phase formation and microstructural evolution will be investigated, including the formation of β-Ni_3Si phases (β_1, β_2 and β_3) in Ni-Si alloys and $L1_2$ (β_1-Ni_3Si) phase in Ni-Fe-Si alloys.

2 Fundamental Theory

The structure of engineering materials (metals and alloys) is very important as it is directly related to its properties. Metals and alloys are usually crystalline in the solid form and normally consist of many very small crystals and thus are polycrystalline. This chapter contains two parts, including some essential theories and concepts that are useful to accomplish the research. The first part concerns the basic theory of crystallography. The second section encompasses the main knowledge of the whole solidification process, comprising the thermodynamics of undercooled liquids, the kinetics of nucleation and crystal growth in a rapid solidification process.

2.1 Fundamentals of Crystallography

Crystals are different from gases and liquids because the atoms, ions or molecules in a crystal arrange in a periodic pattern in three dimensions. Ignoring the actual atoms, ions or molecules, the crystal can be represented as a 'lattice', a three-dimensional array of points (lattice points). Each of the points has identical surroundings. Here, some basics about crystallography are introduced in brief, such as a unit cell, Miller indices, crystal symmetry, crystal systems and so on [22].

2.1.1 Unit Cell

In order to avoid drawing down a greater number of atoms to describe one crystal, the concept of a 'unit cell' is used which is the smallest group of atoms possessing the symmetry of the crystal which will develop into the crystal lattice when the unit cell is repeated in all directions. Unit cells can be defined using six scalar lattice parameters: the lengths of the three lattice translation vectors **a**, **b** and **c** and the three included angles α (between **b** and **c**), β (between **c** and **a**) and γ (between **a** and **b**), are shown in **Figure 2.1**.

2.1.2 Miller Indices

Miller indices, defined as the reciprocals of the fractional intercepts which the plane makes with the crystallographic axes, are widely used in crystallography and crystallization for indexing the orientation of a plane in a lattice [22]. Miller indices of one plane is usually represented as (hkl), which means the plane makes fractional intercepts of X=a/h, Y=b/k and Z=c/l with the axes, as shown in **Figure 2.2**. As for a given plane with the intercepts X, Y and Z, the corresponding Miller indices can be calculated in reverse as follows:

$$h = \frac{a}{X} \qquad k = \frac{b}{Y} \qquad l = \frac{c}{Z} \tag{2-1}$$

There exists a whole set of parallel equi-distant planes in any lattice, therefore, Miller indices (hkl) usually refer to the plane in the set which is nearest the origin and this whole set of equivalent planes can be indexed by $\{hkl\}$ written in a curly brackets. Miller indices commonly use integers and for the plane parallel to a given axis, the corresponding Miller index is zero.

2.1.3 Crystal Symmetry

The crystallographic unit could appear identical to itself by performing certain symmetry operations. For example, a reflection occurs when a crystal structure on one side of a plane passing through the center of a crystal is the mirror image of the structure on the other side. The plane across which the reflection occurs is mirror plane, as shown in **Figure 2.3**a. There are four kinds of symmetry operations: reflection, rotation, inversion and rotation-inversion. If a structure has n-fold rotational symmetry about an axis, it means that a rotation of 360˚/n brings it into self-coincidence. As for the cubic crystal shown in **Figure 2.3**b, it has a 4-fold axis normal to each face, 3-fold axis along each body diagonal and a 2-fold axis joining the centre of the opposite edge. Central inversion and rotation-inversion operations are also shown in **Figure 2.3**c and d [22].

2.1.4 Crystal Systems

The parameters of a unit cell could vary from one to another, but actually there are only practically seven different types of cells including all the possible point lattices. They are known as seven crystal systems, as can be seen in **Table 2.1**. Except for seven different point lattices, there is still some other arrangements of points which fulfil the requirements of a point lattice that each lattice point has identical surroundings. In 1848, Bravais worked on this problem and demonstrated that there are fourteen possible point lattices which can be used to describe any crystal structure, as shown in **Figure 2.4**.

2.2 Thermodynamics of undercooled liquid

Rapid solidification technology has great practical potential for material science and engineering. During this non-equilibrium solidification process, refined microstructures, extended solid solubility and new metastable phases can be obtained at high cooling rates or at high undercooling, which in turn can improve the fatigue, wear, or corrosion resistance of materials. What is more, if the cooling rate is further increased, the undercooled liquid can be transformed directly into the glass phase [10]. In this section, some concepts of thermodynamics, e.g. Entropy, Enthalpy, Gibbs free energy, will be introduced.

2.2.1 Enthalpy

Enthalpy is a measure of the heat content of the system and is given by

$$H=E+PV \tag{2-2}$$

where E is the internal energy of the system, P is the pressure, and V is the volume. Usually, in a system related to solid-liquid phase transition, changes of the PV term are very small in comparison with E, that is, $H \approx E$ [23].

During the solidification process, the system transforms from liquid to solid. The enthalpy changes usually comprise two parts [19]: (1) the decrease in enthalpy due to the transformation from liquid to solid, which is equal to the latent heat of fusion, $\Delta H_{f,}$ (2) the decrease in the enthalpy of the liquid or solid, due to cooling, which is given by:

$$\Delta H = \int C_p dT \tag{2-3}$$

where C_p is the specific heat capacity.

2.2.2 Entropy

From a macroscopic point of view of a system, entropy describes the heat exchanges that occur in thermal processes via the relation:

$$dS = dQ_{rev}/T \tag{2-4}$$

where Q_{rev} denotes the amount of heat and T is the absolute temperature at which the exchange takes place.

While from a microscopic point of view, entropy is a measure of the randomness of the system. The entropy associated with a system in equilibrium is given by:

$$S_m = k_B \ln W \tag{2-5}$$

where k_B is the Boltzmann constant and W is the frequency of occurrence of a macrostate.

2.2.3 Gibbs free energy and equilibrium phase diagram

If a liquid is cooled below its equilibrium melting temperature (T_m), it would have a tendency to solidify under the driving force (G_L-G_S). At constant temperature and pressure, we can introduce Gibbs free energy (G) to denote the relative stability of the system.

$$G = H - TS \tag{2-6}$$

If one system is in its most stable state, it is said to be in equilibrium. So, at constant temperature and pressure, a closed system in a stable state means it has the lowest possible value of the Gibbs free energy, or satisfies the condition:

$$\mathrm{d}G_\mathrm{S} = 0 \tag{2-7}$$

where G_S is the overall Gibbs free energy of the system. Equation (2-7) only shows a necessary, but not sufficient condition for equilibrium.

From **Figure 2.5**, we can easily find that the Gibbs free energy of the A state is much lower than that of the B state, although both of them meet Equation (2-7). So the states like A would be the stable states, while the states like B can be called metastable states, which is less stable than the A state.

For a multiphase system, if the chemical potential of each component is equal in all phases, it is in equilibrium condition, that is:

$$\mu_i^1 = \mu_i^2 = \cdots = \mu_i^n = \cdots \tag{2-8}$$

Any transformation accompanied by a decrease in Gibbs free energy is possible. Therefore, a necessary criterion for any phase transformation can be given by

$$\Delta G = G_2 - G_1 < 0 \tag{2-9}$$

where G_1 and G_2 are the free energies of the initial and final states respectively.

Take a binary system consisting of A and B components with two phases α and β at a certain temperature, as shown in **Figure 2.6**. For an alloy with initial composition, X_0, the equilibrium can be reached only if the tangents to each Gibbs free energy curve at the equilibrium composition lie on a common line.

$$\mu_A^\alpha = \mu_A^\beta \text{ and } \mu_B^\alpha = \mu_B^\beta \tag{2-10}$$

In such cases, the equilibrium compositions of α and β phases are α_e and β_e, and the free energy of the system is minimum, G_e, reduced by $(G_0^\alpha - G_e)$.

According to this equilibrium condition, a phase diagram can be constructed, and the calculated process for one simple binary phase diagram has been shown in **Figure 2.7**. At a high temperature $T_1 > T_A > T_B$, the Gibbs free energy curve of liquid is lower than that of solid α and β, so the liquid will be the stable phase at all compositions as shown in **Figure 2.7**a. Decreasing the temperature to T_2, the Gibbs free energy curve of liquid and α phase has one intersection, while the Gibbs free energy of the β phase is still higher than that of liquid. In such cases, the common tangent line indicates that the alloys with a composition lower than X_M are solid at equilibrium, with composition higher than X_N are liquid, while between X_M and X_N are a mixture of α and liquid. T_4 is the eutectic temperature of this binary system and eutectic reaction ($L=\alpha+\beta$) will take place if the alloy with composition X_E is as shown in **Figure 2.7**d and f. Phase diagrams are very useful because they illustrate the conditions at which specific phases can exist at thermodynamic equilibrium [23].

2.3 Nucleation Kinetics

Theoretically, if the temperature of a metal drops below its melting temperature, it would have a tendency to solidify under the driving force (G_L-G_S). However, in many cases, the melt will stay in the liquid state below its melting temperature. In order to solidify, melts need to achieve a temperature lower than their melting temperature, which is known as undercooling phenomenon, and the difference (T_m-T_L) is the so-called undercooling. Here, nucleation phenomenon will be demonstrated first. It is clear that extra energy is needed to overcome the energy barrier to form a new interface between a solid nucleus and the liquid when solidified. With increasing undercooling, the driving force increases and if it exceeds the energy barrier, a solid-like cluster can thereby transform into a solid. The ΔG_{hom}^{*} in **Figure 2.8** can be used to represent this energy barrier. Nucleation is the initiating process of solidification, which is followed by subsequent growth and there are two classical nucleation theories to describe the crystallization from an undercooled liquid, homogeneous nucleation and heterogeneous nucleation [10].

2.3.1 Homogeneous Nucleation

Homogeneous nucleation means that the solid-like clusters transform into solid without contacting with the container, other phases or molecular species during solidification. If a small volume of solid forms from its liquid, it will cause a difference in free energy and generate a new interface between the solid and the liquid. The change associated with the formation of the solid can release energy, but the change associated with the creation of the interface needs to absorb energy. Both of them are related to the size of the solid. Assuming that the solid is a sphere of radius *r*, the free energy change can be seen in **Figure 2.8**, and is given as:

$$\Delta G_{\boldsymbol{r}} = -\frac{4}{3}\pi r^3 \Delta G_V + 4\pi r^2 \gamma_{SL} \tag{2-11}$$

where ΔG_V is Gibbs free energy difference between the liquid and solid per unit volume and γ_{SL} is the solid/liquid interfacial free energy.

As can be seen from **Figure 2.8**, for a given undercooling, there exists one critical radius, r^*, which is associated with maximum excess free energy. It is clear that, if the particle is of critical size, there are two opposite paths to decrease its free energy, dissolution and growth. That is to say, only if the size of solid-like clusters exceed, or are at least equal to the critical radius, they can transform into a new solid phase.

In order to form a crystal nucleus, the clusters have to overcome the energy barrier of the interface. The maximum excess free energy can be given by differentiation of Equation (2-11):

$$\frac{d(\Delta G_r)}{dr} = -4\pi r^2 \Delta G_V + 8\pi r \gamma_{SL} = 0 \qquad (2\text{-}12)$$

so, the critical size is given by:

$$r^* = \frac{2\gamma_{SL}}{\Delta G_V} \qquad (2\text{-}13)$$

Also, the maximum excess free energy, ΔG^*, is:

$$\Delta G^*_{hom} = \frac{16\pi\gamma_{SL}^3}{3(\Delta G_V)^2} \qquad (2\text{-}14)$$

substituting equation:

$$\Delta G_V = \frac{L_V \Delta T}{T_m} \qquad (2\text{-}15)$$

to the former equations (2-13) and (2-14), gives:

$$r^* = (\frac{2\gamma_{SL} T_m}{L_V})\frac{1}{\Delta T} \qquad (2\text{-}16)$$

$$\Delta G^*_{hom} = (\frac{16\pi\gamma_{SL}^3 T_m^2}{3L_V^2})\frac{1}{(\Delta T)^2} \qquad (2\text{-}17)$$

where L_V is the latent heat of fusion per unit volume.

So, if the temperature decreases below T_m, the ΔG^*_{hom} and r^* will decrease rapidy due to increasing undercooling, ΔT. That is to say, the tendency towards nucleation increases sharply.

2.3.2 Heterogeneous nucleation

Homogeneous nucleation rarely occurs in nature as it needs a very pure alloy system. When the melt contains impurities, or is in contact with a crystalline crucible or oxide layer, nucleation may be facilitated if the activation energy required for nucleation is decreased. This is known as heterogeneous nucleation. From the Equation (2-17) it can be seen that nucleation develops more easily at small undercoolings by reducing the interfacial energy term. Simply, consider a solid embryo forming in contact with a perfectly flat mould wall as depicted in **Figure 2.9**. Assuming γ_{SL} is isotropic, it can be shown that [23], for a given volume of solid, the total interfacial energy of the system is minimized if the embryo has the shape of a spherical cap with a ‘wetting’ angle θ given by the condition that the interfacial tensions γ_{ML}, γ_{SM}, and γ_{SL} balance in the plane of the mould wall.

$$\gamma_{\mathrm{ML}} = \gamma_{\mathrm{SM}} + \gamma_{\mathrm{SL}} \cos\theta \tag{2-18}$$

or

$$\cos\theta = (\gamma_{ML} - \gamma_{SM}) / \gamma_{SL} \tag{2-19}$$

The Gibbs free energy change of the system in heterogeneous nucleation is given as:

$$\Delta G_{het} = \left\{-\frac{4}{3}\pi r^3 \Delta G_V + 4\pi r^2 \gamma_{SL}\right\} S(\theta) \tag{2-20}$$

where

$$S(\theta) = (2 + \cos\theta)(1 - \cos\theta)^2 / 4 \tag{2-21}$$

As can be seen from the Equation (2-20), except for the factor $S(\theta)$, it is the same as the Equation (2-11) for homogeneous nucleation. By differentiation of Equation (2-20) it can be shown that:

$$r^* = \frac{2\gamma_{SL}}{\Delta G_V} \tag{2-22}$$

and

$$\Delta G^*_{het} = \frac{16\pi\gamma_{SL}^3}{3(\Delta G_V)^2} \cdot S(\theta) \tag{2-23}$$

Combining Equation (2-14) and (2-23) gives

$$\Delta G^*_{het} = S(\theta)\Delta G^*_{hom} \tag{2-24}$$

The value of S (θ) varies between 0 and 1, which is related to the wetting angle θ. Therefore, if S (θ) is smaller than 1 the energy barrier for heterogeneous nucleation is lower than that for homogeneous nucleation.

2.3.3 Nucleation rate

The growth of the critical nucleus requires the transfer of atoms from the liquid to the nuclei. The steady–state nucleation rate is given by:

$$I = I_0 \exp\left(-\frac{\Delta G_n^* + \Delta G_d}{k_B T}\right) \qquad (2\text{-}25)$$

Where ΔG_n^* is the free energy of the critical nucleus containing n atoms, ΔG_d is the activation energy for transfer through the solid/liquid interface, k_B is Boltzmann's constant and I_0 is the pre-exponential factor.

With decreasing T, the viscosity of the undercooled liquid increases and fewer atoms will transfer from liquid to nuclei. However, as can be seen from Equations (2-16) and (2-17), it is clear that the critical nuclei size and critical maximum free energy decrease with the increase of undercooling, ΔT, which means that more nuclei will satisfy the growth condition and, in turn, the nucleation rate increases. These two opposing tendencies are illustrated in **Figure 2.10**a, but time factor is neglected here. Taking time into account, the *I-T* diagram can be easily transformed into a *TTT* (Time-Temperature-Transformation) diagram (**Figure 2.10**b).

When liquid metals are cooled normally, the cooling curve will generally cross the nucleation curve (curve 1). However, at very high cooling rate, there may be insufficient time for the formation of nucleus, and the glassy (amorphous) solid results (curve 2) [4, 5].

2.4 Crystal growth in undercooled metallic melts

2.4.1 Heat and solute redistribution

During the solidification process, the liquid must be cooled down to the solidification temperature, and then the heat released by the solidification process at the solid/liquid interface must be extracted. **Figure 2.11** shows the temperature field in front of the solid/liquid interface. From **Figure 2.11** it is clear that columnar grains grow into the hot liquid from the mould from the opposite direction to the heat flow (**Figure 2.11**a and c), while in the process of equiaxed grains growing into the undercooled liquid, the growth direction is the same as the heat flow direction (**Figure 2.11**b and d) [19]. Specific to the drop tube in this project, the equiaxed growth illustrated in (b) and (d) are relevant to the solidification situations, while the situation in (a) and (c) are used for comparison.

In most cases, solidification involves alloys but not pure metals. From the example binary phase diagram (**Figure 2.12**a), it is clear that there should be a local composition difference at the solid/liquid interface due to the smaller solubility of the α phase. In order to simplify the analysis process, the liquidus and the solidus lines of the relevant part of the phase diagram are treated as straight, as can be seen from the lower right diagram in **Figure 2.12**b. During the equilibrium solidification process of an alloy, the equilibrium distribution coefficient (k_e), the ratio between the solid composition and the liquid composition at the interface gives the equation:

$$k_e = \frac{C_s}{C_l} \tag{2-26}$$

here we just take the left hand corner of a phase diagram as an example. The liquid-solidus temperature interval at C_0, ΔT_0, can be given by:

$$\Delta T_0 = T_L(C_0) - T_S(C_0) = -m\Delta C_0 \tag{2-27}$$

where m is the slope of the liquidus line and ΔC_0 is the composition difference between liquid and solid at $T_S(C_0)$, which is given by:

$$\Delta C_0 = \frac{C_0(1-k_e)}{k_e} \tag{2-28}$$

During the solidification of an alloy, the excess solute rejected from the solid in front of the interface will form an enriched boundary layer within a certain distance. With the solid solidifying from the liquid continuously, the composition of the liquid ahead of the interface will rise gradually. After a transient period, the composition distribution will stabilize in a steady state condition. The formation process can be described by **Figure 2.13**. Under these circumstances, the solid composition is equal to that of the liquid value far ahead of the interface, C_0, while the solute composition in the boundary layer decreases from the maximum value, C_0/k_e, at the interface to the initial composition, C_0, and follows the equation:

$$C_l = C_0 + \Delta C_0 \exp(-\frac{xV_g}{D_i}) \tag{2-29}$$

where V_g is the grow velocity, x is the distance ahead of the interface and D_i is the diffusion coefficient in the liquid. The liquid composition is inversely proportional to the growth rate, and the composition curve becomes steeper at high growth rates (V_2>V_1), as shown in **Figure 2.14**.

2.4.2 Undercooling

According to Equation (2-15), if ΔT=0 under the equilibrium temperature, the system is at equilibrium, and no transformation can occur. So undercooling is the necessary condition in the solidification process. Generally under constant pressure, undercooling consists of four parts: kinetic undercooling (ΔT_k), curvature undercooling (ΔT_r), thermal undercooling (ΔT_T) and constitutional undercooling (ΔT_c). To reveal the nature of undercooling, kinetic considerations must be introduced.

1) Kinetic undercooling

When a solid/liquid interface moves forward along with crystal growth, there are two processes: the ‘melting process’ where atoms transfer from solid to liquid and the ‘solidification process’ where atoms transfer from liquid to solid. Under equilibrium conditions, the rate of atoms transferring from these two processes must be equal,

$$(\frac{dn}{dt})_M = (\frac{dn}{dt})_S \tag{2-30}$$

As shown in **Figure 2.15** it is clear that the two curves intersect at T_m. It is not difficult to understand that more atoms must jump from L to S than that from S to L for solidification to occur. Therefore, the actual temperature at the solidifying interface must be lower than T_m, and this temperature difference is called kinetic undercooling, ΔT_k.

2) Curvature undercooling

In the real solidification process, the liquid-solid interface is not planar (flat) in the beginning, because solidification occurs at discrete points in the liquid or at the walls of the container. The surface/volume ratio of a solid particle increases with the volume of the particle in a liquid decreasing which will give rise to the increase of the total free energy of the particle. Therefore, the increase of total free energy of the solid caused by particle size decreasing will result in a decrease of the melting point compared with the equilibrium temperature. The melting point $T_m(r)$ for a small crystal with radius r can be predicted by the Gibbs-Thomson equation [24].

$$T_m(r) = T_m - 4\gamma_{SL}T_m/(r\Delta H_f\rho_s) \tag{2-31}$$

where T_m is the normal melting point, $T_m(r)$ is the melting point of crystal with radius r, ΔH_f is the bulk enthalpy of fusion, γ_{SL} is the surface energy of the S/L interface and ρ_s is the density of the solid.

Curvature undercooling (ΔT_r) is the difference between the normal melting temperature of the metal and actual melting point of the same metal with a finite radius. ΔT_r is a function of the interface curvature. In two dimensions, the curvature of a circle with radius r is K (=1/r), whereas, in three dimensions, the curvature of a sphere with radius r is K (=2/r). In order to simplify the calculation, here the solid particle is assumed to be a sphere with radius r. So when the particle increases by dr, the net increase of the new surface energy, $d(4\pi r^2\gamma)/dr$, must be equal to the decrease of the free volumetric energy, $d(4\pi r^3\Delta G_v/3)/dr$, which gives:

$$\Delta G_v = \gamma_{SL}\frac{2}{r} = \gamma_{SL}K \qquad (2\text{-}32)$$

where γ_{SL} is the liquid-solid surface energy and K is the curvature. Introducing the equation,

$$\Delta T = \frac{\Delta G_v}{\Delta S_v} \qquad (2\text{-}33)$$

Equation (2-33) can be revised as:

$$\Delta T_r = T_m - T_m(r) = \frac{\gamma_{SL}}{\Delta S_v}K = \Gamma K \qquad (2\text{-}34)$$

where Γ is the Gibbs-Thomson coefficient.

3) Thermal undercooling

Thermal undercooling arises from the existing thermal gradient in the liquid, which happens if nucleation is difficult or if the growth of the solid lags the heat transport out of the liquid. The relationship is shown in **Figure 2.16** and equation below [25]:

$$\Delta T_T = T^* - T_\infty \qquad (2\text{-}35)$$

where T^* is the interface temperature and T_∞ is the liquid temperature far from the interface.

4) Constitutional undercooling

As mentioned above, the dendrite grains growing into the undercooled liquid are expected in rapid solidification process. It is clear that solute atoms should be rejected from the solidified solids, which induces a difference in the solute composition in front of the dendrite tip and builds up a diffusion boundary layer, as shown in **Figure 2.17**. The steady-state diffusion boundary layer is shown in **Figure 2.17**a. The liquid composition decreases with distance x from C_0/k_e to C_0, while the corresponding liquidus temperature T_L will increase as indicated by the phase diagram. In the drop tube process, the heat is flowing out from the solid into the undercooled liquid. The thermal gradient in front of the dendrite tip, G_t, should be negative. Therefore, the actual temperature of the liquid in front of the interface is always lower than the equilibrium freezing temperature, which is known as constitutional undercooling.

2.4.3 Interface structure

The subsequent growth of the initial nucleus needs atoms adding to the solid/liquid interface continuously. There are two kinds of solid/liquid interface, which are, faceted and non-faceted at the atomic scale, as shown in **Figure 2.18**. Generally, the solidification of metal usually takes place along with non-faceted interface development, while that of non-metal, intermetallic compounds or minerals commonly develops into a faceted interface.

The kinetics of atomic addition play an important role in the crystal growth process. The non-faceted interface always exposes many favourable sites for the attachment of atoms from the liquid because it is rough and uneven atomically (**Figure 2.18**b). So atoms can readily be added to many sites on the surface facilitating crystal growth rapidly, and such kinds of interface can be exhibited at low undercooling. In contrast, an atomically flat interface (**Figure 2.18**a) only offers a few favourable sites for atom attachment, which has a tendency to close up any gap in its solid/liquid interface atomically. Hence the growth is more difficult and requires surface nucleation or surface defects at an additional high undercooling [19].

The roughness of a surface at the atomic scale depends on the value of entropy of the fusion, and a factor α_f (=$\Delta S_f/R$) has been introduced here. Non-faceted crystal growth is a priority if the values of α are less than 2 with low melting entropy ΔS_f, while faceted growth forms with higher α_f values. The roughness of a surface depends on

α_f as shown in **Figure 2.19**, which shows the surface is quite smooth for high α_f, whereas the transition from liquid to solid takes place over several atomic layers with small α_f. Due to the greater difficulties experienced in attaching atoms to the atomically flat surfaces, undercooling is required. In this case, surface defects are of particular importance, such as, screw dislocations, twin boundaries and rotation boundaries. All of these supply re-entrant corners that cannot be eliminated by growth and can increase the numbers of bonds between the atoms and crystal, which reduces the kinetic undercooling [26].

2.4.4 Departure from local equilibrium

In order to overcome the energy barrier for initial nucleation and subsequent growth in solidification, a certain amount of undercooling is necessary. Generally, a high cooling rate or undercooling are always involved in rapid solidification, which will cause different degrees of departure from full diffusional equilibrium, as shown in **Table 2.2**.

Under equilibrium conditions, the chemical potential of each component must be the same in all phases. Aziz [27] has developed a simple relationship to describe the transformation from local chemical equilibrium to diffusionless solidification. The equation can be given by:

$$k_v = \frac{k_e + (\delta_\mathrm{i} V_g / D_\mathrm{i})}{1 + (\delta_\mathrm{i} V_g / D_\mathrm{i})} \tag{2-36}$$

where D_i is the interfacial diffusion coefficient, δ_i is the diffusion length, and V_g is solidification velocity. The non-equilibrium distribution coefficient, k_v, is defined by the ratio between the solute concentration in the growing solid and that in the liquid at the interface, and the equilibrium distribution coefficient, k_e, is defined by the ratio of the solid and liquid concentrations on the phase diagram.

According to Equation (2-36), it can be concluded that if $V_g << D_i/\delta_i$, k_v is equal to k_e, which corresponds to the interface equilibrium condition in **Figure 2.20**a. With solidification velocity increasing the concept of the local equilibrium at the solid/liquid interface will be no longer valid. In this situation, different degrees of solute trapping ($1>k_v>k_e$) will occur due to the competition between the rate of interface displacement and the rate of atomic diffusion.

If solidification velocity is at an extremely high rate ($V_g >> D_i/\delta_i$), the solid/liquid interface will sweep through the metallic melt. In this case, the atoms have no time to rearrange themselves for nucleation and subsequent crystal growth like normal equilibrium solidification process. Since the distribution coefficient k_v is almost equal to 1, the chemical potential of both phases cannot be equalised, therefore complete solute trapping occurs. Thus, the solid will possess the same composition of the liquid, as shown in **Figure 2.20**b.

Once the complete solute trapping happens, a crystal can be formed from its melt without a change in composition. In order to achieve such transformation, two conditions need to be fulfilled: firstly, the liquid and solid composition at the interface can converge at high cooling rate, and secondly the interface temperature should be below the T_0 temperature of the corresponding composition (**Figure 2.21**). At temperature, T_3, the system just starts to solidify and the equilibrium composition of the alloy should be C_s and C_0 for solid and liquid phases respectively. Therefore solid phase, α, forms first from its melt with a composition of C_s. Decreasing the temperature, the tangent line of the liquid Gibbs free energy line at composition C_0 will cross with a curve G_s. The hatched region (**Figure 2.21**b), represents the range that the Gibbs free energy of the α phase is lower than that of the liquid phase and, therefore, the α phase can form from its melt in this composition region. Similarly, at temperature, T_1, there was also one such hatched region. However, the maximum composition allowed the α phase formation to rise to C_0, the nominal alloy composition. The T_0 line implies the highest temperature at which complete solute trapping can take place, as shown in **Figure 2.21**d, which is achieved by combining the hatched region with the same properties at a different temperature and with the same composition. Each composition has one corresponding temperature, and the locus of T_0 over a range of compositions can constitute a $T_0(c)$ curve [19].

2.4.5 Dendrite growth

Nearly all of the microstructure from the solidification process of a pure metal or an alloy can be divided into two groups: single phase primary crystals and polyphase structures. The former structure, dendrite, will be introduced here and the latter will be described in the following sections including eutectic and peritectic microstructure.

The tree-like primary crystal is one of the most common growth forms in solidification, especially in metals and alloys, which is called dendrite. There are three types of dendrite: (1) Equiaxed dendrites of pure substances (**Figure 2.11**b), (2) Equiaxed dendrites of alloys (**Figure 2.11**d); and (3) columnar alloy dendrites (**Figure 2.11**c). The growth of dendrites in pure metals is heat-flow-controlled while the growth in alloys is mainly a solute-diffusion-controlled process.

During growth, the solid/liquid interface will be disturbed randomly due to insoluble particles, temperature fluctuations and grain boundaries, as well as surface tension of the interface. Under some conditions, the perturbations will be amplified if a marked difference in the growth of the tips and depressions of an unstable planar solid/liquid interface occurred, which will then develop as the onset of dendrite growth. **Figure 2.22** illustrates the continuous growth of the unstable interface in a pure substance. If a crystal grows into an undercooled melt freely, the latent heat will also flow down the negative temperature gradient in the undercooled liquid. Assuming a perturbation exists in the sphere, it is clear that the tip will be subject to a steeper negative temperature (a solid line compared to a dashed line). Therefore, heat extraction will be more effective from the tip of the perturbations allowing its growth preferentially. As a result, the local growth rate is increased and the solid/liquid interface is thus inherently unstable. In the alloy system, since the tip of the marked perturbations can reject solute into the surrounding liquid in its right head as well as in the lateral direction, it will tend to grow more rapidly than a depression, and then perturbations of sinusoidal shape will grow into the form of cells. The solid phase with lower solute composition keeps growing into the undercooled liquid and rejecting solute to the surrounding liquid. In addition, the direction of the primary arms (cellular growth) is always consistent with the direction of heat flow, while it will follow the crystallographically preferred directions. Some preferred dendrite orientations of various materials are listed in **Table 2.3** [19]. The opposite situation takes place in the condition shown in **Figure 2.11**a, in this case, the perturbation will melt back and thus the planar interface is stabilised.

2.4.6 Eutectic solidification

Eutectic solidification is one very common transformation in alloy solidification processes. Taking the binary phase diagram in **Figure 2.7**f for example, the solidification of the liquid with composition, X_E, will involve simultaneous growth of the α and β phases at eutectic temperature, T_e. Considerable theoretical and experimental attention has been paid to the nature of eutectic growth, because the fine periodic microstructures give rise to improved mechanical properties. Here only binary eutectic systems are involved in the discussion. Typical eutectic microstructures formed under different conditions are generally classified as regular and irregular (anomalous) structures.

Based on the previous discussion, phases having low entropies of fusion are prone to solidify with a non-faceted interface, while phases having high entropies of fusion are prone to solidify with a faceted interface. Regular eutectic microstructure can be formed if both phases possess low entropy of fusion, because the growth of the crystals is straightforward following all crystallographic directions forming non-faceted/non faceted eutectic structure. While if one phase has high entropy of fusion, the eutectic morphology often transfers to an anomalous non-faceted/faceted structure. Moreover, in addition to the entropy of fusion, the volume fraction of the two phases also has a great influence on the resultant structure. In the regular eutectic microstructural system, the eutectic will probably be fibrous if the volume fraction (f) of one phase is between 0 and 0.28, while the eutectic will tend to be lamellar with higher volume fraction ($0.28< f <0.50$). When faceting occurs, the regular eutectic structure will be anomalous, that is, fibres in regular eutectic structure will become faceted and regular lamellar structure will become anomalous [10, 19].

As discussed above, during the solidification of a single phase with a plane front, the solute is rejected from the solid/liquid interface and transports along the growth direction forming a long-range diffusion boundary layer in the steady state, as shown in **Figure 2.13**. During lamellar eutectic growth, the α phase will reject B atoms into the melt, while the β phase will reject A atoms, as shown in **Figure 2.23**a. Since the α and β phases are placed side-by-side, B atoms rejected by α phase is in favour of the growth of the β phase, and vice versa. Therefore, the dominant diffusion direction should be parallel to the solid/liquid interface which will reduce the solute accumulation ahead of both phases compared with the large solute build-up in single phase growth. Sideways diffusion is thus the reason to form alternative lamellae of α and β phases.

There are three dominant variables involved in the eutectic solidification process: undercooling (ΔT), growth velocity (V_g) and interlamellar spacing (λ). Jackson and Hunt [28] have firstly analyzed the growth of regular eutectics and derived their relationship as:

$$\Delta T = K_1 \lambda V_g + \frac{K_2}{\lambda} \tag{2-37}$$

where K_1 and K_2 are material-dependent constants. This relationship was deduced with some assumptions: firstly, the lamellar fronts are locally flat and the growth rate is slow. Secondly, the interlamellar spacing is much smaller than the diffusion distance ahead of the interface. Thirdly the interface composition in the liquid is supposed to be close to the eutectic composition.

With the suggestion that the lamellae grow with a spacing which gives a minimum undercooling at the interface, Equation (2-37) can be simplified as:

$$\lambda_e^2 V_g = K_2 / K_1 \tag{2-38}$$

in such cases,

$$(\Delta T_{\mathrm{e}})^2 / V_g = 4 K_1 K_2 \tag{2-39}$$

where ΔT_e and λ_e are the extremum undercooling and extremum lamellar spacing.

Later study by Seetharaman and Trivedi [29] has verified this model that $\lambda_e^2 V_g$ is constant under most experimental conditions. However, their experimental investigations indicate that there is no sharp selection criterion for eutectic intermellar spacing. Instead a band of interlamellar spacings between the extremum λ_e and a somewhat larger λ_m are stable at a given growth velocity.

For irregular faceted/non-faceted eutectic structure, the lamellar spacing cannot be estimated by Equations (2-38) and (2-39), and the extremum criterion is not sufficient to explain it. Actually, the mean spacing is much larger, even with the existing local spacing which corresponds to the extremum condition. Kurz and Fisher [19] developed one convergent and divergent growth mechanism to explain such phenomenon. Due to its atomic structure or defect growth, faceted phase does not freely change growth direction and thus grows in a highly anisotropic manner. In convergent growth, the curvature of both phases will increase with the spacing decreasing. Therefore the growth will stop if the spacing is close to the extremum, λ_e. On the contrary, in divergent growth, the spacing becomes larger and larger, leading to increasing solute accumulation ahead of both phases. This will lead to the formation of depressions at the centre of the major lamellar phase and then minor phase and primary lamellar branching happens. Then the spacing decreases again. Therefore, the spacing in an irregular eutectic is always within the extremun, λ_e and a certain value, λ_b, at which the depression of a minor phase is formed, as shown in **Figure 2.23**b.

In the rapid solidification process, the preconditions proposed by Jackson and Hunt are no longer valid, because the diffusion distance should be quite small and the undercooling can be quite large. Therefore, further study by Trivedi et al. [30] corrected this eutectic growth model for use under rapid solidification conditions. The key different parameter used by Trivedi is the solute Peclet number, $P_e=V_g\lambda/(2D_i)$, which can be larger than 1 at high growth velocity, while Pe was much less than unity under normal solidification conditions. Then Trivedi et al. concluded that there was a maximum velocity beyond which a cooperative lamellar structure cannot be grown, and the relationship, λ^2V_g=constant, is not true but shows a function of V_g and P_e:

$$\lambda^2 V_g = f(V, P_e) \tag{2-40}$$

Directional solidification of eutectic or near-eutectic alloys is one good way to form regular lamellar structure, such as Cr-Cr_3Si alloys [31], Ni-Ni_3Si alloys [32] and so on. The transition of regular eutectic to anomalous eutectic structure with increasing undercooling has also been reported as a common phenomenon under rapid solidification of eutectic alloys, such as Co-Co_5Ge_3 alloys [33] and Ni-Ni_3Sn alloys [34, 35].

2.4.7 Peritectic Solidification

Peritectic solidification is also very common in the solidification of metallic alloys, which can be classified into two different mechanisms, peritectic reaction and peritectic transformation. A hypothetical peritectic phase diagram is shown in **Figure 2.24**.

The peritectic reaction is the formation of peritectic or secondary phase by the reaction between the primary phase and liquid at peritectic temperature:

$$\text{Liquid} + \beta \rightarrow \alpha \tag{2-41}$$

Since decomposition of the β phase is involved in this process, the liquid composition should exceed composition $C_{l\mathrm{p}}$ to ensure the formation of the primary β phase. The composition $C_{\alpha\mathrm{p}}$ located at point P is so-called the peritectic composition at which all of the liquid and primary β phase are consumed completely to form the α phase. Generally, all three phases (α, β and liquid) are expected to contact with each other in a peritectic reaction so that the liquid and the β phase can react directly to form the α phase. The thickness of the α phase increases with lower solidification velocity.

The peritectic transformation occurs directly after the peritectic reaction process. In this process, primary β phase is coated by α phase and the process becomes diffusion controlled through the secondary α phase. The α phase can be precipitated directly from the primary β phase by long-range diffusion and from the liquid [36]. Initially, the thickness of the secondary α phase layer over the primary β phase surface only needed to be a few atoms thick, so its growth rate should be very quick compared with the following growth rate during the peritectic transformation process because it is a diffusion controlled procedure and the solute diffusion rate in the solid is much slower than that in the liquid.

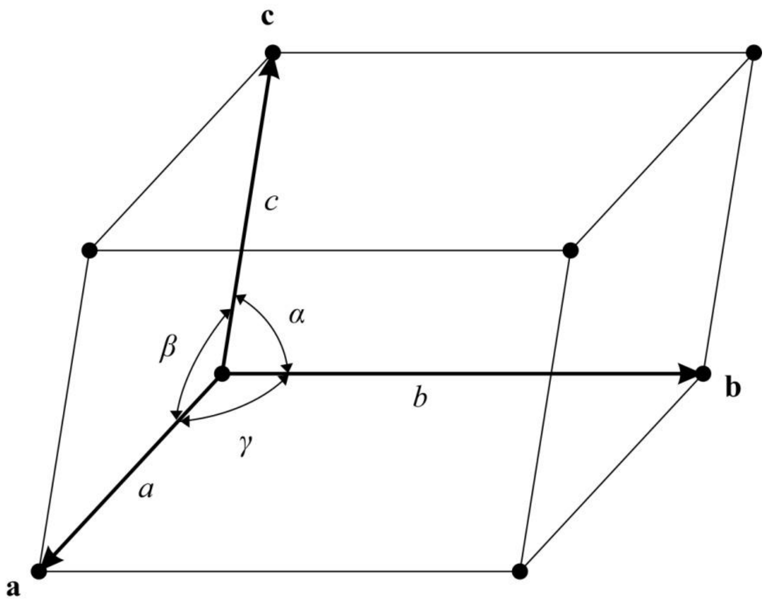

Figure 2.1: Illustration of lattice vectors and included angles (a, b, c and α, β, γ) [22]

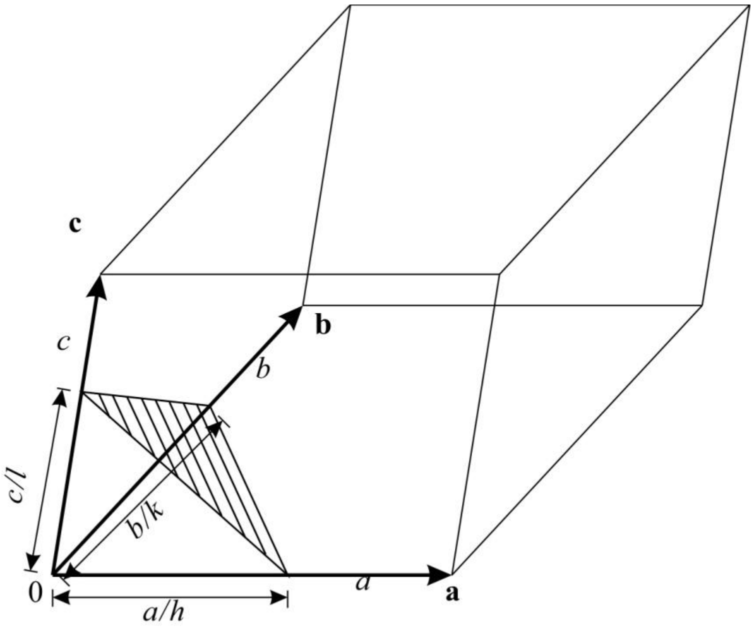

Figure 2.2: Plane designation by Miller indices [22]

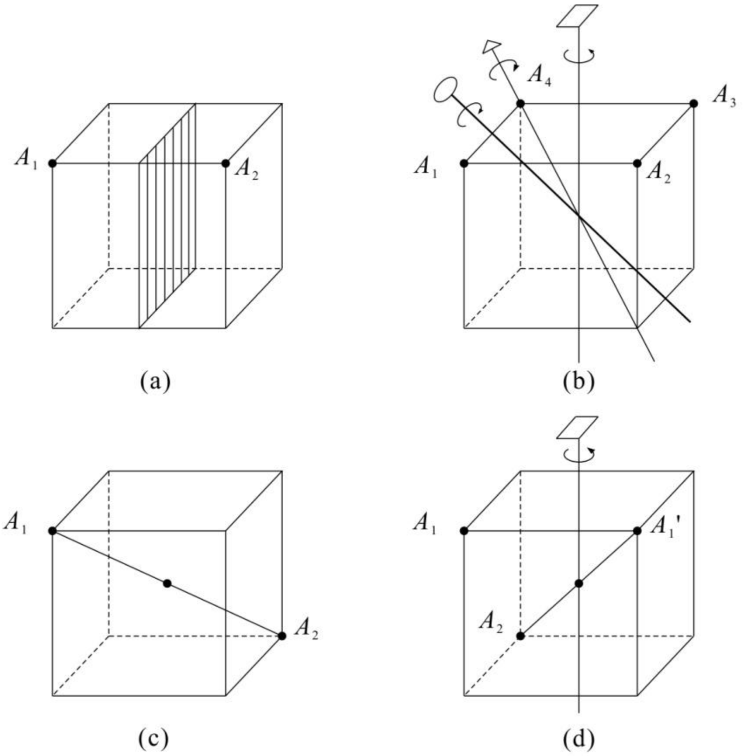

Figure 2.3: Some symmetry elements in a cubic crystal. (a) Reflection plane (b) Rotation axes, 4-fold axis; 3-fold axis; 2-fold axis (c) Inversion centre. (d) Rotation-inversion axis, A_1 becomes A_1' (4-fold axis) and then A_1' becomes A_2 (Inversion centre) [22]

Table 2.1: Seven Crystal Systems and Bravais Lattices

Crystal system	Axial lengths	Angles	Bravais lattice	Lattice symbol
Cubic	a=b=c	α=β=γ=90°	Simple Body-centred Face centred	P I F
Tetragonal	a=b≠c	α=β=γ=90°	Simple Body-centred	P I
Hexagonal	a=b≠c	α=β=90°, γ=120°	Simple	P
Orthorhombic	a≠b≠c	α=β=γ=90°	Simple Body-centred Base-centred Face-centred	P I C F
Trigonal	a=b=c	α=β=γ≠90°	Simple	P
Monoclinic	a≠b≠c	α=γ=90°≠β	Simple Base-centred	P C
Triclinic	a≠b≠c	α≠β≠γ≠90°	Simple	P

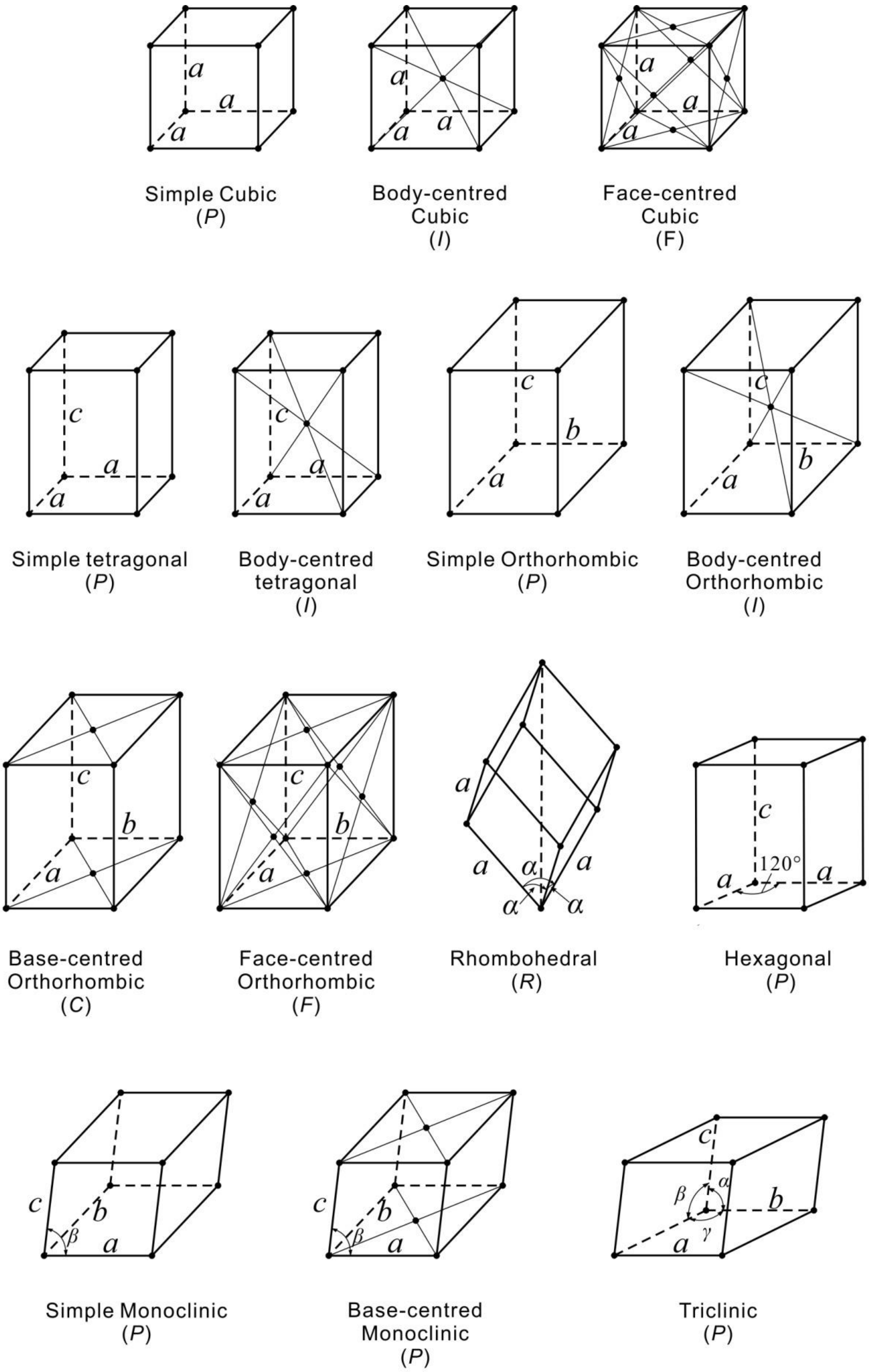

Simple Cubic
(*P*)

Body-centred
Cubic
(*I*)

Face-centred
Cubic
(F)

Simple tetragonal
(*P*)

Body-centred
tetragonal
(*I*)

Simple Orthorhombic
(*P*)

Body-centred
Orthorhombic
(*I*)

Base-centred
Orthorhombic
(*C*)

Face-centred
Orthorhombic
(*F*)

Rhombohedral
(*R*)

Hexagonal
(*P*)

Simple Monoclinic
(*P*)

Base-centred
Monoclinic
(*P*)

Triclinic
(*P*)

Figure 2.4: The Fourteen Bravais Lattices [22]

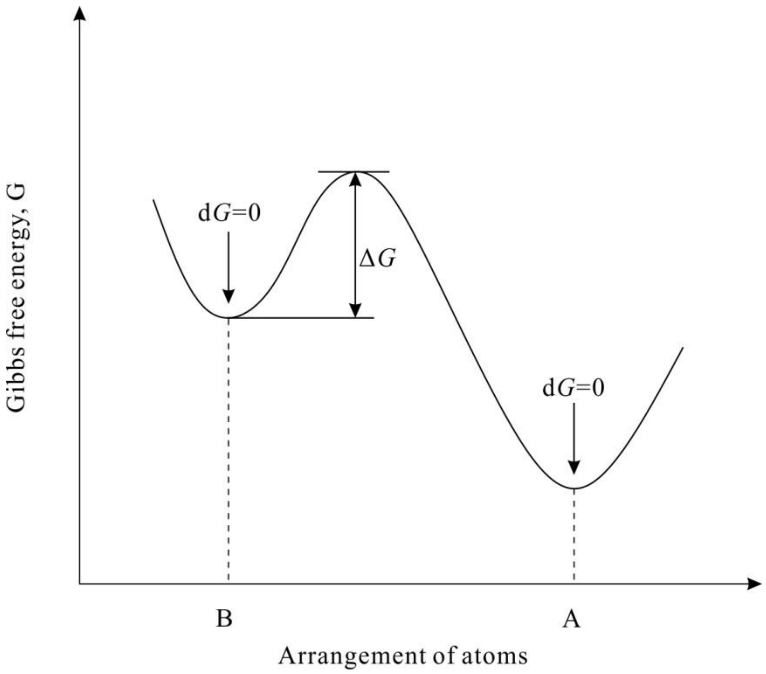

Figure 2.5: Schematic variation of Gibbs free energy of 'local' (B state) and 'global' (A state) equilibrium [23]

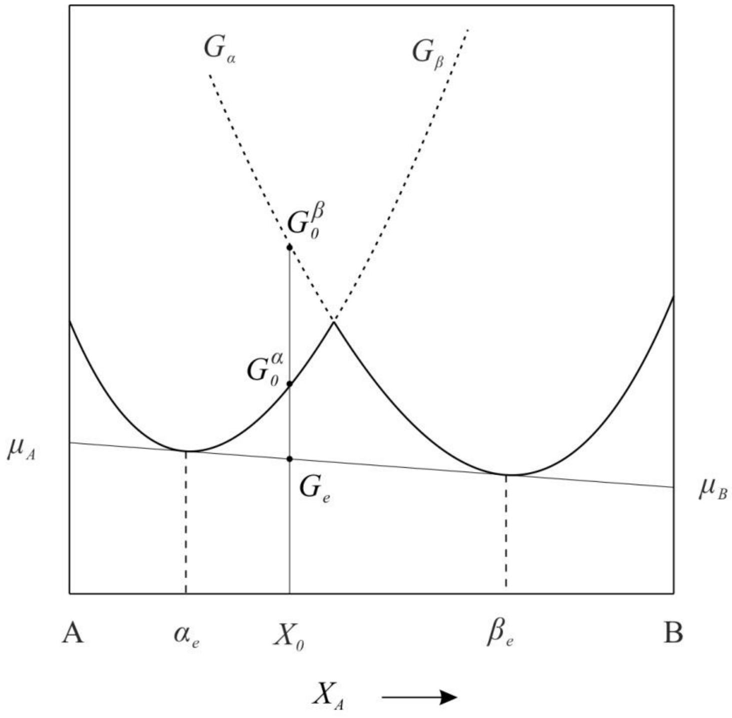

Figure 2.6: A schematic diagram of chemical potential. X_A is the mole fraction of A. G_α and G_β are Gibbs free energy of α and β phases [23]

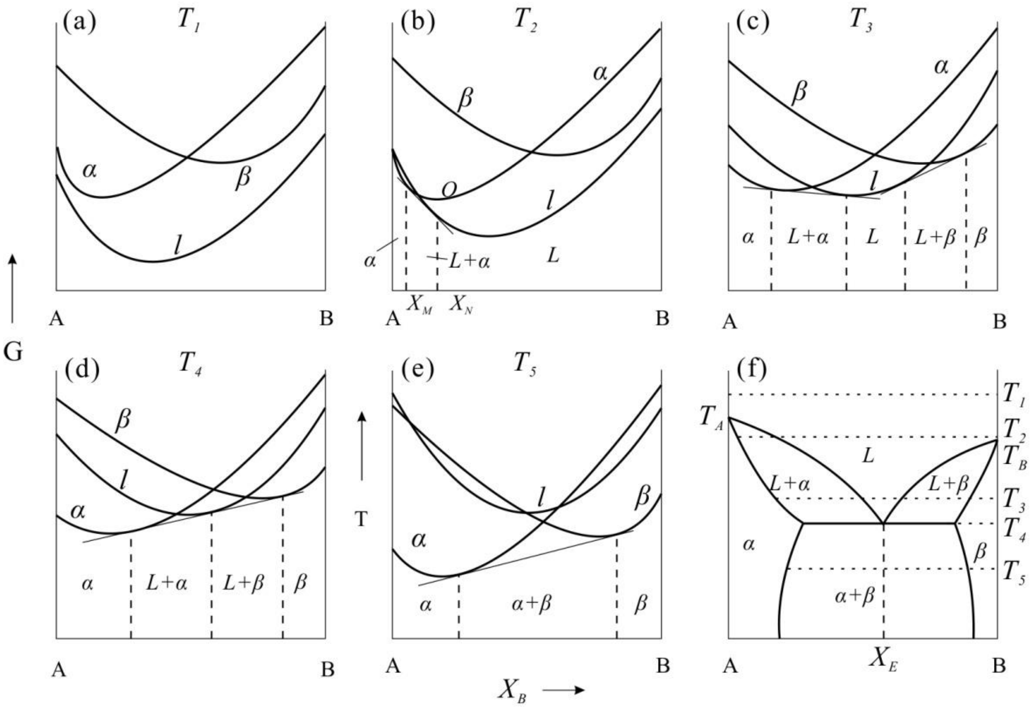

Figure 2.7: The derivation of a eutectic phase diagram [23]

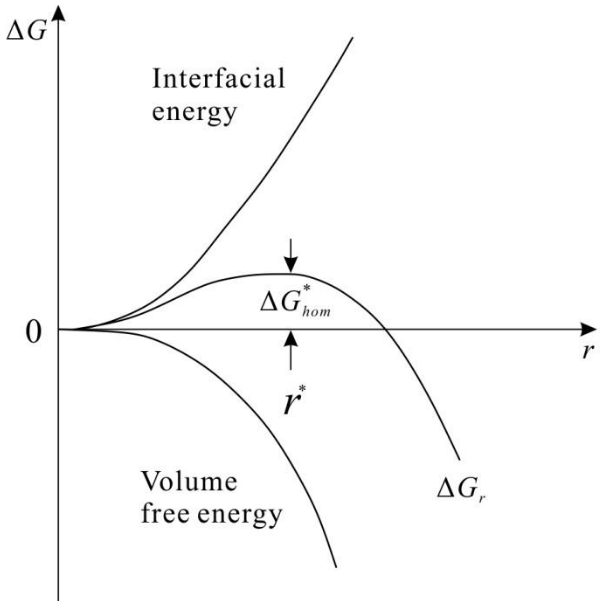

Figure 2.8: Free energy change associated with homogeneous nucleation of a sphere of radius r [23]

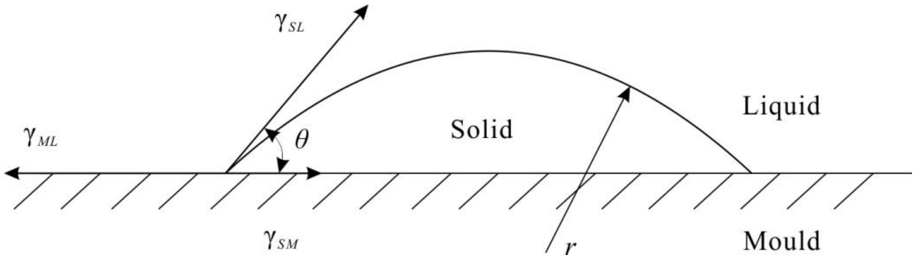

Figure 2.9: Heterogeneous nucleation of a spherical cap on a flat mould wall [23]

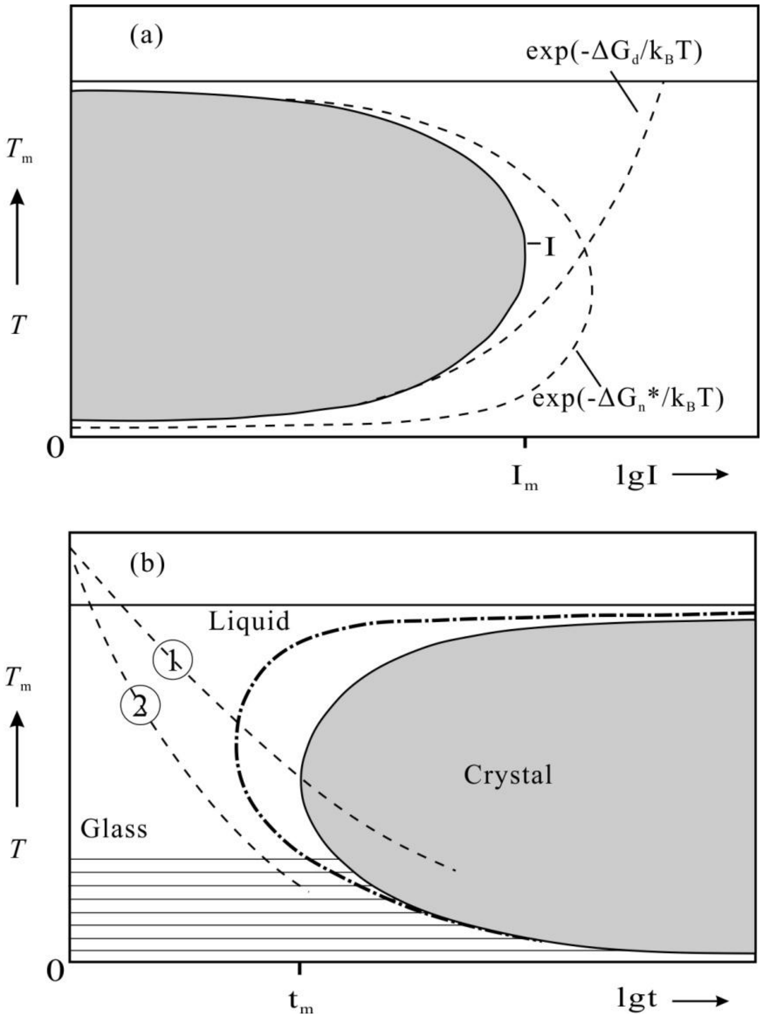

Figure 2.10: Nucleation Rate and Nucleation Time as a Function of Absolute Temperature [19]

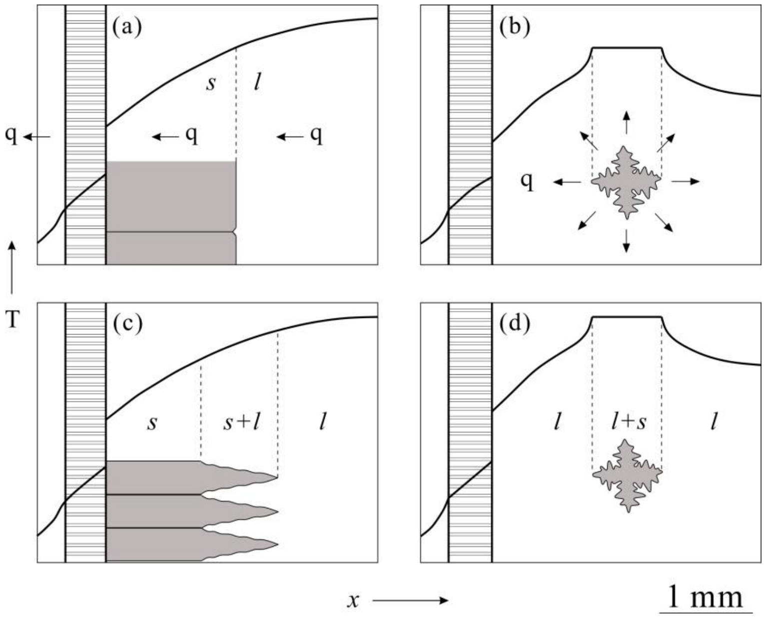

Figure 2.11: Temperature distribution and solid/liquid interface morphology. (a) and (b) show the solidification of the pure metals, while (c) and (d) show the solidification of the alloys. (a) Planar interface; (b, d) Equiaxed growth; (c) Dendritic growth [19]

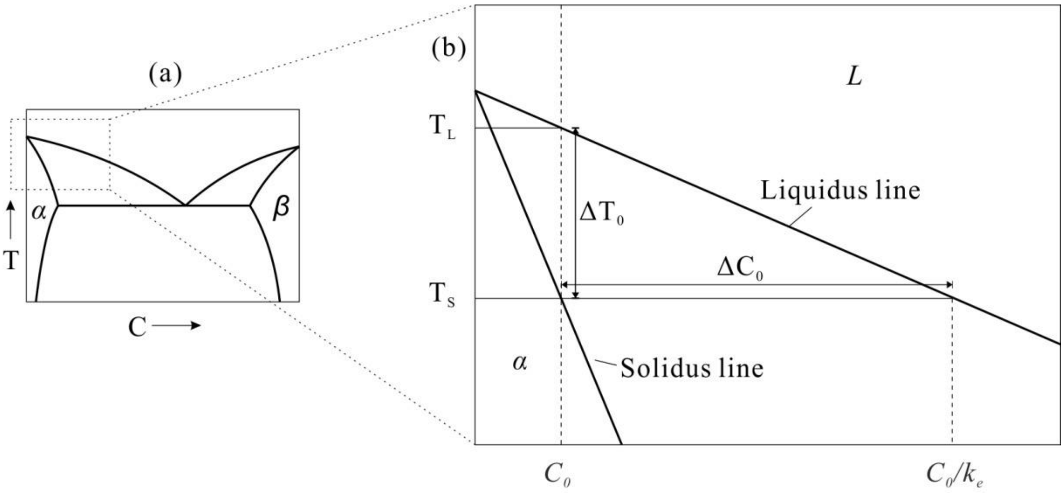

Figure 2.12: Schematic diagram of solid/liquid equilibrium. The equilibrium distribution coefficient, k_e, and the liquidus slope, m, are constant [19].

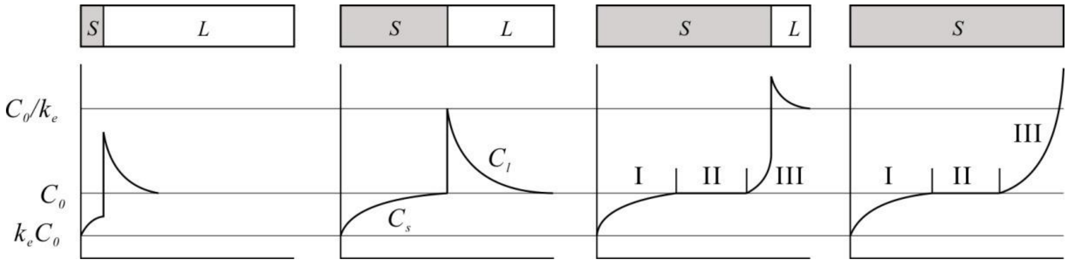

Figure 2.13: Solute distribution for non-equilibrium solidification. No diffusion in solid, limited diffusion in liquid [25].

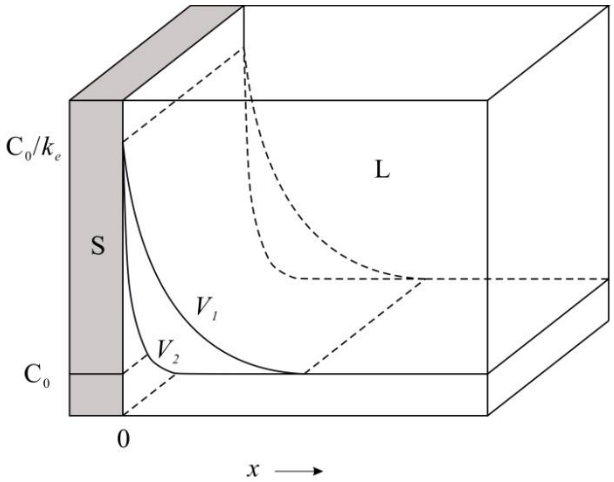

Figure 2.14: Steady-state boundary layer at a planar solid/liquid interface. The composition of the liquid decreases from C_0/k_e at the interface to the nominal value C_0, far from the interface. [19]

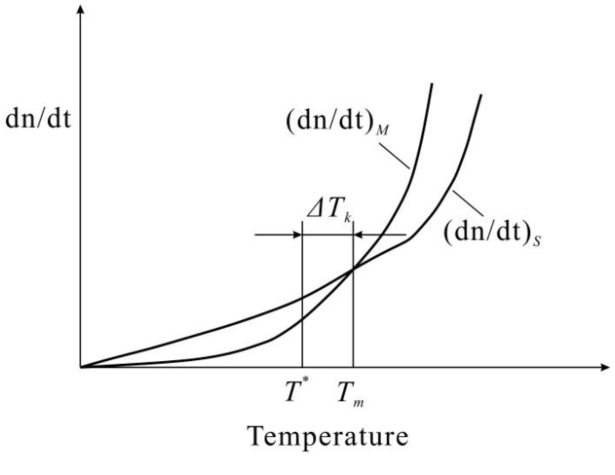

Figure 2.15: Description of the requirements for kinetic undercooling [25]

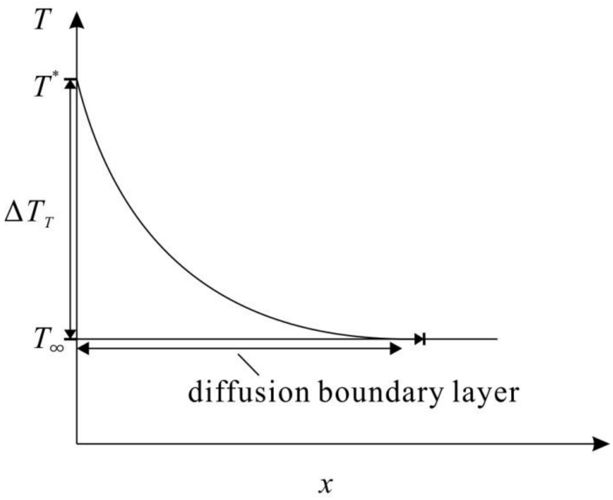

Figure 2.16: Thermal undercooling [25]

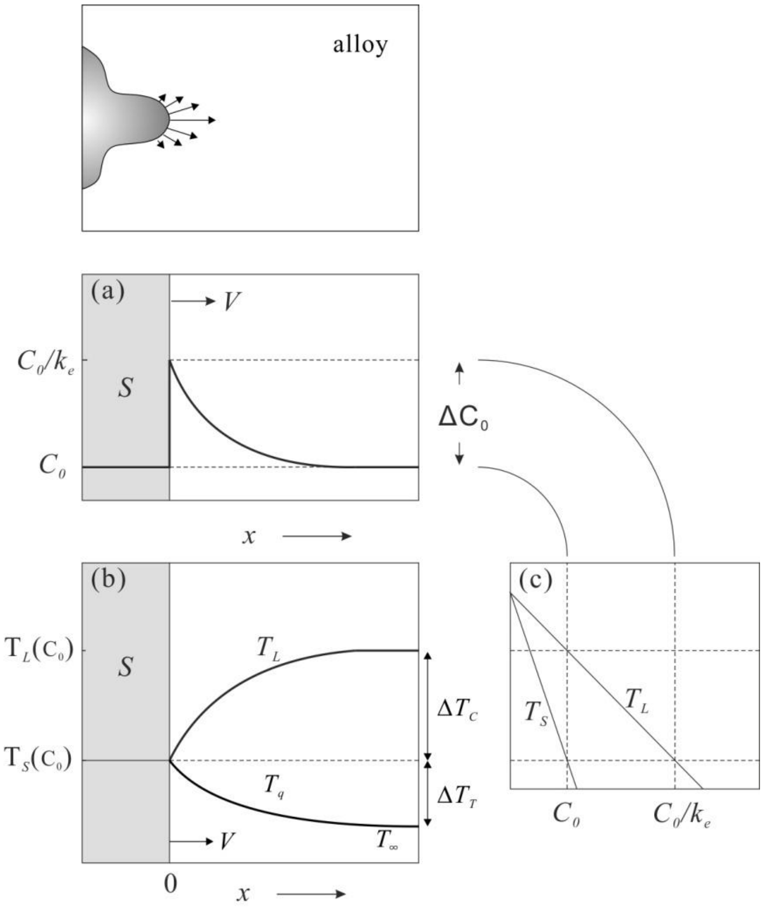

Figure 2.17: Constitutional undercooling in alloys. $T_L(C_0)$ and $T_S(C_0)$ are the liquid and solid temperature corresponding to the initial alloy composition [19].

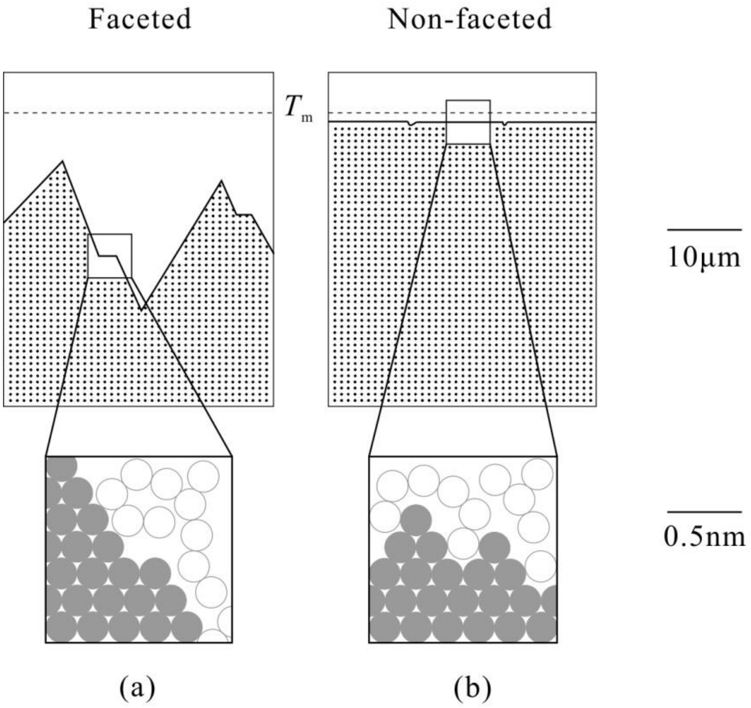

Figure 2.18: Two different kinds of solid/liquid interfaces. (a) Faceted interface with an atomically flat interface (lower diagram), which shows jagged and faceted edges at the microscopic scale (upper diagram); (b) Non-faceted interface with an atomically rough interface (lower diagram), which shows microscopically flat edges with a slight depression [19].

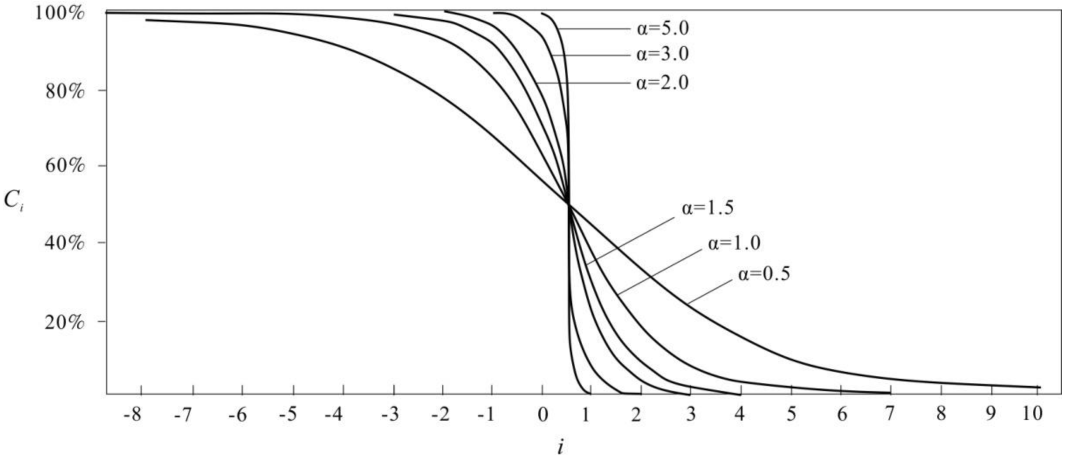

Figure 2.19: Roughness of a crystal surface for various values of α. C_i is the fraction of sites in layer *i* which is occupied by atoms of the crystal [26].

Table 2.2: Hierarchy of equilibrium [19]

Increasing solidification rate/undercooling	I	*Full Diffusional Equilibrium*
		• No chemical potential gradients (phase composition are uniform)
		• No temperature gradients
		• Lever rule applies
	II	*Local Interfacial Equilibrium*
		• Phase diagram gives compositions and temperatures only at liquid/solid interface
		• Corrections made for interface curvature (Gibbs – Thomson effect)
	III	*Metastable Local Interface Equilibrium*
		• Stable phase cannot nucleate or grow sufficiently fast
		• Metastable phase diagram gives the interface conditions
	IV	*Interface Non-Equilibrium*
		• Phase diagram fails at the interface
		• Chemical potentials are not equal at the interface
		• Free energy functions of phases still lead to criteria which predict impossible reactions

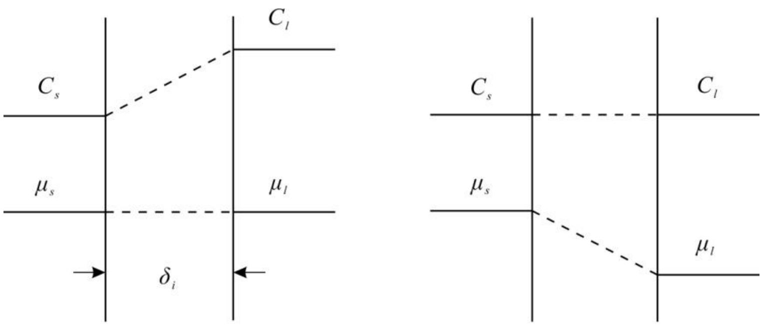

(a) *Interface equilibrium* (b) *Complete solute trapping*

Figure 2.20: Interface composition and chemical potential for equilibrium and diffusionless solidification (complete solute trapping) [25]

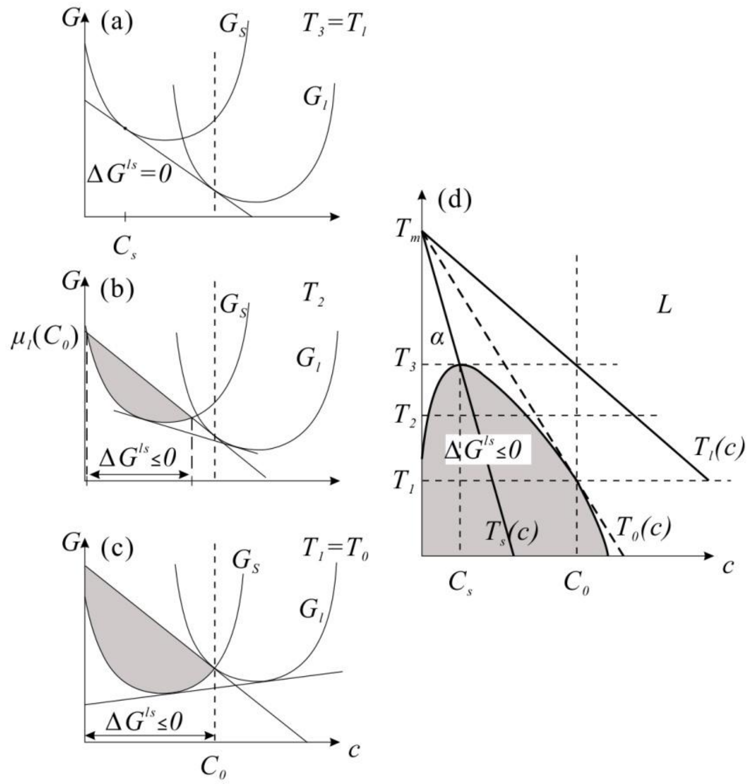

Figure 2.21: The importance of T_0 for diffusionless transformation [19]

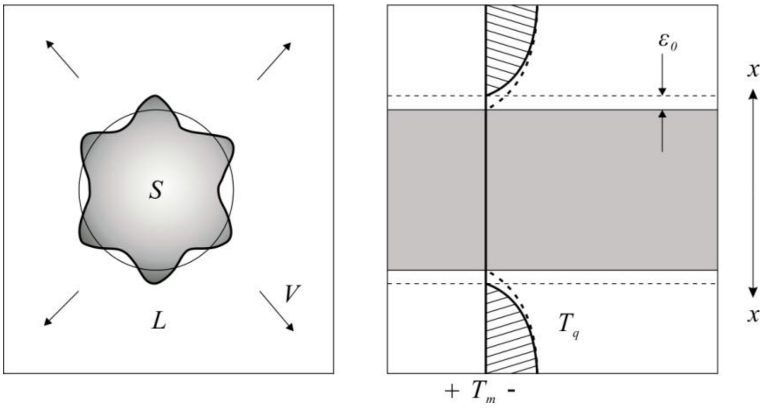

Figure 2.22: Unstable planar development of equiaxed solidification in a pure substance [19]

Table 2.3: Some preferred dendrite orientations of example materials [19]

Structure	Dendrite Orientation	Example
face-centred cubic	<100>	Al
body-centred cubic	<100>	δ-Fe
body-centred tetragonal	<110>	Sn
hexagonal close-packed	<10-10>	H_2O (snow)
	<0001>	$Co_{17}Sm_2(Cu)$

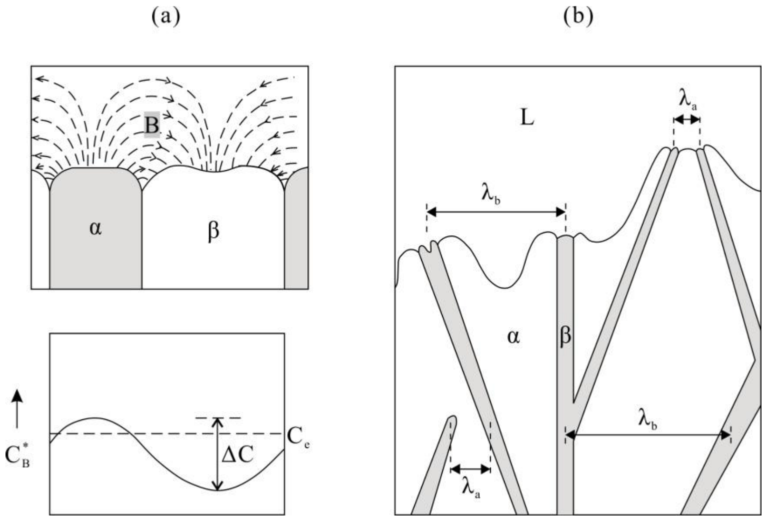

Figure 2.23: Growth models of regular eutectic (a) and irregular eutectic (b) structure [19]

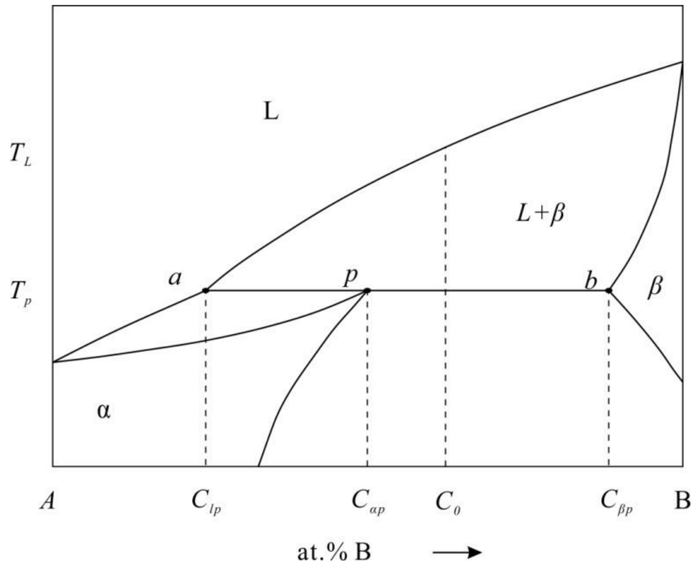

Figure 2.24: A hypothetical peritectic phase diagram [37]

3 Literature Review

In this project, the studies will focus on rapid solidification of intermetallic compounds. Therefore, the formation of the non-equlibrium solid states will be introduced firstly. Then the basic concept of intermetallics, their properties and the trials to overcome their weakness are introduced briefly as well. The main purpose of this chapter is to summarize the non-equilibrium studies in the Ni-rich portion of the Ni-Si binary system and Ni-Fe-Si ternary system, as well as some similar alloy systems. Finally, the aim of this project is presented.

3.1 Possible phase state under non-equilibrium condition

Normally, the possible phase state and morphology can be predicted by using the equilibrium phase diagram. However, rapid solidification always causes departure from equilibrium during the solidification process. Such non-equilibrium conditions, due to high undercooling and high cooling rate, favour producing supersaturated solid solutions, grain refined microstructures, metastable crystalline phases, quasicrystalline alloys and even metallic glasses, which will be further reviewed in this section.

3.1.1 Supersaturated solid solutions

During rapid solidification, it is very common that an extended primary solid solution forms from the liquid. In this process, partial solute trapping occurs in which the solid phase contains more solute than that from equilibrium conditions, that is, a supersaturated solid solution.

As can be seen from **Figure 3.1**, for an alloy of nominal composition c_0, α-phase of concentration c_s may be formed in the temperature interval $\Delta T_0 = T_L - T_e$, where T_e is the eutectic temperature, during the solidification processing. Moreover, if β-phase nucleation is avoided (e.g. α and β have different crystallographic structures), the remaining melt will undercool at a temperature T_1 ($T_1<T_e$) and solidify to a supersaturated α_{ss} solid solution with the concentration corresponding to the metastable extension of the solidus.

Due to recalescence, the temperature will rise to T_0 (**Figure 3.1**b) and the supersaturated solid α_{ss} will transform into a stable α crystallite. On the contrary, if the melt could be undercooled below its hypercooling temperature, T_{hyp} (**Figure 3.1**c), the metastable supersaturated phase will be frozen even at moderate cooling rates [10].

3.1.2 Grain refinement

Refined grain microstructure is considered as one of the factors controlling room ductility of the intermetallic compounds and their benefits have long been appreciated in metallurgical and materials science fields and their production is of continuing technological interest.

Conventionally, grain refinement is achieved by extrinsic mechanical or chemical means. In the first case, grain multiplication results from a fragmentation of the early primary dendritic skeleton using the methods of vigorous stirring during solidification, e.g. vibration [38]. In the second case, some inoculants were added into the liquid in order to increase the density of the nucleation sites and their potency within the liquid [39]. In rapid solidification processing, grain refinement is just one form of microstructural refinement, which includes reductions in dendrite arm spacing, eutectic spacing, and the scale of chemical inhomogeneity, and here, it is intrinsic to solidification processing itself by contrast with conventional solidification processing.

Several mechanisms have been discussed to explain the physical origin of the grain refinement at the critical undercoolings. Grain refinement in undercooled melts was first reported in pure Ni melts in 1956. The grain size abruptly decreased by about 1-2 orders of magnitude when the initial melt undercooling, ΔT, prior to nucleation exceeded a critical value, ΔT^*, a sharp transition region between 140 and 150 K. Since the occurrence of the grain size reduction was accompanied by the emission of sound waves, it was concluded that the refinement resulted from the copious homogeneous nucleation, which is induced by the pressure pulse generated from the collapse of shrinkage cavities. Later, Horvay [40] studied and provided numerical (theoretical) estimates involving the pressures, flow velocities, and time scales, and concluded the grain refinement resulted in copious nucleation due to a pressure pulse. However, these experiments could not be repeated.

More complex behaviour was found in the Ni-Cu alloy system. As can be seen from **Figure 3.2**, the microstructure changes if the undercooling of a $Cu_{70}Ni_{30}$ sample is varied [41, 42]. At small undercoolings a grain refined equiaxed microstructure appears, which changes at a critical undercooling ΔT_1^* to a coarse-grained dendritic microstructure, and then the structure re-enters the grain refined equiaxed microstructure exceeding a critical undercooling ΔT_2^* . This widely observed transition in solidification from a coarse grained dendritic to a grain refined equiaxed microstructure is attributed to the fragmentation of dendrites by remelting during the period following recalescence. In this case, a simple model by Karma [43], is presented to predict the occurrence of these transitions, which involves two characteristic time scales: the dendrite break-up (t_{bu}) time, corresponding to the recalescence time, and the thermal plateau time, corresponding to the post-recalescence solidification period (t_{pl}). According to this model, the transition is possible when it satisfies the condition of $t_{\mathrm{bu}}(\Delta T^*) = t_{\mathrm{pl}}(\Delta T^*)$, and grain refinement can be expected when the thermal plateau time for solidification (t_{pl}) exceeds the time required for break-up of dendrites (t_{bu}). As this model considers only the case of an isolated dendrite, Mullis and Cochrane [44] have presented an extension to this model and pointed out Karma's model cannot work well. They have included the array of dendrites into their study, and found that the wavelength of the instability is a function of the array spacing. According to this relationship, if the array spacing is decreased below a certain value the system is stabilised, in which case the instability of Karma's model is replaced by uniform coarsening. Under these conditions, dendritic fragmentation and grain refinement would have to be considered unlikely.

The microstructure evolution in undercooled Fe-Ge alloy, similar to that in pure Ni, is simpler than the changes in the undercooled Ni-Cu. Biswas et al. [45] reported that the grain size dropped suddenly for the sample of Fe-19 at.% Ge undercooled by 130 K. Neither copious nucleation nor dendrite fragmentation has been used to explain the grain refinement here. One EBSD grain map was produced from the solidification of undercooled Fe-Ge alloy with undercooling at 130 K, in which there were a large number of low-angle grain boundaries in the high undercooled samples. This phenomenon is inconsistent with the dendrite fragmentation model, in which the orientation of the fragments should be randomized by the convective flow. They show that the low-angle boundary clearly indicates a recovery process and the presence of growth twins indicates a recrystallization process. Also, in a previous study, Dragnevski et al. [46] reported the microstructural development in pure Cu samples using a melt-fluxing technique. They found that grain refined microstructures in pure Cu (O_2 < 60 ppm) occurred at the highest achieved undercooling, about 352 K, but the segregation pattern was predominantly dendritic with no presence of spherical elements in individual grains at high undercooling, which would suggest recrystallisation, rather than fragmentation. Also they measured the microhardness under different undercooling, and found that the microhardness dropped significantly at undercooling around 315 K, which supported the deduction.

Furthermore, Mullis and Cochrane presented an analysis of the stability of a dendrite against a small perturbation to the tip velocity, which demonstrated that dendritic growth should be unstable below a lower critical undercooling and above some upper critical undercooling [47]. Also, they proposed a model for spontaneous grain refinement based on repeated multiple tip splitting [48], and got the experimental evidence in deeply undercooled ultrahigh purity Cu at a undercooling of 280 K. Numerous ridges or channels existed that can be associated with dendrite tip splitting [49].

3.1.3 Metastable crystalline phases

In equilibrium solidification processes, the components in the as-solidified materials should be in the most stable state (**Figure 2.5**), while in rapid solidification processes, e.g. high cooling rate or high undercooling, the metastable crystalline phases might be favourable. As can be seen from **Figure 3.3**, the temperature $T_{e\alpha}$ is the equilibrium temperature. If the temperature decreases under $T_{e\alpha}$, the α phase will form. If nucleation of α is suppressed, the β metastable solid will form while the temperature is lower than $T_{e\beta}$. Similarly, if nucleation of both α and β are suppressed, metastable phase γ forms under high undercooling. That is, undercooling is necessary for metastable crystalline phases to form [25]. Metastable crystalline phases can form in an undercooled melt not only relying on spontaneous nucleation, but also by using a particular substrate as a seed to trigger solidification, by which a desired phase can be formed. In the research of the Fe-Ni system, at low nickel concentrations, the metastable bcc phase crystallizes primarily, followed by a secondary fcc solidification, which can be revealed by the detected rapid recalescense. At higher nickel content, using a nucleation trigger made from Fe-Mo alloy, with a bcc structure, metastable bcc phase can also be formed, although the fcc phase is stable and can nucleate spontaneously in this region [50].

There are also lots of high temperature phases existing in the phase diagram, e.g. peritectic phases in Cu-Sn alloy systems and β_2 and β_3 phases in Ni-Si alloy systems. These phases might be attained in the solidified alloys due to lower solute diffusion rate in solids, however, they will disappear in a reasonable heating process. At increasing cooling rate, new phases with different crystal structure might be solidified and retained as well, e.g. $Ni_{25}Si_9$ (or $Ni_{74}Si_{26}$), which is not labelled in the equilibrium phase diagram. By means of heat treatment, the metastable phase transforms into stable phases, β_1-Ni_3Si and $Ni_{31}Si_{12}$. Such a kind of phase transformation is not reversible and detailed experiments regarding this and the resulting properties will be introduced in the later chapters.

3.1.4 Quasicrystalline alloys

Quasicrystalline phases have attracted much interest in recent years, and have special symmetries, which are forbidden for normal crystals. Icosahedral (I-phase) and decagonal ‘T phase’ are two most common quasicrystalline symmetries, and many liquid metals show short range icosahedral ordering. The Icosahedral symmetry is quasiperiodic in three dimensions, and the decagonal one is quasiperiodic in two dimensions and periodic in the third. The required critical cooling rate for the formation of a quasicrystalline phase is lower than that of metallic glass, and therefore should be slow enough to permit its formation but rapid enough to prevent crystallization [51].

For the first time, Shechtman et al. [51] formed a metallic solid with long-range orientational order, but with icosahedral point group symmetry in rapid cooled a Al-Mn alloy. Furthermore, they found that the icosahedral phase was stable at 300 ℃ for 6 h and at 350 ℃ for 1 h and transformed to the stable Al_6Mn phase at 400 ℃ for 1 h. Many quasicrystalline phases are metastable and mostly formed by peritectic reactions. However, not all of the quasicrystalline phases are metastable. The DSC result of quasicrystals of Ga-Mg-Zn formed by Ohashi and Spaepen [52] shows no exothermal peaks at low temperature, and the endothermic peaks presented at high temperatures correspond to the peritectic melting temperature. Moreover, after heat treatment at 638 K for 52 h, the icosahedral phase did not induce any transformations and the electron diffraction pattern remained unchanged. Likewise, studies by Tsai et al. [53, 54] on Al-Cu-Fe, Al-Pd-Mn and Al-Pd-Re alloy systems also support the stable property of some quasicrystals.

3.1.5 Metallic glasses

Further increasing the cooling rate of the liquid alloy, exceeding a critical value, when the temperature is lower than its glass transition temperature, it will ‘freeze’ as a vitreous solid without appreciable crystallisation, that is, metallic glass, or amorphous alloy. The cooling rate must be high enough, and therefore cannot cross the nucleation line (**Figure 2.10**b). Just as described by Telford, ‘metallic glass is less brittle than oxide glass and looks like a metal – opaque, grey, shiny, and smooth’ [55].

Amorphous alloys are non-crystalline materials, so they possess better resistance to wear and corrosion owing to the absence of grain boundaries which remove the weak spots of crystalline materials. Also, the amorphous metals are much tougher and less brittle than oxide glasses and ceramics. In addition, for crystalline magnetic materials there exists crystallographic directions along which the magnetic moments try to align, which subsequently makes it more difficult to switch the direction of the magnetisation. In a glass, with no preferred orientation direction the switching is easier. Moreover, the grain boundaries can act to pin domain wall motion, again preventing switching of the magnetisation direction. In a glass there are no grain boundaries. Therefore, some amorphous alloys possess soft magnetic properties, specifically the alloys of glass formers (B, Si, P) and ferromagnetic transition metals (Fe, Co, Ni) [54]. High electrical resistance leads to low losses by eddy currents, which allows for transformer magnetic cores. Compared with the crystalline alloys, the metallic glasses of similar chemical composition tend to be stronger and have high elasticity but low plasticity. With the discovery of bulk metallic glasses and the development of the composites, the most useful property is that they soften and flow upon heating, which allows material for easy processing. As a result, amorphous alloys have been commercialized for use in sports equipment, medical devices, and even for electronic equipment, information storage materials and biomaterials [56].

According to thermodynamic analysis, a metallic liquid is unstable at temperatures below its melting temperature, and has the tendency to solidify into a crystalline solid. So the pre-condition of glass forming is keeping the metallic liquid stable in a supercooled state. Therefore, to form a glass, crystallization must be suppressed, no matter whether it is homogeneous or heterogeneous. So, the first thing which needs to be done is to circumvent potent nucleation sites, such as the container walls and impurities, to avoid heterogeneous nucleation and achieve high undercooling.

Eutectic regions in the phase diagram are the most likely area for metallic glass formation due to the requirement of long-range diffusion to form the stable phases. At high solidification velocity, solute trapping will occur, and if k=1, partitionless solidification will occur. As is indicated from **Figure 2.21**, T_0 is the upper limit temperature for partitionless solidification. For the eutectic composition, there exist two T_0 lines, as shown in **Figure 3.4**. With a small solid solubility, the T_0 lines drop steeply and cross the glass transition temperature of the system. In addition, eutectic alloys usually possess the low melting temperature and therefore can be easily frozen to glass transition temperature [10].

In 1960, Duwez produced the first metallic glass of Au-Si alloys, near the eutectic composition, using rapid quenching with high cooling rates [57]. Later, Chen [58, 59] cooled alloys of the Au-Ge-Si system to an amorphous solid using splat cooling. With the presence of the melt spinning process for commercial manufacture of metallic glass ribbons, lines, and sheets, metallic glasses developed more quickly in the early 1970s and 1980s. However, the requirement of high cooling rate constrains the dimension of amorphous alloys being thin sheets or lines. Great development of metallic glass has been boosted by strengthening the glass-forming ability in multi-component systems due to increased complexity. Based on this, the bulk metallic glasses with large critical dimensions were formed, such as Pd-M-Si(with M=Au, Ag, or Cu) [60], Pd-Ni-P [61, 62], La-Al-*TM* (*TM* = Ni, Cu or Co) [63-65], and Zr-based alloys [66-68]. Some examples of amorphous alloys and their corresponding experimental parameters are listed in **Table 3.1**. In particular, the Pd-Cu-Ni-P alloys were proved to have good glass-forming ability, especially for $Pd_{42.5}Cu_{30}Ni_{7.5}P_{20}$, since it has the lowest critical cooling rate (about 0.067 K s^{-1}) for glass formation [69].

Duwez also obtained an amorphous phase in Pd-Si alloys, which were stable at room temperature and no crystallization occurred after one month at 250 ℃ [70]. Later, Yao and Fang [71] produced bulk Pd-Si metallic glasses with the diameter being about 6mm even at a slow cooling rate about 8 K s^{-1}. Also, amorphous powder of Ni-Ti alloy has been formed by high-energy ball alloying, as well as some amorphous alloys formed in Ni-based alloy systems, such as Ni-P, Ni-Fe, Ni-B and Ni-Zr [72-76]. As for the Cu-Zr alloy system, the critical casting thickness of $Cu_{64}Zr_{36}$ metallic glass is 2mm by the copper mould casting method [77].

The element, Fe, is also a ferromagnetic transition metal, and some Fe-based amorphous has been also reported, such as $Ni_{49}Fe_{29}P_{14}B_6Si_2$ and Fe-rich Fe-B-Si alloy [78]. Fe-based amorphous metals, especially for bulk metallic glasses (BMGs), are more attractive for engineering application, because they possess many good properties, such as ultra-high strength, good magnetic property, good anti-corrosion property and so on. In addition, they are much cheaper than other BMGs. Especially, the critical size of Fe-based BMGs has been significantly increased recently, which will promote their application as structural and magnetic materials [79-82].

Compared to polycrystalline metals, amorphous alloys have high elasticity and low plasticity. Since the absence of grain boundaries enhances the shear band propagation, their industrial and structural applications have been limited. Therefore, in order to improve their properties, the metallic glass composite emerges, which is reinforced by increasing a ductile crystalline-phase into the amorphous phase (so-called matrix). This can be achieved in two ways: one by adding some metal, ceramic fibres or particles into the matrix, and the other is inducing new phase forming from the melt during the cooling process directly [55].

3.2 Intermetallic compound

Intermetallic compounds are solid phases containing two or more metallic elements, sometimes even with only one or more non-metallic elements. Different from the solid solution phase where the various elements substitute randomly, different elements in intermetallic compounds are ordered into different sites in the structure forming a new crystal different from that of any other constituent. Moveover, the bonds in the intermetallics take on a mixed character, becoming partly metallic, partly covalent and partly ionic, which also gives rise to their properties that are intermediate between those of metals and ceramics. Intermetallics often have a stoichiometric or near stoichiometric composition, e.g. the β_1-Ni_3Si phase has a homogeneity range of 22.6-24.5 at.% Si and the Si composition of γ-$Ni_{31}Si_{12}$ is precise at 27.91 at.%, as shown in **Figure 3.5**.

For at least the past four decades, intermetallic compound materials have been paid great attention for their potential application as high temperature structural and non-structural materials, due to the possibility of combining the ductility of metals and the strength and oxidation resistance of ceramics. One such intermetallic is the βNi_3Si compound for its high melting point, excellent oxidation resistance and great hardness at elevated temperatures. However, like many other intermetallics, it is also brittle at room temperature, which restricts its application owing to fabricating difficulties [3-7].

One potential route to overcome this difficulty is to form intermetallic-metal matrix composites by incorporating a ductile phase into the brittle matrix or solidifying a ductile phase from original melts, like eutectic transformation. The latter is so-called in situ composites [8, 9] and directional solidification is an optional method to obtain the layered composite structures [83]. Another potential route to improve this weakness is non-equilibrium processing via rapid solidification, with the resulting fine grain structure [10-12] and the presence of anti-phase domains and disorder-order structures increasing room temperature ductility [13, 14].

The thesis focuses on the rapid solidification of Ni- 25 at.% Si alloy in 6.5 m drop tube, which allows study of the solidification properties of βNi_3Si, microstructure evolution and phase formation at high cooling rates. In the subsequent stage, the alloy will be extended to the Ni-Fe-Si ternary system with 10 and 15 at.% Fe to investigate the possible differences caused by Fe.

3.3 The Ni-Si binary and Ni-Fe-Si ternary alloy systems

The Ni-Si phase diagram is one of the very complex phase diagrams, especially on the Ni-rich part, and has been corrected many times. The evaluated phase diagram compiled by Massalski et al. [84] is shown in **Figure 3.5**. There are two eutectic reactions in the Ni-rich part, with the alloy compositions being Ni-21.4 at.% Si and Ni-29.8 at.% Si. The eutectic, peritectic and eutectoid reactions in the Ni-rich part are listed in **Table 3.2**. According to the phase diagram, disordered β_3 phase can be precipitated via a peritectic reaction $L + \gamma \rightarrow \beta_3$ at 1170 °C. β_1-Ni_3Si can be formed via the peritectoid reaction α-Ni + $\beta_2 \rightarrow \beta_1$ at 1035 ℃ and also through the eutectoid decomposition $\beta_2 \rightarrow \beta_1 + \gamma$. Obviously, the Ni-Si phase diagram indicates a more complex equilibrium solidification path for the Ni-25.3 at.% Si alloy. As the melt cools down, the primary phase would be γ-$Ni_{31}Si_{12}$, which would transform to β_3-Ni_3Si via a peritectic reaction below 1443 K. There is an ordered and disordered transformation between β_3-Ni_3Si and β_2-Ni_3Si below 1388 K, before finally transforming to β_1-Ni_3Si and γ-$Ni_{31}Si_{12}$ via a subsequent eutectoid reaction. In addition, there is one metastable phase [85], $Ni_{25}Si_9$, which is not included in the equilibrium phase diagram and generally can be obtained at rapid solidification process, e.g. rapid quenching [86] and melt spinning [87].

The rapid solidification experiments in the second stage of this investigation were concerned with the $Ni_{64.7}Fe_{10}Si_{25.3}$ and $Ni_{59.7}Fe_{15}Si_{25.3}$ alloys (with the substitution of 10 and 15 at.% Fe for Ni in primary Ni-25.3 at.% Si alloy). From the Ni-Fe phase diagram (**Figure 3.6**), it is clear that Fe and Ni can form a continuous solid solution phase in some temperature regions. Chemically, Ni and Fe are very similar, so direct substitution of Fe for Ni would be expected at such levels of Fe doping. The Ni-Fe-Si ternary phase diagram can be calculated using MTDATA software [88], and the Ni-rich part of the phase diagram is shown in **Figure 3.7**. All of the α, β and γ phases have their stable regions in the Ni-Fe-Si ternary phase diagram, which also supports the substitution possibility between Fe and Ni. The equilibrium solidification process of $Ni_{64.7}Fe_{10}Si_{25.3}$ and $Ni_{59.7}Fe_{15}Si_{25.3}$ alloys is to the primary growth of the γ-$Ni_{31}Si_{12}$ phase. The composition of the remaining liquid would depart from the Ni-Si axis due to Fe being rejected from the solid and eventually solidify into the α and γ phases via a eutectic reaction. Moreover, the vertical section of the isopleth phase diagram was calculated using MTDATA software as well (**Figure 3.8**). The melting temperatures of $Ni_{64.7}Fe_{10}Si_{25.3}$ and $Ni_{59.7}Fe_{15}Si_{25.3}$ alloys are confirmed to be about 1444 K and 1402 K. From **Figure 3.8** it is clear that the final phases in the solidified sample should be the α and γ phases. If the undercooling is extremely high, the solid solution of the BCC phase might also be formed, e.g. $\Delta T > 496K$ for $Ni_{59.7}Fe_{15}Si_{25.3}$ alloy.

3.4 Crystal structures of the potential phases

In this project, the phases possibly involved are α solid solution, the β phase (β_1, β_2 and β_3), γ-$Ni_{31}Si_{12}$ and the metastable $Ni_{25}Si_9$ and $Ni_{74}Si_{26}$ phases. Solid solution α-Ni has the same structure as the pure Ni (Fcc) [89]. There are three different kinds of Ni_3Si, the low temperature form (β_1) and high temperature forms (β_2 and β_3). Intermetallic β_1-Ni_3Si has the ordered $L1_2$ crystal structure with the similar structure and cell parameters of α-Ni, as shown in **Figure 3.9**. Generally, the ordered $L1_2$ phase and α-Ni are treated as co-existing in solidified Ni-Si alloys with Si composition lower than 27.9 at.%. The only clear difference is that β_1-Ni_3Si has additional XRD diffraction peaks, e.g. (100) and (110), which present as the super-lattice spots in TEM diffraction patterns because the Ni and Si in β_1-Ni_3Si occupy different lattice points. The origin of the difference will be explained in the next chapter. Similarly, both the γ-$Ni_{31}Si_{12}$ and metastable $Ni_{25}Si_9$ are hexagonal structures giving rise to complex diffraction patterns. Although it seems easy to identify the $Ni_{31}Si_{12}$ and $Ni_{25}Si_9$ from XRD results, it is very difficult to distinguish them using TEM diffraction patterns unless the diffraction spots corresponding to the largest d-spacing are present. The diffraction patterns of phases[1], α-Ni, β_1Ni_3Si, $Ni_{25}Si_9$ and γ-$Ni_{31}Si_{12}$ are simulated by Crystal Maker software, as illustrated in **Figure 3.10** and **Figure 3.11**. The structures and standard diffraction data of all these phases are listed in Appendix I. The lattice constant 'c' of the $Ni_{74}Si_{26}$ phase (c=28.855 Å) is three times of that of the $Ni_{25}Si_9$ phase (c=9.618 Å), with the same 'b' and 'c' values. Therefore, the structure of the metastable phase $Ni_{74}Si_{26}$ is a stacking variant of $Ni_{25}Si_9$ which gives rise to the difficulty to distinguish these two phases [85]. Moreover, the structure and diffraction data of the $Ni_{74}Si_{26}$ are not complete to date. Therefore, these two metastable phases are treated as the same phase in this project.

3.5 Recent progresses

Considerable attention has been paid to the Ni-rich part of the Ni-Si binary alloy system and many experiments have been carried out to reveal microstructures and properties. The microstructural and mechanical characterization of Ni-Si alloys with

---

[1] The diffraction patterns of β_2, β_3 and $Ni_{25}Si_9$ cannot be presented due to the lack of structural information

increased Si composition have been investigated by Çadırlı et al. [90]. By using the arc-melting technique, four Ni-Si alloys were produced with Si compositions 10, 21.4, 25 and 35 at.%, indicating and showing that the micro-hardness increases with increased Si content. The eutectic microstructure of α and β_1 phases was observed in the solidified Ni-21.4 at.% Si. A similar structure has also been reported by Ercan Karaköse [91]. Moreover, several studies particularly focus on the eutectic alloy, Ni-21.4 at.% Si, aiming to form α-Ni and β_1-Ni_3Si composite materials. The directional solidification method is used and regular eutectic Ni-Ni_3Si structures are formed [32, 92]. Directional solidification experiments were performed at relatively low cooling rate or a controlled cooling rate.

Non-equilibrium processing, such as rapid solidification, gives rise to a number of effects including grain refinement, metastable phase formation and production of non-crystalline phases due to high cooling rate and undercooling, which provides one new possible route to improve the microstructure and properties of metals and alloys. Rapid solidification can be achieved not only by rapid quenching using an external substrate, but also by rapid growth into bulk undercooled liquid and containerless rapid solidifying in protective atmosphere in a drop tube. Up to now, many non-equilibrium studies on the Ni-21.4 at.% Si alloy have been reported. After achieving the highest undercooling at 550 K using a glass fluxing and cyclic superheated method, Liu et al. [93] and Lu et al. [94] observed a complex microstructural evolution from regular lamellar eutectic, via irregular lamellar eutectic, coarse directional dendritic to quasi-spherical eutectic colonies, and fine directional dendrite to superfine anomalous eutectic. The significant grain refinement was attributed to enhanced nucleation rate [95]. Conversely, a study by Goetzinger et al. [96] revealed a gradual transition from lamellar eutectic microstructure ($\Delta T<30$ K) to anomalous eutectic microstructure as the undercooling increased, with the transition being complete at $\Delta T>150$ K. Similarly to the former studies performed by using the arc melting technique or directional solidification method, one common feature here was that only α-Ni and β_1-Ni_3Si were formed in these alloys, a result also found in the drop tube experiment by Çadırlı et al. [86]. However, managing high cooling rate throughout the entire solidification process, the formation of the metastable phase $Ni_{25}Si_9$ was observed by Leonhardt et al. [17] by quenching the undercooled sample onto a chilled substrate and Dutra et al. [87] using a melt-spinning technique to cool down the same alloy.

Recently, Lu et al. [97] have extended their study to include Ni-29.8 at.% Si eutectic alloy, wherein they observed a so-called interlaced morphology. This they attributed to the mechanism that the initial formation of γ-$Ni_{31}Si_{12}$, which subsequently remelted during recalescence to be replaced by an ordered δ-Ni_2Si phase. A transition from a regular to a quasi-regular structure was observed when the undercooling exceeded 340 K, which was attributed to the evolution from a faceted/faceted eutectic to non-faceted/non faceted eutectic [98]. Particularly, a small amount of an amorphous phase was formed at an undercooling in excess of 240 K with a low cooling rate of > 1 K s^{-1} [18], which gave a significant low cooling rate for amorphous phase formation in a binary alloy.

In order to study the properties of the β-Ni_3Si phase, it might be better to perform direct rapid solidification experiments of this specific composition. The first undercooling experiments on the hypereutectic alloy Ni-25.3 at% Si were carried out by Ahmad et al. [15] using a melt-fluxing technique. However, despite obtaining the required undercooling they were unable to obtain the single-phase β-Ni_3Si. Even so, they reported that the detected velocities were extremely low, with a maximum value of 0.018 m s^{-1} at maximum undercooling, 160 K. Indeed, these exceptionally low growth velocities are consistent with the general trend revealed by previous studies of the Ni-Si alloys. **Figure 3.12** shows the various growth velocities of the undercooling experiments of Ni-Si alloys, which indicates that the solidification velocity drops with increasing Si concentration. The highest velocities were measured by Cochrane et al. [16] on pure Ni and Ni-Si alloys with Si composition < 4.09 at.%, with growth velocities of 50-60 m s^{-1} (ΔT=250 K). With Si composition increased to 11.77 at.%, the growth velocities decreased gradually to about 24 m s^{-1} ($\Delta T \approx 260$ K). Furthermore, the maximum growth velocity of Ni-21.4 at.% Si eutectic alloy measured by Leonhardt et al. [17] was only 1.5 m s^{-1} (ΔT=220 K). Recorded low growth velocity by Ahmad et al. [15] proved that the growth velocities are strongly dependent on the Si composition. Secondly, Ahmad et al. [15] observed a eutectic structure at all undercoolings comprising alternating lamellae of single phase γ-$Ni_{31}Si_{12}$ and Ni-rich lamellae containing a mixed structure of β-Ni_3Si and α-

Ni. The solidification pathway experienced two stages: firstly, different from the thermodynamic equilibrium analysis, the direct solidification to β-Ni_3Si from the melt was suppressed, with a α-γ eutectic structure being formed instead in the first stage of the non-equilibrium processing. Secondly, the primary supersaturated α-Ni decomposed to β_1-Ni_3Si and α-Ni via a subsequent eutectoid reaction, which did not change the original lamellae structure morphology of the samples. This two-stage solidification corresponded to the observed double recalescence in the experimental process. Another important result was that small amounts of metastable phase, $Ni_{25}Si_9$ and β_3, were retained in fluxed samples in which a cooling rate of < 10 K s^{-1} would be expected.

In order to reveal the mechanism of the peritectic system, a unidirectional solidification technique has been used in which the samples can be quenched and the peritectic reaction interface can be frozen for further investigation. Study by Fredriksson and Nylén [99] observed the typical microstructure corresponding to the classical peritectic reaction in the Cu-20.wt% Sn system, that primary α-Cu is surrounded by a fairly thick layer of β-$Cu_{0.85}Sn_{0.15}$ intermetallic phase. At a small range of undercooling (ΔT<12K) and a slow solidification rate (1 mm min^{-1}), the volume fraction of primary α-Cu increases again following an initial reduction, while the fraction of secondary β phase increases very quickly after the start of the peritectic reaction and decreased again (ΔT > 8 K). Increasing the solidification rate to 100 mm min^{-1}, the fraction of primary α phase declined steadily and the fraction of secondary β phase monotonically increased with increasing undercooling. However, in experiments on the same alloy system but for Cu-70wt.%Sn, the primary ε phase keeps the initial solidification structure and only a thin layer of the peritectic η phase precipitated on the ε plates even at slow solidification rate. The peritectic reaction can take place only at near equilibrium solidification conditions (small undercooling) and the thickness of the secondary layer depends not only on the solidification rate but also on the solute diffusion rate in solids. The reduction of the thickness of secondary β phase supported that the peritectic transformation should be diffusion controlled. In addition, primary precipitation of the β phase (peritectic phase) has also been observed, indicating the direct nucleation and growth of secondary phase in the liquid without contact with the theoretically primary α-Cu phase. This result has been confirmed by StJohn [37] for the same alloy, Cu-70wt.%

Sn, who indicates that the necessary undercooling for solidification also favoured the direct crystallization of the secondary phase from thermodynamic analysis. Study of the Pb-Bi system by Barker and Hellawell [100] concluded that the primary Pb-rich phase is inefficient as a heterogeneous nucleant of the secondary phase, and the nucleation of the peritectic phase took place at many other sites in the liquid. Therefore, the peritectic reaction and diffusion controlled peritectic transformation are not expected in a normal casting process while the precipitation of the peritectic phase from the melt might be dominate. Such a situation might be more serious in rapid solidification due to enhanced short-range diffusion at high cooling rates.

The results by Ahmad et al. [15] also proved that it would be difficult for a peritectic reaction to occur, as well as the subsequent peritectic transformation. In the solidification process of undercooled Ni-25.3 at% Si melt, γ-$Ni_{31}Si_{12}$ and supersaturated solid solution (α-Ni) formed via a pseudo eutectic reaction, with the α-Ni following the extension of the equilibrium liquidus line. As a matter of fact, similar behaviour had been observed in Nb-xSi (x=21.0-27.0 at.%) alloys [101], where solidification of the peritectic phase Nb_3Si from the melt should be observed under undercoolings in excess of 270 K (based on the thermodynamic equilibrium analysis). Bertero et al. [101] revealed an alternative solidification mechanism of the growth competition between β-Nb_5Si_3 and Nb_3Si: in levitated drops of these alloys (containerless solidification processing), the solidification was to a metastable α-Nb and β-Nb_5Si_3 eutectic, without any evidence of the Nb_3Si phase. Direct formation of the Nb_3Si phase from the melt was only observed in the splat-quenched alloys, no matter the undercooling prior to splat quenching. They attributed this phenomenon to difficulty in nucleating the Nb_3Si phase, which can grow at high cooling rate due to enhanced short-range diffusion and possible heterogeneous sites on the splat. Moreover, a thin layer of amorphous phase of Nb-25 at.% Si alloy was produced adjacent to the chill surface due to the extremely high cooling rate in this region [102].

The stability of the $L1_2$ ordered phase has also been investigated by Himuro et al. [20, 103, 104], who performed several experiments on Ni_3Fe-Ni_3Si pseudo-binary system. One of the studies focused on the $Ni_{25}Fe_{67.5}Si_{7.5}$ alloy, which was austenitized at 1100 ℃ for 3 hours in an evacuated quartz tube and aged at 600 and 700 ℃ for ten days and then rapidly quenched into ice water. The specimen quenched from 700 ℃

had the disordered FCC structure, which is consistent with the result at the equilibrium experimental condition [105]. However, the specimen quenched from 600 ℃ showed superlattice reflections from the $L1_2$ ordered structure. TEM analysis also observed that the nanoscale $L1_2$ ordered phase had precipitated in the austenite matrix. Similar results were also observed in the Ni-rich side of the Ni-Fe-Si alloys. From the thermodynamic equilibrium phase diagram, the equilibrium solidified phase of the $Ni_{75}Fe_{15}Si_{10}$ alloy should be the alpha-solid solution. However, Himuro et al. also detected the superlattice reflections from the $L1_2$ ordered structure in the $Ni_{75}Fe_{15}Si_{10}$ alloys quenched from 800 ℃, while the specimen quenched from 850 ℃ had no superlattice reflections. The transition temperature of these ordered precipitates was found to be 840 ℃ using electrical resistivity measurement. Particularly, the single $L1_2$ phase structure was obtained by quenching the $Ni_{75}Fe_{13}Si_{12}$ alloy that was austenitized at 1100 ℃ and then aged at 550 ℃ in advance [20].

3.6 Project aims and objectives

The aim of this project is to perform the rapid solidification experiments using drop tube technique for understanding the phase formation and microstructure evolution at high cooling rates. Two alloy systems, Ni-Si and Ni-Fe-Si, are selected. The study on Ni-25.3 at.% Si alloy extends the previous work of the same alloy by flux-melting experiments, with the specific objectives:

- To assess the different microstructure solidified at high cooling rates in comparison with the observed α-γ eutectic structure in the flux-undercooled samples (cooling rate < 10 K s^{-1}).
- To assess the formation of the metastable phases at high cooling rates, e.g. supersaturated solid solution, metastable phase and metallic glass.

Chemically, Fe and Ni are very similar. They can form a continuous solid solution phase in some temperature range. The objectives of the study of the Ni-Fe-Si alloys (10 and 15 at.% Fe substituting for Ni) are:

- To assess whether the substitution of Fe for Ni can occur, or whether there is other behaviours of Fe in the solidification process.
- To assess the formation of the metastable phase at high cooling rates.

- To assess the microstructure evolution with decreasing particle size and to study the microstructure difference in comparison with the predicted structure by the phase diagram.

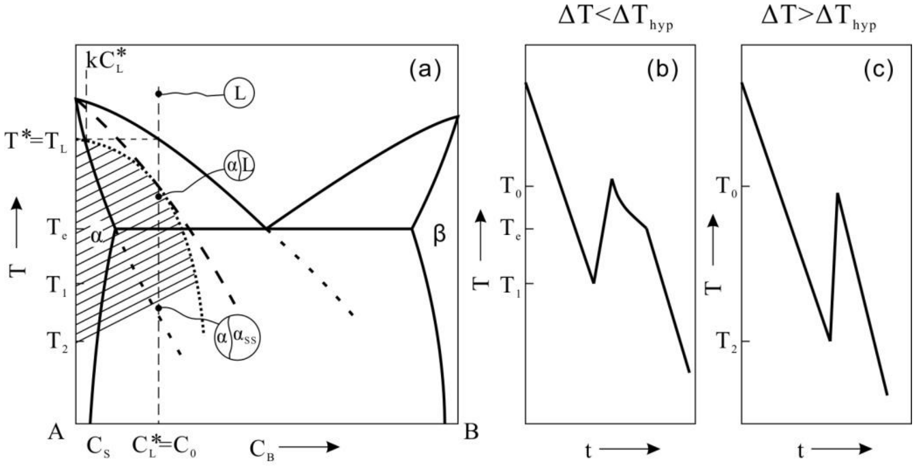

Figure 3.1: Eutectic phase diagram showing the thermodynamic and kinetic constraints for solute trapping and segregation free crystallisation under conditions of rapid solidification [10]

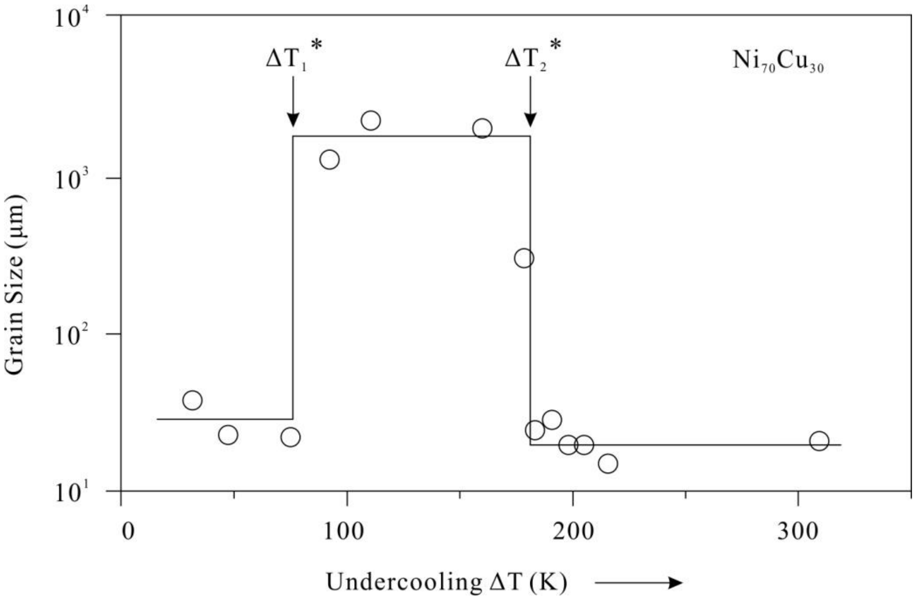

Figure 3.2: Grain diameter d as a function of undercooling for a $Ni_{70}Cu_{30}$ sample [42]

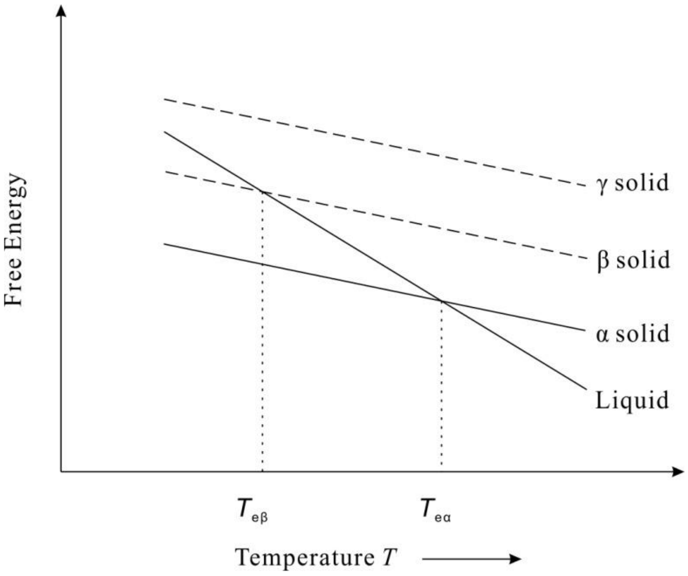

Figure 3.3: Variation of the free energy of the liquid and solid with temperature [25]

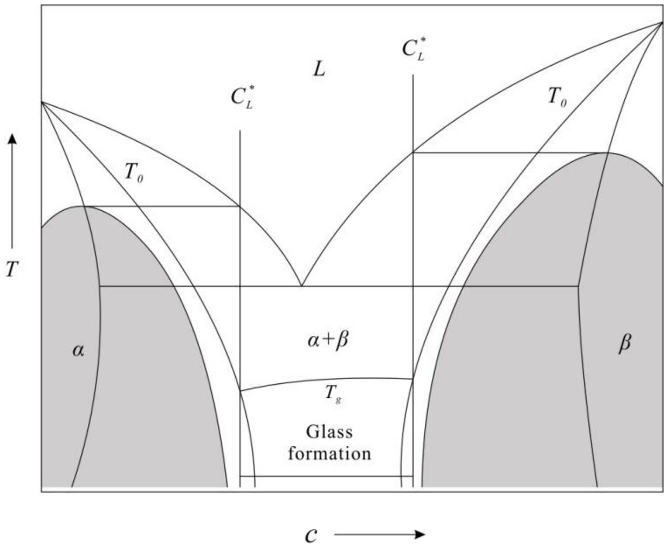

Figure 3.4: Eutectic phase diagram of a glass-forming alloy. The T_0 lines depend strongly on the two sides of the phase diagram. In the intermediate concentration range, solidification is either by eutectic crystallization or by glass formation [10]

Table 3.1: Some examples of the amorphous alloys and their corresponding experimental parameters

Author	Alloy system	Critical cooling rate (K s^{-1})	Scale
Chen et al.[60]	Pd-M-Si (M=Au, Ag or Cu)	100	1 mm (thickness)
Turnbull et al.[61, 62]	$Pd_{40}Ni_{40}P_{20}$	1.4	1 cm (thickness)
Inoue et al.[63]	$La_{55}Al_{25}(Ni/Cu)_{20}$ $La_{55}Al_{25}Ni_{10}Cu_{10}$ $La_{55}Al_{25}Ni_{10}Cu_{5}Co_{5}$	55-120	3mm (diameter) 7mm (diameter) 9mm (diameter)
Inoue et al. [66]	$Zr_{65}Al_{7.5}Ni_{10}Cu_{17.5}$	1.5	16 mm (diameter)
Peker et al. [67]	$Zr_{41.2}Ti_{13.8}Cu_{12.5}Ni_{10.0}Be_{22.5}$	10	14 mm (diameter)

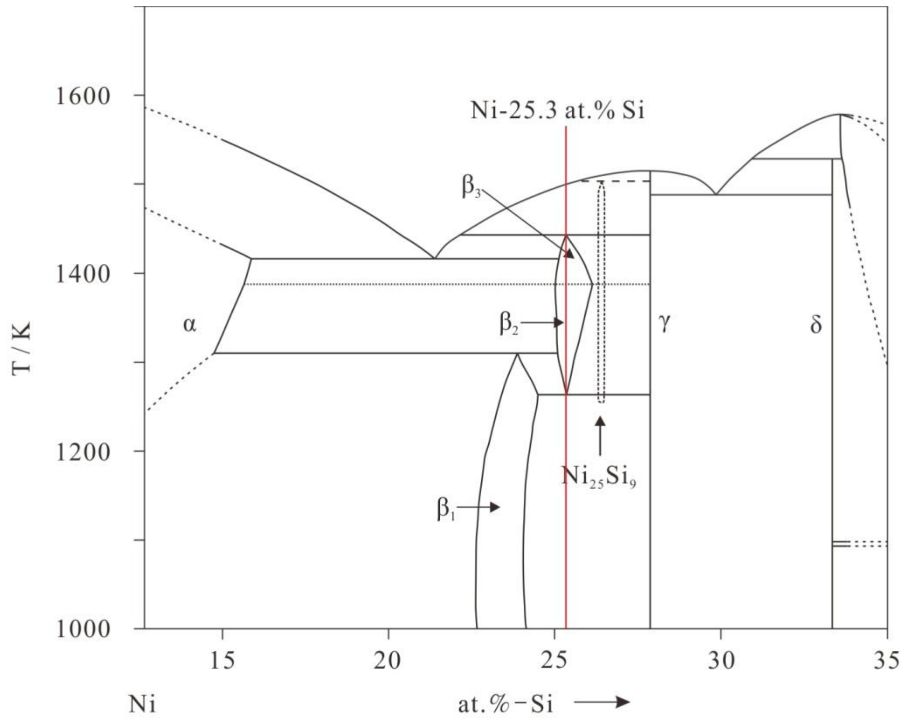

Figure 3.5: Ni-rich part of Ni-Si binary phase diagram with metastable phase $Ni_{25}Si_{9}$ [17]

Table 3.2: Reactions in the Ni-Si Phase Diagram [89, 106]

Reaction	Compositions of the respective phases, at.% Si			Temperature, ℃	Reaction type
L → α(Ni)+β_3	21.4	15.8	25.0	1143	Eutectic
α(Ni)+β_2 → β_1	14.7	25.1	23.7	1035	Peritectoid
β_2 → β_1+γ	25.2	24.5	27.9	990	Eutectoid
L+γ → β_3	22	27.9	25.2	1170	Peritectic
L → γ+δ	29.8	27.9	33.3	1215	Eutectic

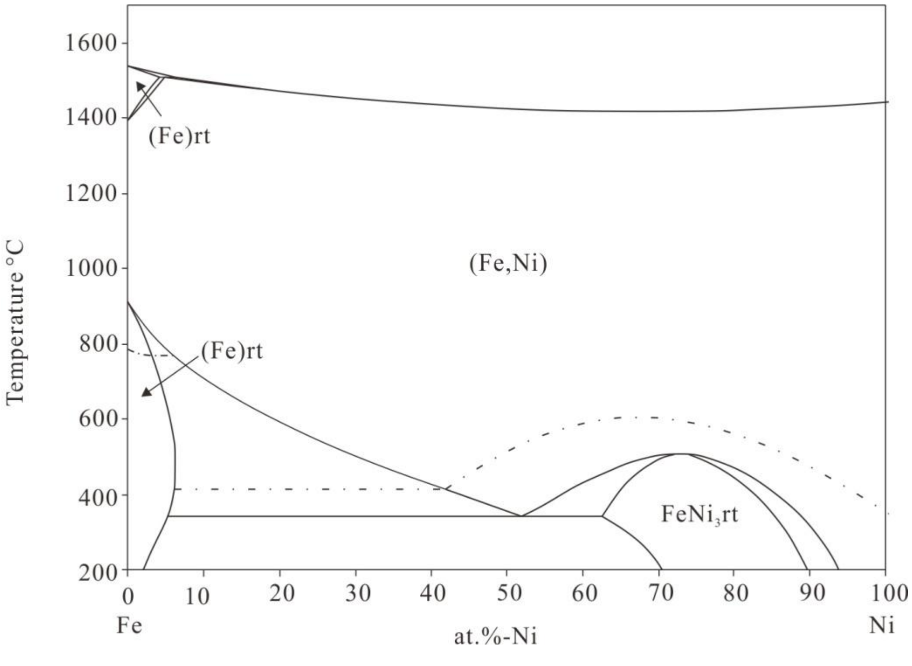

Figure 3.6: Ni-Fe phase diagram [84]

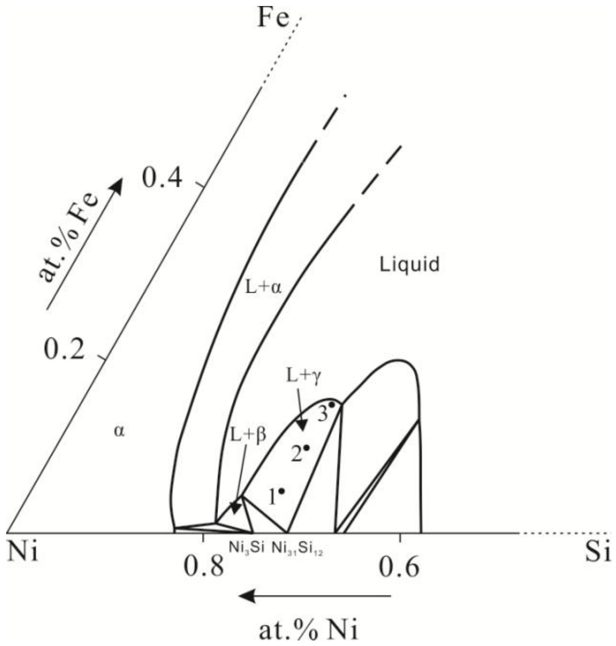

Figure 3.7: Ni-rich part of Ni-Fe-Si equilibrium phase diagram at 1400K. 1, 2 and 3 represent the composition of $Ni_{69.7}Fe_5Si_{25.3}$, $Ni_{64.7}Fe_{10}Si_{25.3}$ and $Ni_{59.7}Fe_{15}Si_{25.3}$ [88]

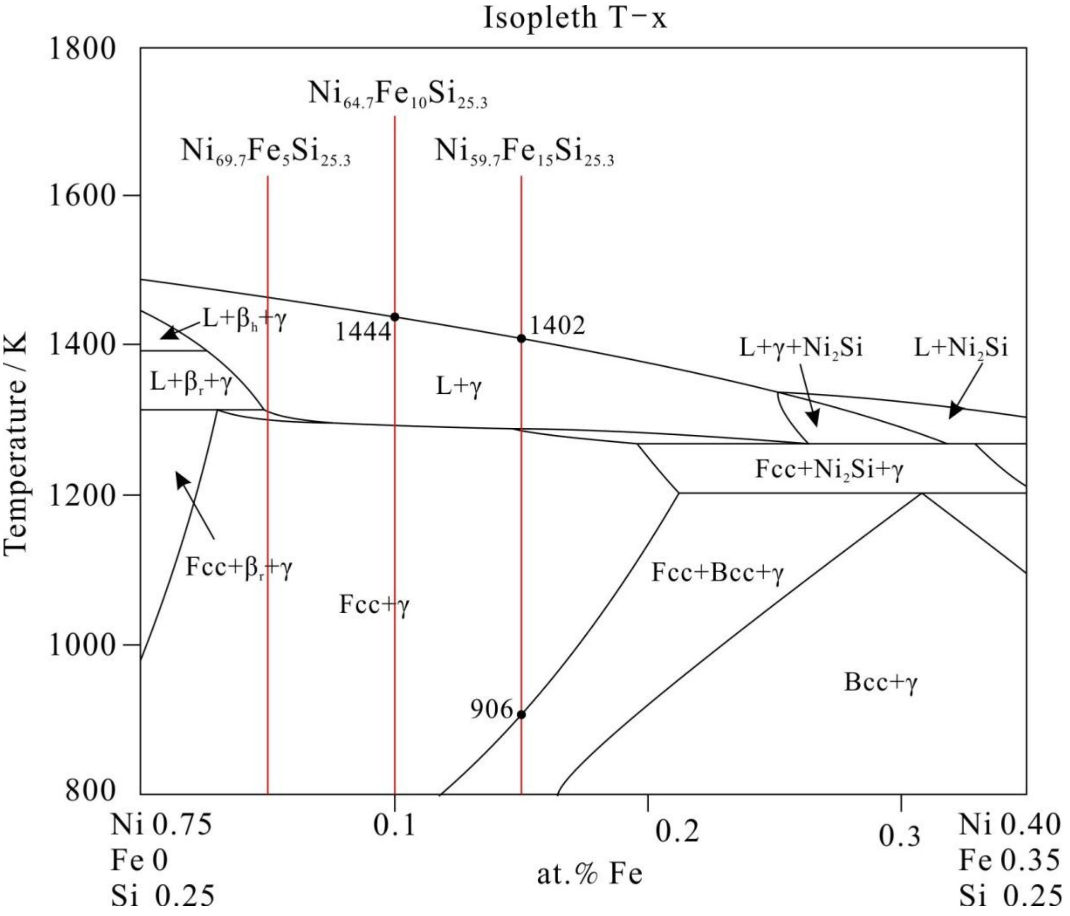

Figure 3.8: Vertical section of the Ni-Fe-Si quasibinary phase diagram at 25 at.% Si [88]

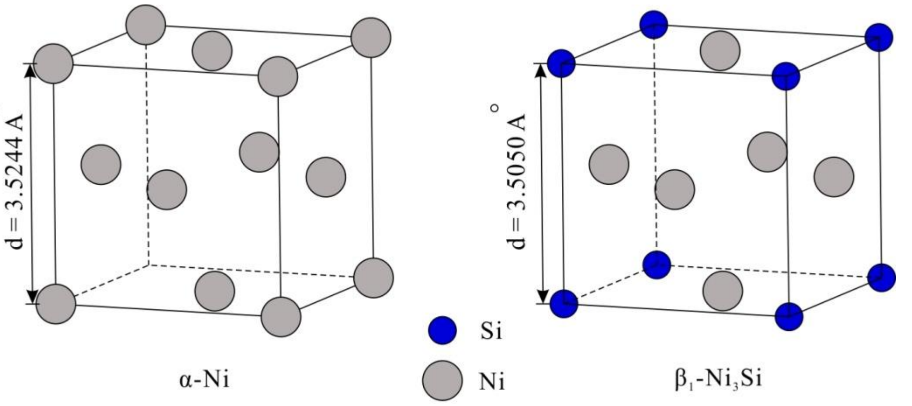

Figure 3.9: Crystal structure diagrams of α-Ni and β_1-Ni_3Si

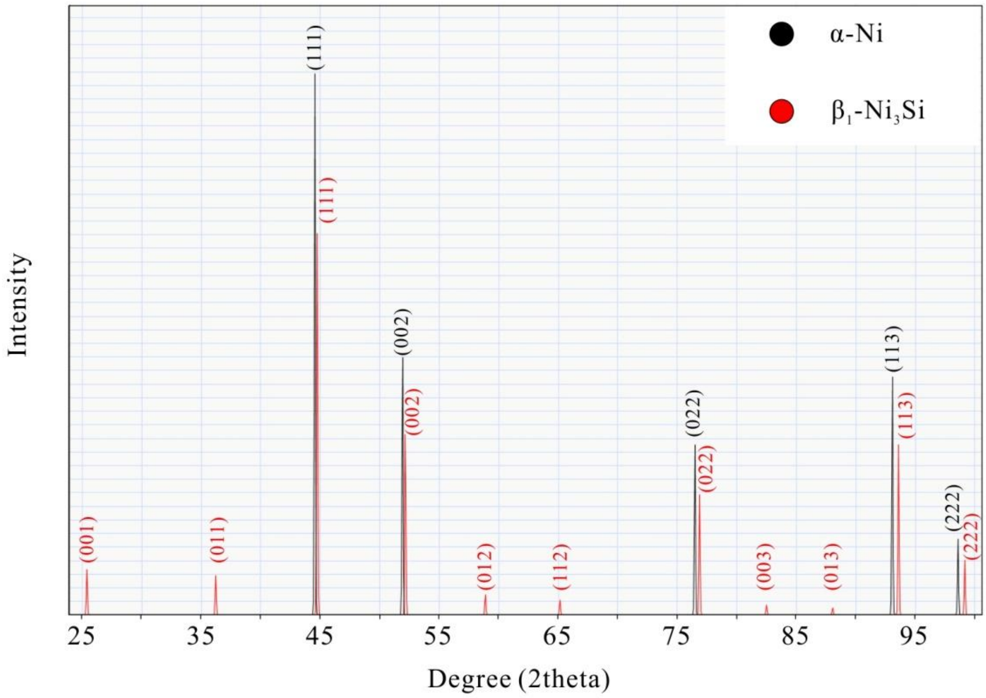

Figure 3.10: The diffraction patterns of αNi and intermetallic β_1-Ni_3Si (mass fraction ratio 1:1)

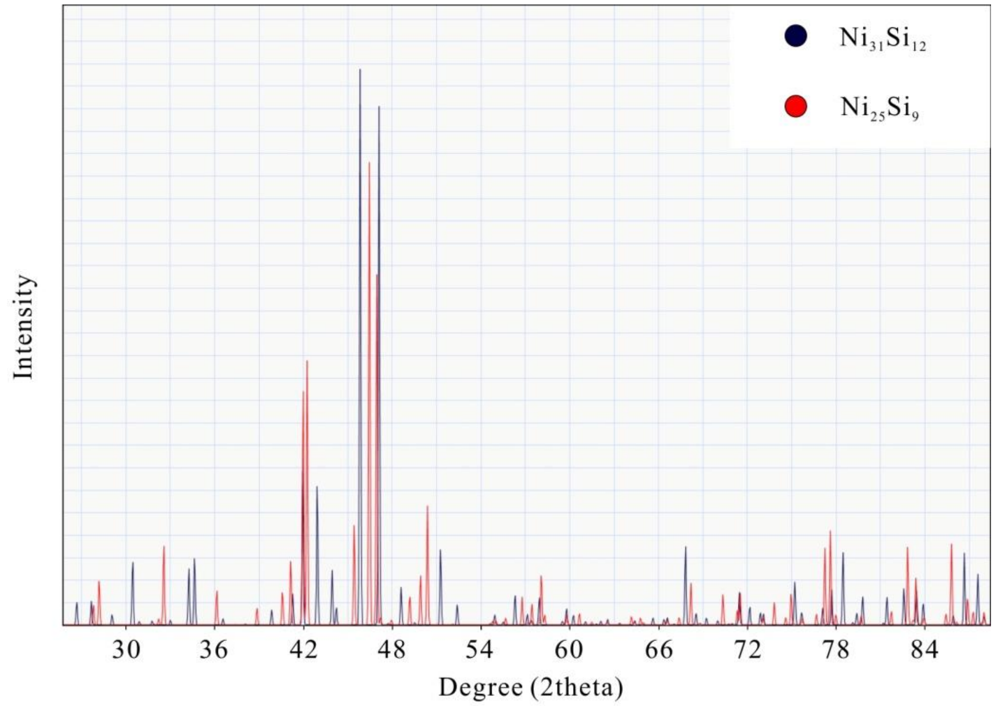

Figure 3.11: The diffraction patterns of the intermetallics, $Ni_{25}Si_9$ and $Ni_{31}Si_{12}$ (mass fraction ratio 1:1)

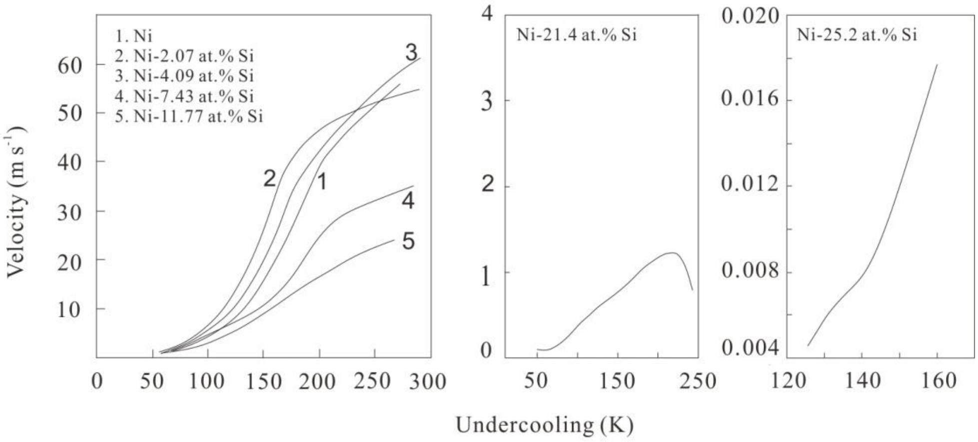

Figure 3.12: Velocity-undercooling curve for the solidification of Ni-Si alloys [15-17]

4 Equipment and Methodology

In this project, an arc-melting furnace and drop tube equipment were used. The former was used to prepare master alloys and the latter was used to carry out the non-equilibrium experiments and produce the solidified samples. Therefore, both of these pieces of equipment are introduced, including the key constructions and experimental procedures and conditions. The main task of the project was the microstructural characterization for the specific alloys formed in the rapid solidification process. Details concerning sample preparation, characterization techniques and the relative analysis method are also described. These include the Optical Microscopy, Scanning Electron Microscopy (SEM), X-Ray Diffraction (XRD), Transmission Electron Microscopy (TEM), Differential Thermal Analysis (DTA).

4.1 Equipment

Two main pieces of equipment were used in this project: an arc-melting furnace and a 6.5 m drop tube. The former was used to melt the high temperature materials Ni (T_m=1782 K) and Si (T_m=1687 K) together. The latter was used to melt and spray the master alloys produced by the arc-melting furnace to obtain the particles of different diameters, which are appropriate to investigate the relationship between the microstructure and cooling rate.

4.1.1 Arc-melting equipment

An arc-melting furnace provides a low pressure, inert atmosphere environment in which to prepare refractory metals and other high melting temperature alloys, especially for protective-atmosphere melting of easy to oxidize metals. Because of its simplicity, ease of internal access and small volume, the arc-melting furnace is easily purged before using for melting samples and quickly evacuated. The arc melting furnace used to prepare master alloys for drop tube experiments in this project is shown in **Figure 4.1**. The chamber and upper bell jar are fabricated from stainless steel with copper cooling coils bonded to the outer surface. A hinge at the rear of the unit permits access to the specimen materials by swinging the entire bell jar backwards. The electrode (handle) shaft penetrates the top of the bell jar, and the handle shaft is sealed at the top of the bell jar by means of a ball joint and rubber bellows. The ball joint allows the electrode to be pointed in any direction and provides a sliding seal for moving the electrode into and out of the chamber. The hearth is fabricated from pure copper for efficient cooling. A water jacket covers the lower surface under the entire active area of the hearth. A swaged tungsten striker on the tip of the electrode is provided for starting the arc. Various cavity configurations can be provided on the copper hearth, as can be seen from the inset of **Figure 4.1**. Light and window ports facilitate inside observation. Pressure compensation is incorporated into the seal design to control pressure in the chamber. One two-stage vacuum pump located beneath the furnace frame for evacuation and the furnace chamber are connected by one screw valve which makes the repeated evacuation and back-filling operation simple and convenient.

Using a two-stage, oil sealed pump the chamber was evacuated to about 5×10^{-4} Pa and backfilled the chamber to about 3.4×10^{3} Pa with Ar. This procedure was repeated 5 times before the melting process. In order to ensure the homogeneity of master alloys, the alloy buttons were turned over and melted four times before elongation using a centre rod-shaped cavity.

4.1.2 Drop tube

A 6.5 m drop tube was involved in the present project with nitrogen acting as the protective inert gas throughout the experiment. Except for the 6-m stainless steel tube which permits free-fall solidification and rapid in-flight cooling, there are three other main sub-systems: 1) Top furnace for heating and spraying samples, as shown in **Figure 4.2**; 2) Pumping system; 3) Gas supply and cooling water system.

The schematic diagram in **Figure 4.2**(a) shows the core part of the drop tube, designed for sample heating and melt spraying. A crucible with 3 laser drilled holes (300 μm diameter) in the base is located into the graphite susceptor and used for melting and spraying samples. The graphite susceptor here is fixed beneath the steel lid by clamping both end ports of the lid and the susceptor. There is also a 10 mm hole in the base of the susceptor, aiming to provide a channel for spraying melt beams. An alumina shell hung up by steel wires was located between the susceptor and copper coil, acting as a radiation shield to prevent heat loss from the susceptor via thermal radiation.

The rf-coil was wound around the outer side of the alumina shell to heat samples by induction through the graphite susceptor. The coil was made from 5 mm external diameter copper tube, which was connected to the RF-generator, and the blank copper pipe gives access to a chilled water supply. The R-Type thermocouple was fixed on the top steel lid and extended into the crucible, which was hung up on the top of the melted sample. The other side of the thermocouple was connected to the digital monitor for temperature output. In order to spray the melt sample, the crucible is also connected to a small gas supply store which is pressurised with pure nitrogen after the alloy is melted completely. One solenoid valve was placed between the furnace and the gas store to achieve this manipulation.

During the experimental process, the sample were put into the crucible first and then core components were assembled together beneath the furnace, as shown in **Figure 4.2**(b), which was fixed onto the drop tube, as shown in **Figure 4.2**(a). During the evacuation process, the system was finally filled to a pressure of 40 kPa with dried, oxygen free N_2 gas, having previously been flushed three times with N_2 and evacuated to a pressure of 4×10^{-3} Pa achieved by a mechanical rotary pump and turbo-molecular pump. After the protective atmosphere conditions have been created, the turbo-pump was switched off. Then the alloy sample was heated by induction. Once it had reached the expected temperature, the gas store was pressurised with nitrogen (usually 3×10^{5} Pa) and then the melt sample was sprayed. The rapidly solidified particles were collected at the bottom of the drop tube after the system temperature dropped to room temperature.

4.2 Sample preparation

The alloy particles were classified into different size groups. The sizes of the sieves used were 850 μm, 500 μm, 300 μm, 212 μm, 150 μm, 106 μm, 75 μm and 53 μm. Then, the particles were hot mounted in suitable mediums, Bakelite for XRD and conductive powder filled with carbon for SEM. After mounting, the samples were ground down using a series of progressively finer SiC grinding papers starting with 240, 400, then 800 and lastly 1200 grit. During this process, some of the SiC papers with 240, 400 and 800 grit were not needed for smaller particles. For example, for the particles of diameter 106-75 μm, 1200 grit SiC paper was enough, since coarser paper may grind the fine particles away from the medium. Throughout this process, optical microscopy was used to check the diameter of average particle grinding cross-section, to avoid over grinding, which might damage the finished polished quality. Well ground samples were then polished with diamond compounds using 6 μm, 3 μm, 1 μm and 0.25 μm polishing cloths on the automatic machines. The samples were washed using dilute detergent and methanol, and then dried in an electrical drier. An optical microscope was used for checking surface scratches to confirm whether the samples are well polished. Well polished samples are good for SEM-EDX analysis to identify the composition. To reveal the microstructure the well polished samples were etched with suitable etchant to obtain SEM high resolution images. The etchants for Ni-Si and Ni-Fe-Si alloy particles are listed in **Table 4.1**. The etching time varied, so the optical microscope was also used during the etching process.

The optical microscope used here has a 10 times eyepiece with six objectives (5, 10, 20, 50 and 100 times). In addition, the microscope can be used to observe sample surface topography using polarized light and Differential Interference Contrast (DIC). An Axiocam MRC5 Zeiss digital camera is installed on the top of the microscope and is used for taking images.

In this project, TEM was also used to identify the phases of the refined microstructure. The technique for preparing the TEM samples will be introduced in a latter section.

4.3 Microstructure and composition analysis

Scanning electron microscopy (SEM) is similar to optical microscopy but offers much higher resolution at higher magnification. The reason for its high resolution can be explained by the Rayleigh criterion, as shown in Equation (4-1) [107].

$$r_1 = \frac{d_1}{2} = \frac{0.61\lambda_w}{\mu sin\alpha} \tag{4-1}$$

where d_1 is the limit distance between the two centres of Airy rings from two neighbouring pinholes, λ_w is the wavelength of the electron beam, μ is the refractive index of the medium between the object and the objective lens. The product, μsinα is usually called the numerical aperture. So it is clear that the limit of resolution or the smallest distance between two points (i.e. the smallest r_1) is proportional to the incident wavelength.

Both wave and particle properties can be applied to light and electrons, with the wavelength being about 400-700 nm and 0.001-0.01 nm respectively. The limit of resolution for light microscopy is 150 nm (0.15 μm) using green light (λ_w = 400 nm) for example, whereas electrons can achieve a resolution of approximately 0.02 nm using reasonable values of λ_w = 0.0037 nm (the wavelength of 100 kV electrons) and α = 0.1 radians [107]. However, electrons are very much more strongly scattered by gases than by light. Therefore, in order to use electrons in microscopy all the electron-optical paths must be evacuated.

The interaction of electrons with a specimen can result in various secondary emissions from the specimen, as shown in **Figure 4.3**. Normally, all scanning electron microscopes have facilities for detecting secondary and backscattered electrons. Secondary electrons are emitted by atoms excited by the incident electron beam with low energies (< 50 eV), and these electrons come from a short distance below the specimen surface. By far, the secondary electron signal is the most widely used signal in SEM for the study of specimen surface features. Back scattered electrons are reflected electrons from the sample by elastic scattering. The relationship of the secondary electron coefficient (δ_s) and the backscattered electron coefficient (η_s) and the atomic number of the specimen is shown in **Figure 4.4**. η_s is strongly dependent on the average atomic number, while δ_s is not dependent. Therefore, BSE images can provide information about the distribution of different phases with different average atomic numbers in the sample. From **Figure 4.4**b it is clear that the total electron yield is a complex function of the accelerating voltage, with a maximum between 1 and 5 keV. This voltage is much lower than the normal operating voltage of most SEMs. For clean metal specimens (like the alloys and conductive resin) there is no difficulty in imaging. However, if the specimen is a non-conductive one, normally the sample will charge due to electron aggregation and coating with a thin conducting layer (like gold or carbon) is necessary.

If one electron of inner energy state has been knocked out of an atom and then a single outer electron jumps into this inner shell vacancy, a characteristic X-ray is emitted. The energy of the X-ray is the difference between the energies of the two excited electron states. Because the energies and wavelengths are different for each atomic species, they can be measured to determine the different elements in the specimen which is chemical analysis in SEM.

The etched sample surface was further examined using a LEO 1530 Gemini FEGSEM operated at 3 kV accelerating voltage with 3 mm working distance to take high resolution images. The samples were placed on the aluminium stub using adhesive carbon disc, sometimes also using additional conductive carbon paste, to gain better conductivity and avoid the charging effect. EDX and BSE detections were carried out at 8 mm working distance. Besides the area scanning, point scanning is also allowed to check the element composition of the specific phase.

Meanwhile, the composition of the single phase was also checked by EPMA (electron microprobe analysis) to verify the reliability of the EDX results. The electron microprobe is a close relative of the SEM but is designed primarily for analysis, by which, accuracy approaching ± 1% is obtainable and detection limits down to tens of parts per million can be obtained [108]. All of the EDX or WDX results are from the polished but un-etched samples.

4.4 Phase identification

Two main techniques are used here to identify the phases solidified in the particles: XRD and TEM. The former can provide general information of the phases existing in the particles, while the latter allows the specific phases of the structure to be checked.

4.4.1 X-ray Diffraction (XRD)

The X-ray diffraction technique is a simple and effective method to characterise the structure of crystalline materials. It is clear that X-rays are electromagnetic radiation of exactly the same nature as light but of very much shorter wavelength, and the wavelength used in diffraction is approximately in the range of 0.5-2.5 Å. The geometry of crystals has been discussed in the preceding chapter, which, together with X-ray illumination, constitutes the foundation of the crystal diffraction.

Diffraction occurs at such a condition that two or more waves of electromagnetic radiation are ‘reflected’, and the path difference of the incident wave and reflecting wave is equal to an integer number of wavelengths. This condition was discovered by W. H. Bragg and his son, W. L. Bragg, and is known as Bragg’s law,

$$n\lambda_w = 2d_{hkl}sin\theta \tag{4-2}$$

where d_{hkl} is the distance between successive planes, and θ is the incident/diffracted angle of the X-ray beam, and its geometrical relationship is shown in **Figure 4.5**.

When an X-ray beam encounters an atom, each electron in it will scatter part of the radiation. Here the relationship between the intensity of the beam scattered by a single electron and the mass of scattering particle can be given by:

$$I_{scattered\ radiation} \propto \frac{1}{m^2_{scattering\ particle}} \tag{4-3}$$

The nucleus has an extremely large mass relative to that of the electron and cannot be oscillated to any appreciable extent. So scattering by an atom is due only to the electrons contained in that atom [22].

In fact, if the scattering is in the forward direction ($2\theta = 0$) an atom of atomic number Z scatters Z times the amplitude of the incident wave because the waves scattered by all the electrons of the atom are in phase, such as the wave front XX' shown in **Figure 4.6**. However, it is not true for other scattering directions, since the electrons of an atom are situated at different points in space giving rise to differences in phase in between the waves scattered by different electrons. From **Figure 4.6** it is clear that the other scattered waves have a path difference equal to (CB-AD) and are somewhat out of phase along a wave front such as YY'. So in other directions ($2\theta \neq 0$) partial interferences take place and the net amplitude of the wave scattered in these directions is smaller than Z times of amplitude. The scattering efficiency of a given atom is therefore described by the atom scattering factor (f_a), which is defined as a ratio of amplitudes:

$$f_a = \frac{amplitude\ \ of\ the\ wave\ scattered\ \ by\ an\ atom}{amplitude\ \ of\ the\ wave\ scattered\ \ by\ one\ electron} \tag{4-4}$$

The structure factor is the resultant wave scattered by all the atoms of the unit cell, describing the atom arrangement. It is obtained by simply adding together all the waves scattered by the individual atoms, given by fractional co-ordinates u, v and w for each atom. If a unit cell contains atoms 1, 2, 3… N, then the structure factor for the *hkl* reflection is given by:

$$F = f_1 e^{2\pi i(hu_1+kv_1+lw_1)} + f_2 e^{2\pi i(hu_2+kv_2+lw_2)} + f_3 e^{2\pi i(hu_3+kv_3+lw_3)} + \cdots \tag{4-5}$$

or

$$F_{hkl} = \sum_{1}^{N} f_n e^{2\pi i(hu_n + kv_n + lw_n)} \qquad (4\text{-}6)$$

This equation is a very important relation in X-ray diffraction crystallography, because it can be used to calculate the intensity of any *hkl* reflection from the atomic positions.

Rietveld refinement is a technique for use in the characterisation of crystalline materials, based on a “structure factor least squares” computer programme written by Hugo Rietveld [109, 110]. The programme takes into account the overall isotropic temperature factors, scale factors, background, atomic coordinates, scattering factors and instrumental factors to refine a theoretical line profile until it matches the measured profile.

Several software packages have been written to analyze the powder diffraction results. The two most popular examples are the freeware packages, General Structure and Analysis Software (GSAS) [111] and the FullProf suite [112]. The quality of the agreement between the observed and simulated profiles can be expressed in terms of the weighted profile factor (R_{wp}) and expected weighted profile (R_{exp}), both of which are determined by functions of profile intensity, standard deviation of the profile intensity, calculated counts, and number of points. Ideally, the final (R_{wp}) should approach the statistically expected value, R_{exp}, which reflects the quality of the data. The conventional indicator of “goodness of fit” is chi^2= $(R_{wp}/R_{exp})^2$, which should also approach 1 [113].

In this work, only one result was analyzed by Rietveld refinement method in order to estimate the phase fraction. The analysis was carried out using the software X’Pert HighScore Plus (PANalytical B.V., Almelo, The Netherlands), which is packaged as part of the X’Pert MPD X-ray diffractometer used at the University of Leeds. The automatic semi-quantitative analysis can be performed based on the RIR (Reference Intensity Ratio) method. The RIR method scales all diffraction data to a standard. Generally, corundum is used as the international reference. By using ratios and measuring peak areas, the RIR method can be used to determine concentrations.

In this project, the quantities of particles for each size group are limited. XRD analysis, including XRD with in-situ heating, was conducted to identify the phase constitution of the samples (Cu K_α radiation, P'Analytical X'Pert MPD, Almelo, The Netherlands). The particles were first mounted in transoptic resin and then prepared as described in Section 4.2. Then the well-polished samples were fixed on the bracket, which was clamped on the XRD instrument for scanning, as shown in **Figure 4.7**. Before that, XRD detection had been carried out on two blank matrixes made by Transoptic powder and Bakelite respectively, as shown in **Figure 4.8**. The Bakelite matrix produces lots of sharp diffraction peaks with the strongest one at about 30 °, which might complicate the XRD diffraction pattern and influence the following analysis process. On the contrary, the transoptic resin has only three relatively weak smooth peaks at low angle without any sharp and strong diffraction peaks. Therefore, Transoptic powder is chosen as the sample holder for XRD detection here. A detected diffraction pattern from a sample will be analyzed and compared with the standard diffraction cards in a large database of patterns for known crystalline materials to identify the target phases in the solidified alloys.

In-situ XRD was carried out in a sealed chamber at high vacuum ($\approx 1.68 \times 10^{-4}$ Pa), in which the sample is allowed to be heated up to 1200 ℃. The sample was heated from 25 to 450 ℃, which was not calibrated. Data were collected at room temperature 25 ℃, then at high temperatures 300 ℃, 400 ℃, 450 ℃ and finally at room temperature again after the sample cooled down, wherein slow scanning was performed. With the consideration that the time of the slow scanning might be too long to observe the precise transformation temperature, the detection was repeated using quick scanning. The sample was heated from 250 ℃ to 325 ℃, wherein data were collected several times at each temperature step (every 25 ℃).

4.4.2 Transmission Electron Microscopy (TEM)

The transmission electron microscope (TEM) is also one of the most important tools for the microstructural characterization of materials. In fact, X-ray techniques can obtain more quantitative diffraction pattern analysis than electron diffraction patterns, but electrons can be focused more easily. Also compared with SEM, both of them employ the same electron beam system, e.g. an electron gun, condenser lenses and vacuum system. However, the ways to form the images are entirely different, because TEM is a transmission technique and provides information about the internal structure of thin specimens, whereas the SEM is primarily used to study the surface structure of bulk specimens [107]. When one electron beam passes through a thin specimen, variations in the intensity of electron diffraction, result in "diffraction contrast" in the image, which is useful to characterize the microstructures and defects such as second phase particles, dislocations and interfaces [114]. Selected-area diffraction (SAD) is also one common and useful technique which allows observation of diffraction patterns from small areas of the specimen. In addition, high-resolution transmission electron microscopy (HRTEM) can be used to form images of columns of atoms.

Diffraction in TEM also occurs when the reflected and the incident electron beams meet Bragg's law (Equation (4-2)). Details of the diffraction pattern are shown in **Figure 4.9**.

From Bragg's law, for small θ:

$$sin\theta \sim \theta = \lambda_w / 2d_{hkl} \tag{4-7}$$

According to the geometrical relationship in **Figure 4.9**,

$$R_0 / L_0 = tan2\theta \sim 2\theta \tag{4-8}$$

Combination of equations (4-7) and (4-8), gives

$$d_{hkl} R_0 = \lambda_w L_0 \tag{4-9}$$

$\lambda_w L_0$ is known as the camera constant, which can be calibrated in the operation process. The d-spacing corresponding to the reflection can be calculated directly once R has been measured.

In fact, the diffraction angle θ shown in **Figure 4.9** is quite small. Taking a crystal plane with d-spacing of 0.5 nm for example, the Bragg angle for 200 kV electrons is 0.14°. Therefore, the diffracted electron beams from crystal planes are almost parallel to the electron beam. If there are several planes parallel to the electron beam, a set of diffraction spots with a distance of $1/d_{hkl}$ will occur from the centre of the diffraction pattern in the normal direction to the plane. The relationship is shown in **Figure 4.10**, in which the formed lattice of spots bears a reciprocal relationship to the real lattice of the crystal, known as the reciprocal lattice. The angle φ is equal to the angle between the normal directions to the planes. This is the basis of TEM analysis to identify the phase, with the related equations listed in **Table 4.2**.

As mentioned above, polycrystalline materials are very common, comprising lots of small crystals with random orientation. Different from the diffraction pattern from a single crystal (**Figure 4.11**a), if the specimen contains several crystals of different orientations, the diffraction pattern is more complicated and a sum of individual patterns. As shown in **Figure 4.11**b (right), the spots are not randomly distributed but fall on rings (dashed ring). If the grain size is much smaller, that is, the detected area contains many crystals of random orientation (**Figure 4.11**c), the spots on the dished rings (**Figure 4.11**b) are so close together that the rings appear continuous. Therefore, rather than individual diffraction spots, the diffraction pattern of a fine polycrystalline material is composed of a series of concentric circles (**Figure 4.11**c).

Accompanying the advantages of the TEM, there are still some drawbacks. Firstly, the prepared sample for TEM detection must be small and thin, which is only a small part of the sample. Therefore, general structural information is better to be examined with other techniques under low magnification, like optical microscopy and scanning electron microscopy. Secondly, the specimens for TEM have to be thin enough to transmit sufficient electrons so that enough transmitted intensity falls on the screen to form an interpretable image [115]. Drop tube particles are fine with diameters in the range 75-850 μm, and the microstructures are complicated even with nano-crystalline phase grains as well. In order to make the TEM specimens from the specific areas accurately, the precise Focus Ion Beam (FIB) linked to the FEI Nova 200 NanoLab FEGSEM was used. The length and width of the resulting lamellar specimen are 15 μm and 8 μm respectively, with the thickness smaller than 100 nm. A brief sequence of this operating technique is shown in **Figure 4.12**. The first step was to find the detected area. Then a thin, narrow layer of Pt was coated on the surface of the target area in order to protect the surface during the cutting session. After the desired lamellar specimen was produced, it was welded on the tip of a tungsten micro-manipulator before it was completely broken away from the particle. Once the lamella was fixed on the TEM grid (Cu), the central area of the lamella was sliced to ensure the thickness was lower than 100nm. Well prepared specimens were stored in a vacuum vessel before TEM analysis. The TEM used in this project was a

Philips CM 200 FEG transmission electron microscope operating at 200 kV fitted with an ISIS EDX system analysis facility.

4.5 Differential Thermal Analysis

Differential thermal analysis (DTA) is one of the most widely used thermal analysis techniques, which works based on the difference in temperature between a substance and a reference material as both samples are subjected to the same heating programme. The classical heating programme is a linear temperature change with respect to time. Changes in the sample, either exothermic or endothermic, can be detected and recorded to report the resulting thermal analysis curve (**Figure 4.13**), showing the relationship between the temperature difference between the sample and reference and temperature (or time). Generally, there are a series of peaks in a DTA curve which provide data on the transformations that occur in the heating or cooling process, such as phase transformation and melting. In a DTA curve, the position is determined by the properties of the detected materials and the heating rate, while the area is related to the energy involved in the corresponding reaction [116]. In the present project, DTA measurements were performed using a Perkin Elmer DTA 7 to determine the onset temperature of the metastable phase transformation.

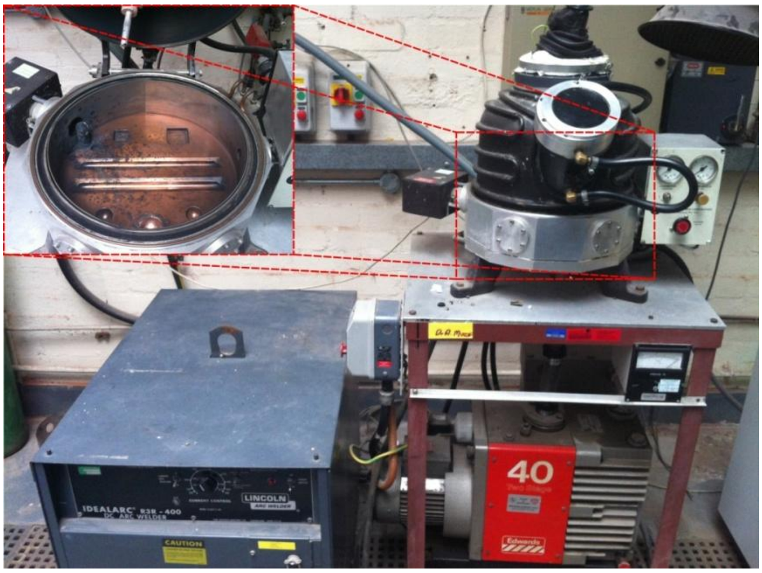

Figure 4.1: Arc-melting equipment for melting high melting metals or alloys. Inset is the chamber of the arc-melting furnace.

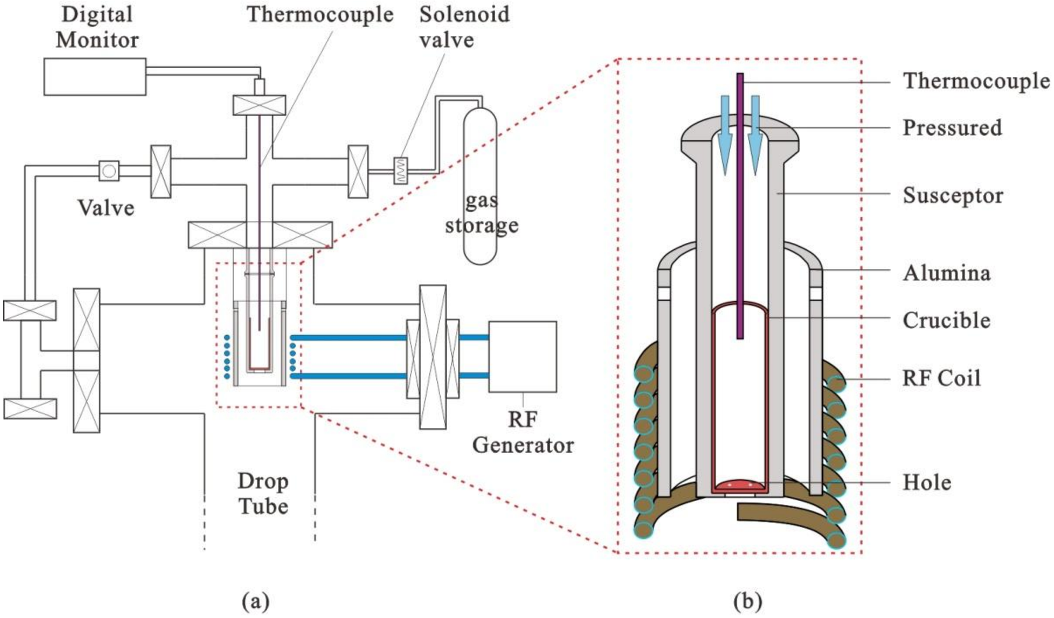

Figure 4.2: (a) the schematic diagram of the top furnace part of the drop tube; (b) the detailed configuration of the red rectangular part in the left diagram.

Table 4.1: Etchants used for each material

Alloy	Etchant	Time[2]
Ni-Si	HF (5ml), H_2O_2 (5ml) and H_2O (10ml)	20-30 second
Ni-Fe-Si	HF (5ml), H_2O_2 (5ml) and H_2O (30ml)	10-20 second

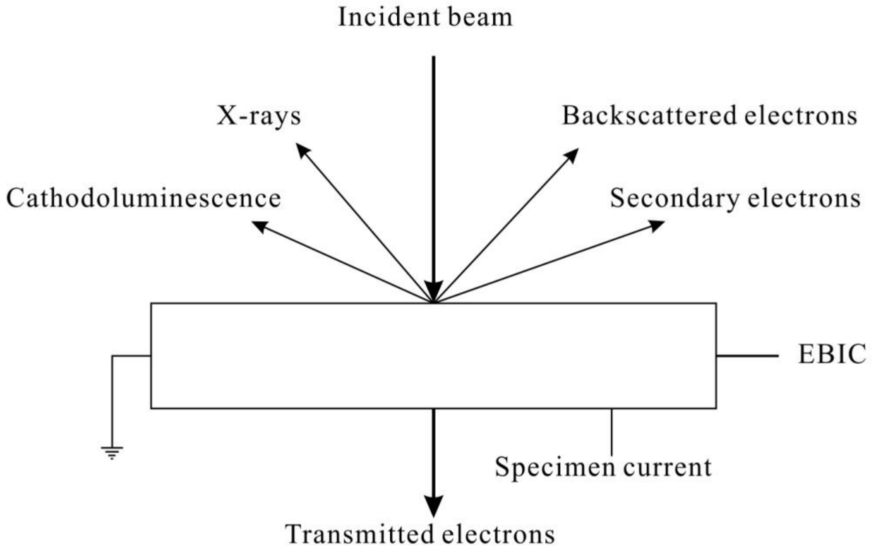

Figure 4.3: Some of the signals which may be used in SEM [107]

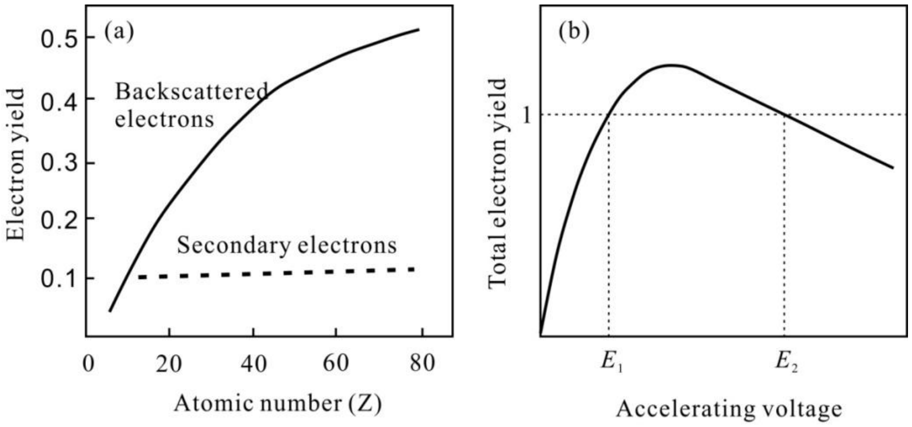

Figure 4.4: (a) The effect of atomic number on the yield of backscattered electron (η_s) and secondary electron (δ_s); (b) The relationship of the total electron yield ($\eta_s + \delta_s$) and the accelerating voltage [107].

---

[2] The sample needs to be checked using the optical microscope every 5 seconds.

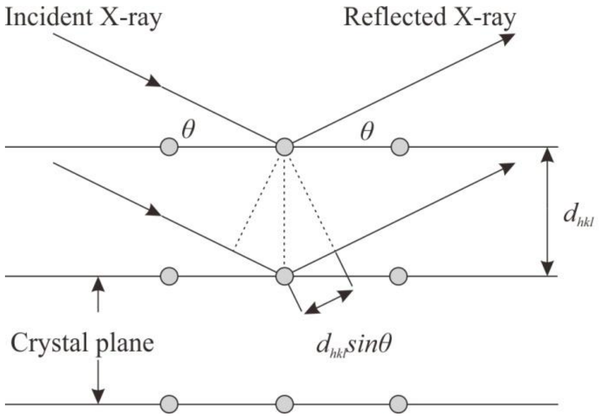

Figure 4.5: Diffraction of X-rays by a crystal [22]

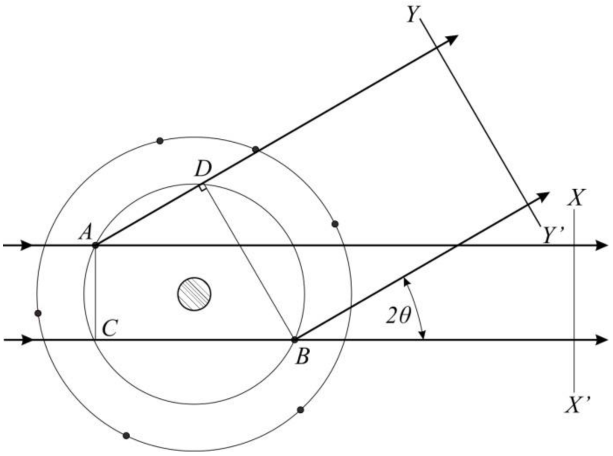

Figure 4.6: X-ray scattering by an atom [22]

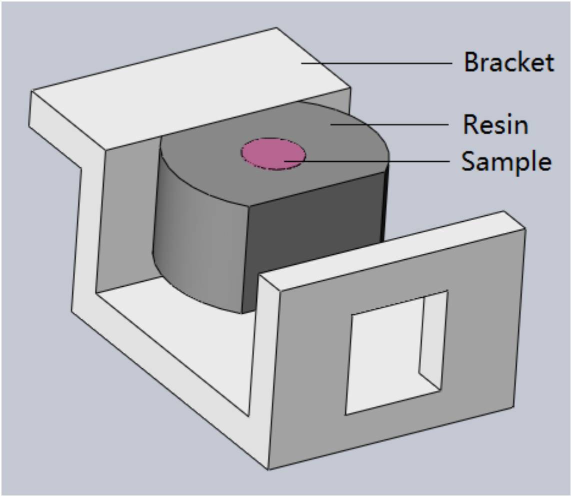

Figure 4.7: Schematic of the XRD bracket and sample holder

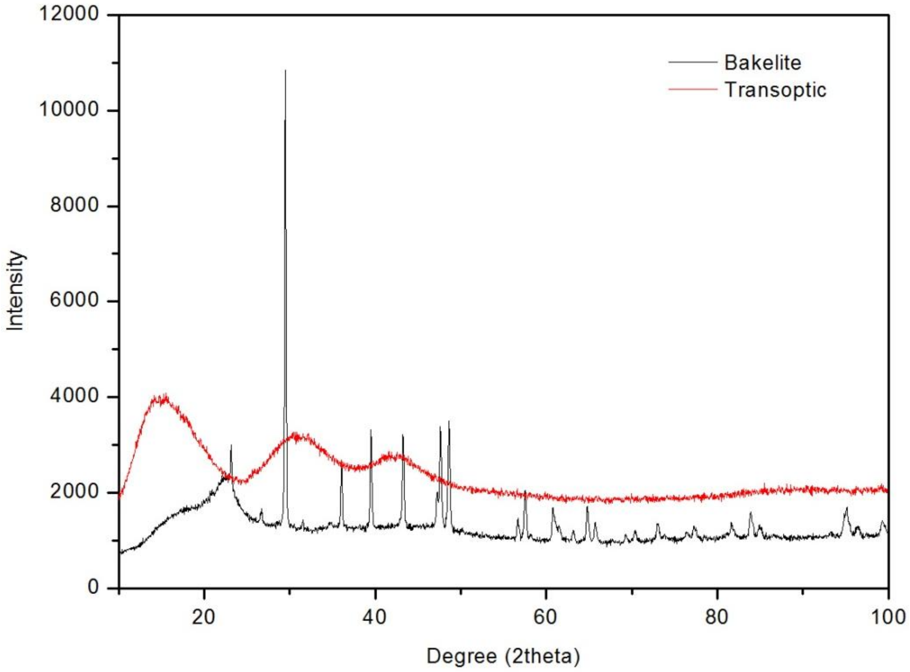

Figure 4.8: XRD diffraction patterns for Bakelite and Transoptic resin.

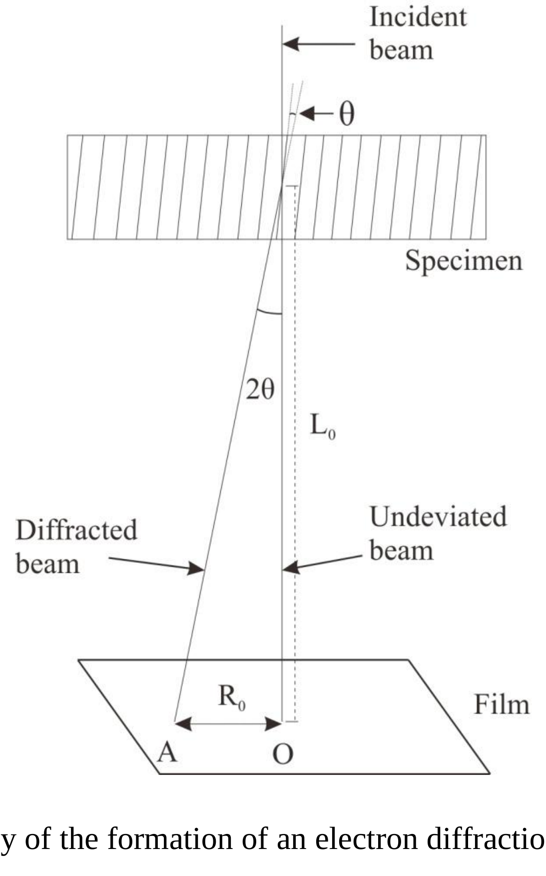

Figure 4.9: Geometry of the formation of an electron diffraction pattern. On the film, the diffracted spot A occurs at a distance R_0 from the central spot, O in a direction perpendicular to the planes. L_0 is known as the camera length [117].

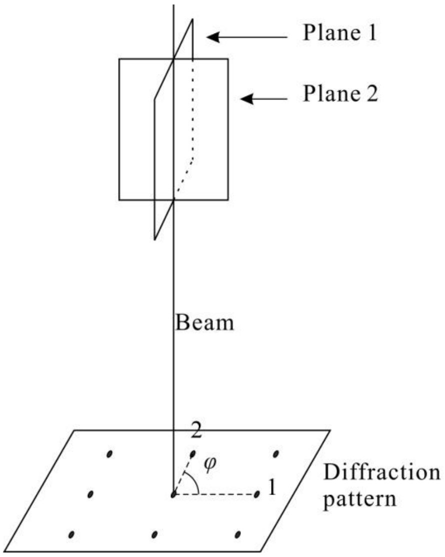

Figure 4.10: Geometry of the formation of an electron diffraction pattern from a single crystal in TEM. The beam is parallel to a zone axis including two planes (1 and 2). The included angle φ is equal to the angle between the normal directions of the planes [117].

Table 4.2: Calculation of interplanar angle, θ, between planes ($h_1k_1l_1$) and ($h_2k_2l_2$) and interplanar spacing, d_{hkl} in cubical and hexagonal crystals [117].

Crystal structure	cosθ	d_{hkl}
Cubic	$cos\theta = \frac{h_1h_2 + k_1k_2 + l_1l_2}{\sqrt{(h_1^2 + k_1^2 + l_1^2)(h_2^2 + k_2^2 + l_2^2)}}$	$\frac{1}{d_{hkl}^2} = \frac{h^2 + k^2 + l^2}{a^2}$
Hexagonal	$cos\theta = \frac{h_1h_2 + k_1k_2 + \frac{1}{2}(h_1k_2 + h_2k_1) + \left(\frac{3a^2}{4c^2}\right)l_1l_2}{\sqrt{\left[h_1^2 + k_1^2 + h_1k_1 + \left(\frac{3a^2}{4c^2}\right)l_1^2\right] + \left[h_2^2 + k_2^2 + h_2k_2 + \left(\frac{3a^2}{4c^2}\right)l_2^2\right]}}$	$\frac{1}{d_{hkl}^2} = \frac{4}{3}\left(\frac{h^2 + hk + k^2}{a^2}\right) + \left(\frac{l}{c}\right)^2$

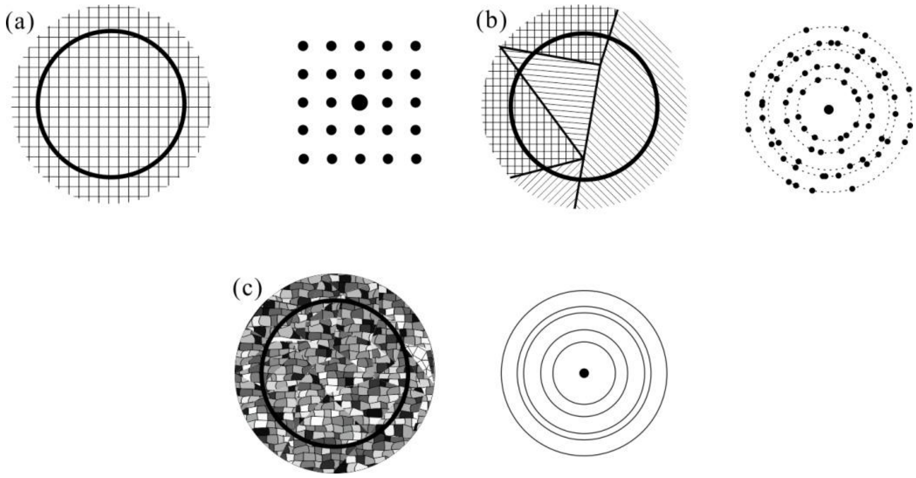

Figure 4.11: Types of diffraction pattern which arise from different microstructures. (a) A single crystal; (b) A small number of grains – five grains circled here; (c) A large number of fine grains with random orientation. Dashed ring of diffraction pattern in (b) does not actually exist and is just placed here for explanation [107].

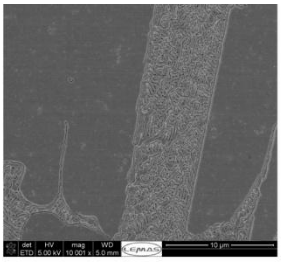
1. Selected target area

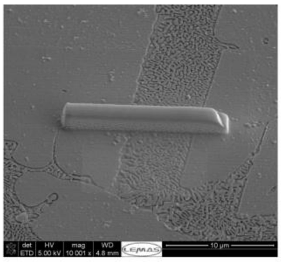
2. Coated by platinum

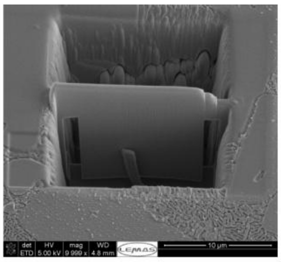
3. Sectioned lamella

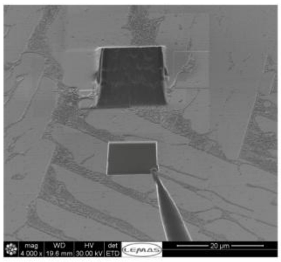
4. Lamella moved by fine needle

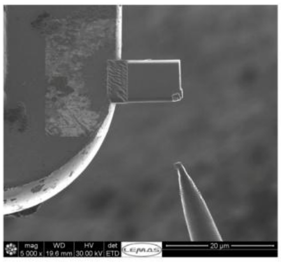
5. Welded lamella on the TEM grid

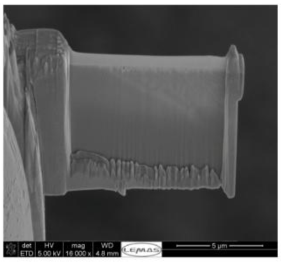
6. Lamella was sliced by Ga ion beam

Figure 4.12: FIB operation technique for TEM sample preparation

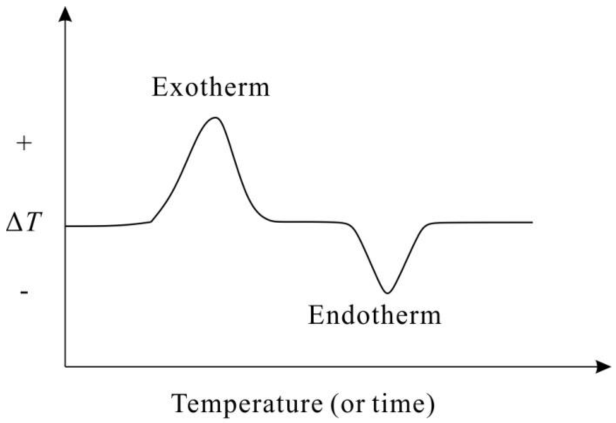

Figure 4.13: A schematic of a typical DTA curve after [118]

5 Experimental results

This chapter contains all of the experimental results related to $Ni_{74.7-x}Fe_xSi_{25.3}$[3] (x = 0, 5, 10 and 15 at.%) alloys. Firstly, the cooling rates as a function of droplet diameter in the drop tube are calculated according to the reference equations. Then the results of the characterisation of the alloys produced using the arc-melting technique are presented. The main emphasis is placed on the phase formation and microstructural evolution in the drop tube processed samples.

5.1 Calculated cooling rate in the drop tube

During the rapid solidification process in the drop tube, it is not possible to measure or record the temperature of droplets with different diameters of size in the micrometer range. Nevertheless, there are two methods to estimate the cooling rate in the drop tube process. Firstly, the cooling rate can be calculated from the mathematical models based on the balance of thermal fluxes [86]. Secondly, the cooling rate can be determined from the mathematical models based on the measurements of the secondary dendrite arm spacing of solidified microstructures [19, 119]. Here, we use the first method to evaluate the cooling rate. The second method will be discussed in detail in the next chapter.

Falling through the nitrogen atmosphere, the cooling rate of droplets depends strongly on their sizes. There are two mechanisms for heat transfer: heat radiation and heat convection. According to the reference [120], the cooling rate of freely falling droplets can be expressed as:

$$\dot{T} = \frac{6}{\rho C_p D}\left[\varepsilon\sigma(T^4 - T_{\mathrm{a}}^4) + h(T - T_{\mathrm{a}})\right] \tag{5-1}$$

where ρ is the density of the metal, C_p is the heat capacity of undercooled melt, D is the droplet diameter, ε is the surface emissivity, σ is the Stefan-Boltzmann constant, T is the droplet temperature during free fall, T_a is the ambient temperature, and h is the heat transfer coefficient of droplets. Assuming that the falling droplet is spherical, the value of heat transfer coefficient can be determined by:

---

[3] The subscripts in the formula denote the nominal compositions in at % of the corresponding metals in this thesis.

$$h = \frac{\lambda_g}{D}[2 + 0.6\left(\frac{V_r D\rho_g}{\eta_g}\right)^{1/2}(\frac{c_g\eta_g}{\lambda_g})^{1/3}] \tag{5-2}$$

where λ_g, ρ_g, η_g and c_g are the thermal conductivity, density, dynamic viscosity and heat capacity of the ambient inert gas respectively and v_r is the relative velocity between the droplet and gas. The thermal conductivity, dynamic viscosity and heat capacity are not directly related to the pressure at low pressure. Therefore, these data for N_2 are obtained from the reference [121] at 300 K and 1 atmosphere pressure. However, the density of the gas has a strong relationship with the pressure, which is calculated by:

$$PV = nRT \tag{5-3}$$

and

$$\rho_g = \frac{m_g}{V} = \frac{nM}{V} \tag{5-4}$$

where P, V and T are the pressure, volume and temperature of the chamber, m_g, n and M are the mass, mole number and mole mass of the nitrogen, and R is the gas constant. The pressure and the temperature in the drop tube were around 5×10^4 Pa and 300 K, respectively. In the present project, the melt (≈ 12 g) was ejected from the crucible with 3 drilled holes (300 μm diameter) within 2 seconds, wherein we would estimate the initial average velocity of the particles away from the crucible to be about 1.1 m s^{-1}. The maximum velocity at the bottom of the tube would be about 12.4 m s^{-1} on the assumption that the particle dropped under vacuum condition (gravitational acceleration being 9.8 m s^{-2}). The instantaneous velocity is only related to the heat convection term in Equation (5-1). The error of the calculated cooling rate is estimated on the basis of the calculated results with the velocities being 1.1 m s^{-1} and 12.4 m s^{-1} respectively. The physical parameters used to calculate the cooling rate and the heat-transfer coefficient are presented in **Table 5.1** and **Table 5.2**.

Since Ni and Fe are similar chemically and have close properties, the calculated cooling rates of $Ni_{74.7-x}Fe_xSi_{25.3}$ (x = 0, 10 and 15 at.%) are also close. Here the cooling rate of the $Ni_{64.7}Fe_{10}Si_{25.3}$ alloy is calculated: 1) the minimum and maximum calculated droplet diameters are 50 μm and 850 μm; 2) the melting temperature of $Ni_{64.7}Fe_{10}Si_{25.3}$ alloy is 1444 K. The calculated results of cooling rate as a function of droplet diameter are shown in **Figure 5.1**. It can be seen that the cooling rate increases when the droplet diameter decreases. Corresponding to the maximum, medium and minimum droplets of $Ni_{64.7}Fe_{10}Si_{25.3}$ alloy with diameters 850 μm, 210 μm and 50 μm, the calculated cooling rates were 3.88×10^{2}, 3.38×10^{3} and 4.11×10^{4} K s^{-1}.

Table 5.1: Thermal physical properties of nitrogen gas at room temperature [121-124]

λ_g (J m^{-1} s^{-1} K^{-1})	0.0249[a]
ρ_g (kg m^{-3})	0.561[b]
η_g (kg m^{-1} s^{-1})	0.0000179[a]
c_g (J kg^{-1} K^{-1})	1038.310[a]
M (kg mol^{-1})	0.028
R (J mol^{-1} K^{-1})	8.314

[a] The parameters are approximate values at 300 K and 1 atmosphere pressure.
[b] The density is calculated by Equations (5-3) and (5-4) ($P=5\times10^4$ Pa, $T=300$ K)

Table 5.2: Physical parameters of $Ni_{64.7}Fe_{10}Si_{25.3}$ alloy[a]

Mass density ρ, kg m^{-3}	6.458×10^{3}[b]
Heat capacity C_p, J kg^{-1} K^{-1}	743.76[b]
Surface emissivity ε	0.4002[b]
Stefan-Boltzmann constant σ, W m^{-2} K^{-4}	5.67×10^{-8}
Relative drop velocity V_r, m s^{-1}	1.1
The melting temperature of alloy T, K	1444
Ambient temperature T_a, K	300[c]

[a] The parameter are calculated by pure elements according to their atomic fractions and the data of pure Ni, Fe and Si.
[b] Metal Reference Book [125].

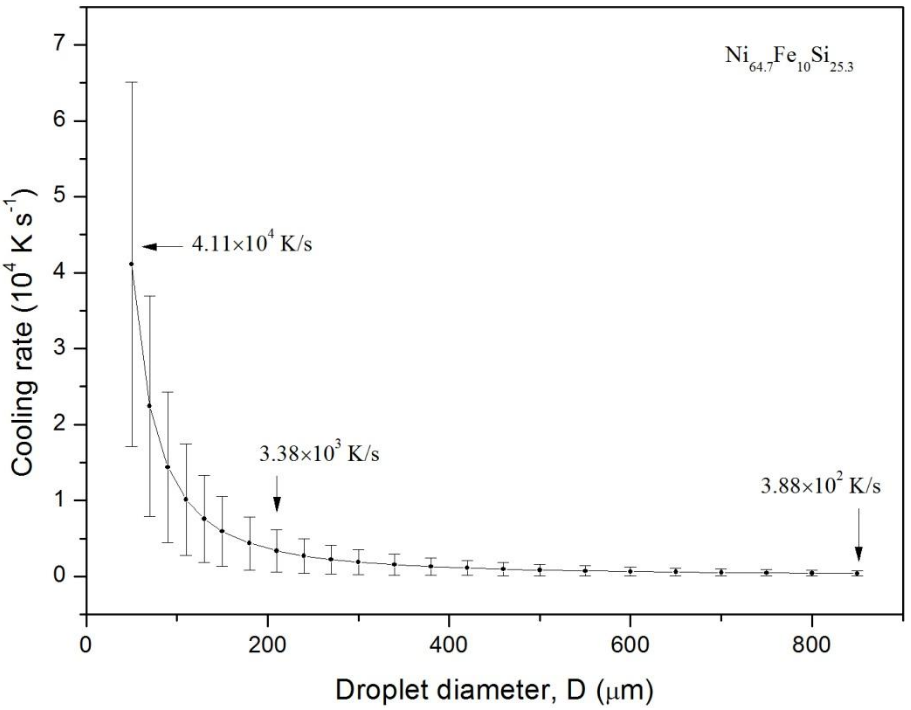

Figure 5.1: Calculated cooling rate versus droplet diameter

5.2 Ni-Fe-Si arc-melted samples

Four $Ni_{74.7-x}Fe_xSi_{25.3}$ (x = 0, 5, 10 and 15 at.%) alloys were produced in the arc-melting furnace. All of these alloys were melted 10 times to ensure thorough mixing of the constituent elements. XRD and SEM (BSE and EDX) detection techniques were carried out to reveal the phases and microstructures of the alloys. The solidification process in the arc-melting furnace corresponds to moderate cooling rates, with expected high cooling rate in the region adjacent to the chilled copper hearth. All of the results presented here will be useful to understand the solidification behaviour at moderate cooling rate and act as the comparative experiments relative to later drop tube experiments.

5.2.1 X-ray diffraction analysis

XRD analysis was performed to identify the phases of the Ni-25.3 at.% Si arc-melted alloy. The XRD result of the Ni-25.3 at.% Si alloy was analysed by the technique of Rietveld refinement to estimate the amounts of different phases. The Ni-Fe-Si[4] arc-melted alloys showed regular and coarse microstructures (see section 5.2.2). Therefore, the arc-melted Ni-Fe-Si alloys were crushed manually to destroy the texture of the regular lamellar structures.

The diffraction pattern of the Ni-25.3 at.% Si is shown in **Figure 5.2**. It shows the presence of three phases: β_1-Ni_3Si, γ-$Ni_{31}Si_{12}$ and metastable phase, $Ni_{25}Si_9$[5]. Besides the structural similarity, the cell parameters of β_1-Ni_3Si and α-Ni are also quite close (**Figure 3.9**). Therefore, the positions (2theta) of their characteristic diffraction peaks occurring are also very close (**Figure 3.10**), which leads to the difficulty to distinguish them. So, the formation of α-Ni cannot be confirmed by XRD. The amounts of different phases were analyzed by Rietveld refinement technique with two different assumptions about whether α-Ni formed in the arc-melted sample or not. The simulated results are shown in **Figure 5.3** and **Figure 5.4**. The quality of fitting is assessed from the simulated fit parameters, including weighted residual error (R_w), expected error (R_{exp}) and good of fit (GoF), which are also shown in **Figure 5.3** and **Figure 5.4** revealing good fitting [113]. No matter whether α-Ni

---

[4] Here, Ni-Fe-Si arc-melted alloys denote the arc-melted $Ni_{74.7-x}Fe_xSi_{25.3}$ (x = 5, 10 and 15 at.%) alloys.

[5] $Ni_{74}Si_{26}$ is a stacking variant of $Ni_{25}Si_9$, so only $Ni_{25}Si_9$ is referred for further discussion.

formed, both of the simulated results[6] indicate that β_1-Ni_3Si formed as the dominant phase (> 61.9 %). Even if α-Ni formed in the sample, the fraction is low, being 7.0 %. In both cases, the fractions of $Ni_{31}Si_{12}$ are almost the same, being 22.0% (without α-Ni) and 22.3 % (with α-Ni), while the fraction of $Ni_{25}Si_9$ is 8.8 %.

The XRD results of these three arc-melted Ni-Fe-Si alloys are similar, showing the presence of γ-$Ni_{31}Si_{12}$, as shown in **Figure 5.5**(b, c and d). Similarly, due to the difficulty to distinguish α and β_1 phases, the phase here co-existing with the γ-$Ni_{31}Si_{12}$ phase cannot be confirmed by XRD results, which will be further discussed in the next chapter. Meanwhile the observed microstructures are simple and clear (see section 5.2.2), so the quantitative analysis has not been done by the Rietveld refinement method.

5.2.2 Composition and Microstructure

EDX analysis was carried out to check the compositions on the polished but unetched samples and several regions were measured randomly to gain the average composition.

The EDX results of these four arc-melted solidified samples are shown in **Table 5.3**, indicating the detected compositions are close to the nominal compositions. **Figure 5.6** represents the general microstructure of the arc-melted Ni-25.3 at.% Si alloy, showing a quite irregular and refined microstructure with the dominant phase (M) dispersing randomly in the sample. The measured Si composition of the M phase was 24.08 ± 0.33 at.%. Therefore, M phase is identified as β_1-Ni_3Si (22.6-24.5 at.% Si), which is consistent with the XRD analysis of that β_1-Ni_3Si is the dominant phase. **Figure 5.7** shows the microstructures of the arc-melted $Ni_{74.7-x}Fe_xSi_{25.3}$ (x=5, 10 and 15) alloys, which are quite different from that of the arc-melted Ni-25.3 at.% Si sample. Even with 5 at.% Fe, the microstructure shows a regular lamellar structure comprising alternating lamellae of single phase and eutectic/eutectoid structure[7], as shown in **Figure 5.7**c. Similar structures were also observed in the solidified $Ni_{64.7}Fe_{10}Si_{25.3}$ and $Ni_{59.7}Fe_{15}Si_{25.3}$ samples (**Figure 5.7** d and e).

---

[6] The fitting results by Rietveld analysis are mass fraction.

[7] The solidification mechanism is not studied here, so it is referred as the eutectic/eutectoid structure.

The average compositions of the single-phase lamellar and eutectic/eutectoid area in the arc-melted Ni-Fe-Si samples were also analysed by EDX and are given in **Table 5.4**. Here, the single lamellae in the Ni-Fe-Si samples can be considered as the γ-$Ni_{31}Si_{12}$ phase for the following two reasons. Firstly, the XRD analysis has suggested the presence of the γ-$Ni_{31}Si_{12}$. Secondly, the Si compositions of the single lamellae were close to the composition of the γ-$Ni_{31}Si_{12}$ (27.91 at.% Si) in the Ni-Si binary system. The formation of the single γ-$Ni_{31}Si_{12}$ phase will also be a feature of later drop tube processed Ni-Fe-Si samples. The Si compositions of the eutectic areas are also close to the binary $\alpha + \beta_3$ eutectic composition (21.4 at.% Si) (Table 3.2). Moreover, The Fe concentration in the *γ* phase increased with the increase of the nominal Fe composition, but it was always lower than the nominal values (**Table 5.4**). The surplus Fe partitioned segregated in the eutectic/eutectoid areas as well, which is consistent with the element X-ray map (**Figure 5.8**). Lamellar structure was perpendicular to the copper hearth and roughly opposite to the direction of heat conduction.

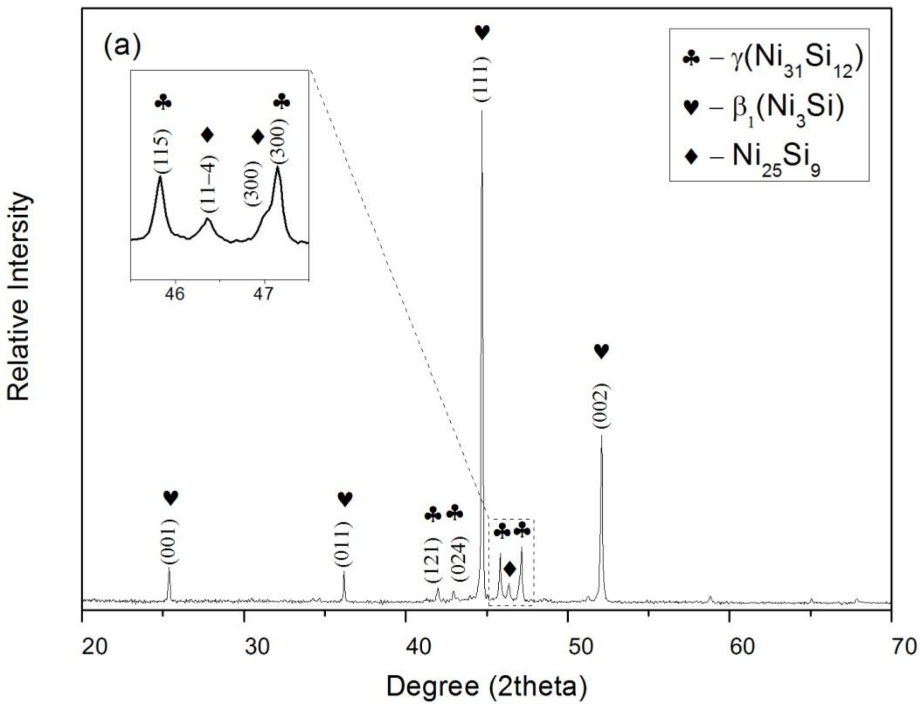

Figure 5.2: XRD results of the arc-melted Ni-25.3 at.% Si alloy

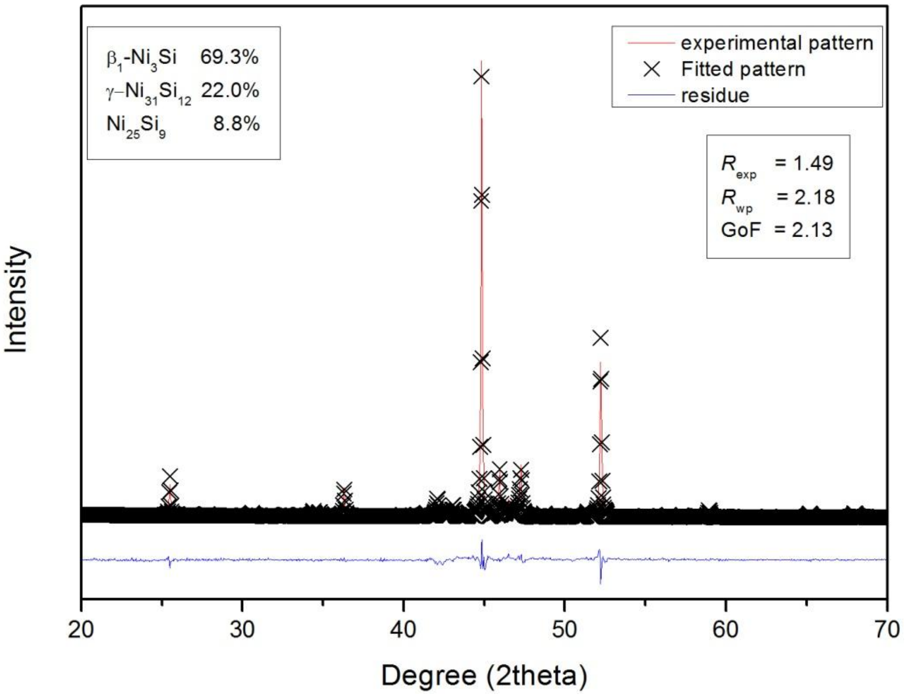

Figure 5.3: Quantitative analysis of the Ni-25.3 at.% Si alloy using Rietveld refinement with the assumption that α-Ni did not form in the sample.

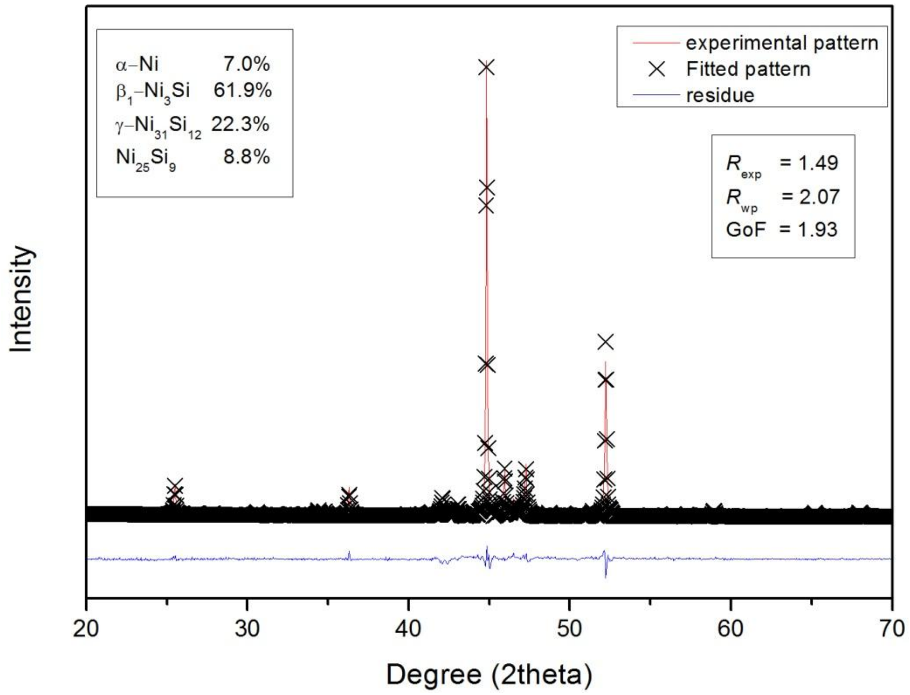

Figure 5.4: Quantitative analysis of the Ni-25.3 at.% Si alloy using Rietveld refinement with the assumption that α-Ni formed in the sample.

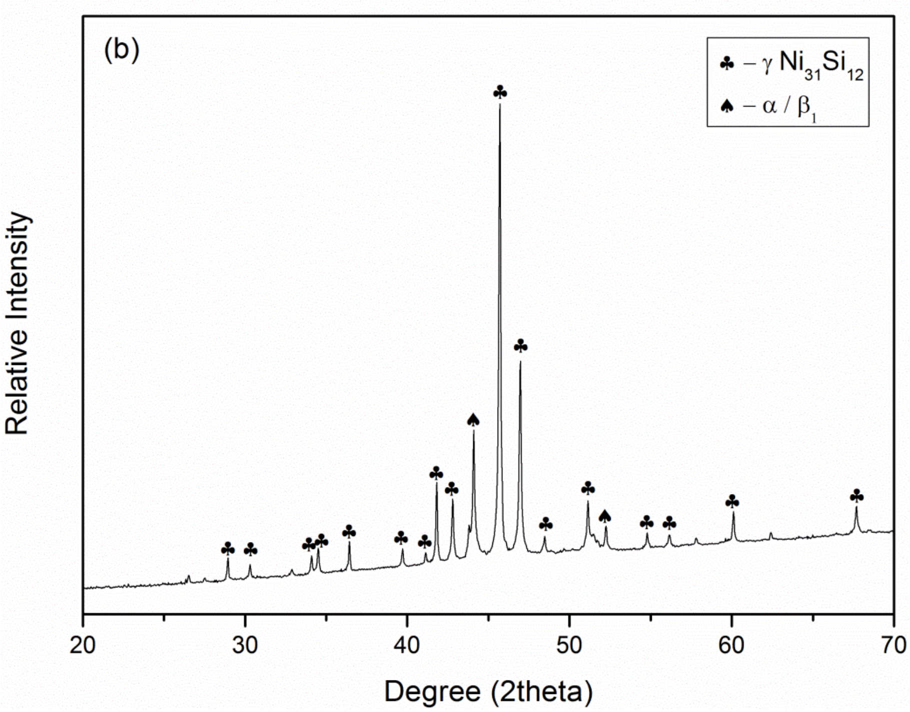

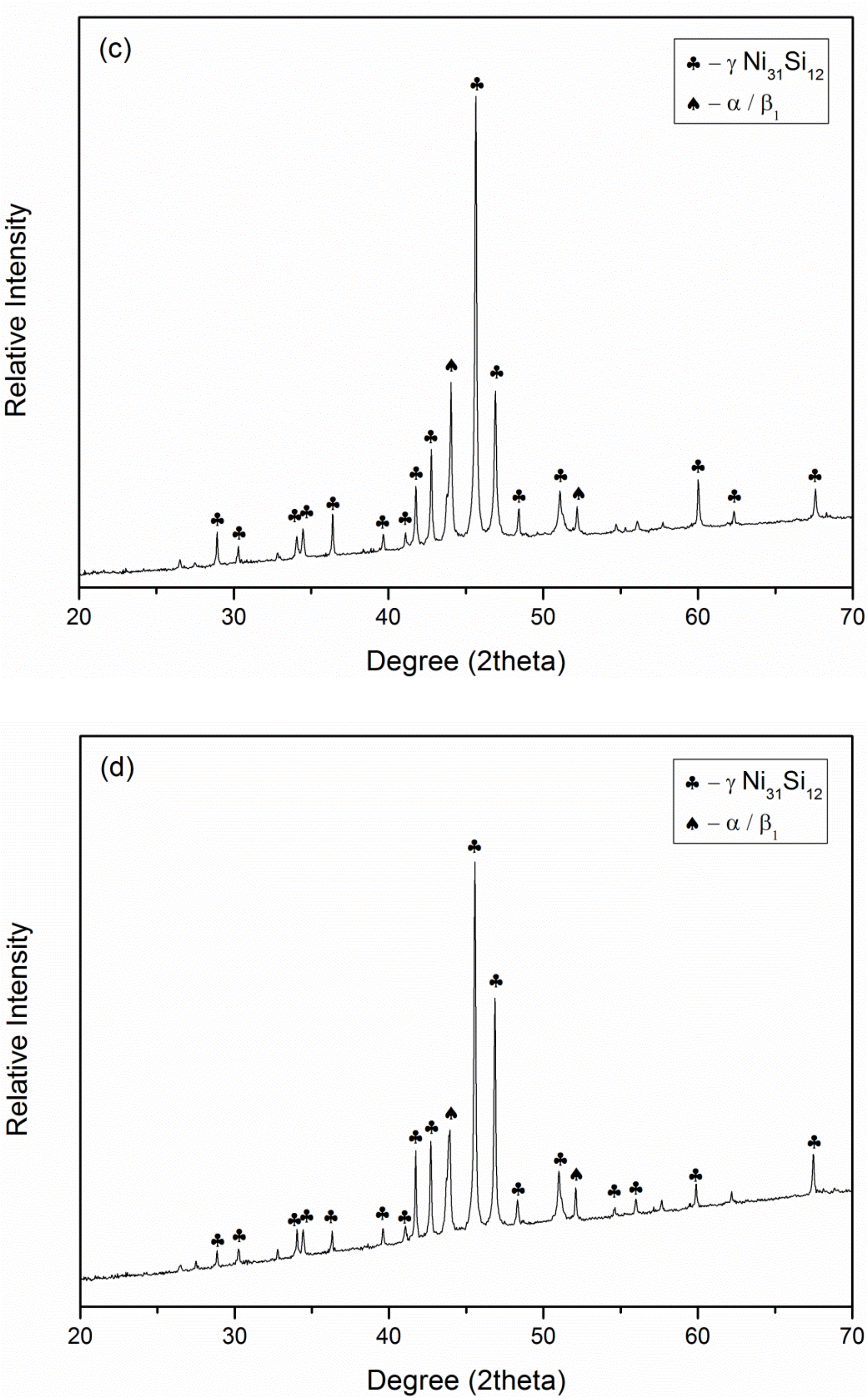

Figure 5.5: XRD results of the arc-melted Ni-Fe-Si alloys: (b) $Ni_{69.7}Fe_5Si_{25.3}$; (c) $Ni_{64.7}Fe_{10}Si_{25.3}$; (d) $Ni_{59.7}Fe_{15}Si_{25.3}$.

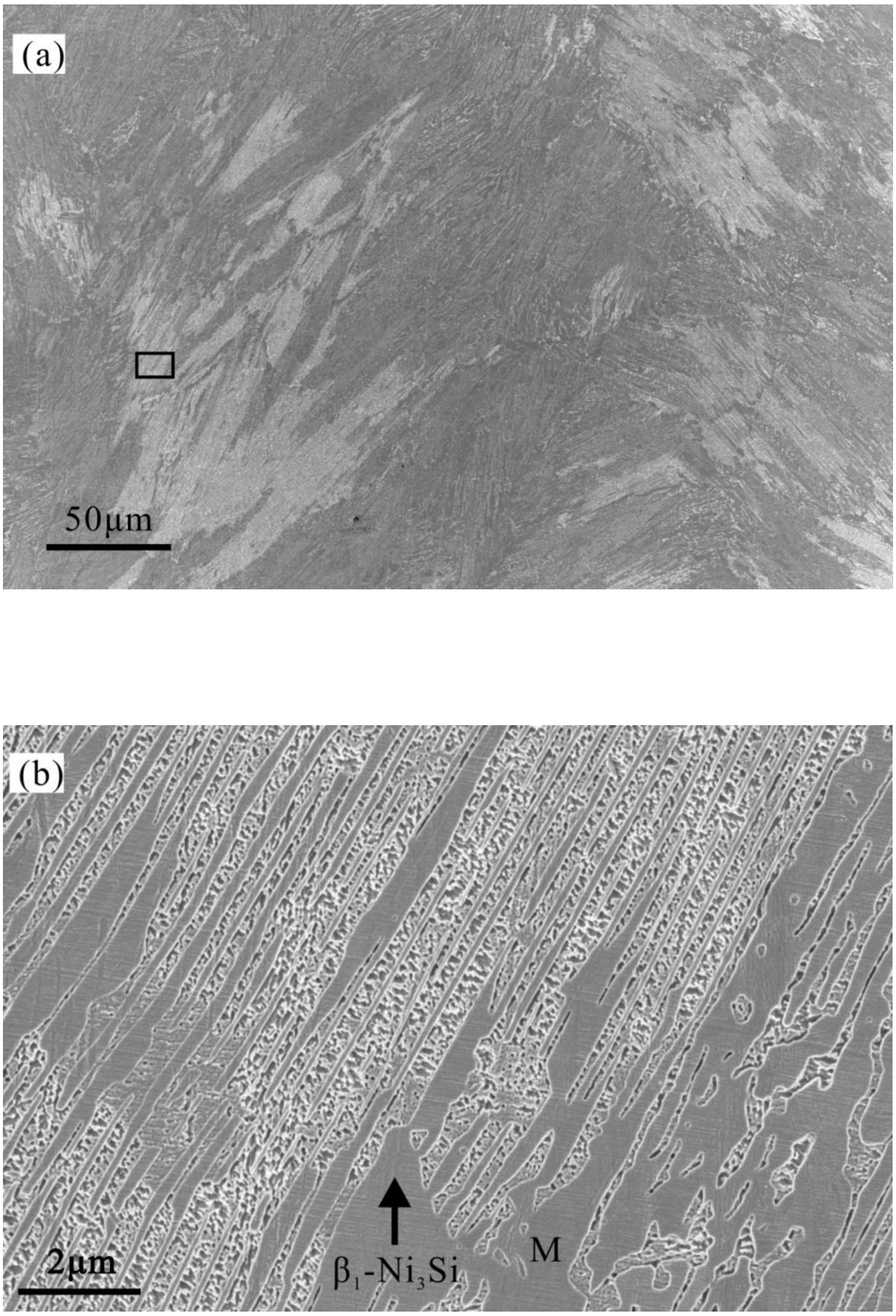

Figure 5.6: SEM micrograph (a) showing the fine microstructure of Ni-25.3 at.% Si arc-melted sample; Magnified image (b) from the area highlighted by the black square.

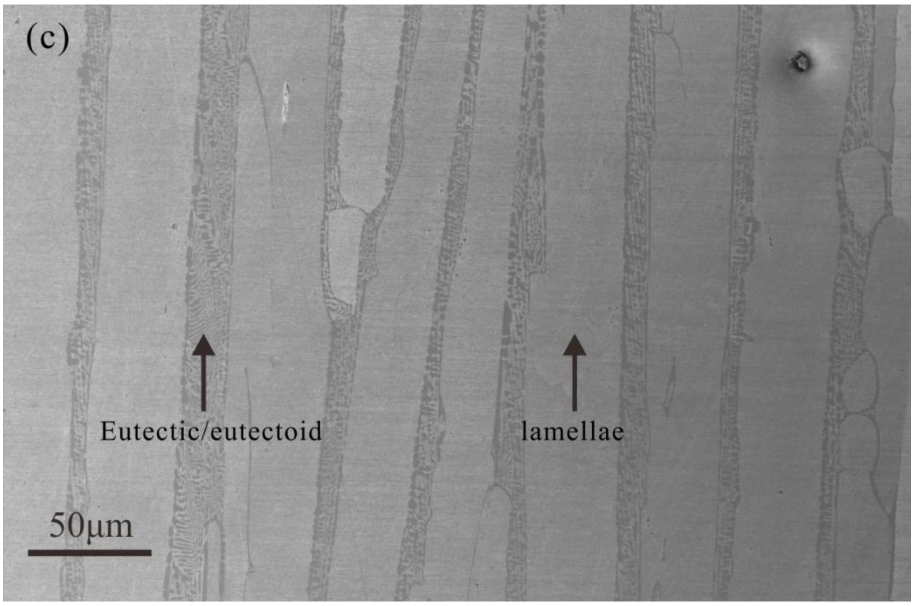
(c)
Eutectic/eutectoid
lamellae
50μm

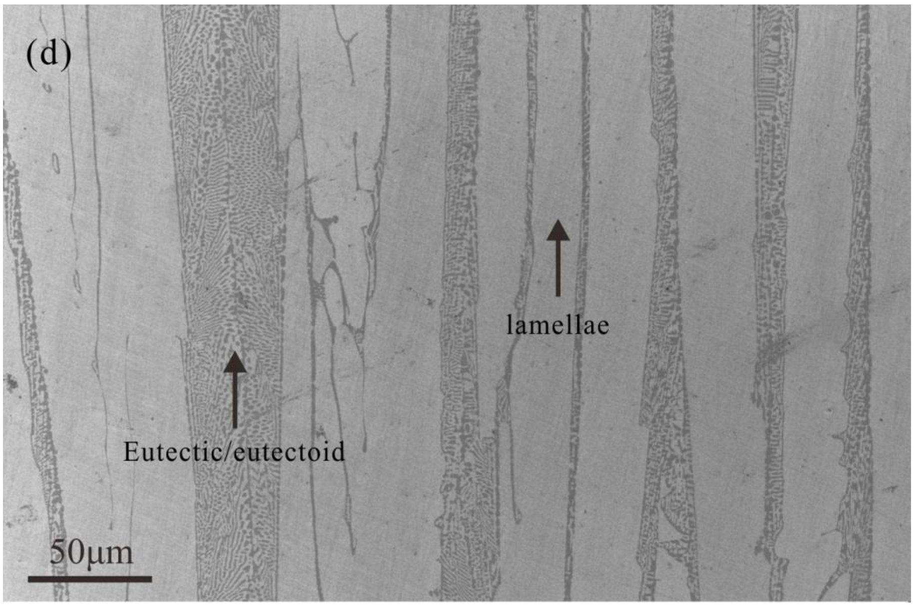
(d)
lamellae
Eutectic/eutectoid
50μm

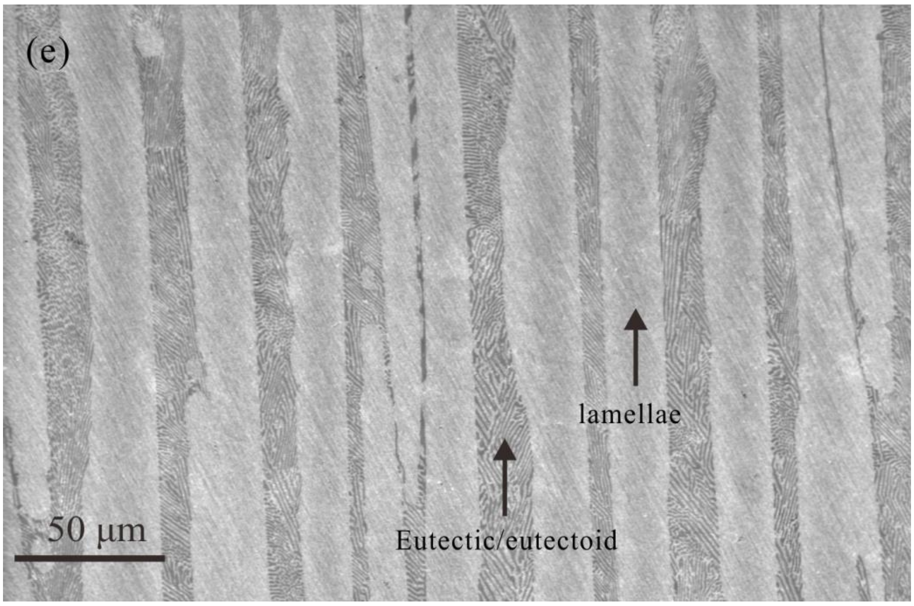

Figure 5.7: SEM images showing the structures of the Ni-Fe-Si arc-melted samples: (c) $Ni_{69.7}Fe_5Si_{25.3}$; (d) $Ni_{64.7}Fe_{10}Si_{25.3}$; (e) $Ni_{59.7}Fe_{15}Si_{25.3}$. The compositions of the coarse phase and eutectic/eutectoid area are shown in **Table 5.4**.

Table 5.3: Average EDX composition of the arc-melted samples

Sample	Compositions					
	Ni (at.%)	STDEV	Fe (at.%)	STDEV	Si (at.%)	STDEV
$Ni_{74.7}Si_{25.3}$	76.00	0.16	0	-	24.00	0.16
$Ni_{69.7}Fe_5Si_{25.3}$	70.14	0.12	5.17	0.24	24.69	0.30
$Ni_{64.7}Fe_{10}Si_{25.3}$	64.85	0.26	10.19	0.48	24.97	0.32
$Ni_{59.7}Fe_{15}Si_{25.3}$	59.67	0.22	15.57	0.20	24.75	0.14

The samples were measured by EDX before being etched and several different areas were checked randomly for each sample.

Table 5.4: Average EDX composition of coarse lamellar phase and eutectic/eutectoid area for arc-melted samples

Sample	Compositions (at.%)					
	Coarse γ phase			Eutectic/eutectoid structure		
	Ni (STDEV)	Fe (STDEV)	Si (STDEV)	Ni (STDEV)	Fe (STDEV)	Si (STDEV)
$Ni_{69.7}Fe_5Si_{25.3}$	70.50(0.17)	2.91(0.19)	26.59(0.13)	69.70(0.10)	10.72(0.31)	19.58(0.38)
$Ni_{64.7}Fe_{10}Si_{25.3}$	66.27(0.28)	6.82(0.23)	26.91(0.14)	61.89(0.28)	17.96(0.55)	20.15(0.62)
$Ni_{59.7}Fe_{15}Si_{25.3}$	61.98(0.28)	10.98(0.41)	27.04(0.22)	56.06(0.55)	22.83(0.78)	21.11(0.38)

Similarly, several different areas have been checked randomly for each sample.

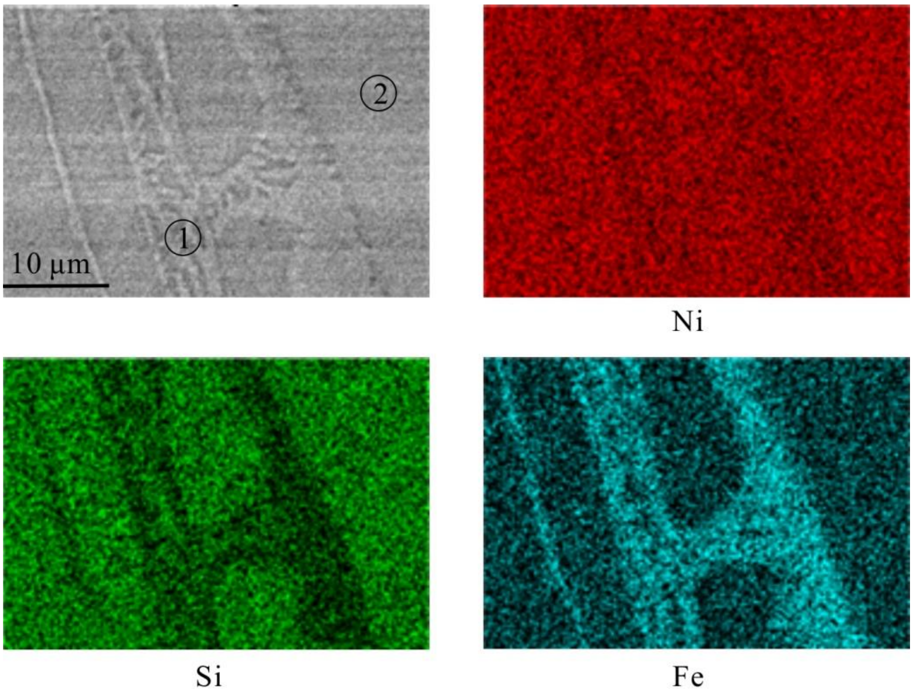

Figure 5.8: The element X-ray map of the $Ni_{64.7}Fe_{10}Si_{25.3}$ alloy and SEM image. The areas of (1) and (2) correspond to the eutectic/eutectoid area and single lamellae. The element compositions are in proportion to the intensity.

5.3 Ni-25.3 at.% Si drop tube samples

The drop tube experiments of the Ni-25.3 at.% Si alloy were performed twice to obtain enough particles (75-850 μm). The first batch of the particles was used to do some trial test and training, so the results were mainly obtained from the second batch of the particles. Firstly, EDX analysis was carried out to check the compositions of all ranges of the particles. Here, the average composition was achieved by analysing particles randomly using area scanning and at least 10 particles were analysed in each size range. The measured compositions were within the range 24.97-25.46 at.% for Si, as illustrated in **Figure 5.9**. Therefore, all ranges of the particles have the average compositions close to the nominal composition. Then, several analysis techniques were used, e.g. XRD, SEM and TEM, to identify the solidified phases, study the microstructural evolution and confirm the specific phases of the typical microstructures.

5.3.1 X-ray diffraction

X-ray diffraction analysis was carried out on the solidified particles (second batch) with diameters in the range 75-850 μm, as shown in **Figure 5.10**. All diffraction patterns showed the same result, even for the smallest range of particles (highest cooling rate), the presence of three phases namely: γ-$Ni_{31}Si_{12}$, β_1-Ni_3Si and metastable $Ni_{25}Si_9$. In comparison with the arc-melted Ni-25.3 at.% Si alloy, the metastable $Ni_{25}Si_9$ in the drop tube sample, instead of the β_1-Ni_3Si phase, solidified as the dominant phase here, which will be discussed in detail later. As mentioned earlier, it is difficult to distinguish between α-Ni and β_1-Ni_3Si phases due to their similar structure and diffraction patterns. Fortunately, for two batches of the 500-850 μm particles, the XRD diffraction patterns showed the existence of the β_1-Ni_3Si according to the presence of characteristic peaks corresponding to the (100) and (110) planes (**Figure 5.11**). The α-Ni phase might exist in the solidified particles.

It has been mentioned earlier that the mixed metastable phases ($Ni_{25}Si_9$ and $Ni_{74}Si_{26}$) are referred to as $Ni_{25}Si_9$. Due to the lack of structural information for $Ni_{74}Si_{26}$, the XRD patterns have not been analyzed by the Reitveld refinement technique.

5.3.2 Microstructural characterization

The microstructures of the Ni-25.3 at.% Si particles were mainly studied by SEM at high magnification due to the refined microstructure. In summary, there were three typical microstructures, as shown in **Figure 5.12**: (I) regular lamellar structure; (II) heteroclite structure; (III) anomalous eutectic structure. **Figure 5.13** shows the microstructure of one typical particle, which includes these typical structures (I, II and III) and one single phase (M_1). **Figure 5.14** and **Figure 5.15** show the detailed microstructures of A and B areas in **Figure 5.13**. It is clear that the structure (I) displays a regular lamellar morphology, while the structure (III) is always observed in several small isolated regions with anomalous morphology. In addition, **Figure 5.16** shows two another types of the particles, with one having entire heteroclite structure II and the other having the mixed structure (II, III and single phase M_1[8]). Moreover, there are two other phases (M_2 and M_3[8]), as shown in **Figure 5.17** and **Figure 5.18**. The phase M_2 is surrounded by the regular lamellar structure (I), while the phase M_3 grows continuously throughout the whole particle.

In order to study the microstructural evolution as the cooling rate was increased, the Ni-25.3 at.% Si alloy particles were classified into two different categories (A and B) according to the microstructure difference, as listed in **Table 5.5**. The particles of type A presented only the heteroclite structure (II). This kind of the particles was quite easily distinguishable, even with optical microscopy, once the particles had been etched. The rest of the particles belonged to type B, which presented complicated microstructures, including several of the structures I, II, III, M_1, M_2 and M_3.

The fractions of the type A particle in all size ranges of the particles were counted. The numbers of counted particles were 230 (300-500 μm), 295 (212-300 μm), 304 (150-212 μm), 428 (106-150 μm) and 394 (75-106 μm). The results are illustrated in **Figure 5.19**, showing that the fraction of the type A particle with the entire heteroclite structure (II) increased as the particle size decreased, from 13.91% (300-500 μm) to 40.1% (75-106 μm). There was no particle with only the heteroclite structure in the 500-850 μm particles.

---

[8] The regions M_1, M_2 and M_3 will subsequently be identified as the different phases by TEM.

Although the microstructures of type B particles (75-850 μm) were complex, the formation of the regular lamellar structure changed regularly. Firstly, it was easy to be observed in big particles (212-850 μm). As the diameter was decreased, the difficulty to observe this structure increased gradually. Finally, the regular lamellar structure almost disappeared in all of the 75-106 μm particles. **Figure 5.20** gives the general information showing this decreasing trend with decreasing particle size.

5.3.3 Phase confirmation

In order to determine the origin of these three typical structures (I, II and III), TEM specimens (12 × 8 μm) were prepared using the site specific Focus Ion Beam (FIB) lift-out technique.

It is clear that the regular lamellar structure (I) comprises two phases, which were also observed with TEM bright field imaging. **Figure 5.21**a shows alternating regular lamellae comprising wide (≈ 200 nm) and narrow (≈ 20 nm) bands. Because of the similar structures of α-Ni and β_1-Ni_3Si, direct confirmation of the narrow band phase has not been achieved. However, from **Figure 5.21**a and **Figure 5.22** it is clear that the thin bands are continuous with, and therefore the same phase as, the single phase regions embedded within the lamellar structure. A selected area diffraction pattern confirmed this single phase region, and therefore the thin lamellae were the intermetallic phase β_1-Ni_3Si (inset of **Figure 5.21**a). A similar selected area diffraction pattern confirms that the wide lamellar phase is the metastable phase $Ni_{25}Si_9$ (inset in **Figure 5.21**b).

The heteroclite structure (II) also comprises two phases, with a small fraction of a fine phase with a curved morphology dispersed in the matrix. A bright field TEM micrograph is shown in **Figure 5.23**. Selected area diffraction confirmed that the coarse grain (the matrix) is the metastable phase $Ni_{25}Si_9$ (**Figure 5.24**). Twinned growth was also confirmed by TEM analysis due to the typical diffraction pattern of the twinned structure. The thickness of the fine phase was less than 20 nm, so it was difficult to confirm this fine phase. However, it has been shown by XRD and TEM (**Figure 5.21**) that β_1-Ni_3Si can form even in 300-500 μm particles with an average cooling rate of 1.20×10^3 K s^{-1} (400 μm), so the fine curved phase might be β_1-Ni_3Si.

The anomalous eutectic structure (III) and the single phase (M_1) were also analyzed by TEM, as shown in **Figure 5.25**. The TEM selected area diffraction patterns confirmed that the anomalous eutectic structure (III) comprised the metastable $Ni_{25}Si_9$ and stable β_1-Ni_3Si phases. Therefore, the structures, I and III, were composed of the same phases. The differences are that the structure III displays an anomalous morphology and can be only observed in some isolated regions. The single phase M_1 was identified as the stable γ-$Ni_{31}Si_{12}$ phase. Meanwhile, the phase M_2 surrounded by lamellar structure was identified as $Ni_{25}Si_9$ (**Figure 5.26**a), while the single phase M_3 was identified as β_1-Ni_3Si (**Figure 5.26**b). The identification of β_1-Ni_3Si provides the direct evidence that β_1-Ni_3Si can form directly from the undercooled liquid at high cooling rate. Moreover, the phase formed next to the β_1-Ni_3Si was identified as $Ni_{25}Si_9$ (**Figure 5.26**b), which supports the co-growth mechanism of the $Ni_{25}Si_9$ and β_1-Ni_3Si under non-equilibrium conditions.

The results of the phase identification by TEM are summarized in **Table 5.6**. The structures, I and III, consist of the $Ni_{25}Si_9$ and β_1-Ni_3Si phases. The coarse phase (matrix) in the heteroclite structure (II) is $Ni_{25}Si_9$. In addition, the formation of the single phases, γ-$Ni_{31}Si_{12}$ (M_1), $Ni_{25}Si_9$ (M_2) and β_1-Ni_3Si (M_3) are also confirmed.

All the particles had fine microstructures, indicating that the XRD patterns would be close to the non-oriented powder diffraction pattern. Thus, the relative intensities of the peaks should depend strongly on the fractions of the corresponding phases. It has been identified that M_2 is the metastable $Ni_{25}Si_9$ phase and $Ni_{25}Si_9$ is included in all these three structures. Therefore, according to its strong relative peak intensity, the metastable phase $Ni_{25}Si_9$ should be the dominant phase in all ranges of the Ni-25.3 at.% Si particles.

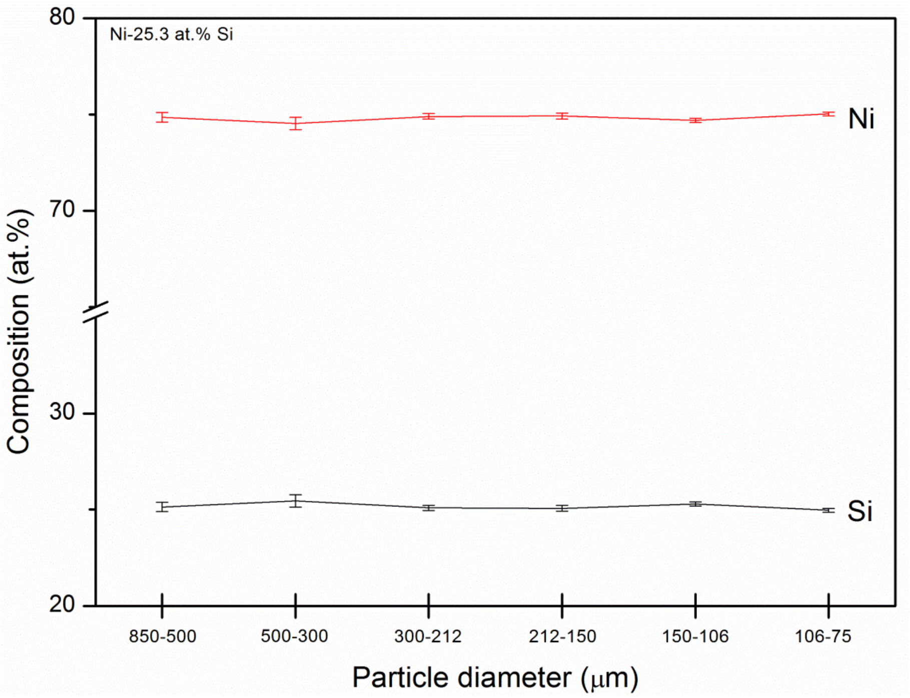

Figure 5.9: Average EDX compositions of Ni and Si of the Ni-25.3 at.% Si particles. At least 10 particles were analysed in each size range.

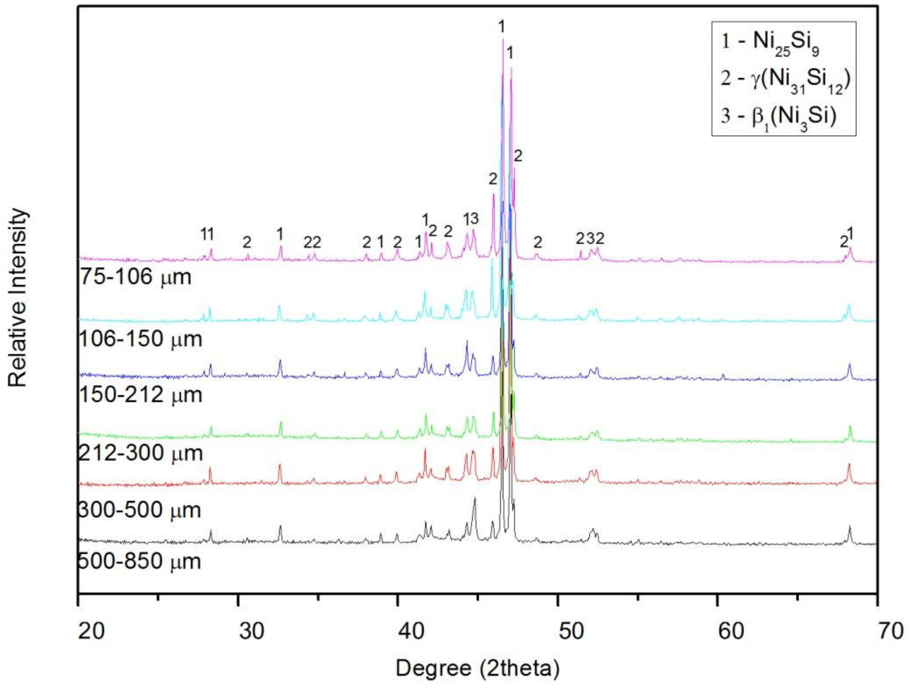

Figure 5.10: XRD results of the Ni-25.3 at.% Si particles with diameters in the range of 75-850 μm

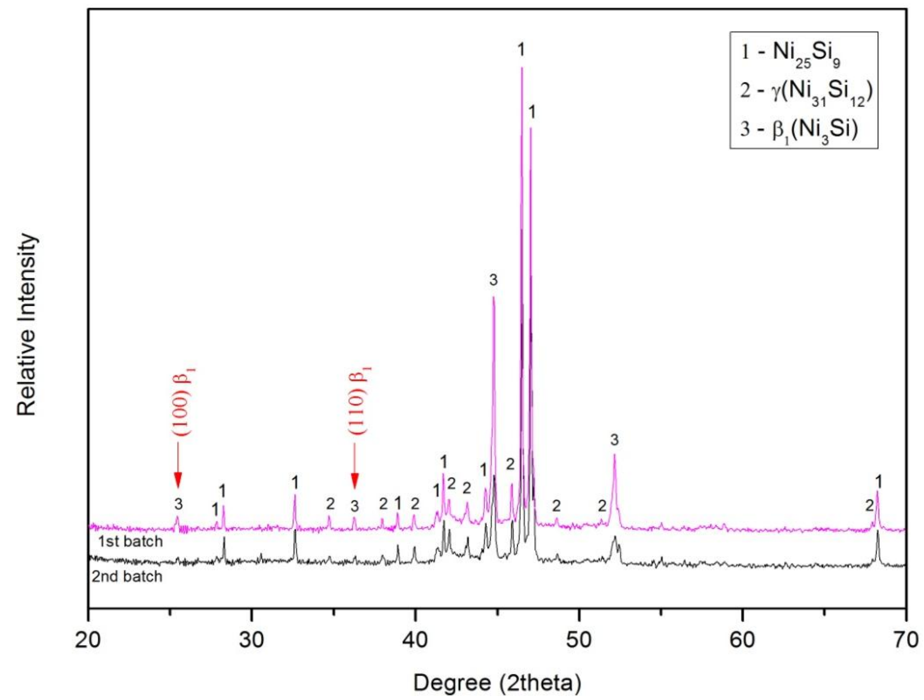

Figure 5.11: XRD pattern of the Ni-25.3 at.% Si particles with diameter being 500-850 μm (the first batch and the second batch).

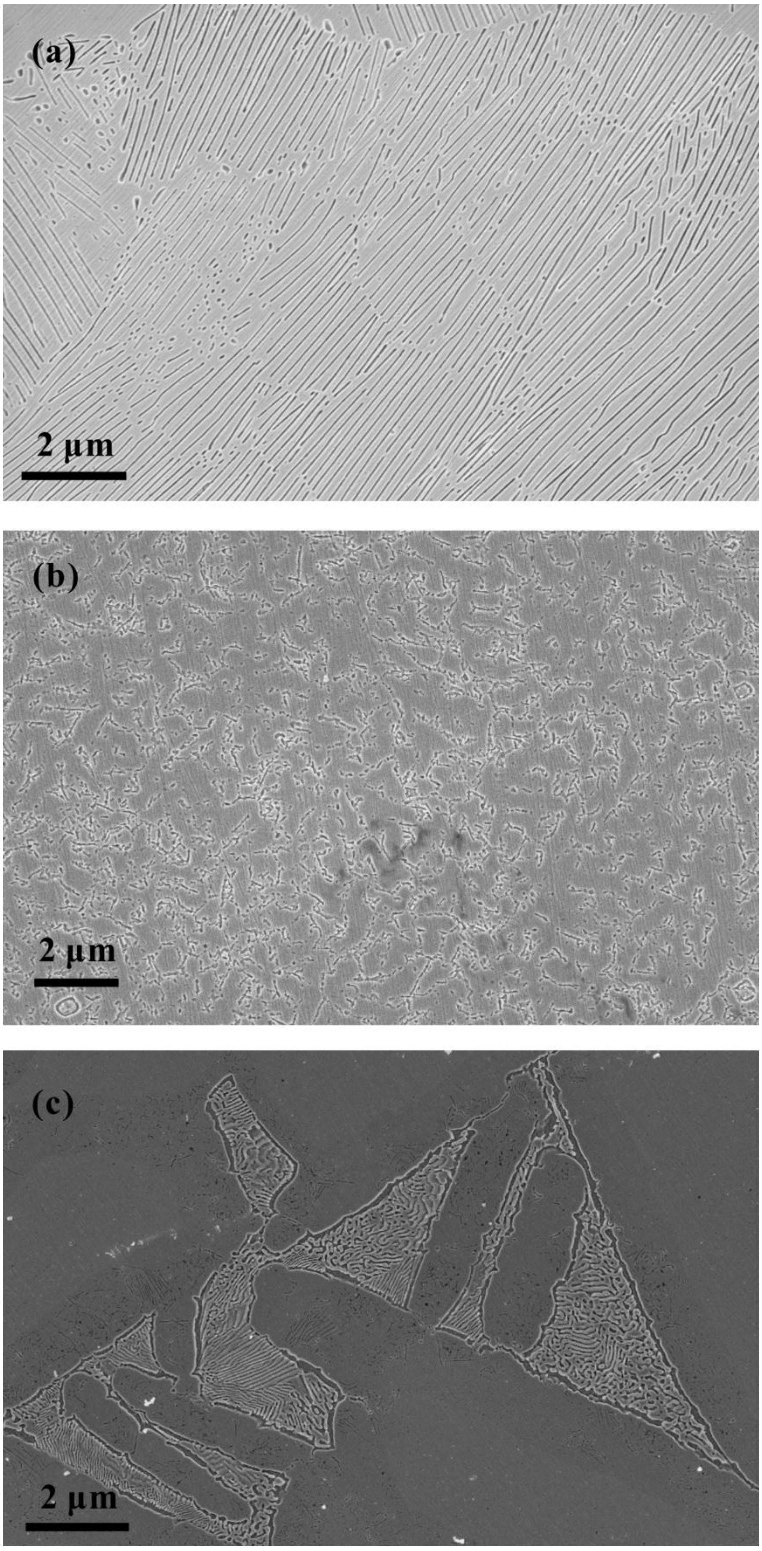

Figure 5.12: SEM images of three typical microstructures of Ni-25 at.% Si drop tube samples: (a) regular lamellar structure, I; (b) heteroclite structure, II; (c) anomalous eutectic structure, III.

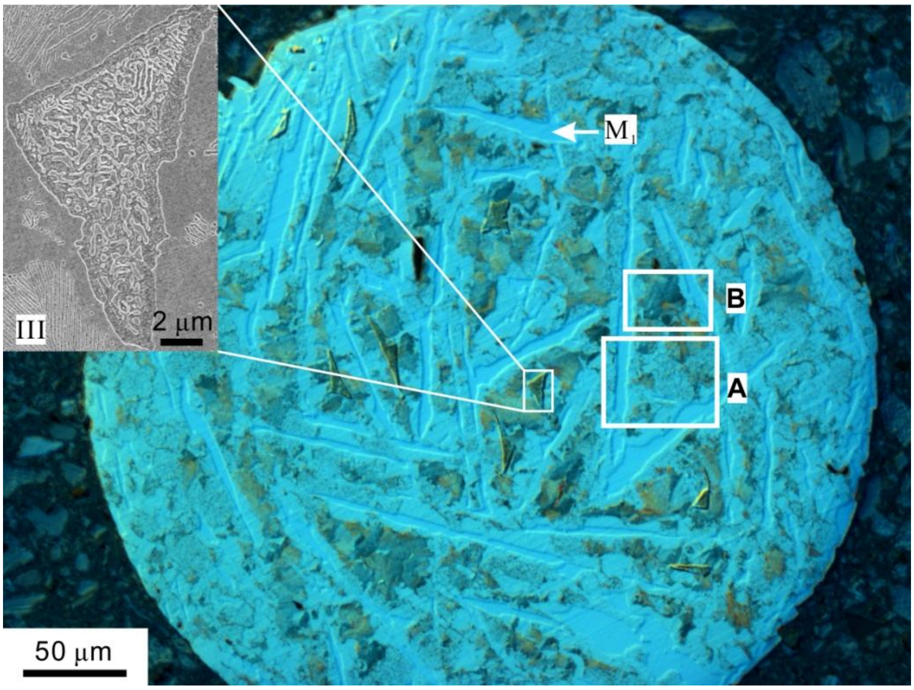

Figure 5.13: The DIC image of a particle from the 300-500 μm size range of Ni-25.3 at.% Si particles. The microstructures of the rectangular areas (A and B) are shown in **Figure 5.14** and **Figure 5.15**. The extended single phases (M_1) was analysed by TEM. Inset is the SEM image of the anomalous eutectic structure.

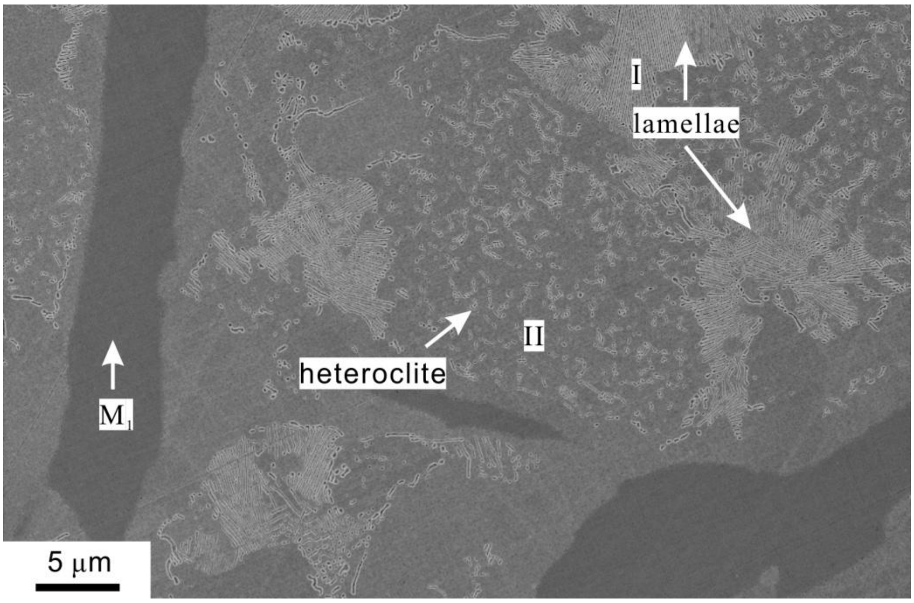

Figure 5.14: SEM image of the microstructure of the area ‘A’ marked in **Figure 5.13**. The clearer lamellar structure is also shown in **Figure 5.15**.

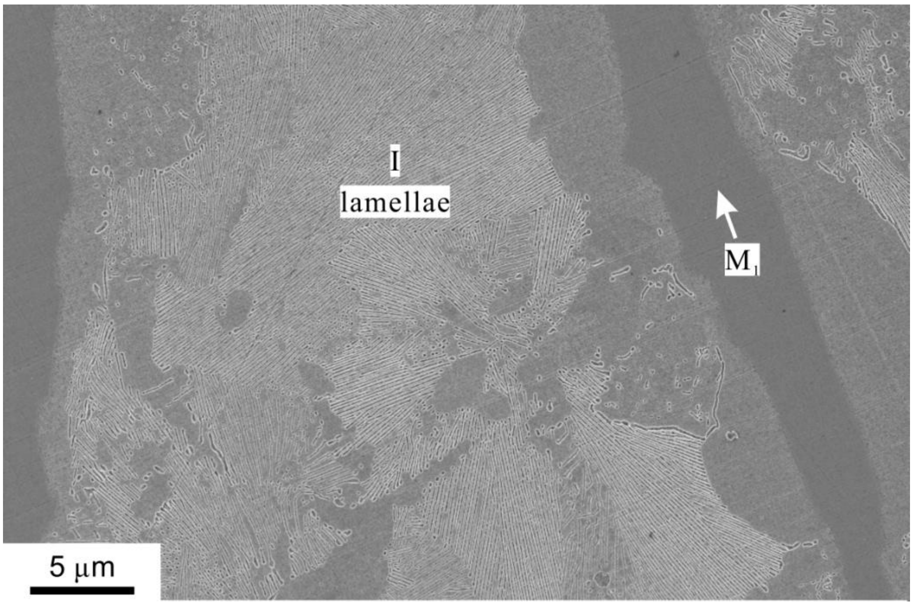

Figure 5.15: The microstructure of the area ‘B’ marked in **Figure 5.13**, showing the lamellar structure (I).

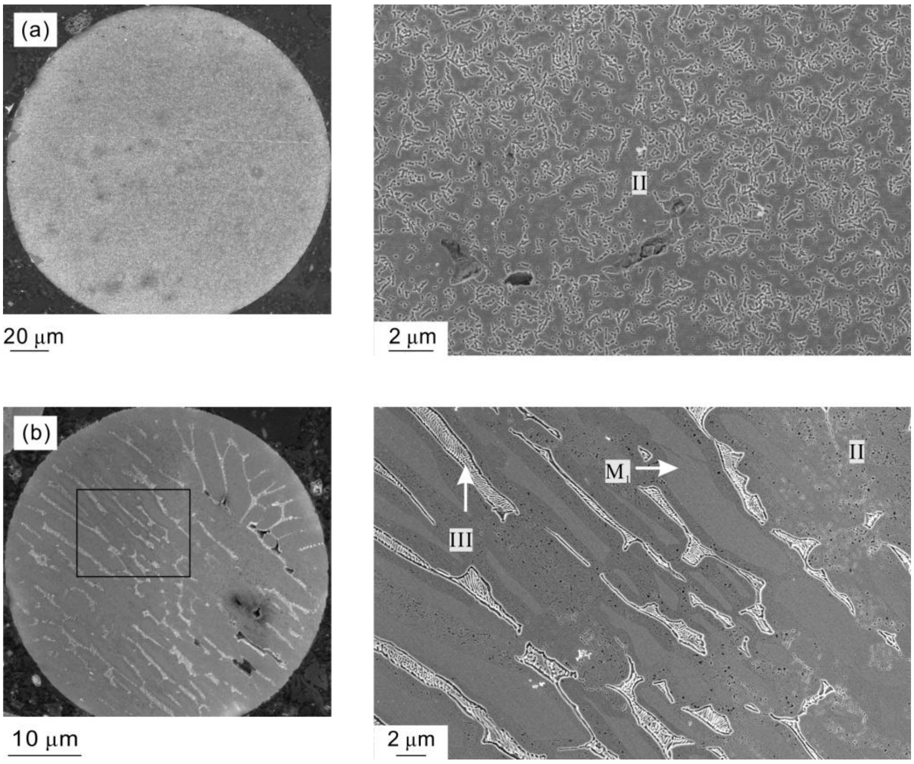

Figure 5.16: (a) SEM image of the 150-212 μm particle with entire heteroclite microstructure; (b) SEM image of the 75-106 μm particle with the structures of II and III and the single phase (M_1)

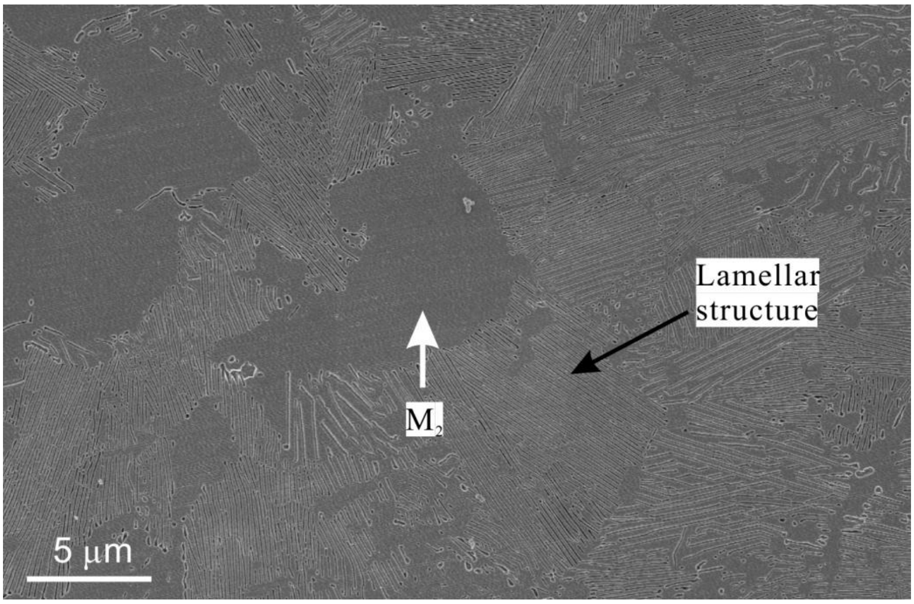

Figure 5.17: SEM micrograph of one 300-500 μm particle, showing the coarse phase M_2 surrounded by the lamellar structure

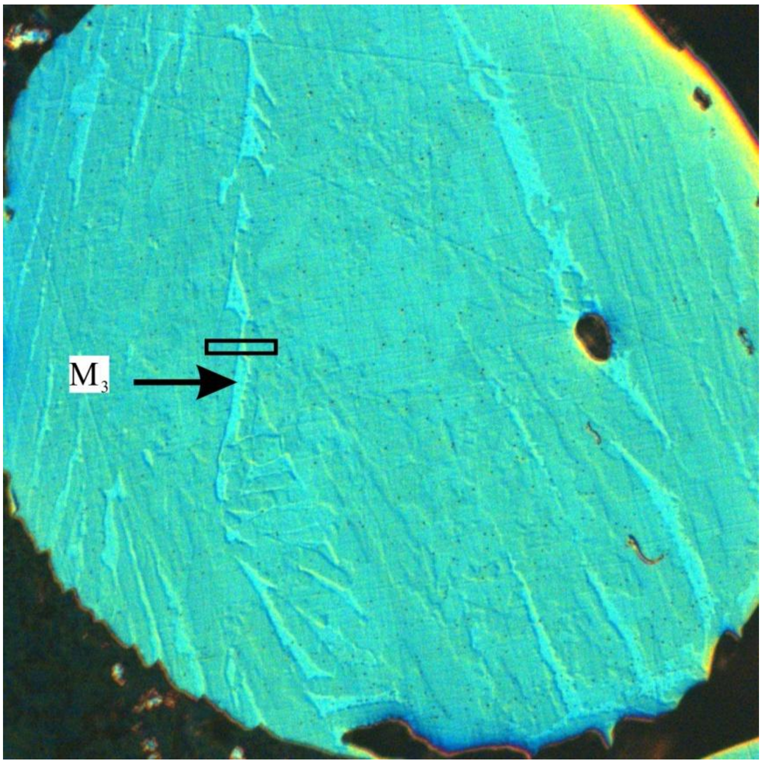

Figure 5.18: DIC micrograph of one 300-500 μm particle, showing the phase M_3 solidified continuously throughout the whole particle. The black square refers to the area analyzed by TEM.

Table 5.5: Two different categories of the Ni-25.3 at.% Si particles based on the microstructure difference

Particle category	Microstructure	Example
Type A	II	**Figure 5.16**a
Type B	The mixed structures of I, II, III, M_1, M_2 and M_3	**Figure 5.13** and **Figure 5.16**b

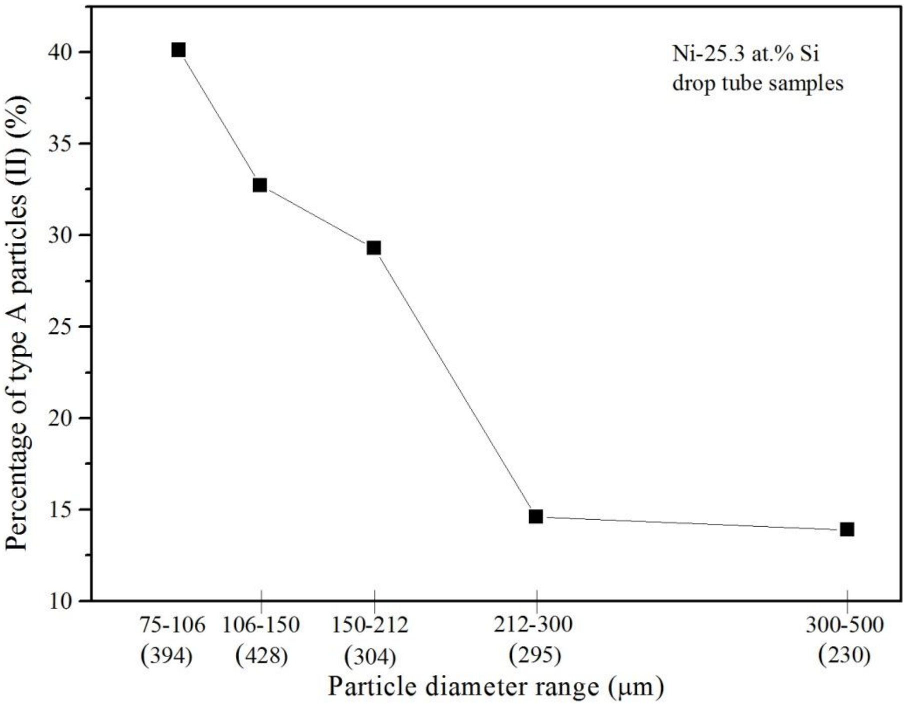

Figure 5.19: The fractions of the Ni-25.3 at.% Si particles with only the heteroclite structure in different particle ranges. The numbers of the counted particles are listed in the brackets under the x-coordinate.

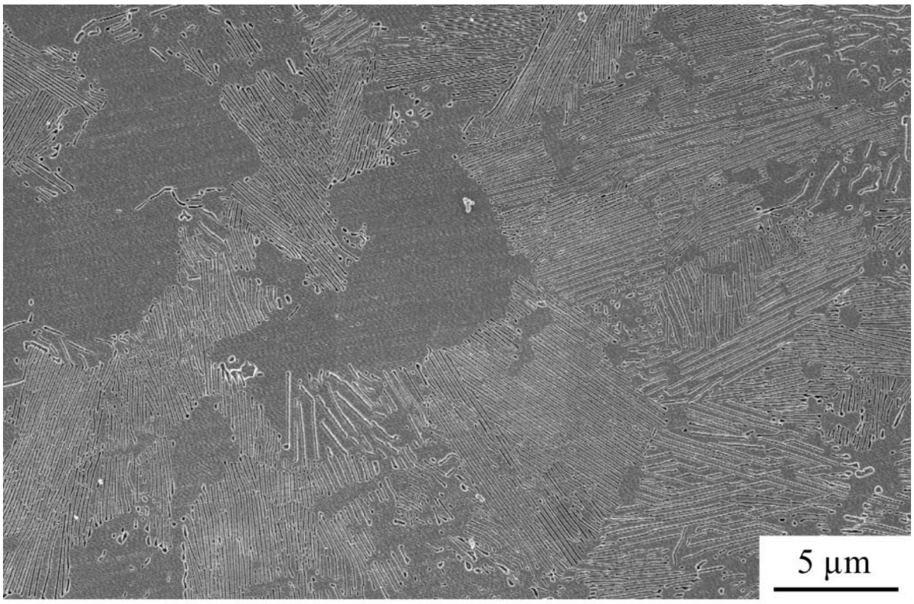

300-500 µm

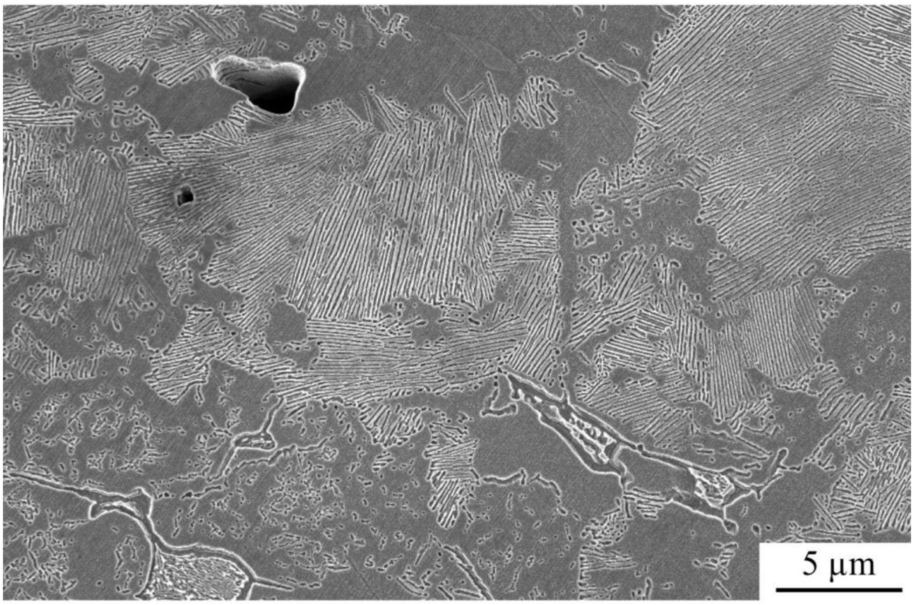

212-300 µm

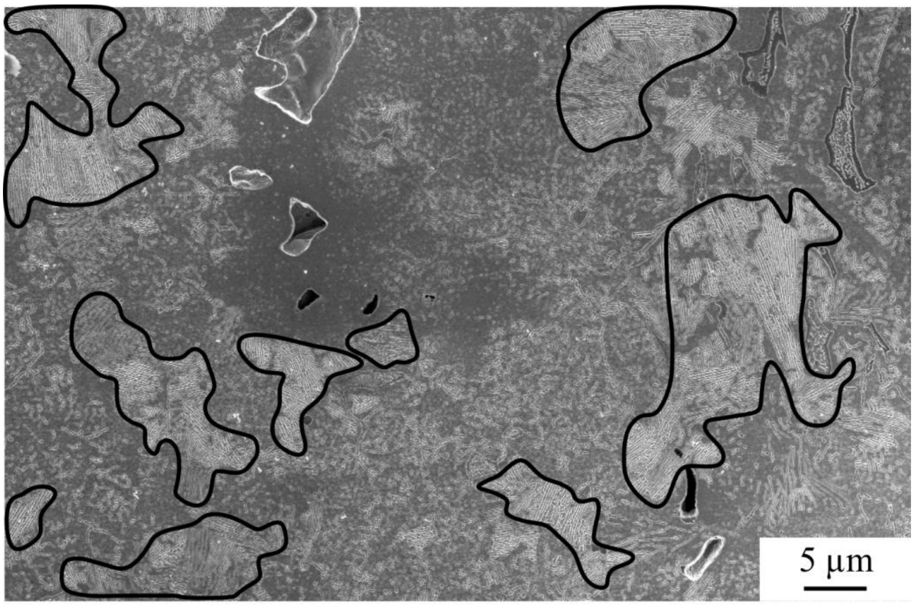

150-212 μm

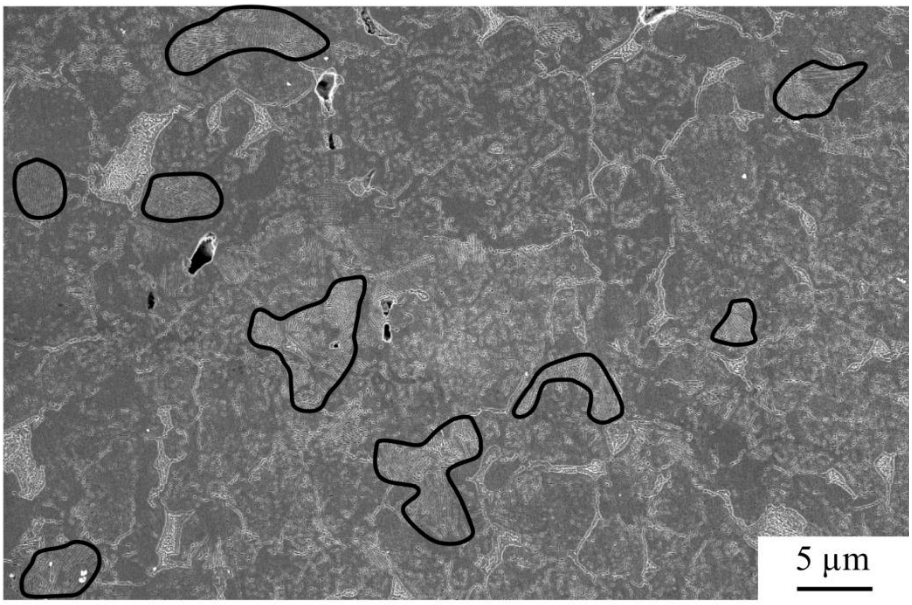

106-150 μm

Figure 5.20: SEM high resolution images of Ni-25.3 at.% Si 106-500 μm drop tube particles with the existence of the lamellar structure, showing the reduced fraction with decreasing particle size. The regions of the lamellar structure are highlighted by black curves in 106-150 and 150-212 μm particles.

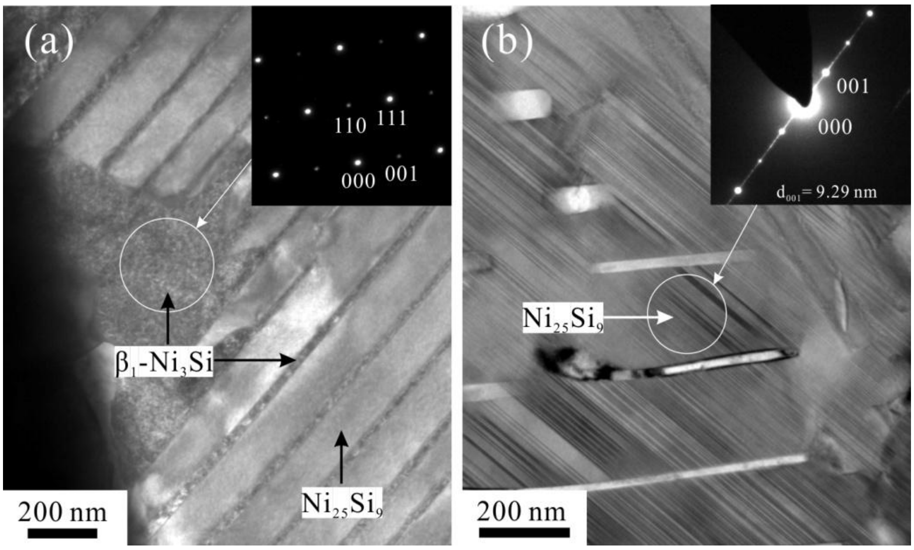

Figure 5.21: Phase identification of the regular lamellar structure (I), as shown in **Figure 5.12**a. Inset diffraction pattern in (a) is obtained from the bulk dark phase (white circle) identifying the single phase region, and therefore the thin lamellae, as β_1-Ni_3Si. Inset diffraction pattern in (b) is obtained from the lamellar area (white circle) identifying the wide band phase as metastable $Ni_{25}Si_9$.

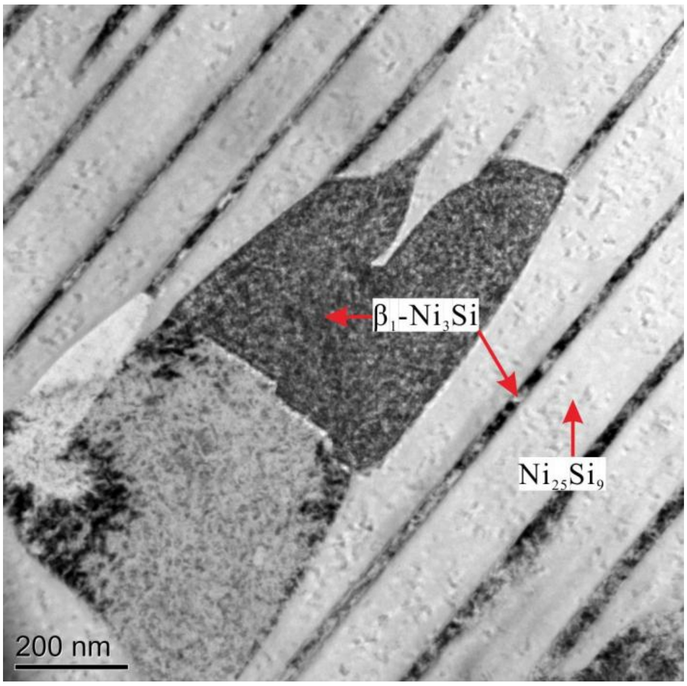

Figure 5.22: TEM bright field image of the lamellar structure in Ni-25.3 at.% Si particles, also indicating the narrow band and the bulk phase are the same phase, being β_1-Ni_3Si.

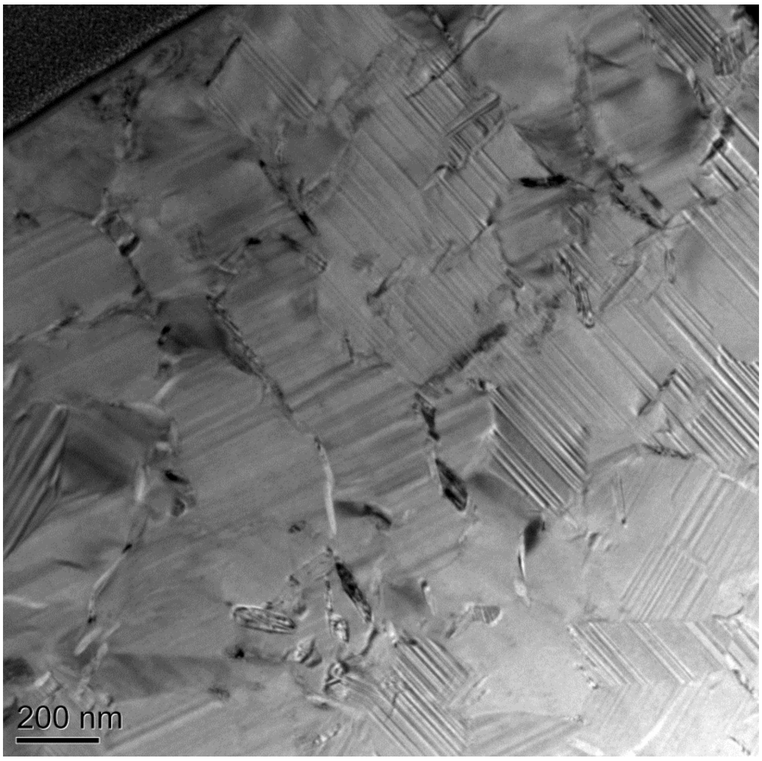

Figure 5.23: TEM bright field image of the heteroclite structure (**Figure 5.12**b)

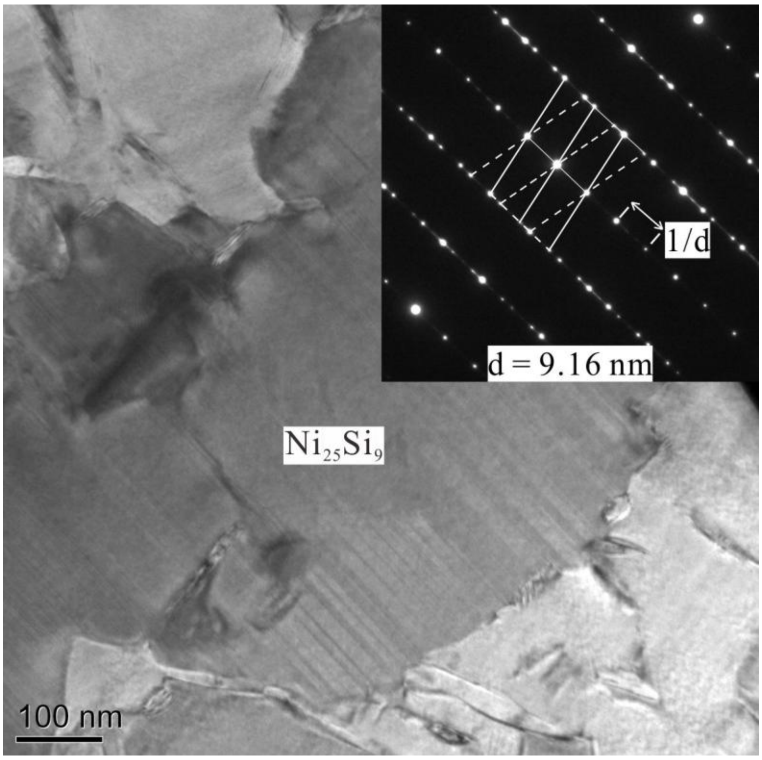

Figure 5.24: Phase identification of the heteroclite structure (II). The inset is the selected diffraction pattern of the coarse phase, identifying the twinned growth of the $Ni_{25}Si_9$.

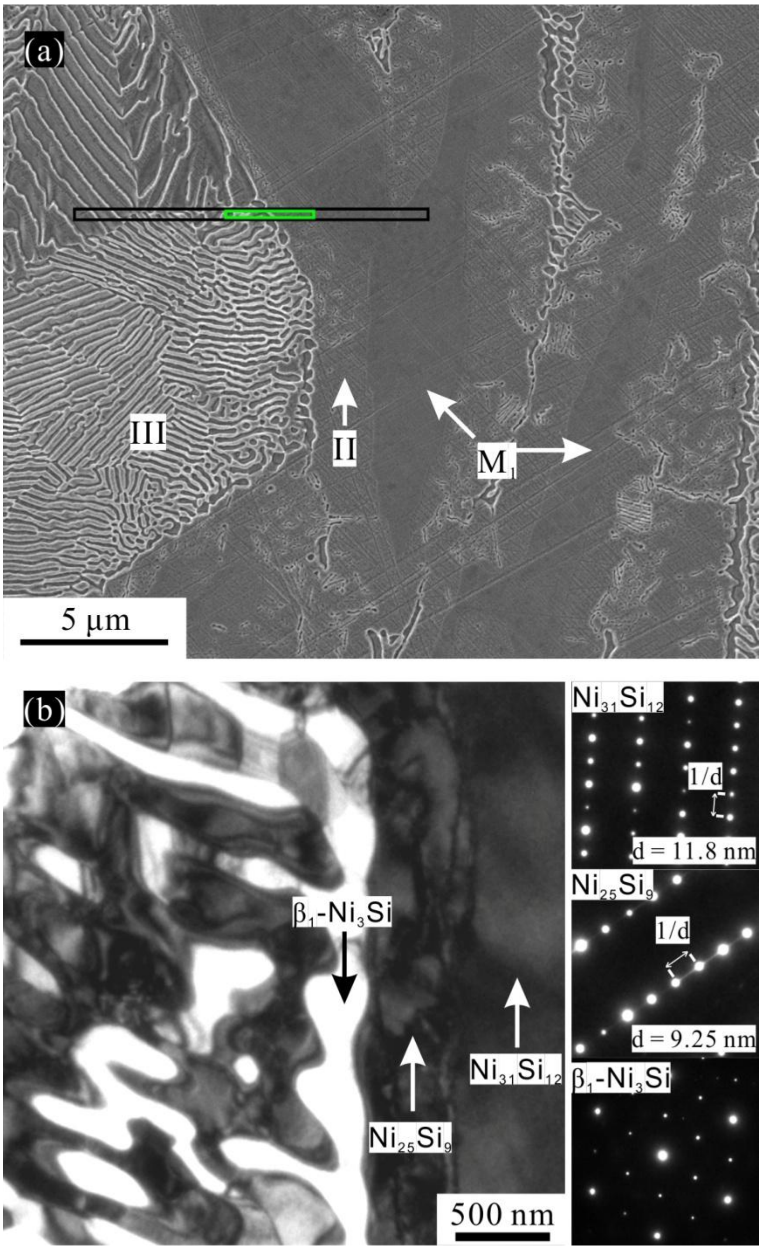

Figure 5.25: Phase identification of the anomalous eutectic structure: (a) SEM micrographs showing the structure in a 75-106 μm Ni-25.3 at.% Si particle. The black square refers to the area from which the TEM specimen was taken, while the green square refers to the area analyzed by TEM; (b) TEM bright field image and the corresponding diffraction patterns. The single phase M_1 is γ-$Ni_{31}Si_{12}$. The eutectic structure consists of the $Ni_{25}Si_9$ and β_1-Ni_3Si phases.

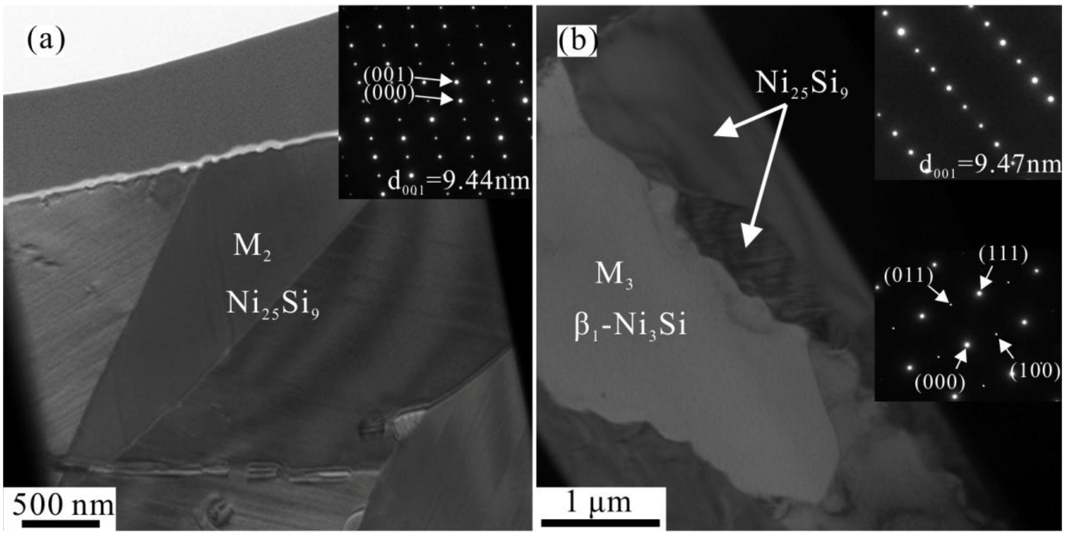

Figure 5.26: TEM analysis of the M_2 and M_3 phases, which were identified as $Ni_{25}Si_9$ and β_1-Ni_3Si, respectively. The phase next to β_1-Ni_3Si (M_3) was identified as $Ni_{25}Si_9$.

Table 5.6: The results of the phase identification by TEM

Structure type	Feature in SEM	Phase
I	Regular lamellar structure, **Figure 5.12**a	$Ni_{25}Si_9$ (wide band) β_1-Ni_3Si(narrow band)
II	Heteroclite structure, **Figure 5.12**b	$Ni_{25}Si_9$ (coarse phase)
III	Anomalous eutectic structure, **Figure 5.12**c	$Ni_{25}Si_9$ and β_1-Ni_3Si
M_1	**Figure 5.13 - Figure 5.15**	γ-$Ni_{31}Si_{12}$
M_2	**Figure 5.17**	$Ni_{25}Si_9$
M_3	**Figure 5.18**	β_1-Ni_3Si

5.4 Phase transformations

XRD confirmed the formation of metastable phase, $Ni_{25}Si_9$. DTA and in-situ XRD were performed to examine the phase transformations and the results will be presented in this section. Moreover, the microstructures of drop tube particles after heat treatment were also studied.

5.4.1 DTA analysis

The Ni-25.3 at.% Si drop tube particles with diameter in the range 300-500 μm were subjected to DTA analysis with heating rates of 20 K min^{-1} and 10 K min^{-1}. The trace of the first circle displayed an exothermic reaction near 542 ℃, which is ascribed to the phase transformation of the metastable $Ni_{25}Si_9$ (**Figure 5.27**). The onset temperature is about 516 ℃. On the basis of the equilibrium phase diagram, the endothermic peaks near 1008 ℃ and 1064 °C are due to the $\beta_1 + \gamma \rightarrow \beta_2$ transformation and the $\beta_1 \rightarrow \alpha$-Ni + β_2 transformation, respectively. The strong peak at 1133 °C is due to the $\beta_2 \rightarrow \beta_3$ transformation. The peaks at 1223 and 1246 ℃ represent the peritectic reaction and final melting process. The temperature departures of these reactions from the equilibrium phase diagram are listed in **Table 5.7**. There is no exothermic peak in the repeated DTA run of the sample, which implies that the metastable phase completely disappeared. At the high temperature of the repeated heating curve, there is a weak endothermic peak at 1160 ℃, which is possibly due to the eutectic melting $\alpha + \beta_3 \rightarrow L$. The α phase might be formed in the solidification process of the first cooling period.

The repeated experiment was carried out with heating rate of 10 K min^{-1}, as shown in **Figure 5.28**. The exothermic peak corresponding to the phase transformation of $Ni_{25}Si_9$ only appears in the first run, with the onset temperature being 491 ℃, which is 25 ℃ lower than that detected at the heating rate of 20 K min^{-1}.

5.4.2 In-situ XRD results

In order to check the difference between the measured and the phase diagram temperature at the experimental condition, Fe was chosen as the testing sample to calibrate the temperature. The phase transformation of Fe from BCC to FCC structure is about 912 ℃, but the measured transformation temperature was 760 ℃

using the same apparatus under the same experimental conditions, as illustrated in **Figure 5.29**. The measured temperature was 152 ℃ lower than the expected value, which implied that the detected temperature at the experimental vacuum condition of in-situ XRD is lower than the expected temperature. Therefore, in this project, we take the DTA result as its transformation temperature, namely that the onset temperature of the phase transformation ($Ni_{25}Si_9$) is about 491 ℃ with heating rate of 10 K min^{-1}.

The XRD results at elevated temperatures show a gradual phase transformation (**Figure 5.30**). Metastable $Ni_{25}Si_9$ is stable at low temperatures (< 300 ℃). The phase transformation took place after the temperature exceeded 300 ℃, and finished at 400 ℃. Comparing the XRD patterns of the sample before and after heat treatment at 25 ℃, it indicates that the metastable phase $Ni_{25}Si_9$ disappears and converts to β_1-Ni_3Si and γ-$Ni_{31}Si_{12}$. The results of the repeated detection with quick scanning are shown in **Figure 5.31**, indicating that the onset temperature of the transformation is at about 275 ℃ with the terminal temperature being 325 ℃. The time of the transformation is longer than 3 hours within the current designed temperature schedule.

5.4.3 Microstructure of the heat-treated samples

The 300-500μm particles were chosen randomly for in-situ XRD, which included both types of particles (A and B). The microstructures of the particles after the in-situ XRD were also studied. Moreover, in order to have direct evidence of the microstructure change, the specific particle with entire heteroclite microstructure was taken out from the resin manually and heated up to 594 ℃ for 30 minutes in the N_2 protective atmospheric chamber.

All particles (type A and B) after in-situ XRD showed similar final microstructure (**Figure 5.32**), showing the cellular zones dispersed on the single-phase matrix. The microstructure of the heat-treated particle is shown in **Figure 5.33**, showing a similar microstructure but with fine single phases (M_4) dispersing in the single-phase matrix (M_5). To identify the phases, one TEM specimen was prepared by FIB lift-out technique. TEM selected area diffraction was performed proving that the M_4 (fine single phase) and M_5 (matrix) were γ-$Ni_{31}Si_{12}$ and β_1-Ni_3Si phases, respectively, as shown in **Figure 5.34**.

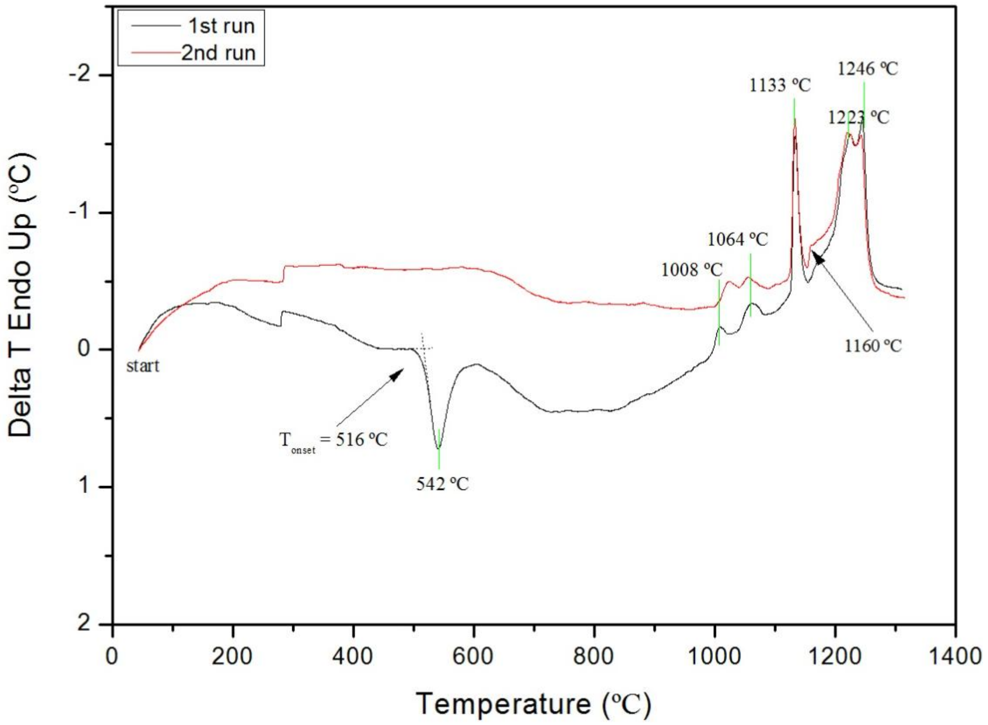

Figure 5.27: DTA traces of the Ni-25.3 at.% Si drop tube particles with the heating rate being 20 K min^{-1}. There is an exothermic peak at 542 ℃ in the first heating process, which disappeared in the repeated run.

Table 5.7: The measured and the phase diagram temperatures of the reactions

Reaction	Measured temperature/ ℃	Phase diagram temperature/ ℃	ΔT/°C
$\beta_1 + \gamma \rightarrow \beta_2$	1008	990	18
$\beta_1 \rightarrow \alpha\text{-Ni} + \beta_2$	1064	1035	29
$\beta_2 \rightarrow \beta_3$	1133	1115	18
$\alpha + \beta_3 \rightarrow L$	1160	1143	17
$\beta_3 \rightarrow \gamma + L$	1223	1170	53

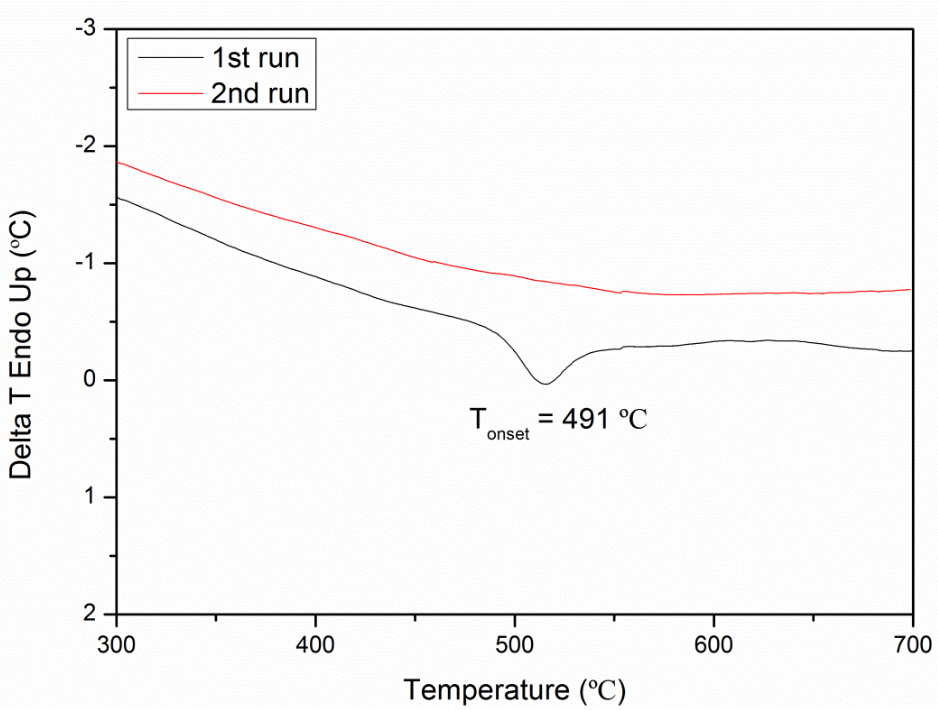

Figure 5.28: DTA trace of the Ni-25.3 at.% Si drop tube particles with the heating rate of 10 K min^{-1}. The onset temperature of the metastable phase transformation ($Ni_{25}Si_9$) is 491 ℃.

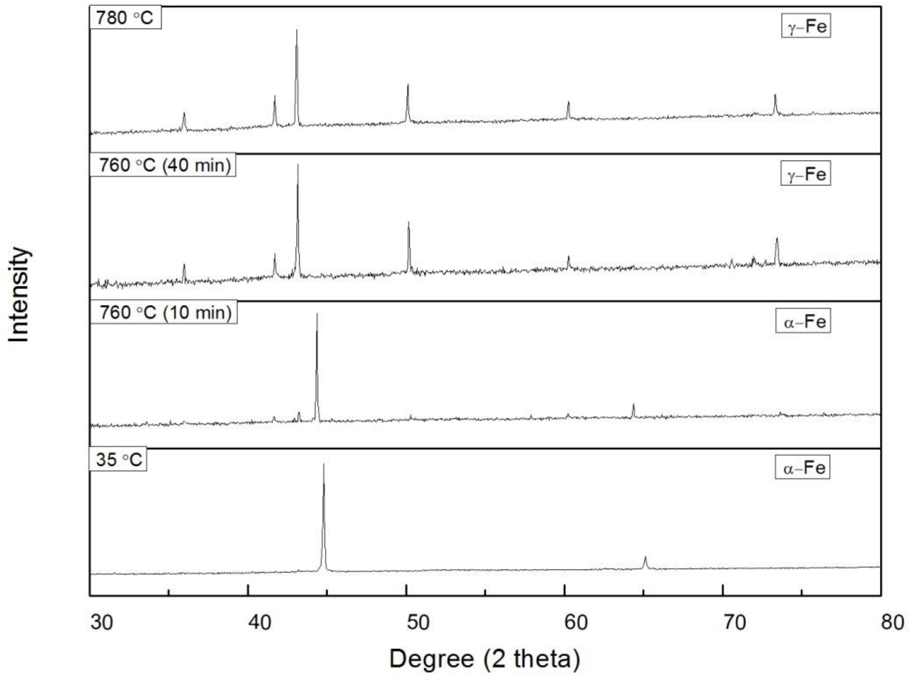

Figure 5.29: In-situ XRD on pure Fe. The measured transformation temperature is 760 ℃, which is lower than the expected value (912 ℃).

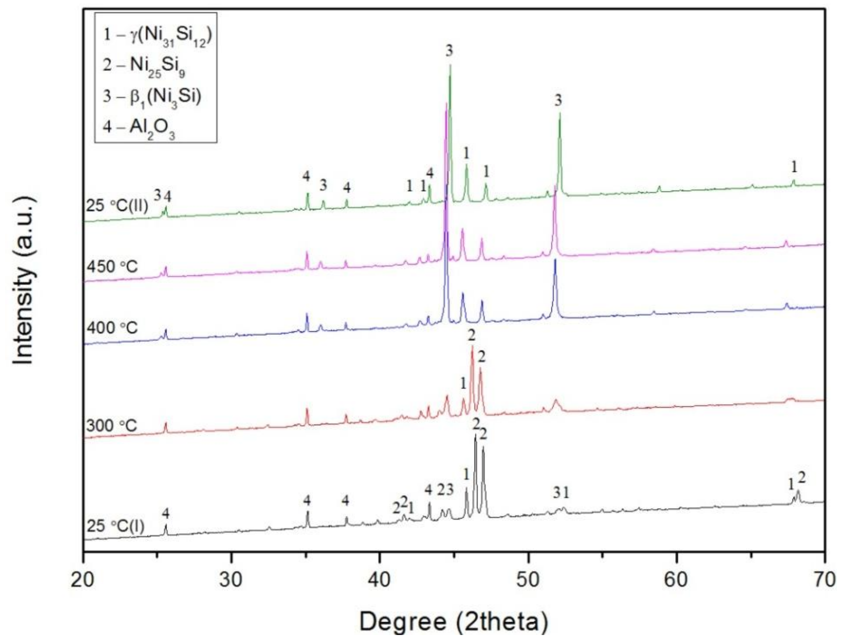

Figure 5.30: In-situ XRD results of the 300-500 µm Ni-25.3 at.% Si particles. The samples were heated from 25 ℃(I) to 450 ℃ and cooled down to 25 ℃(II) again. The data shows that the metastable phase $Ni_{25}Si_9$ converts to β_1 and γ-$Ni_{31}Si_{12}$ phase. The temperatures are uncalibrated, therefore the onset temperature of phase transformation is determined by DTA.

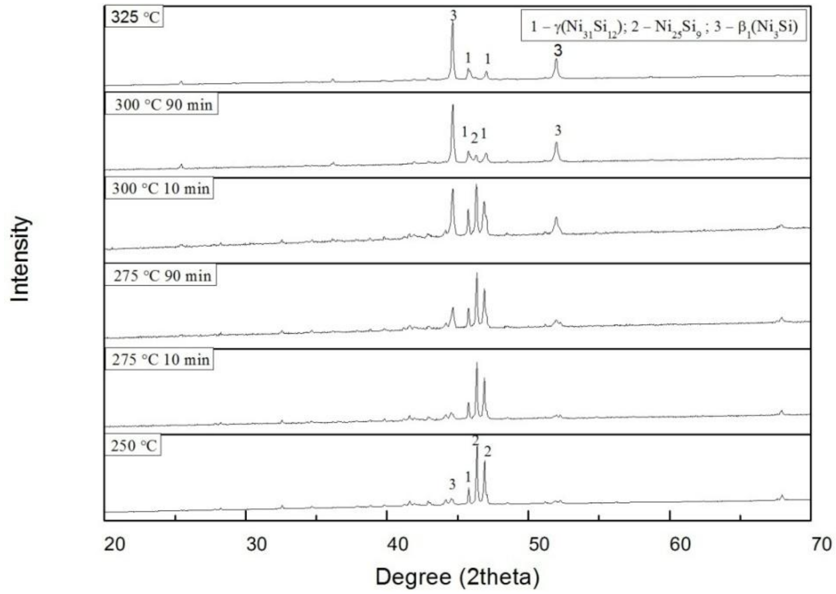

Figure 5.31: In-situ XRD of the 300-500 µm Ni-25.3 at.% Si particles with quick scanning option, showing the phase transformation with increasing temperature. The temperatures are uncalibrated.

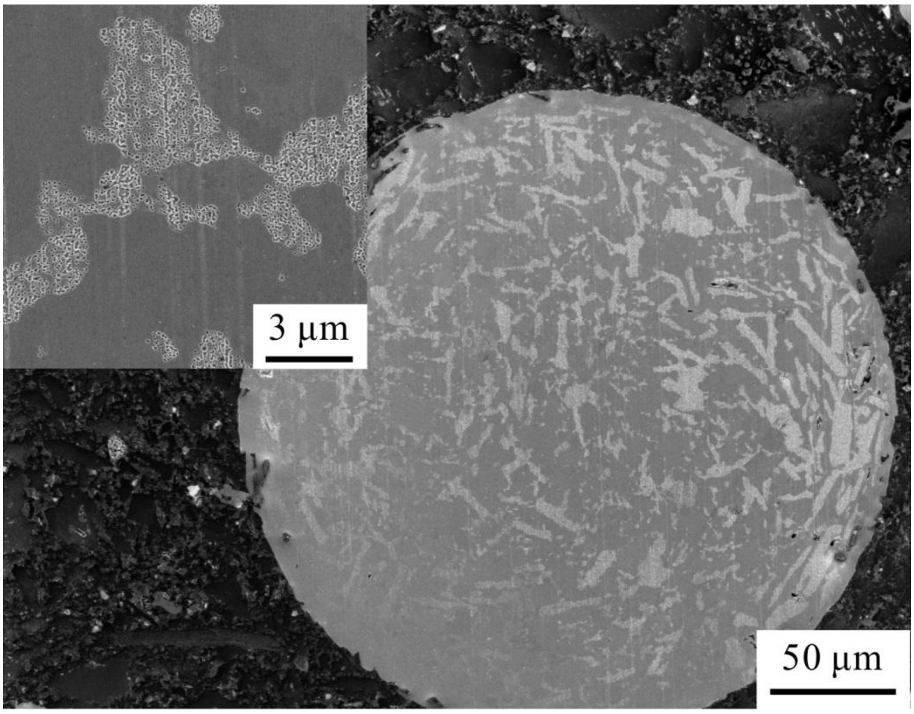

Figure 5.32: SEM image showing the typical microstructure of the 300-500 μm particles (type A and B) after in-situ XRD

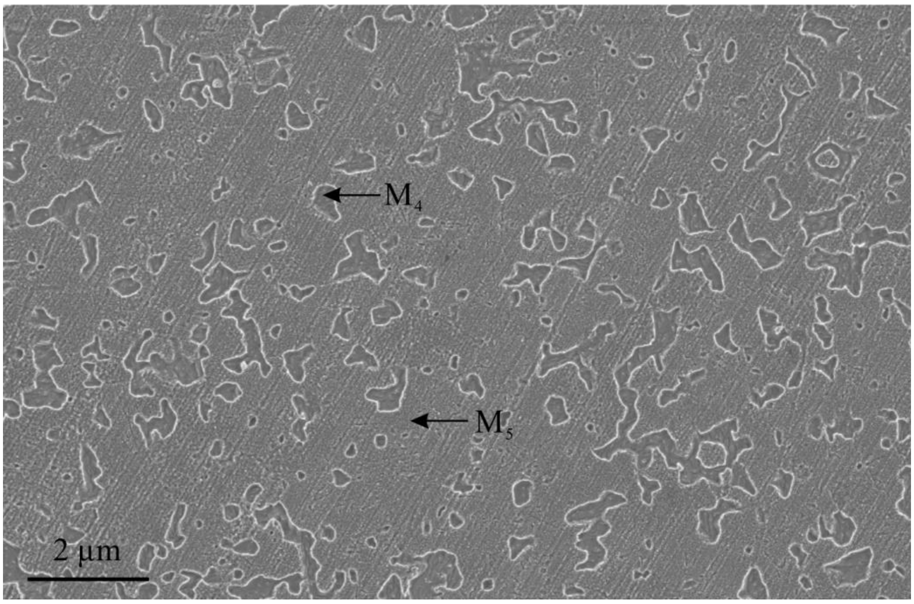

Figure 5.33: The microstructure of the heat-treated particle (type A) with fine single phase (M_4) dispersing in the single-phase matrix (M_5). The original particle before heat-treatment presents the entire heteroclite structure. The heat-treated condition: 594 ℃ for about 30 minutes. M_4 and M_5 will be identified by TEM.

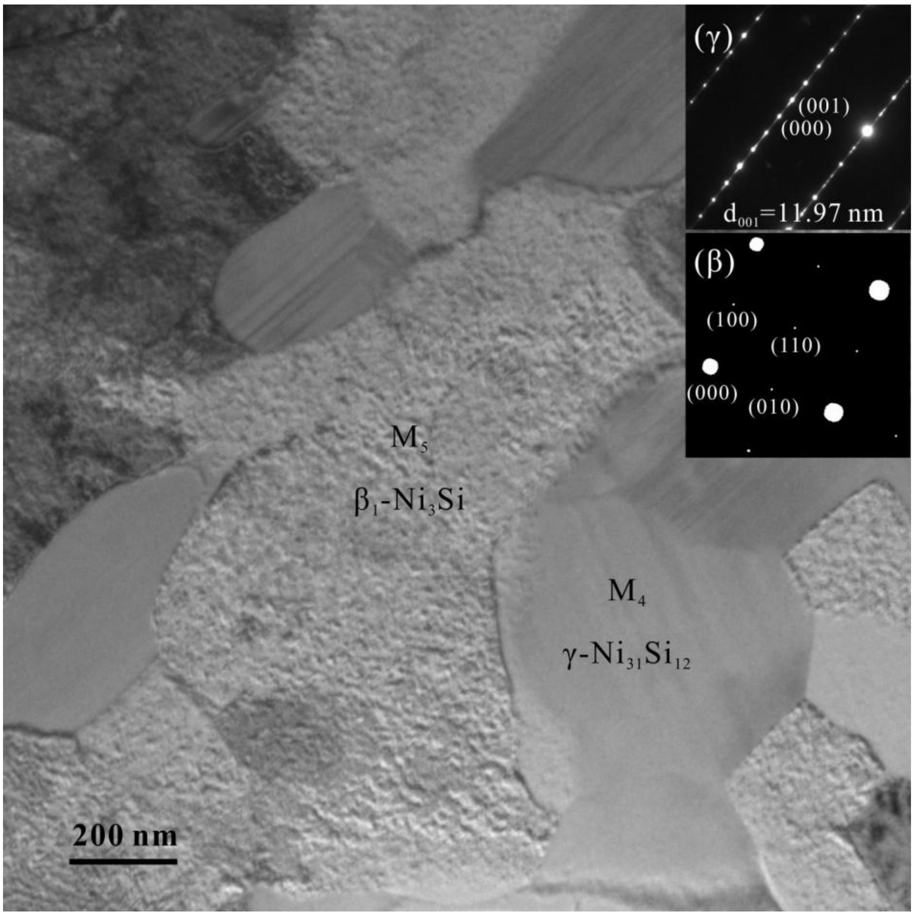

Figure 5.34: TEM image showing the structure of heat-treatment sample. The selected-area diffraction patterns indicate M_4 and M_5 are γ and β_1 phases (matrix), respectively.

5.5 $Ni_{64.7}Fe_{10}Si_{25.3}$ and $Ni_{59.7}Fe_{15}Si_{25.3}$ drop tube samples

The $Ni_{64.7}Fe_{10}Si_{25.3}$ and $Ni_{59.7}Fe_{15}Si_{25.3}$ master alloys were produced using the arc-melting technique and then melted and sprayed in the drop tube. EDX analysis showed that the resulting particles had the desired composition (**Figure 5.35** and **Figure 5.36**). The same characteristic techniques, namely XRD, SEM and TEM, were used to identify the specific phases of the typical microstructures. The results for the $Ni_{64.7}Fe_{10}Si_{25.3}$ and $Ni_{59.7}Fe_{15}Si_{25.3}$ drop tube solidified particles are presented in this section.

5.5.1 X-ray diffraction

The XRD results of the $Ni_{64.7}Fe_{10}Si_{25.3}$ alloy are shown in **Figure 5.37** and **Figure 5.38**. Compared with the results of the arc-melted $Ni_{64.7}Fe_{10}Si_{25.3}$ alloy, the γ-$Ni_{31}Si_{12}$ phase was also formed in all ranges of the drop tube solidified particles, especially in the large particles. The metastable phase, $Ni_{25}Si_9$, was also identified in the small particles.

Figure 5.39 and **Figure 5.40** shows the XRD results of the $Ni_{59.7}Fe_{15}Si_{25.3}$ alloy, which indicate that the γ phase was formed in all ranges of the drop tube particles. The formation of the metastable $Ni_{25}Si_9$ was confirmed by XRD of 106-150 μm particles. Moreover, the XRD patterns of 75-106 μm and 53-75 μm particles showed the strong characteristic peaks of $Ni_{25}Si_9$, which is similar to the XRD results of the drop tube processed Ni-25.3 at.% Si samples.

There is one common problem for both the $Ni_{64.7}Fe_{10}Si_{25.3}$ and $Ni_{59.7}Fe_{15}Si_{25.3}$ alloys. As was discussed before, it is difficult to distinguish the α and β_1 phases by XRD. Thus, XRD did not confirmed which of these phases was present and they were identified by TEM analysis.

The Ni-Fe-Si drop tube solidified particles presented the coarse structure in the large particles (see section 5.5.2), so the resulting X-ray diffraction patterns cannot be treated as the powder diffraction patterns. The diffraction patterns of the small particles had a strong background from the resin. Therefore, the quantitative analysis has not been done by the Rietveld refinement method.

5.5.2 Microstructural characterization and phase confirmation

Interesting microstructural evolution was expected in the particles, based on the XRD data that showed that the metastable $Ni_{25}Si_9$ formed in the small particles. To confirm this, the etched samples were observed by optical microscopy and scanning electronic microscopy.

Firstly, there were two different types of particles with entire coarse structure in all ranges of the $Ni_{64.7}Fe_{10}Si_{25.3}$ and $Ni_{59.7}Fe_{15}Si_{25.3}$ particles with one being random structure (**Figure 5.41**a and c) and the other being lamellar structure (**Figure 5.41**b and d). These two structures were further studied at high magnification, as shown in **Figure 5.42**. XRD indicated that only two phases were formed in the large particles, γ-$Ni_{31}Si_{12}$ and β_1[9]. Therefore, the random and lamellar structures should consist of the same phases, which will be analyzed by TEM later. Here, these two structures are referred as the regular structure. Secondly, the study also revealed that some of the particles presented fine structures in the smaller particles (< 212 μm), which were analyzed by SEM. The representative particles with different fine microstructures are shown in **Figure 5.43-Figure 5.49**. Based on the microstructural analysis by using optical microscopy and scanning electron microscopy, only three typical microstructures were summarized in all ranges of the particles, as shown in **Figure 5.50**: (I) regular structure. It includes the single phase and eutectic structure; (II) refined lamellar structure with two phases growing alternately; (III) anomalous structure with fine phase dispersed in the matrix.

To confirm the origin of these three different structures, two TEM specimens were prepared by FIB, one for coarse phase and eutectic structure and the other for fine lamellar and anomalous structures, as shown in **Figure 5.51**. TEM selected area diffraction patterns confirmed that the bulk phase (I_1) and one of the eutectic phase (I_2) are the γ-$Ni_{31}Si_{12}$ phase (**Figure 5.52**). However, the selected area diffraction pattern from I_3 displays the super-lattice spot (**Figure 5.52**b), indicating that I_3 is the ordered $L1_2$ phase. Here, we label it as the β_1 phase. A similar selected area diffraction pattern analysis confirms that the wide band (I_4) in the fine lamellar structure is also γ-$Ni_{31}Si_{12}$ (**Figure 5.53**a), while the matrix-phase (I_5) in the anomalous structure is identified as the metastable phase, $Ni_{25}Si_9$, as shown in

---

[9] The β_1 phase here will be confirmed by TEM.

Figure 5.53b. The $L1_2$ ordered phase forms together with the γ phase at low cooling rates (big particles), therefore, the phases of the narrow band in the fine lamellar structure are expected to be $L1_2$ ordered phase as well at high cooling rates (small particles).

In order to study the microstructure evolution as the cooling rate is increased, the $Ni_{64.7}Fe_{10}Si_{25.3}$ and $Ni_{59.7}Fe_{15}Si_{25.3}$ particles were classified into three different categories (A, B and C) according to the microstructure difference, as listed in **Table 5.8**. Type A presents the entire regular structure, consisting of the coarse single phase and eutectic structure. Type B presents the mixture structure, including two or three of the different typical structures. Type C presents the entire anomalous structure or mainly anomalous structure with a small fraction of refined lamellar structure.

Then, the fractions of these three types of particles in all ranges of the particles were counted. The numbers of the counted $Ni_{64.7}Fe_{10}Si_{25.3}$ particles were 463 (150-212 μm), 514 (106-150 μm), 2182 (75-106 μm) and 1844 (53-75 μm), while the numbers of the counted $Ni_{59.7}Fe_{15}Si_{25.3}$ particles were 219 (150-212 μm), 505 (106-150 μm), 692 (75-106 μm) and 1909 (53-75 μm). The results are shown in **Figure 5.54**. Here, it should be noted that, because the refined lamellar structure was difficult to be found in the $Ni_{59.7}Fe_{15}Si_{25.3}$ particles, the particle consisting of the structures I and II was not found, and the type B particle being counted mainly consisted of I and III structures.

For the $Ni_{64.7}Fe_{10}Si_{25.3}$ alloy, the fractions of particle (type A) were 100% in the large size ranges (212-850 μm), which decreased slightly to 98.5 % (150-212 μm) and then dropped down to 28.69% (53-75 μm) quickly. Meanwhile, the fractions of the particle (type B) increased gradually from 1.5% (150-212 μm) to 31.21% (53-75 μm). The type C particle was firstly observed in the 106-150 μm particles, with the fraction being 8.56 %, which increased to 39.1% in the 53-75 μm particles.

For the $Ni_{59.7}Fe_{15}Si_{25.3}$ alloy, the fractions of particle (type A) had a similar trend compared with that of the $Ni_{64.7}Fe_{10}Si_{25.3}$ alloy, which were 100% (212-850 μm) and then reduce to 14.82% (53-75 μm). The total fractions of the particles (type B and C) increased as the diameters decreased, which is up to 66.62% in 75-106 μm particles and reached 85.17% in the smallest particles (53-75 μm). Different from the results for the $Ni_{64.7}Fe_{10}Si_{25.3}$ alloy, the fraction of type C particle with entire anomalous structure increased monotonically from 29.11% (150-212 μm) to 82.24% (53-75 μm), while the proportion of the type B particle decreased to 2.93% (53-75 μm) again after reaching a maximum of 18.02% (106-150 μm).

The counted results are quite consistent with the XRD and TEM analysis. The type C particles (with metastable phase $Ni_{25}Si_9$ as matrix) increased with decreasing particle size, being 39.1 % for 53-75 μm $Ni_{64.7}Fe_{10}Si_{25.3}$ particles and 82.24 % for 53-75 μm $Ni_{59.7}Fe_{15}Si_{25.3}$ particles. Therefore, it can be concluded that the metastable phase, $Ni_{25}Si_9$, formed in the small particles and even formed as dominant phase in the 53-75 μm $Ni_{59.7}Fe_{15}Si_{25.3}$ particles.

The microstructures of the 150-212 μm $Ni_{64.7}Fe_{10}Si_{25.3}$ particles were studied in detail to understand the microstructural evolution, because the microstructural change from I to II and III occurred firstly in this size range. In fact, 463 particles were mounted and analyzed. 456 particles presented the regular structure (type A) and only 5 particles presented a mixed structure of regular and refined lamellar structure, as shown in **Figure 5.43**. The remaining 2 particles included all three typical structures, as shown in **Figure 5.45**. The transition from the coarse lamellar structure to fine lamellar structure was observed, as illustrated in **Figure 5.55**. Meanwhile, **Figure 5.56** indicates that the fine lamellar structure can grow not only via a transition from the coarse lamellar structure, but also directly on the normal side of a single γ-$Ni_{31}Si_{12}$ phase. There is no particle with the entire anomalous structure. The direct transition from the regular structure I to anomalous structure III was firstly observed in the 106-150 μm particles (**Figure 5.57**), which also included some particles with the entire anomalous structure.

As mentioned above, the lamellar structure was difficult to be found in the $Ni_{59.7}Fe_{15}Si_{25.3}$ particles. Therefore, the 150-212 μm $Ni_{64.7}Fe_{10}Si_{25.3}$ particles showed a slightly different microstructural change: firstly, direct transition from the regular structure (I) to anomalous structure (III) can be observed in this size range. Secondly, 6.39 % of the type C particles solidified into the entire anomalous structure.

5.5.3 EDX and EPMA analysis

As mentioned above, particles with diameters in the range 53-850 μm were produced in a drop tube and three different kinds of microstructures were observed. In order to confirm that the solidified particles indeed had the expected composition, EDX analysis was also carried out of the general composition, including the average composition and the coarse γ phase. Here, the average composition was achieved by measuring particles randomly using area scanning and at least 10 particles have been analysed. The coarse γ phases were also measured randomly using point scanning and at least 20 spectra were obtained. All these data are shown in **Figure 5.35** and **Figure 5.36**. It is clear that the average compositions of both $Ni_{64.7}Fe_{10}Si_{25.3}$ and $Ni_{59.7}Fe_{15}Si_{25.3}$ alloy particles were quite close to the nominal composition. Meanwhile, the compositions of the particles with completely anomalous structure were also analysed, and the results are given in **Table 5.9** and **Table 5.10**. The results show that, in each alloy system, the particles with general structure and entire anomalous phase have the same composition close to the nominal composition. The average composition of the γ phase in $Ni_{64.7}Fe_{10}Si_{25.3}$ particles was around 27.15 at.% Si which is quite close to the composition of the γ phase in the Ni-Si binary system. A similar result was also found in the $Ni_{59.7}Fe_{15}Si_{25.3}$ particles where the average Si composition of the γ phase was about 27.01 at.%. The Fe composition of the γ phase was about 6.99 at.%, and was higher in the $Ni_{59.7}Fe_{15}Si_{25.3}$ particles, 11.32 at.%. However, the Fe composition of the γ phase in both alloys are lower than their individual average Fe compositions (10.57 at.% and 15.65 at.% Fe). Microprobe analysis was also used to analyse the composition of the γ phase and the results (compared with the EDX analysis) are shown in **Table 5.11**.

In the particles with the γ phase growing randomly, there were also some eutectic areas between the γ phase. Microprobe analysis was carried out on these areas and the results are given in **Table 5.11**. The composition of the eutectic area was 20.63 at.%, 19.11 at.% and 60.27 at.% for Si, Fe and Ni respectively. The Si composition is close to the eutectic composition in the Ni-Si binary system, 21.4 at.% Si.

The average Fe composition of the eutectic in the $Ni_{64.7}Fe_{10}Si_{25.3}$ particles was quite high, being 19.11 at.% (compared with the average value 10.57 at.%), implying the Fe segregation occurred even at high cooling rates during the solidification process.

Similar to the observation in the arc-melted samples, the surplus Fe was also accumulated into the eutectic areas. Line scanning results (**Figure 5.58**) also showed the change of the composition in the γ phase and eutectic region, with the latter possessing relatively high Fe concentration. **Figure 5.59** shows the line scanning results towards the metastable and primary γ phases, showing that the average Ni, Fe and Si composition of the metastable phase zone was in between the average values of the γ phases and the eutectic zones.

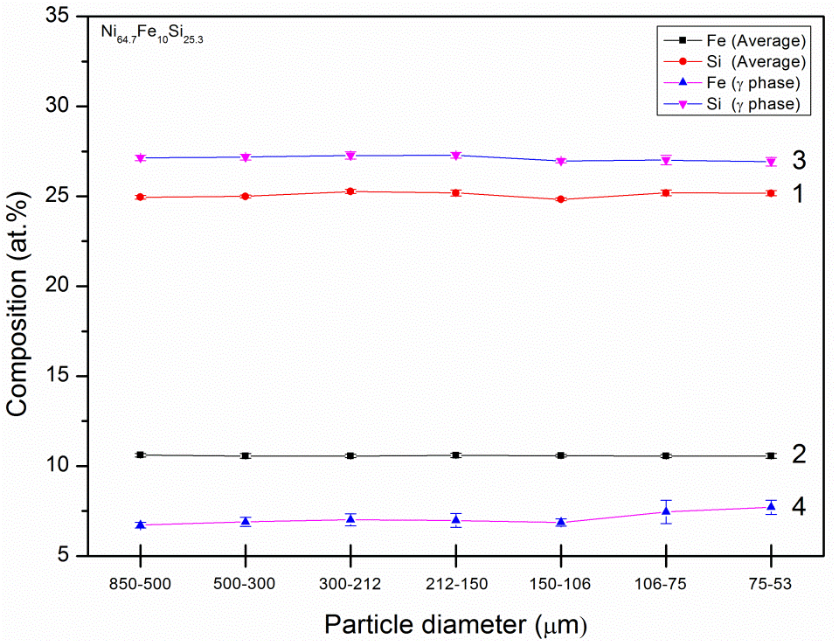

Figure 5.35: Average EDX composition of Fe and Si in the $Ni_{64.7}Fe_{10}Si_{25.3}$ drolplets. Results 1 and 2 are average Si and Fe composition of the particles, while results 3 and 4 are average Si and Fe compositions of the γ phase in the relative particle ranges. The γ phase will be identified by TEM analysis later.

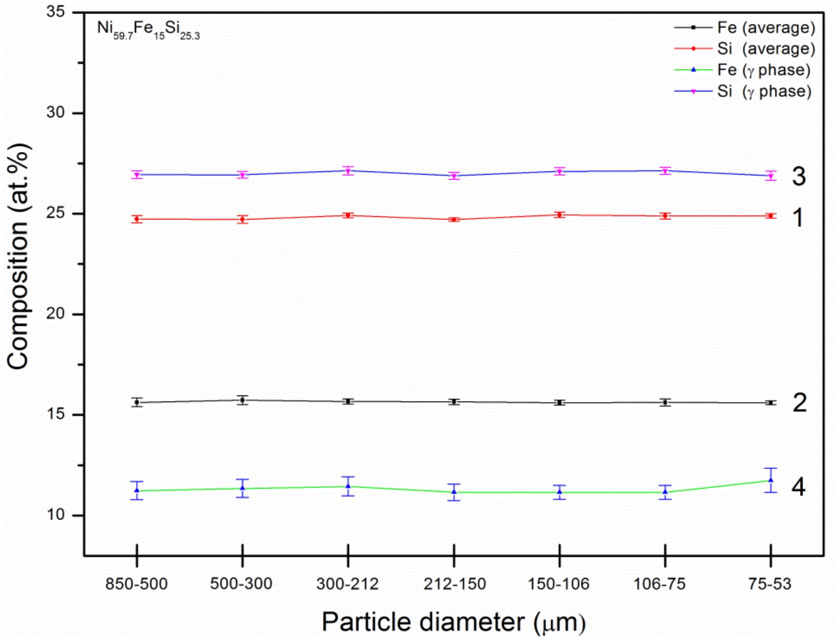

Figure 5.36: Average EDX composition of Fe and Si in the $Ni_{59.7}Fe_{15}Si_{25.3}$ particles. Results 1 and 2 are average Si and Fe composition of the particles, while results 3 and 4 are average Si and Fe compositions of the γ phase in the relative particle ranges. The γ phase will be identified by TEM analysis later.

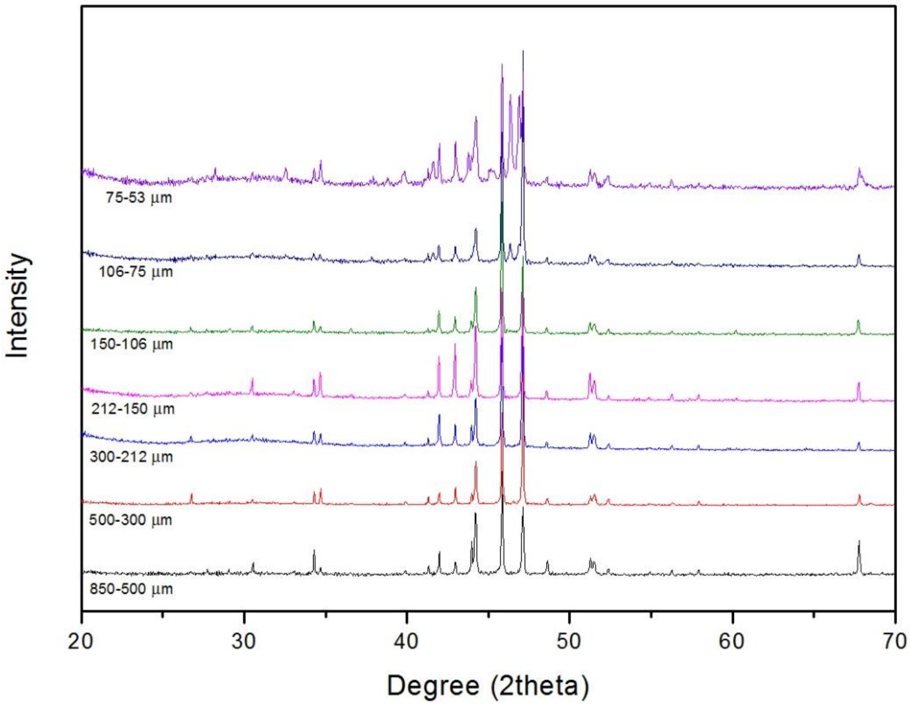

Figure 5.37: The XRD results of the $Ni_{64.7}Fe_{10}Si_{25.3}$ alloy with different size groups (20 °-70 °)

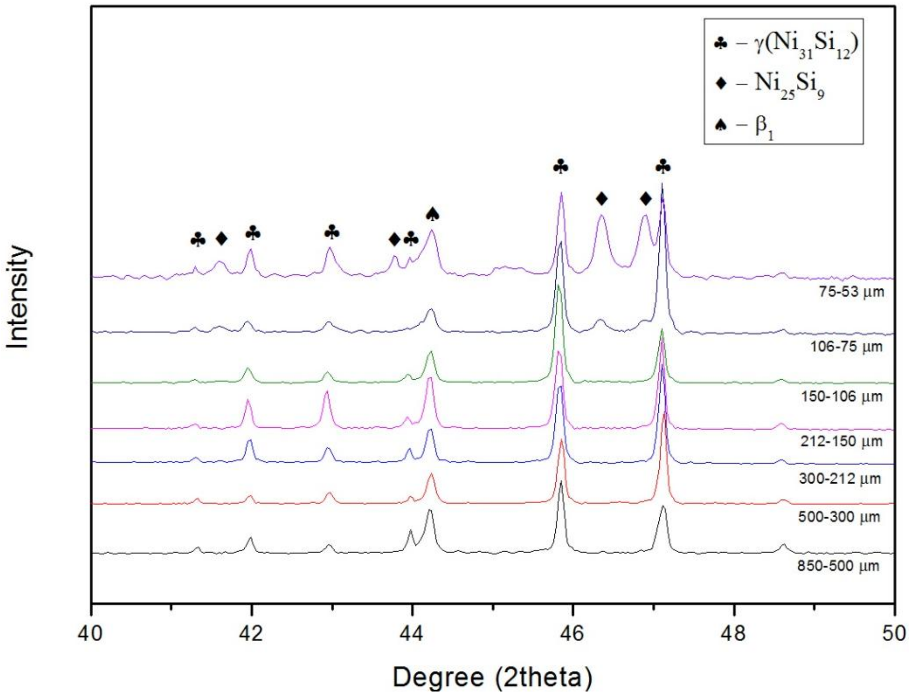

Figure 5.38: The XRD results of the $Ni_{64.7}Fe_{10}Si_{25.3}$ alloy with different size groups (40 °-50 °), showing the formation of $Ni_{25}Si_9$ in the small particles.

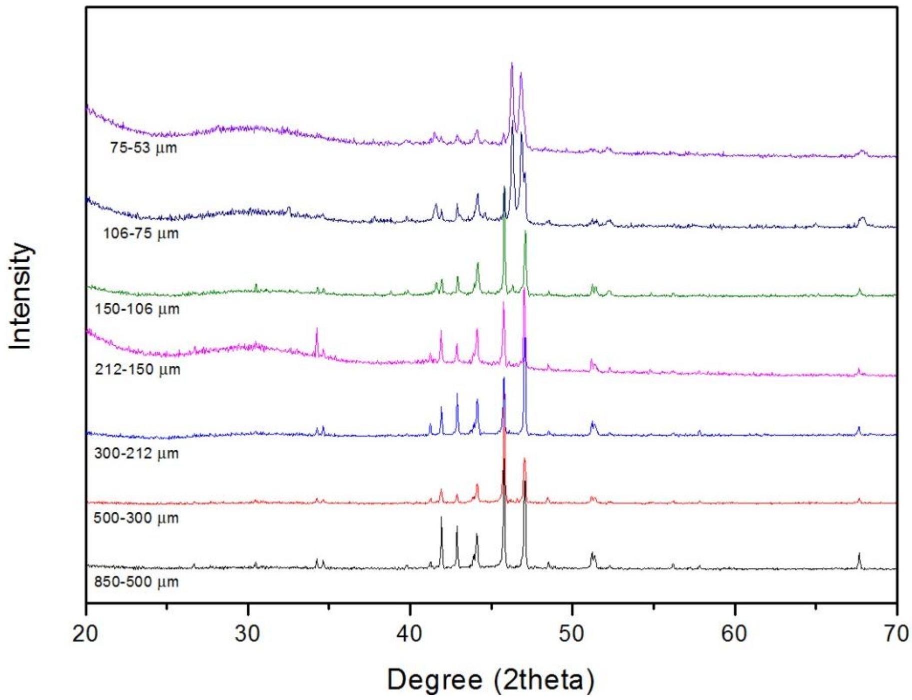

Figure 5.39: The XRD results of the $Ni_{59.7}Fe_{15}Si_{25.3}$ alloy with different size groups (20 °-70 °)

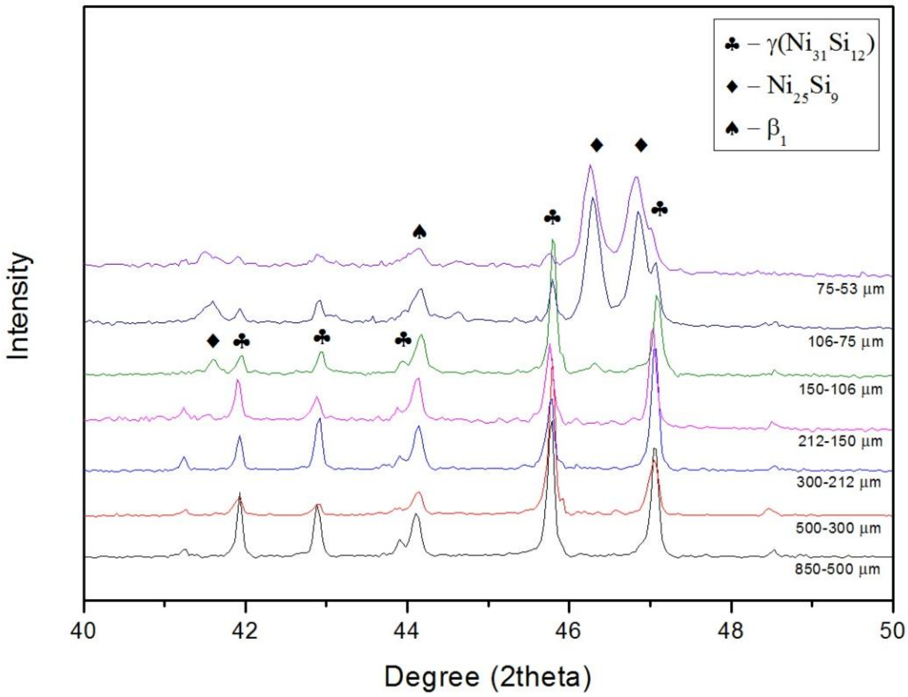

Figure 5.40: The XRD results of the $Ni_{59.7}Fe_{15}Si_{25.3}$ alloy with different size groups (40 °-50 °), showing the formation of $Ni_{25}Si_9$ in the small particles.

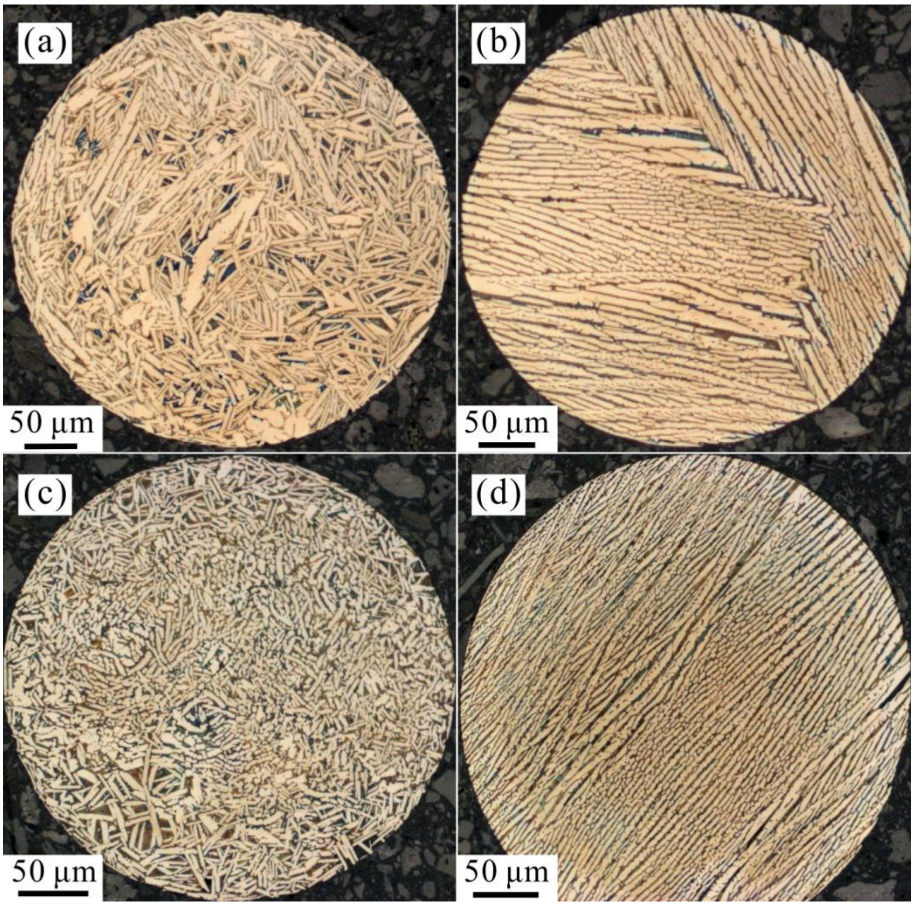

Figure 5.41: Optical micrographs of the general structures of the 300-500 μm particles with entire coarse structure. (a) and (c) random structure of $Ni_{64.7}Fe_{10}Si_{25.3}$ and $Ni_{59.7}Fe_{15}Si_{25.3}$ particles; (b) and (d) lamellar structure of $Ni_{64.7}Fe_{10}Si_{25.3}$ and $Ni_{59.7}Fe_{15}Si_{25.3}$ particles.

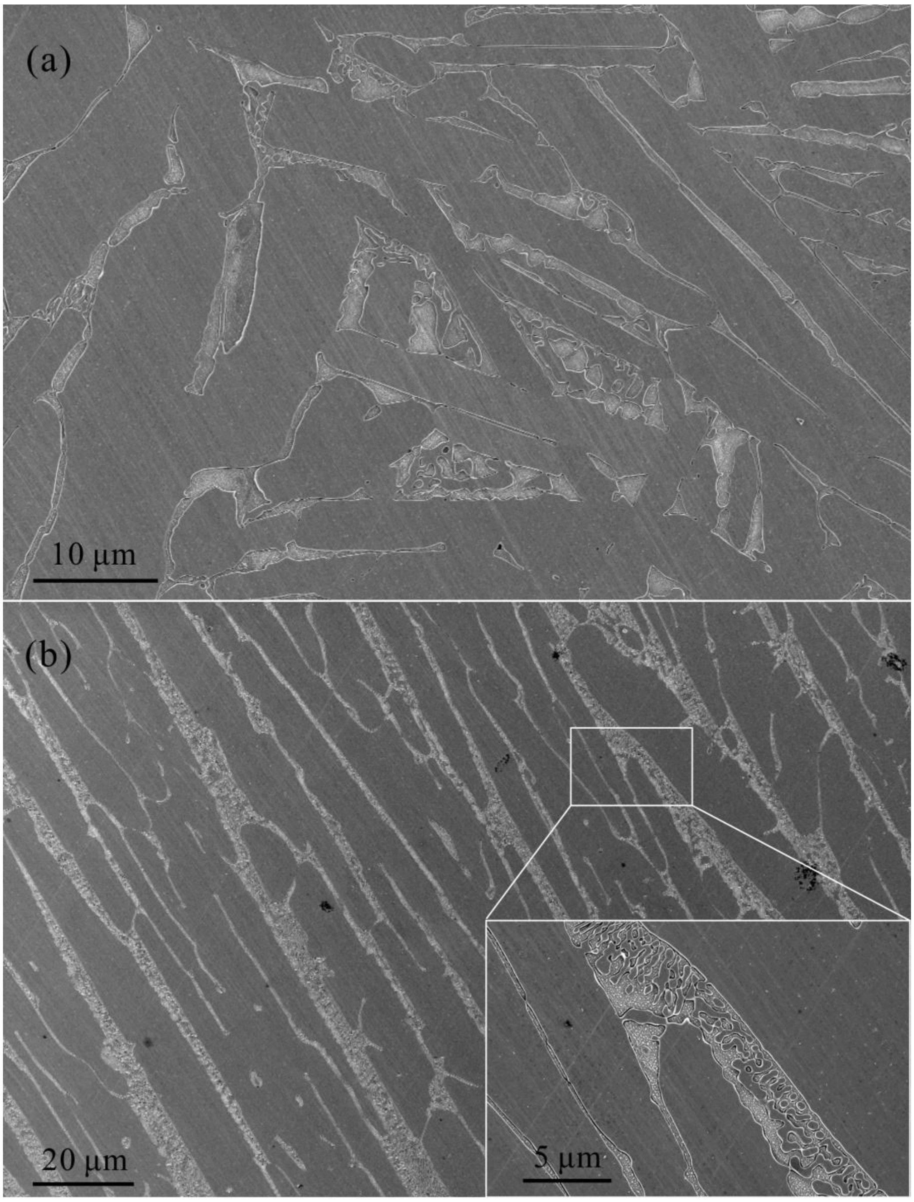

Figure 5.42: The coarse structures of the 300-500 μm $Ni_{64.7}Fe_{10}Si_{25.3}$ particles at high magnification in the SEM: (a) corresponding to the random structure in **Figure 5.41**a; (b) corresponding to the lamellar structure in **Figure 5.41**b. These two images were taken from other particles rather than the particles shown in **Figure 5.41**.

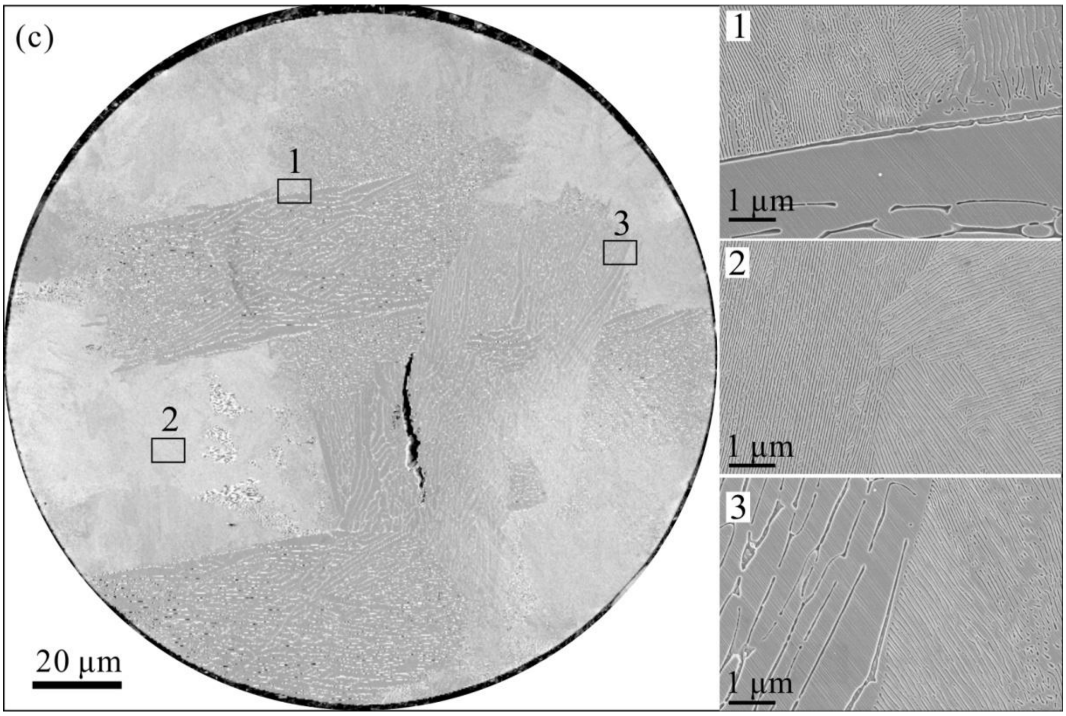

Figure 5.43: SEM images of one of the 150-212 μm $Ni_{64.7}Fe_{10}Si_{25.3}$ particles, consisting of the regular coarse structure and the refined lamellar structures.

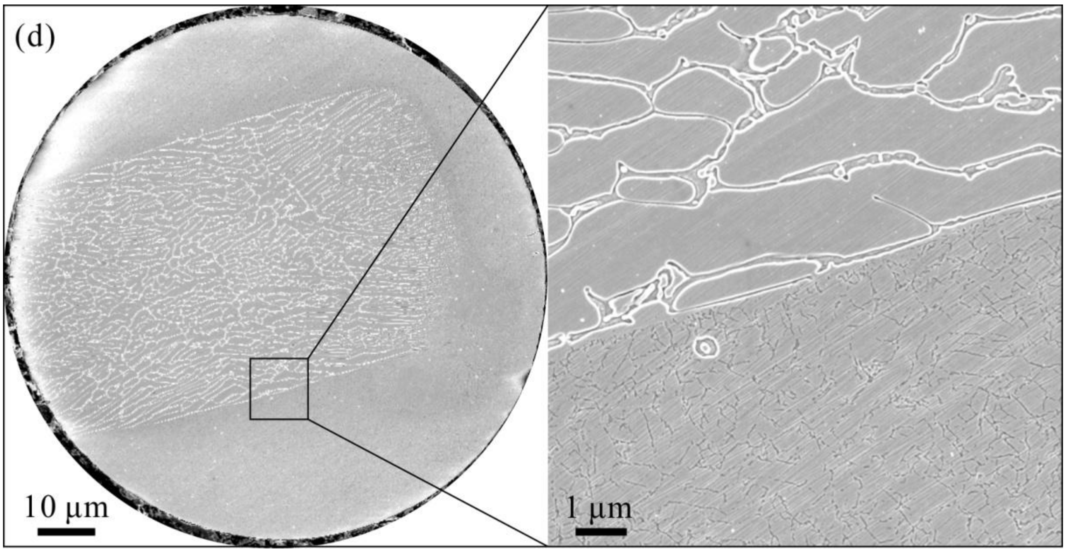

Figure 5.44: SEM images of one of the 75-106 μm $Ni_{64.7}Fe_{10}Si_{25.3}$ particles, consisting of the regular coarse and anomalous structures.

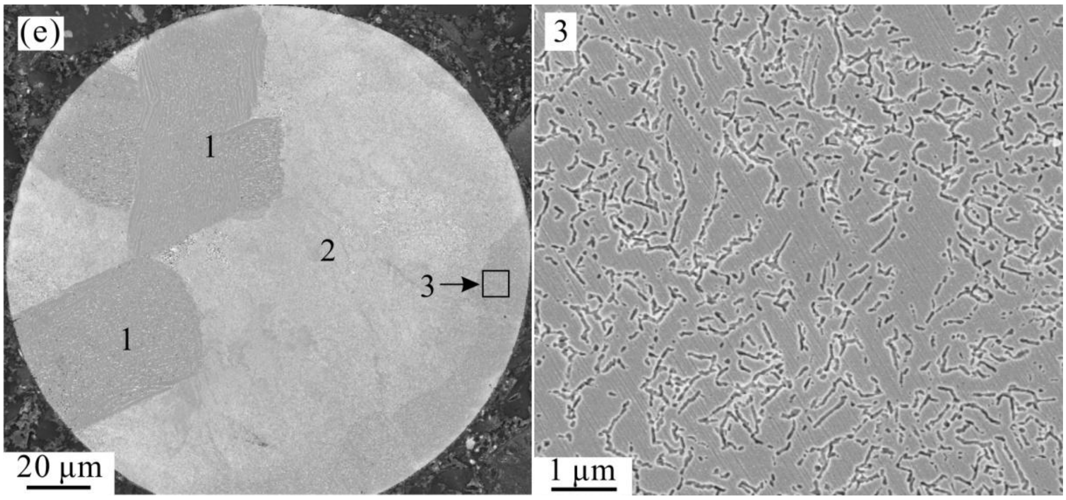

Figure 5.45: SEM images of one of the 150-212 µm $Ni_{64.7}Fe_{10}Si_{25.3}$ particles, consisting of the regular coarse structure, refined lamellar structure and anomalous structure. The structures labelled as “1” and “2” correspond to the regular coarse structure and refined lamellar structure, as shown in **Figure 5.43**.

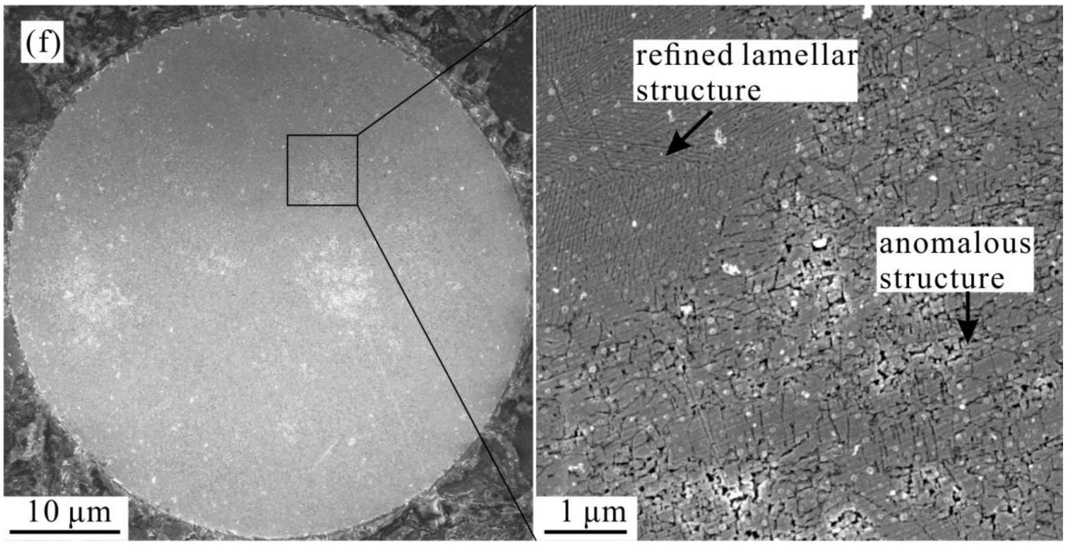

Figure 5.46: SEM images of one of the 53-75 µm $Ni_{64.7}Fe_{10}Si_{25.3}$ particles, consisting of the refined lamellar and anomalous structures

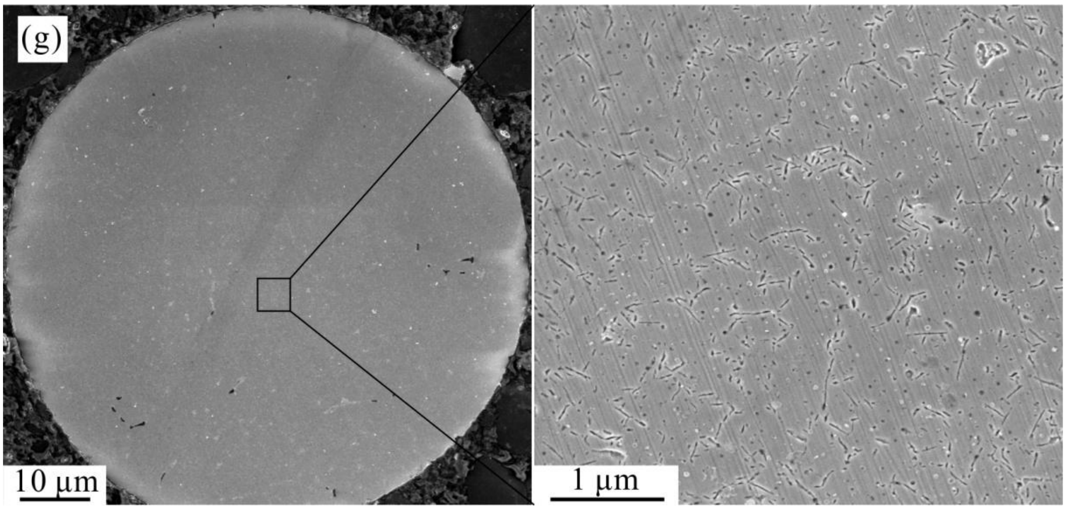

Figure 5.47: SEM images of one of the 75-106 µm $Ni_{64.7}Fe_{10}Si_{25.3}$ particles, showing the entire anomalous structure

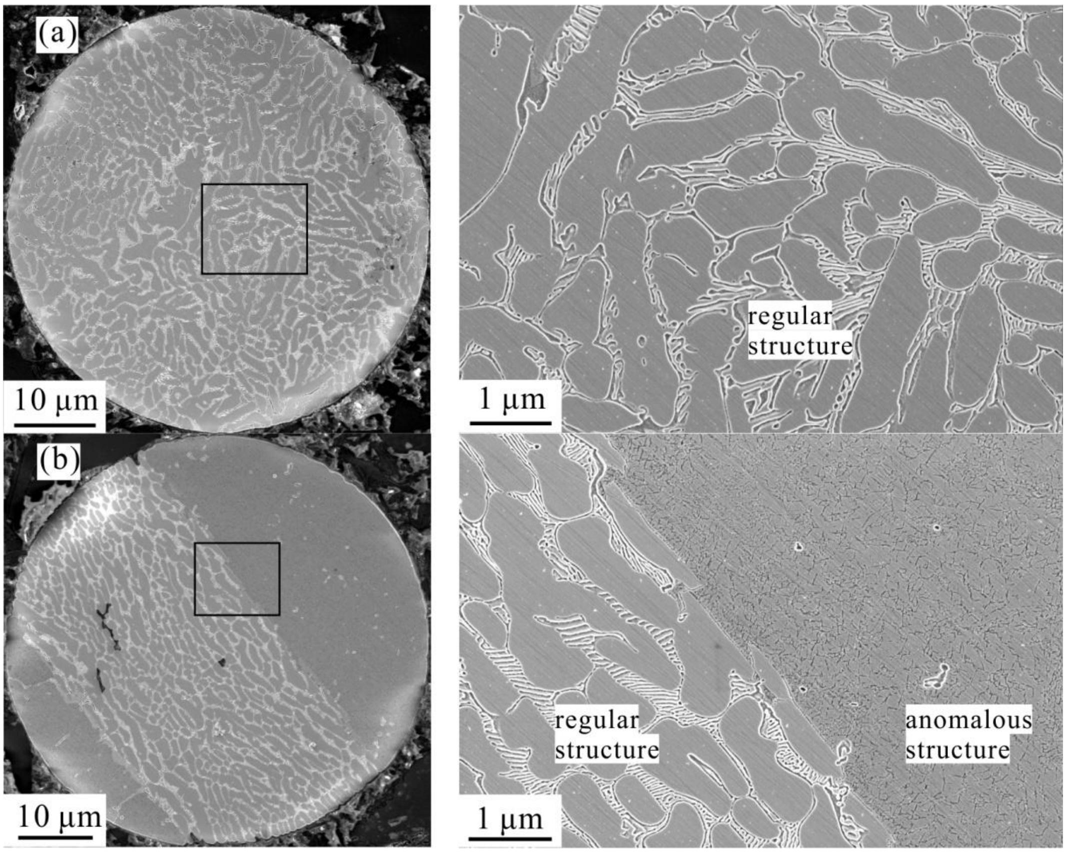

Figure 5.48: SEM high-resolution images of two of the 53-75 µm $Ni_{59.7}Fe_{15}Si_{25.3}$ particles showing (a) regular structure; (b) regular structure and anomalous structure.

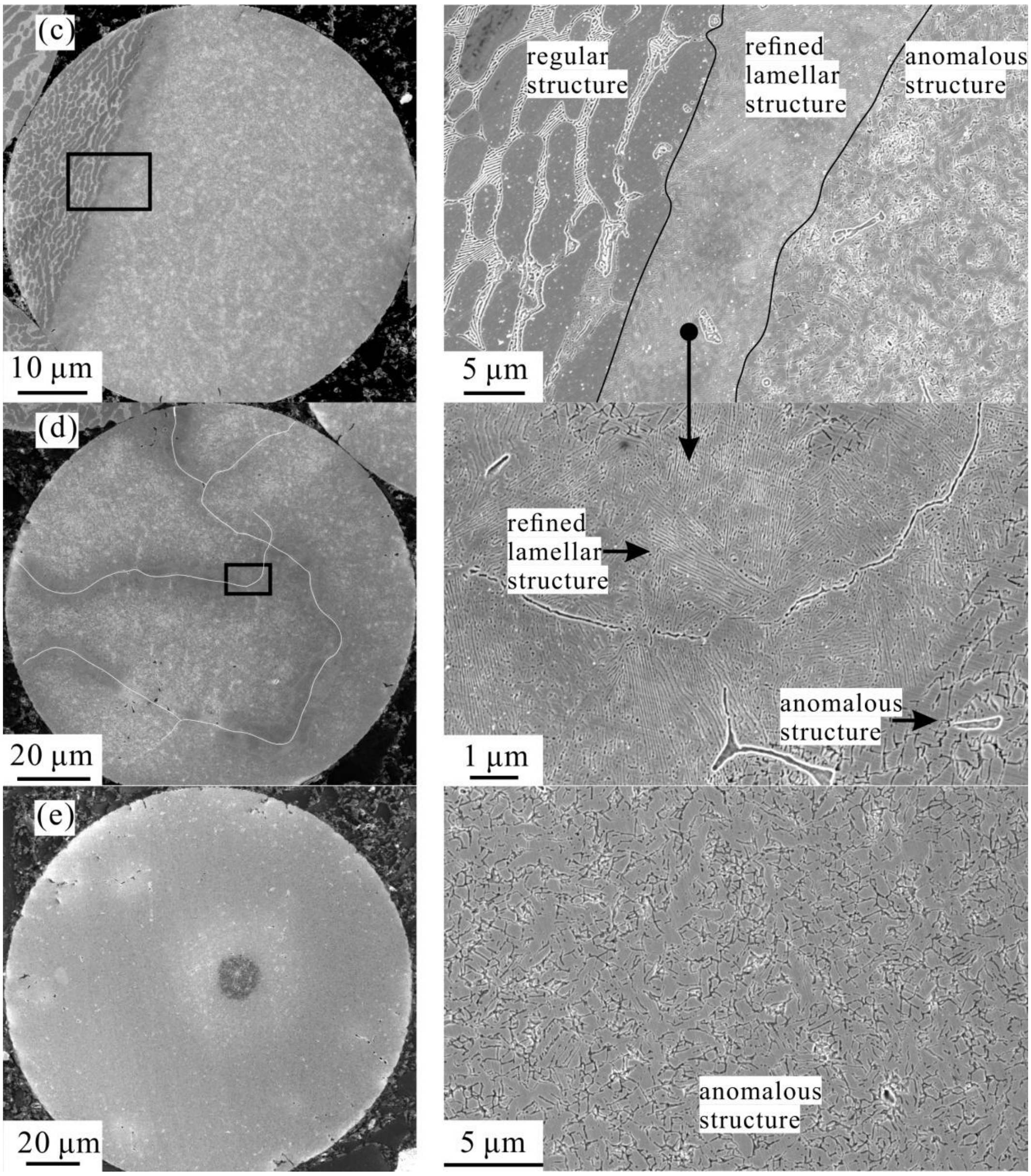

Figure 5.49: SEM high-resolution images of the $Ni_{59.7}Fe_{15}Si_{25.3}$ drop tube solidified particles showing (c) regular structure and anomalous structure isolated by lamellar structure transition zone (106-150 μm particle); (d) anomalous structure with small fraction of lamellar structure, which is located around the white line (106-150 μm particle). (e) entire anomalous structure (150-212 μm particle).

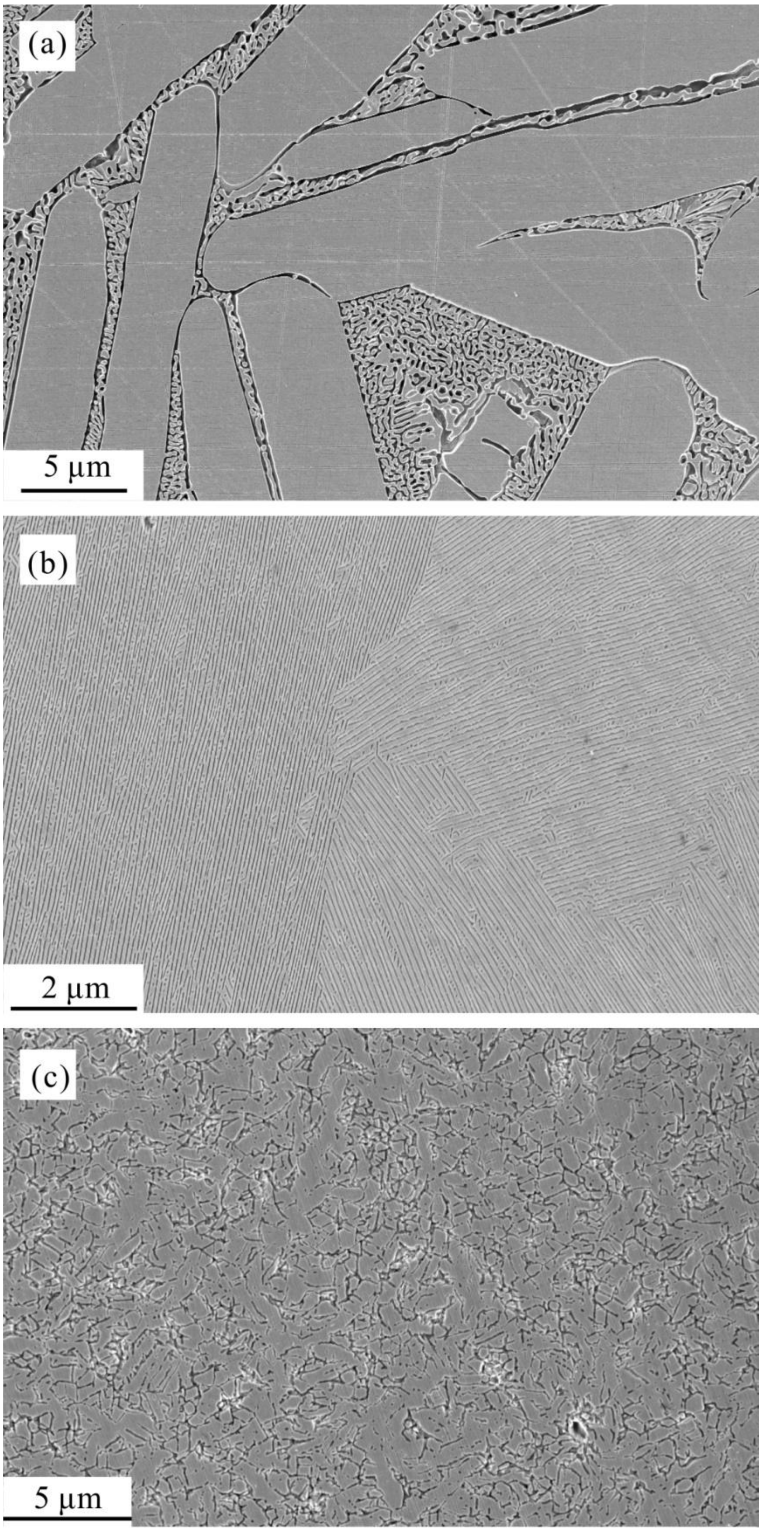

Figure 5.50: High resolution SEM micrographs of three different microstructures in the Ni-Fe-Si drop tube samples. (a) regular microstructure, I; (b) refined lamellar structure, II; (c) anomalous structure, III.

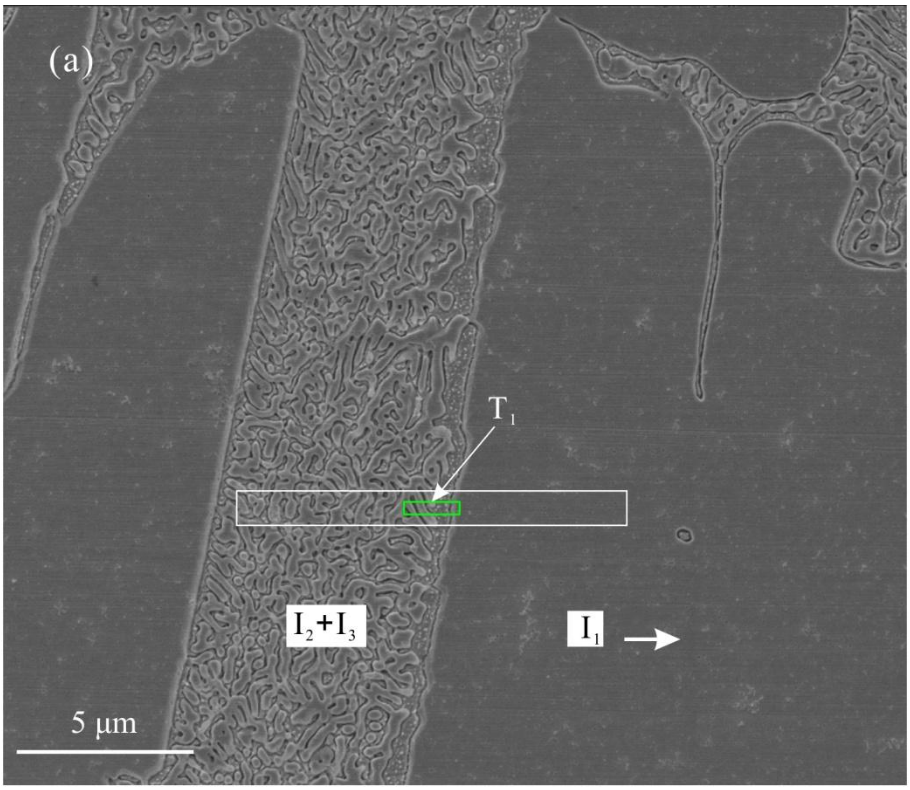

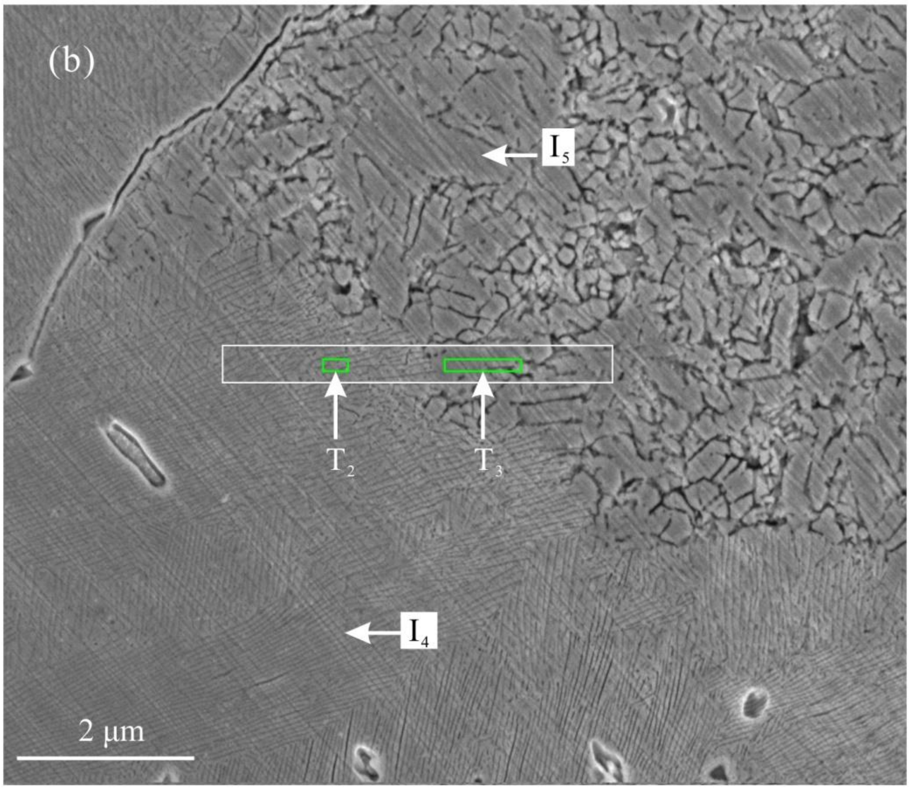

Figure 5.51: Micrographs showing the regions from which TEM specimens were taken (white squares). (a) and (b) correspond to the 300-500μm and 53-75 μm $Ni_{64.7}Fe_{10}Si_{25.3}$ particles . The green squares T_1, T_2 and T_3 refer to the areas analyzed by TEM aiming to confirm the phases, I_1-I_5.

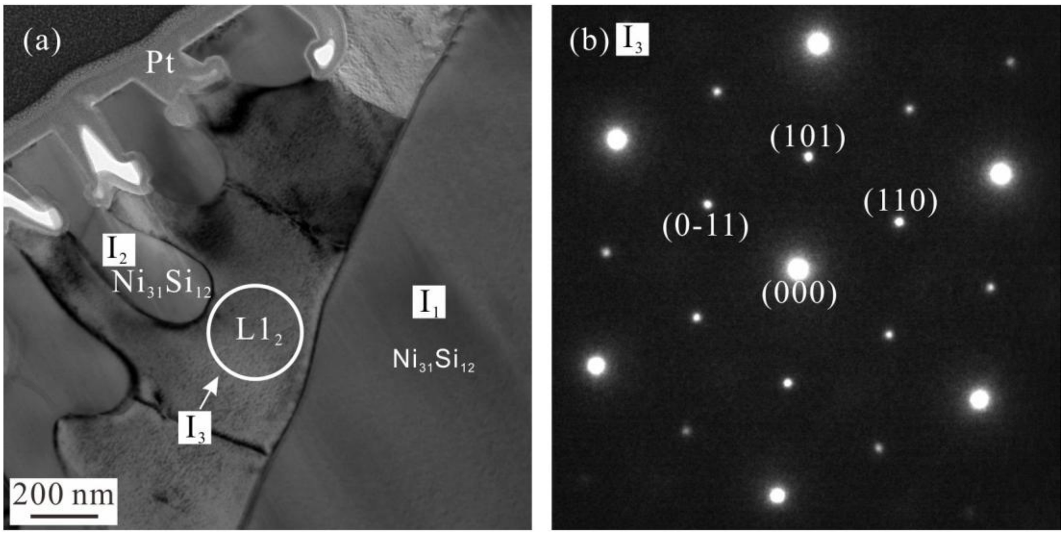

Figure 5.52: TEM bright field images and corresponding diffraction patterns of the regular structure. (a) the results of the TEM analysis on the area, T_1, identifying that the single phase I_1 is γ-$Ni_{31}Si_{12}$, and the eutectic structure consists of γ-$Ni_{31}Si_{12}$ (I_2) and ordered $L1_2$ phase (I_3); (b) TEM selected area diffraction pattern of the white circle area in (a), showing the super-lattice reflections from the $L1_2$ ordered structure.

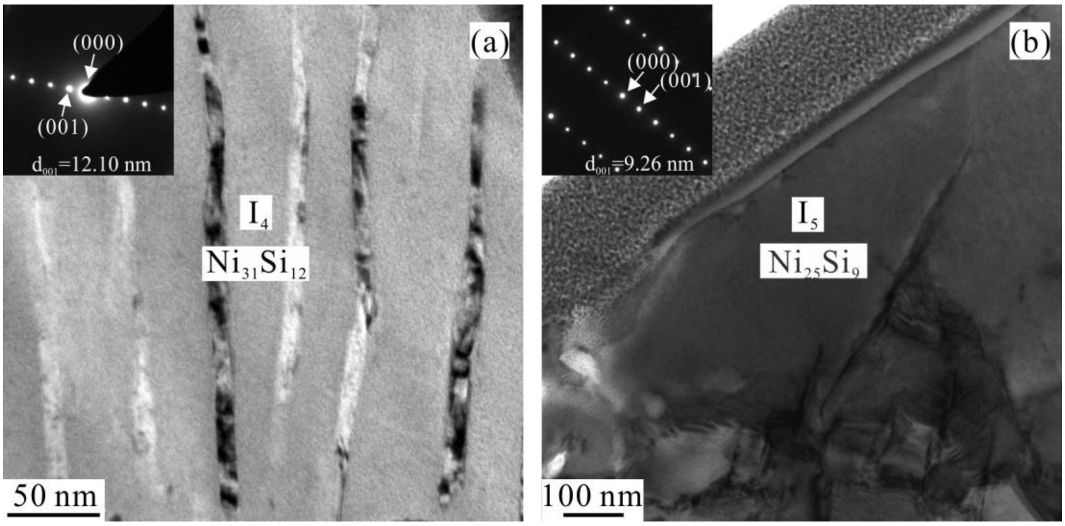

Figure 5.53: TEM bright field images and corresponding diffraction patterns of the lamellar and anomalous structure: (a) the results of the TEM analysis on the area, T_2, identifying wide band I_4 in lamellae structure as γ-$Ni_{31}Si_{12}$; (b) the results of the TEM analysis on the area, T_3, identifying the primary coarse phase (I_5) in anomalous as metastable $Ni_{25}Si_9$ phase. The insets in (a) and (b) are the TEM diffraction patterns of the γ-$Ni_{31}Si_{12}$ and $Ni_{25}Si_9$, respectively.

Table 5.8: Three different categories of the $Ni_{64.7}Fe_{10}Si_{25.3}$ and $Ni_{59.7}Fe_{15}Si_{25.3}$ particles based on the microstructure difference.

Particle category	Microstructure	Example	
		$Ni_{64.7}Fe_{10}Si_{25.3}$	$Ni_{59.7}Fe_{15}Si_{25.3}$
Type A	(I)	**Figure 5.41**a and b	**Figure 5.41**c and d, **Figure 5.48**a
Type B	(I) + (II)	**Figure 5.43**	– [a]
	(I) + (III)	**Figure 5.44**	**Figure 5.48**b
	(I) + (II) + (III)	**Figure 5.45**	**Figure 5.49**c
Type C	(II) + (III)	**Figure 5.46**	**Figure 5.49**d
	(III)	**Figure 5.47**	**Figure 5.49**e

[a] This type of the particles have not been observed in the $Ni_{59.7}Fe_{15}Si_{25.3}$ alloys.

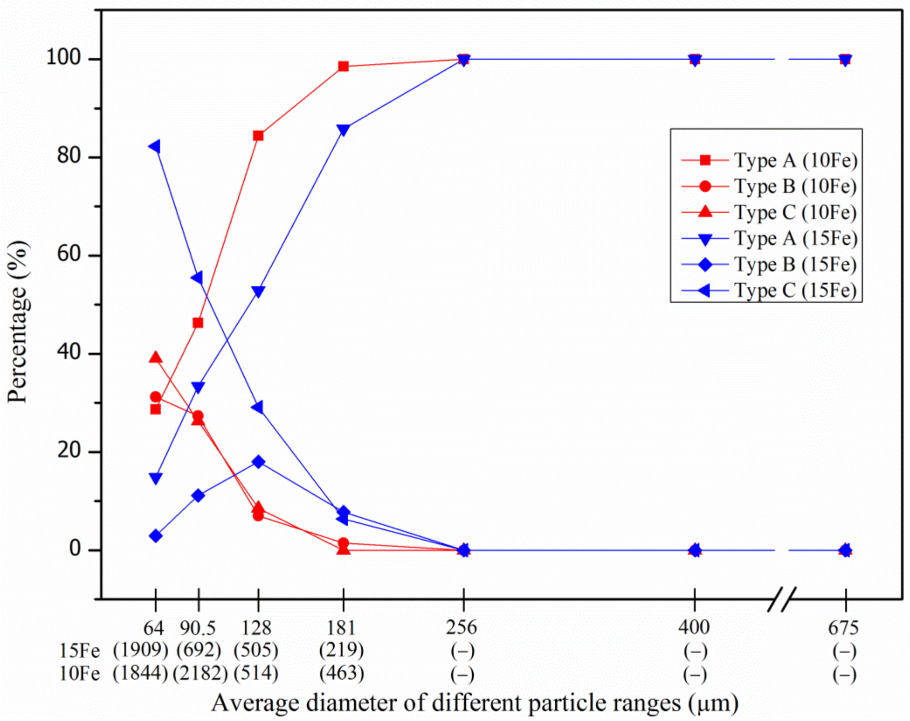

Figure 5.54: Percentage of the different types of particles (type A, B and C) in all ranges of the $Ni_{64.7}Fe_{10}Si_{25.3}$ (red curves) and $Ni_{59.7}Fe_{15}Si_{25.3}$ (blue curves) alloys. The numbers of the particles counted are also listed in the brackets beneath the *x*-coordinate. The numbers of the big particles (>212 μm) have not been counted here. 10Fe and 15Fe in the diagram denote the $Ni_{64.7}Fe_{10}Si_{25.3}$ and $Ni_{59.7}Fe_{15}Si_{25.3}$ alloys.

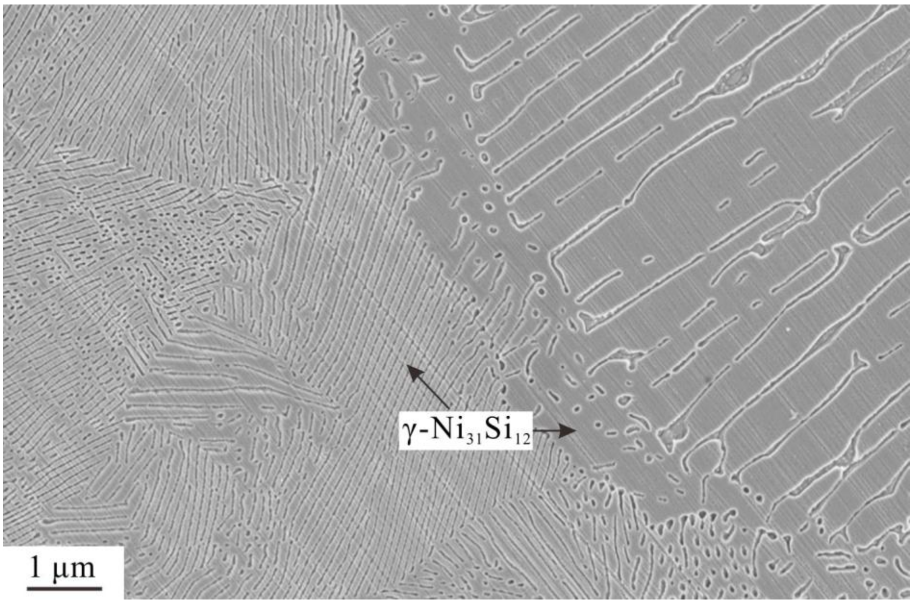

Figure 5.55: SEM image of fine lamellar structure found in one 212-150 μm particle ($Ni_{64.7}Fe_{10}Si_{25.3}$), showing the direct transition from structure I to II.

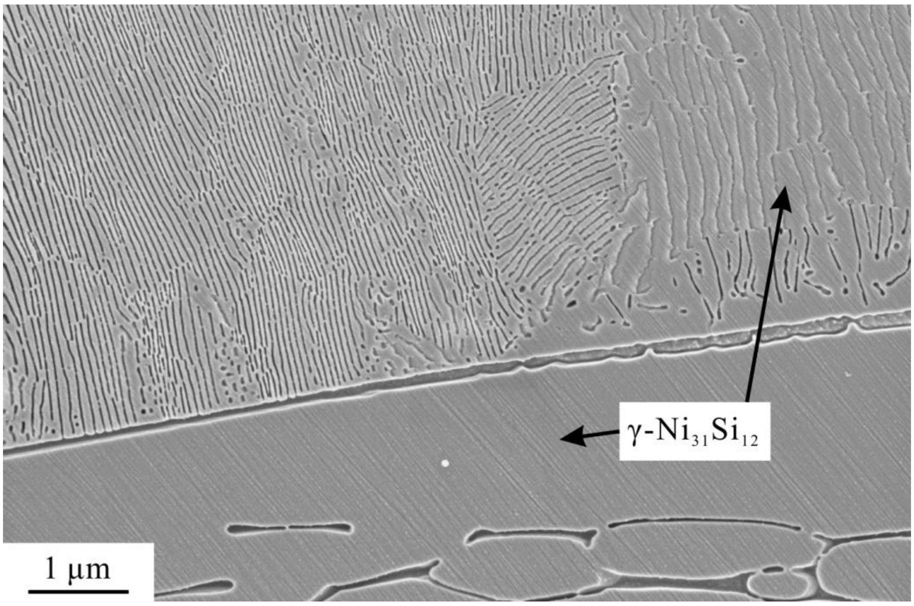

Figure 5.56: SEM image of fine lamellar structure found in one 212-150 μm particle ($Ni_{64.7}Fe_{10}Si_{25.3}$), showing the development of structure II from the normal surface of the γ-$Ni_{31}Si_{12}$ phase.

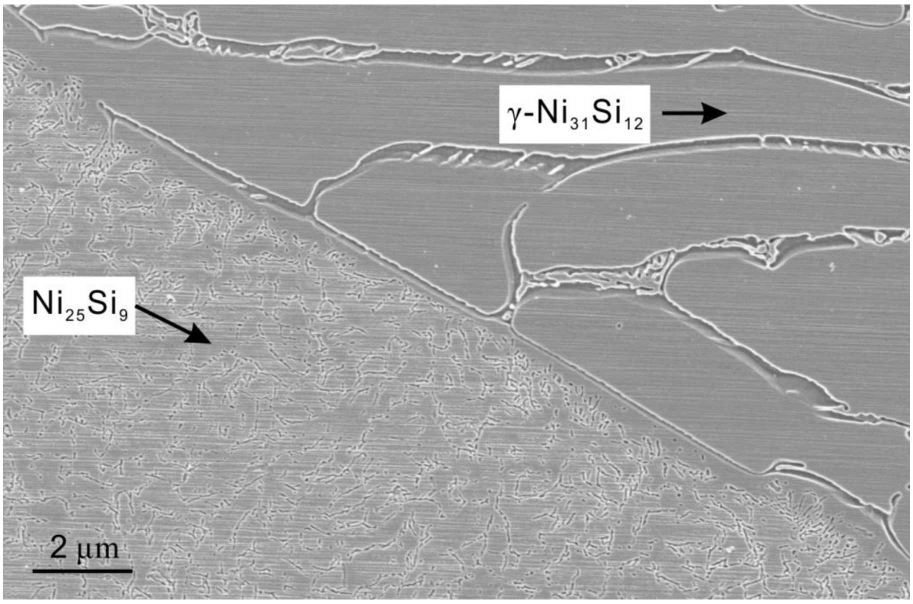

Figure 5.57: SEM high-resolution image of one 150-106 μm particle ($Ni_{64.7}Fe_{10}Si_{25.3}$), showing the connected regions of the structures I and III.

Table 5.9: Composition (at.%) of the $Ni_{64.7}Fe_{10}Si_{25.3}$ particles with general and anomalous structures in the range 75-150 μm by EDX

Diameter (μm)	Compositions (anomalous particles)				Compositions (general particles)			
	Fe	STDEV	Si	STDEV	Fe	STDEV	Si	STDEV
106-150	10.56	0.05	24.85	0.09	10.60	0.08	24.82	0.07
75-106	10.52	0.05	25.25	0.13	10.57	0.11	25.14	0.16

Table 5.10: Composition (at.%) of the $Ni_{59.7}Fe_{15}Si_{25.3}$ particles with general and anomalous structures in the range of 75-150 μm by EDX

Diameter (μm)	Compositions (General particles)				Compositions (anomalous particles)			
	Fe	STDEV	Si	STDEV	Fe	STDEV	Si	STDEV
106-150	15.66	0.15	24.92	0.10	15.56	0.07	24.98	0.15
75-106	15.66	0.18	24.86	0.16	15.59	0.15	24.92	0.14

Table 5.11: The compositions of single phase and eutectic area for 500-850 μm $Ni_{64.7}Fe_{10}Si_{25.3}$ particles using the Microprobe technique*

Phase	Ni (at.%)	STDEV	Fe (at.%)	STDEV	Si (at.%)	STDEV
Single γ phase	65.73	0.23	6.86	0.24	27.40	0.06
Eutectic	60.27	0.80	19.11	0.92	20.63	0.51

*15 different areas are detected for single γ phase and eutectic area separately;

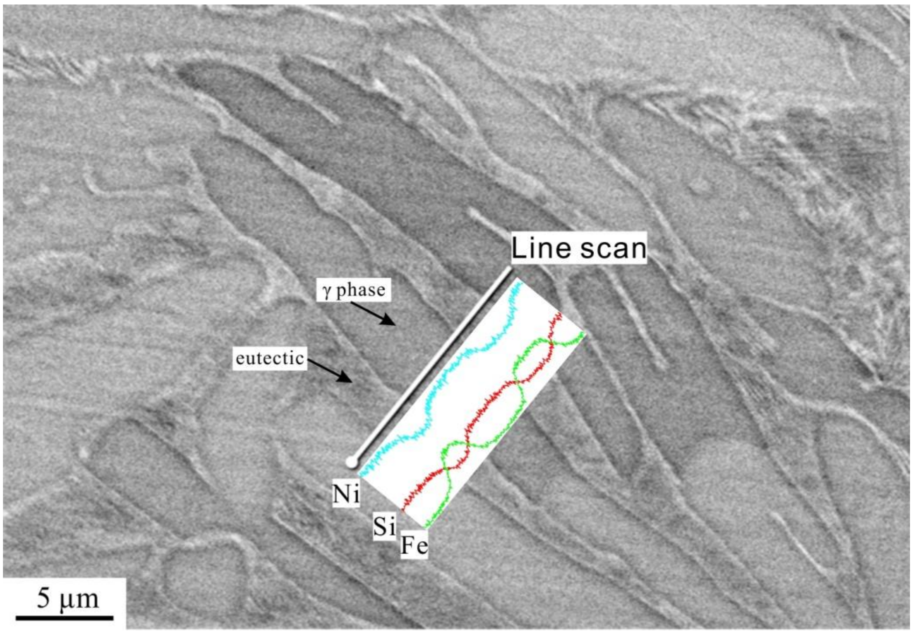

Figure 5.58: EDX line scanning analysis of the general structure including the primary γ phase and eutectic regions, showing the eutectic has a high Fe composition but lower Ni and Si compositions.

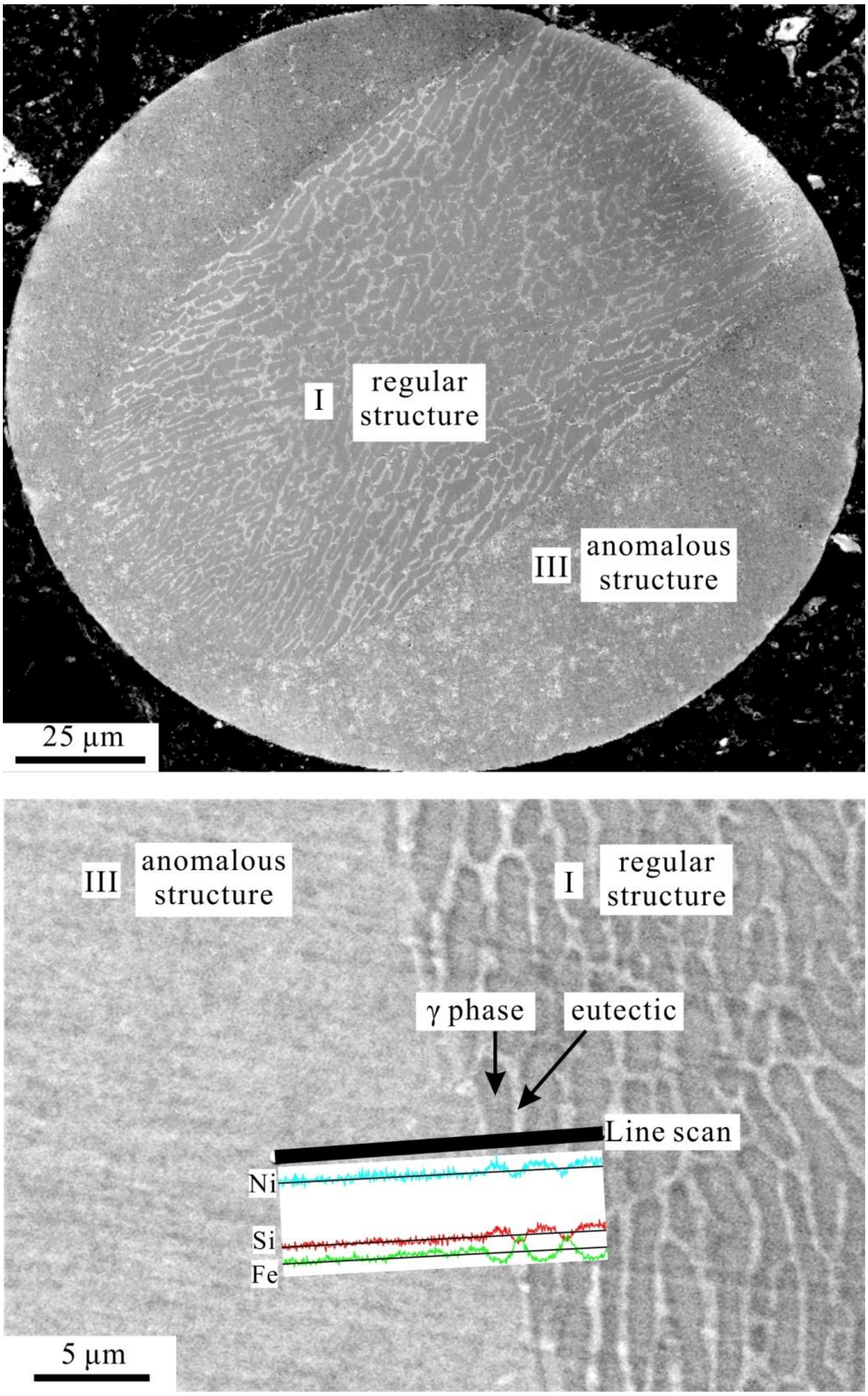

Figure 5.59: Line scanning analysis towards contiguous area of the metastable and primary phase

6 Discussion

The results presented in the last chapter will be discussed here. The discussion will mainly focus on the phase formation and microstructural evolution at high cooling rates (drop tube), with the results of the arc-melted samples used for comparison.

6.1 Cooling rate in the drop tube

As mentioned above, dendrite growth is the common mechanism of crystallization from metallic melts and the morphology consists of an array of dendrites with secondary and even high order branches. The analysis of primary (λ_1) and secondary (λ_2) dendrite arm spacings [126, 127] indicated that the primary spacings do not coarsen with time and can be accurately measured from the microstructure and compared with growth models, while the secondary spacings are seen to rapidly coarsen during solidification. Meanwhile, the scale of dendrite structure is recognized to be dependent on the solidification conditions, namely, fast cooling usually results in fine dendrite spacings [39]. Therefore, the secondary arm spacing can be used to calculate the cooling rate in the solidification processes where the cooling rates could not be measured, e.g. the drop tube solidification process. The secondary arm spacing, $\lambda_{2,}$ can be described as [19]:

$$\lambda_2 = 5.5\ (M' t_f)^{1/3} \tag{6-1}$$

with

$$M' = \frac{\Gamma D_i ln(C_e/C_0)}{m(1-k)(C_0-C_e)} \tag{6-2}$$

where t_f is the local solidification time, which can be obtained by:

$$t_f = \frac{\Delta T}{(\frac{dT}{dt})} \tag{6-3}$$

where ΔT is the difference between the tip temperature and the melting point of the last interdendritic liquid and the latter is often equal to the eutectic temperature if a eutectic reaction exists in the system.

Recently, a drop tube experiment was carried out by Kasperovich et al. [128] on the Al-4 wt.% Cu alloy. Firstly, they calculated the cooling rate according to the heat balance as a function of the droplet size D (mm), with the relationship:

$$\frac{dT}{dt} = 256.36 * D^{-1.784} \tag{6-4}$$

They also measured the secondary arm spacings (λ_2) in the dendritic structures, which were consistent with the results from the simulated dendritic structures at different cooling rates using the two-dimensional pseudo-front tracking method. The relationship fitted to the experimental secondary dendrite arm spacings and the cooling rates can was given as:

$$\lambda_2 = 54.5 \left(\frac{dT}{dt}\right)^{-0.328} \tag{6-5}$$

In Equation (6-5), the exponent, -0.328, is close to the value 1/3 in the Equation (6-1). Both Equation (6-1) and (6-5) showed that the secondary dendrite arm spacing can be used to estimate the cooling rate.

Therefore, both methods based on the heat balance or on the measured secondary dendrite arm spacing can be used to estimate the cooling rate in the drop tube. In this project, the cooling rate was calculated based on the heat balance. The power-law fitting using the EXCEL was used to calculate the cooling rate of $Ni_{64.7}Fe_{10}Si_{25.3}$ alloy (**Figure 5.1**), which can be written as:

$$\frac{dT}{dt} = 258.47 * D^{-1.624} \tag{6-6}$$

The calculated cooling rate in the present project is lower than the calculated values by Kasperovich et al. [128] because of the different parameters in the Ni-Fe-Si alloy (present) and Al-Cu alloy (Kasperovich et al.), e.g. the surface emissivity (ε) and the melting temperature. In fact, the accelerated velocity of the droplet during the flight process is lower than the gravitational acceleration (≈ 9.8 m s^{-2}) due to the effect of the dynamic drag. The instantaneous velocity at any height of the drop tube should be lower than 12.4 m s^{-1} and thus the actual error of the calculated cooling rate of each corresponding particle should be smaller than the error in **Figure 5.1**.

6.2 Ni-25.3 at.% Si

According to the Ni-Si equilibrium phase diagram (**Figure 6.1**), the equilibrium solidification pathway for the Ni-25.3 at.% Si alloy would begin with the primary growth of the γ-$Ni_{31}Si_{12}$, with the subsequent transformation to the disordered β_3 via a peritectic reaction below 1443 K. Subsequently the β_3 will transform to ordered β_2, which will finally transform to $\beta_1 + \gamma$ via a eutectoid reaction. Neither α-Ni nor metastable $Ni_{25}Si_9$ would be expected in the solidified samples. However, in a practical way, the structures and the phases always have a strong relationship with dynamic factors, e.g. high cooling rate or high undercooling in the non-equilibrium process, which gives rise to the formation of supersaturated solid solution, metastable phase and even metallic glass [10]. In addition, the mechanisms with the slow reaction rates would be greatly affected, e.g. peritectic reaction and transformation [99].

The results of the Ni-25.3 at.% Si alloy will be discussed here, including the arc-melted experiment and the rapid solidification experiment in the drop tube. Combined with the results at different cooling rates, the solidification properties of β and metastable $Ni_{25}Si_9$ phases were studied, resulting in a new solidification pathway.

6.2.1 Arc-melted sample

XRD analysis of the arc-melted Ni-25.3 at.% Si alloy showed the presence of γ-$Ni_{31}Si_{12}$, β_1-Ni_3Si and metastable $Ni_{25}Si_9$. Based on the Rietveld analysis, β_1-Ni_3Si formed as the dominant phase in the arc-melted alloy. The microstructure showed that the β_1 phase disperses widely in the sample. The diffraction patterns of the α-Ni and β_1-Ni_3Si are quite similar, so it is difficult to distinguish them. The XRD patterns of Ni-Si alloys in previous references [17, 91] also showed the overlapping of the α-Ni and β_1-Ni_3Si phases. Here, two alternative Rietveld analyses have been done, one with both α-Ni and β_1 phases and one with just β_1. On the basis of this analysis if α-Ni is present, its fraction has an upper limit of 7 %.

The formation of the metastable phase, $Ni_{25}Si_9$, has been observed in the rapid solidification experiments by Leonhardt et al. [17], who rapidly quenched undercooled Ni-21.4 at.% Si melts onto a chilled substrate. The sample produced in the arc-melting furnace was also subject to a series of cooling rates, with the high cooling rate in the region close to the chiller (copper hearth). So, the presence of the metastable $Ni_{25}Si_9$ (8.8%) here is also attributed to the high cooling rate in these regions.

6.2.2 Drop tube solidified particles

All of the powder particles showed fine microstructures. The XRD patterns would be close to the non-oriented powder diffraction patterns, and therefore the relative peak intensities should depend strongly on the fractions of the corresponding phases. It has been shown that $Ni_{25}Si_9$ was included in all three structures. The single phase M_2 was also $Ni_{25}Si_9$ (**Figure 5.17**). Therefore, according to its strong relative peak intensities (**Figure 5.10**), the metastable phase $Ni_{25}Si_9$ should be the dominant phase in all size ranges of the particles. For the arc-melted Ni-25.3 at.% Si alloy, XRD analysis indicated the fraction of the α-Ni phase was lower than 7.0 %. By inference, the fraction of the α-Ni phase was also expected to be lower than this value. Therefore, the formation of the α-Ni phase will not be included in the discussion section as such a low fraction will not influence the results.

Previous studies [15-17] on the Ni-rich end of the Ni-Si phase diagram indicated that the growth velocity of Ni-Si melts drops with increasing Si composition. The highest velocities measured by Cochrane et al. [16] on pure Ni and Ni-Si melts for Si < 4.09 at.% were 50-60 m s^{-1} (ΔT=250 K), while the maximum of Ni-21.4 at.% Si alloy measured by Leonhardt et al. was only 1.5 m s^{-1} (ΔT=220 K). The growth velocity of the Ni-25.3 at.% Si melt recorded by Ahmad et al. was about 0.018 m s^{-1} (ΔT=160 K), which was consistent with the measured unusual viscosity in their study. The high viscosity was attributed to the semi-conductive metal, Si, which has covalently bonded Si-Si networks. The growth velocity is related to viscosity which, in turn, would affect the atomic diffusion coefficient. Based on this concept, for Ni-25.3 at.% Si melt, low atomic mobility would be expected in the liquid at high cooling rates, which could manifest itself by favouring the formation of phases with composition close to the liquid, e.g. $Ni_{25}Si_9$ (26.47 at.% Si), in comparison with γ-$Ni_{31}Si_{12}$ (27.91 at.% Si), or features with very fine length scales (fine lamellae) or both.

The onset temperature of the phase transformation of $Ni_{25}Si_9$ was shown by DTA, to be about 491 ℃ with the heating rate being 10 K min^{-1}, which is consistent with Leonhardt et al. [17] and Dutra et al. [87]. Such a low transformation temperature compared with the melting temperature of 1230 ℃ points to its poor thermal stability. In-situ XRD indicated that the metastable phase decomposes to the β_1-Ni_3Si and γ-$Ni_{31}Si_{12}$ phases, a result consistent with the microstructure change of the heat-treated particle (**Figure 5.34**). The formation of $Ni_{25}Si_9$ was not observed in the undercooling experiments of the Ni-21.4 at.% alloy [95, 96], and only a small fraction was observed in the Ni-25.3 at.% Si alloy [15]. Conversely, it was obtained in the rapidly solidified eutectic Ni-21.4 at.% Si alloys by Leonhardt et al. [17] who quenched the undercooled sample onto a chilled substrate and by Dutra et al. [87] using a melt-spinning technique. This indicates that high cooling rate is necessary to form and retain the metastable phase $Ni_{25}Si_9$. The corresponding cooling rates of the 850 μm and 75 μm particles are estimated to be 3.88×10^2 and 1.98×10^4 K s^{-1} in this project. In the solidification process experiencing such high cooling rates, both post recalescence solid-liquid and solid-solid phase transformations will be inhibited to a great extent. Therefore, the metastable phase $Ni_{25}Si_9$ could form as the dominant phase in all ranges of the particles.

If the heat released during the solidification cannot be extracted quickly, even if the solidification condition favours the formation of the $Ni_{25}Si_9$ phase, it would transform to the β_1-Ni_3Si and γ-$Ni_{31}Si_{12}$ phases in the post-recalesence and subsequent cooling period. Therefore, we might postulate that $Ni_{25}Si_9$ might have solidified in the initial stage of the solidification experiments in the previous flux undercooling studies [95, 96], but it decomposed again because the cooling rate was not enough to retain it during the recalescence event and post-solidification process. This might then be the reason that $Ni_{25}Si_9$ was not observed in the final samples of undercooling experiments, but formed in the rapid solidification experiments on the same alloy (eutectic Ni-21.4 at.%). However, the above cannot account for results of Ahmad et al., because the mixed structure of γ-$Ni_{31}Si_{12}$ and β_1-Ni_3Si was not observed in the resulting microstructure. Instead, the γ-$Ni_{31}Si_{12}$ phase was the primary phase and was retained in the final microstructure. However, a small fraction of $Ni_{25}Si_9$ was retained at the highest undercooling (160 K).

The microstructure studies indicated that, except for the 500-850 μm powder particles (completely type B), both types A and B existed in all ranges of the particles. This variation was attributed to the interplay of cooling rate and undercooling. The particles of the same size will be subjected approximately to the same cooling rate. Meanwhile, high undercoolings might be achieved in small alloy particles produced by atomization due to high heat extraction rate (high surface area/volume ratio) in the drop tube process [129]. However, it is not true that all particles of the same size will solidify at the same undercooling as this is controlled by nucleation, which is a stochastic process, namely that the nucleant in the melt can be distributed to the droplets randomly. Solidification of a liquid sample might be catalyzed by the potent nucleation site present, e.g. oxides, and, in such case, deep undercooling is not expected due to the heterogeneous nucleation. The catalytic effect of potent agents can be restricted by dispersing the liquid into a large number of small particles that can solidify individually [130]. One such method is the drop tube technique with gas atomization involved. In this stochastic process, a series of undercoolings from low to quite high would be achieved in each size range of the particles due to the variation of nucleant potence. The particles can be divided into two populations, one containing very potent nucleants and the other not. Correspondingly, there should be two different kinds of particles in each size range, one with high undercooling and one with low undercooling and hence present two completely different microstructures. Meanwhile, at a given nucleant density, the probability of a given particle containing an active nucleant decreases as the volume of the droplet decreases. So high undercooing is much more likely in a population of small particles. A consistent result was observed in **Figure 5.19**, showing that the proportion of type A powder particle (entire heteroclite structure) increases with decreasing particle size, from 13.91% (300-500 μm) to 40.1% (75-106 μm). This suggests that type A particle had experienced the high undercooling.

By inference type B particle with the presence of the mixed structures must be subject to low undercoolings, so that the corresponding solidification path is perhaps following the metastable extension of the $Ni_{25}Si_9$ liquidus line. The average Si composition of Ni-25.3 at.% particle by EDX analysis is within the range 24.97-25.46 at.%, which is just in between the compositions of the β_1-Ni_3Si (22.6-24.5 at.%) and $Ni_{25}Si_9$ (26.47 at.%). According to the metastable liquidus line (**Figure 6.1**) shown by Leonhartdt et al. [17], with the formation of the $Ni_{25}Si_9$ phase, the possible eutectic structure would be $Ni_{25}Si_9$ and α-Ni (or a Ni-rich supersaturated solid solution) in the non-equilibrium process. A similar result was observed by Ahmad et al. who formed the metastable lamellar structure of the γ and a supersaturated solid solution in the undercooling experiments of the Ni-25.3 at.% Si alloy. However, the discovery here of $Ni_{25}Si_9$ and β_1-Ni_3Si eutectic would imply that the metastable liquidus line of $Ni_{25}Si_9$ would be dropping much more steeply with regard to the formation of the β_1-Ni_3Si phase.

The eutectic structures I and III have similarities with the structure of pearlite [131], which is a two phase, lamellar structure composed of alternating layers of α-ferrite and cementite formed via a eutectoid transition. As can be seen from the Ni-Si phase diagram, there are two high temperature forms of the β-phase (disordered β_3 and ordered β_2). If the high cooling rates achieved in the drop-tube it would favour the formation of β_3 or β_2, then their subsequent decomposition would give a possible route for the observed β_1-$Ni_{25}Si_9$ lamellar structure. However, the experimental results refute this route. Firstly, the XRD studies failed to indicate the presence of any β_3 and β_2, as some residual β_3/β_2 would be expected to remain at the highest cooling rates, particularly as Ahmad et al. observed extensive retained β_3 in fluxed samples in which a cooling rate < 10 K s^{-1} would be expected. Secondly, the microstructural analysis also failed to observe mixed structure of β_1-Ni_3Si + γ-$Ni_{31}Si_{12}$, which might be expected via the eutectoid reaction, $\beta_2 \rightarrow \beta_1 + \gamma$ (according to the equilibrium phase diagram) if this assumption is correct. On the other hand, high cooling rates would, to a great extent, inhibit post recalescence phase transformations. So the structure of the particles is expected to be retained with their original morphologies. Therefore, the lamellar microstructure would have formed form from the undercooled liquid directly. This result indicates that the observed lamellar structure formed as a result of a hitherto unobserved eutectic reaction between β_1 and $Ni_{25}Si_9$, in an alloy with composition close to the eutectic composition.

Although both structures I and III have the same phase constitution, β_1-Ni_3Si and $Ni_{25}Si_9$, the structure III has the feature of an anomalous eutectic wherein the continuous lamellar morphology of the structure (I) cannot be observed. Unlike the normal eutectic growth, the microstructure from regular eutectic to anomalous can be easily examined with increasing undercooling [96]. The clear boundary of the transition from I to III cannot be known since both structures exist even in the same particle. The structure III can be observed in all ranges of type B particles, while the fraction of the regular structure (I) decreases with decreasing particle size and the regular structure almost disappears in all of the 75-106 μm particles. A similar result has been observed in the undercooled experiments of a Ag-Cu eutectic alloy by Clopet et al. [132], wherein a mixed structure consisting of the anomalous and lamellar eutectic was observed, with the volume fraction of the irregular eutectic increasing with increasing undercooling, a result also found in the studies in [133]. Therefore, variability in the balance between the structures I and III will be a consequence of the undercooling attained by individual particles. This could be possible because a series of undercoolings (from very low to quite high) would be achieved in reality, although we have simply classified the particles into high and low undercooling forms. Meanwhile, in some eutectic systems, e.g. Ni-Sn [134], the coupled eutectic growth will break down in favour of single phase growth if the liquid experienced high undercoolings. According to the metastable phase diagram, at high undercooling the Ni-25.3 at.% Si particle might be solidified directly to the phase that is close to the single phase $Ni_{25}Si_9$, with only a small residual of another phase. With the conclusion of the eutectic reaction between β_1-Ni_3Si and $Ni_{25}Si_9$, perhaps type A particles have been undercooled below the metastable extension of the $Ni_{25}Si_9$ solidus line. In this case, the particles formed into the entire heteroclite structure (A type), in which the primary solidification of $Ni_{25}Si_9$ occurs.

It can be summarized that at high cooling rates the single phases β_1-Ni_3Si and $Ni_{25}Si_9$ can solidify directly from the melts and even as a eutectic structure. These solidification behaviours are not only different from the prediction of the phase diagram, but also different from the studies by Ahmad et al., who observed the eutectic structure of γ-$Ni_{31}Si_{12}$ and supersaturated α-Ni with the suppression of growth of the β-phase. Similar effect of the cooling rate was also observed in hypereutectic Nb-xSi (x = 21.0-27.0 at.%) alloys by Bertero et al. [101], who performed a series of experiments using the levitation technique and a combination of levitation and splat quenching techniques. Different from the theoretical prediction (**Figure 6.2**) that solidification to primary Nb_3Si should have occurred for undercoolings in excess of 270 K, solidification was to a metastable eutectic of α-Nb and β-Nb_5Si_3 in levitated samples. Conversely, the formation of Nb_3Si was observed in splat quenched samples, which, as they described, was irrelevant to the undercooling prior to splat quenching. They attributed this phenomenon to difficulty in nucleating the Nb_3Si phase, which can grow at high cooling rate due to enhanced short-range diffusion and possible heterogeneous sites on the splat. Therefore, in the present work, high cooling rate should be the factor controlling for the formation of the single phases and the observed microstructures, in which the short-range diffusion mechanism is preferential. This is also consistent with the nanostructure morphology in β_1-$Ni_{25}Si_9$ eutectic structures with narrow lamellae spacings.

Meanwhile, there is one common characteristic in the solidification processes of Nb-25 at.% Si and Ni-25.3 at.% Si alloys at high undercooling and high cooling rate, and that is the suppression of the peritectic reaction. It is accepted that the peritectic phase can be formed via peritectic reaction, wherein the primary phase is expected to be coated by a thin layer of peritectic phase quickly in the early stage and the subsequent reaction becomes the diffusion-controlled process [99]. StJohn et al. [37] pointed out that the necessary undercooling for solidification would also favour the crystallization of the secondary phase from the liquid. This suggestion was supported by Barker and Hellawell [100], who concluded that the primary Pb-rich phase was inefficient as a heterogeneous nucleant for the secondary phase, and the nucleation of secondary phase took place at many other sites in the Pb-Bi liquid. The observation of Nb_3Si at high cooling rate by Bertero et al. [101] might be a consequence of the second mechanism. In the study of Ahmad et al. [15], a small amount of β_3 phase was observed in fluxed samples, however the primary solidification was always the eutectic of γ-$Ni_{31}Si_{12}$ and supersaturated α-Ni. In the present work, the β_3 and β_2 phases were not observed and phase identification indicated the presence of the rest of the phases predicted by the metastable phase diagram, e.g. β_1, $Ni_{31}Si_{12}$ and $Ni_{25}Si_9$. This might be because the peritectic reaction was completely suppressed and the nucleation of β_3 and β_2 from the liquid was difficult. However, the origin is not clear here.

Rapid solidification at high cooling rates is an effective way to form metallic glass, especially for deep eutectics [10], because these alloys have a high reduced glass transition temperature due to their low melting point. Recently, Lu et al. [18] obtained an amorphous phase in the eutectic $Ni_{70.2}Si_{29.8}$ alloy under slow cooling conditions (about 1 K s^{-1}). Meanwhile, in the Nb-Si system, Benderdky et al. formed an amorphous phase in the narrow region adjacent to the chill surface in the melt-spinning experiment of the hypereutectic Nb-25at.% Si alloy [102]. Therefore, at high cooling rates, the melts of eutectic or near eutectic composition can be frozen into the amorphous state. It has been postulated that the melt with high viscosity, e.g. the Ni-25.3 Si melt here, could possess a good glass-forming property [19]. However, the as-solidified particles were crystalline according to the XRD. The amorphous phase was not observed even in the smallest particle range. This is mainly because the formation of $Ni_{25}Si_9$ (26.47 at.% Si) and β_1-Ni_3Si (22.6-24.5 at.% Si) can occur by short-range diffusion. Conversely, the condition is different for the Nb-Si alloys, in which the formation of the stable phases, α-Nb (<3.44 at.% Si) and α-Nb_5Si_3 (37.5-38.6 at.% Si), from the melt needs long-range diffusion.

In summary, the phases in the solidified arc-melted Ni-25.3 at.% Si alloy were $Ni_{25}Si_9$, γ-$Ni_{31}Si_{12}$ and β_1-Ni_3Si, the latter being the dominant phase. On the contrary, in the drop tube processed Ni-25.3 at.% Si particles, $Ni_{25}Si_9$ formed as the dominant phase in all size ranges of the particles, which we attribute to the high cooling rates in the drop tube. Furthermore, the formation of the β_2 and β_3 phases was suppressed, and the β_1 phase could solidify directly from the liquid. The metastable phase, $Ni_{25}Si_9$, possesses poor thermal stability and decomposed to the β_1-Ni_3Si and γ-$Ni_{31}Si_{12}$ phases at about 491 ℃ (at a heating rate of 10 K min^{-1}).

The regular and anomalous eutectic structures indicate that there is a novel, metastable eutectic reaction between the $Ni_{25}Si_9$ and β_1-Ni_3Si phases in Ni-Si binary phase diagram. At high undercooling the particles appear to be able to bypass the newly identified eutectic and form a near single phase $Ni_{25}Si_9$ structure (heteroclite structure). The fraction of the particles with entire heteroclite structure increases from 13.91% (300-500 μm) to 40.1% (75-106 μm). An amorphous phase could not be obtained, because, in the drop tube process, the nucleation and growth of the β_1 phase and metastable phase $Ni_{25}Si_9$ are favourable even under the condition of short-range atomic diffusion induced by high cooling rate.

6.3 Ni-Fe-Si

According to the Ni-Fe-Si equilibrium phase diagram (**Figure 6.3**), both $Ni_{64.7}Fe_{10}Si_{25.3}$ and $Ni_{59.7}Fe_{15}Si_{25.3}$ alloys are on the hypereutectic side of the α-γ eutectic, the βNi_3Si phase being suppressed by the presence of iron. Therefore, the predicted solidification path would be that the single phase γ should form first, which will lower the Si concentration of the remaining liquid until this hits the eutectic composition wherein all residual liquid will solidify to the α-γ eutectic structure. The fractions of the primary phase and the eutectic structure in the solidified samples were calculated using MTDATA software with the assumption that the eutectic contains α-Ni which has a low Si concentration. The calculated fractions of the single-phase γ-$Ni_{31}Si_{12}$ and eutectic phases are 61.4% and 38.6% for $Ni_{64.7}Fe_{10}Si_{25.3}$ alloy, and 53.4% and 46.6% for $Ni_{59.7}Fe_{15}Si_{25.3}$ alloy.

All of the arc-melted Ni-Fe-Si samples showed the same lamellar structure, comprising alternating lamellae of the single phase γ-$Ni_{31}Si_{12}$ and a eutectic/eutectoid structure, which seems to be as expected from the equilibrium phase diagram. Conversely, three different microstructures were summarized in the drop tube processed samples: (I) regular structure, which is also expected at equilibrium solidification condition; (II) refined lamellar structure; (III) anomalous structure. According to the microstructure difference, the powder particles were divided into three different types, A, B and C (**Table 5.8**), and their fractions as a function of cooling rate are shown in **Figure 6.4**.

From **Figure 5.54**, it is clear that the proportions of type C particles increase with decreasing particle size in both alloy systems, from 8.56% (106-150 μm) to 39.1% (53-75 μm) for $Ni_{64.7}Fe_{10}Si_{25.3}$ samples and from 29.11% (150-212 μm) to 82.24% (53-75 μm) for $Ni_{59.7}Fe_{15}Si_{25.3}$ samples. These results are consistent with the XRD and TEM analysis that $Ni_{25}Si_9$ formed in the small particles and even formed as the dominant phase in 53-106 μm $Ni_{59.7}Fe_{15}Si_{25.3}$ particles. Therefore, type C particles, by analogy with the explanation in the Ni-Si binary system, are the high undercooling forms and can be undercooled into the $Ni_{25}Si_9$ stability field, wherein the copious nucleation of $Ni_{25}Si_9$ occurs. Consequently, the particles present the entire anomalous microstructure, comprising the single phase $Ni_{25}Si_9$ and a small residual of another phase.

The formation of the $Ni_{25}Si_9$ phase in Ni-Fe-Si phase diagram has not been reported to date. Different from the results in the Ni-Si system that $Ni_{25}Si_9$ formed as the dominant phase in all ranges of the particles, in the Ni-Fe-Si ternary system, $Ni_{25}Si_9$ only formed at high cooling rates. It indicates that there is an extended $Ni_{25}Si_9$ stability field at low temperature, i.e. at high undercooling, in the Ni-rich part of the non-equilibrium Ni-Fe-Si ternary phase diagram.

Conversely, we surmise that type A particles are the low undercooling form and, thus, cannot be undercooled into the $Ni_{25}Si_9$ stability field. Therefore, they present a feature of entire regular structure, which seems like what might be expected at equilibrium condition. However, the origins of low undercooling should be different for the different particles. On the one hand, high undercoolings are not expected in the large particles as they are subjected to low cooling rates, so all of the 212-850 μm particles are A type. On the other hand, in the small size ranges (<212 μm), a few of the particles still contain some active nucleants due to the melt sub-division effect. High undercooling cannot be achieved due to the heterogeneous nucleation caused by the active nucleant. From **Figure 5.54** it is clear that the proportion of type A particles decreases with decreasing particle size, which is consistent with the stochastic model that the probability of a given particle containing an active nucleant decreases with decreasing volume at a given nucleation density.

Type B particles were first observed in 150-212 μm particles, which provided some detailed information about the microstructural development. Firstly, **Figure 5.55** indicates that the growth can evolve from the regular structure (I) to the refined lamellar structure (II), with the wide bands of both structures being the γ-$Ni_{31}Si_{12}$ phase. Meanwhile, the refined lamellar structure can develop from the normal surface of the γ-$Ni_{31}Si_{12}$ and $Ni_{25}Si_9$ phases (**Figure 5.56** and **Figure 6.5**). As a result, the development of the refined structure might mainly depend on the cooling rate, although the existence of the γ-$Ni_{31}Si_{12}$ and $Ni_{25}Si_9$ phases is also favourable.

The mixed structure of type B particles might be because of multiple nucleation. It has been postulated that the viscosity of the melt is high due to the existence of the covalently bonded Si-Si network. Therefore, the growth velocity would be slow in Ni-Fe-Si melt, wherein the evolved latent heat might result in the growth conditions changing during solidification. For example, if one particle contains a small amount of active nucleant, these might give rise to a difference in the local nucleus distribution. In this case, the particles still can be undercooled into the $Ni_{25}Si_9$ stability field due to high cooling rates, which results in copious nucleation of $Ni_{25}Si_9$ and finally forms the anomalous structure in the pure region. In the meantime, heterogeneous nucleation occurs in the active region of the same particle, giving rise to the growth of the regular structure along a certain direction, as shown in **Figure 5.44** and **Figure 5.48**b. This might be possible because some crystals possess their preferred growth direction (**Table 2.3**). In this solidification model, the solidification processes of the structures I and III are two independent courses but occur simultaneously. Therefore, the connected regions of the structure I and III always show the sharp interface. Furthermore, the refined lamellar structure might form from the remaining liquid (in the adjacent region of the structure I and III) which separates the structures I and III. In addition, the formation of the $Ni_{25}Si_9$ might not occur in some particles, wherein the regular structure (I) forms first in some region due to the active nucleant and then develops into the refined lamellar structure in the subsequent rapid solidification process, resulting in the mixed structure of I and II in some particles. There are also some particles containing a small fraction of the refined lamellar structures, which are surrounded by a large fraction of the anomalous structure (**Figure 5.49**d). This might imply that, in the final stage of the anomalous structure formation, the solidification converted to the growth of the refined lamellar structure because of the reduced nucleation and growth.

From **Figure 6.4**, it is clear that much more $Ni_{59.7}Fe_{15}Si_{25.3}$ particles form into the entire anomalous structure in the size range of 53-106 μm, in comparison with that of the $Ni_{64.7}Fe_{10}Si_{25.3}$ particles. If the density of nuclei is the same in both alloy systems, this result might indicate that a higher undercooling is required to enter the $Ni_{25}Si_9$ stability field in the $Ni_{64.7}Fe_{10}Si_{25.3}$ samples than in the $Ni_{59.7}Fe_{15}Si_{25.3}$ samples.

As can be seen in **Figure 6.6**, the regular structure looks like what might be expected at equilibrium. TEM analysis confirmed that the single phase (I_1) and phase (I_2) in the eutectic structure are the γ phase, However, the diffraction pattern from the phase I_3 displays the super-lattice reflections, which implies that the eutectic phase formed with the γ-$Ni_{31}Si_{12}$ phase (I_2) is the $L1_2$ phase but not the α-Ni (FCC) phase. Here, the composition of the eutectic structure in $Ni_{64.7}Fe_{10}Si_{25.3}$ particles (**Figure 6.6**) was 60.27, 19.11 and 20.63 at.% for Ni, Fe and Si respectively. With the formation of the γ phase, the calculated composition[10] of the $L1_2$ phase was 57.07 ± 0.65, 25.75 ± 1.34 and 17.18 ± 0.69 at.% for Ni, Fe and Si respectively. Similar results have been reported by Himuro et al. [20, 21], who observed the formation of the $L1_2$ precipitates from the α matrix by ageing the $Ni_{60}Fe_{30}Si_{10}$ alloy for a short time.

---

[10] This calculation is based on the assumptions: (1) the volume fraction ratio of α and γ phases (eutectic area) is 1.2 ± 0.2; (2) the compositions of the γ phase (primary and eutectic) are the same.

Meanwhile, the solidification behaviours of the $Ni_{75}Fe_{15}Si_{10}$ and $Ni_{75}Fe_{13}Si_{12}$ alloys have also been investigated. In comparison with the $Ni_{64.7}Fe_{10}Si_{25.3}$ and $Ni_{59.7}Fe_{15}Si_{25.3}$ alloys in the present work, the Fe in the alloys was originally designed to substitute for Si. First, the $Ni_{75}Fe_{15}Si_{10}$ alloys were quenched at 850 ℃ and 800 ℃ after solution-treatment at 1100 ℃. TEM analysis indicated the superlattice reflections in the sample rapidly quenched from 800 ℃, while that quenched from 850 ℃ had no superlattice reflections. Similarly, the $L1_2$ single-phase structure was also obtained by quenching the $Ni_{75}Fe_{13}Si_{12}$ alloy at 550 ℃, while that quenched at 600 ℃ presented the mixed structure of α + $L1_2$ phases. Therefore, the formation of the $L1_2$ phase is possible in the drop tube processed samples.

In addition, Himuro et al. attributed the formation of the $L1_2$ ordered phase to the argument that Fe atoms have a tendency to mainly substitute for Si in the Ni_3Si phase, and consequently, the $L1_2$ phase was represented by $Ni_3(Si,Fe)$ in their work. Based on this argument, the substitution of Fe for Si would occur in quite large measure in order to form the $L1_2$ phase $(Ni,Fe)_3(Fe,Si)$ in the present work. By this inference, the same should also be expected in the γ-$Ni_{31}Si_{12}$ phase. However, the detected Si compositions of the single-phase γ-$Ni_{31}Si_{12}$ in $Ni_{64.7}Fe_{10}Si_{25.3}$ and $Ni_{59.7}Fe_{15}Si_{25.3}$ alloys were close, being 27.15 at.% and 27.01 at.%, respectively, which are also close to the stoichiometry of the γ-$Ni_{31}Si_{12}$ (27.91 at.%). Meanwhile, type C particle of Ni-Fe-Si alloy and type A particle of Ni-Si alloy present the same structure, with the matrix being $Ni_{25}Si_9$. Therefore, this argument is controversial here. Instead, these results appear to indicate the substitution of Fe for Ni but not Si, which is consistent with the prediction of Ni-Fe phase diagram that Fe and Ni can form a continuous solid solution phase in a large temperature region (**Figure 3.6**). The formation of the $L1_2$ phase might be because of the behaviour of Fe segregation in the rapid solidification process. However, the origin is not clear here.

Although the $L1_2$ phase obtained in the present work seems like a single phase (**Figure 6.7**), the TEM data is still insufficient. Therefore, the origin of the regular structure might be for the growth of the primary γ-$Ni_{31}Si_{12}$ phase, followed by a eutectic reaction between γ-$Ni_{31}Si_{12}$ and a certain phase. In consideration of the results of Himuro et al. and Ahmad et al., this certain phase in the eutectic structure of the drop tube solidified alloys and, by inference, the arc-melted samples might be:

(1) the $L1_2$ single phase; (2) the mixed structure of α-Ni and $L1_2$ phases; or even (3) the supersaturated α-Ni.

In summary, it has been proved that there is an extended stability field of $Ni_{25}Si_9$ in the Ni-Fe-Si phase diagram. At low cooling rates ($< 2.44\times10^3$ K s^{-1}), the solidified phases were γ-$Ni_{31}Si_{12}$ and β_1 phases. At high cooling rates ($> 2.44\times10^3$ K s^{-1}), the additional metastable phase, $Ni_{25}S_9$ can be obtained. The formation of the γ-$Ni_{31}Si_{12}$ indicated the substitution of Fe for Ni. In the arc-melted Ni-Fe-Si samples, the typical lamellar structure was observed, comprising the single phase γ-$Ni_{31}Si_{12}$ and the eutectic structure. Similarly, all of the 212-850 μm particles also presented the regular structure. As the cooling rate increased ($> 2.44\times10^3$ K s^{-1}), the microstructure can change from the regular structure to the refined lamellar structure and the anomalous structure. The refined lamellar structure was an intermediate but not a necessary stage in the microstructure development process, which mainly depended on the cooling rate. With the increase of cooling rate, an increasing fraction of small particles experience high undercoolings and, therefore, can be undercooled into the $Ni_{25}Si_9$ stability field forming the entire anomalous structure.

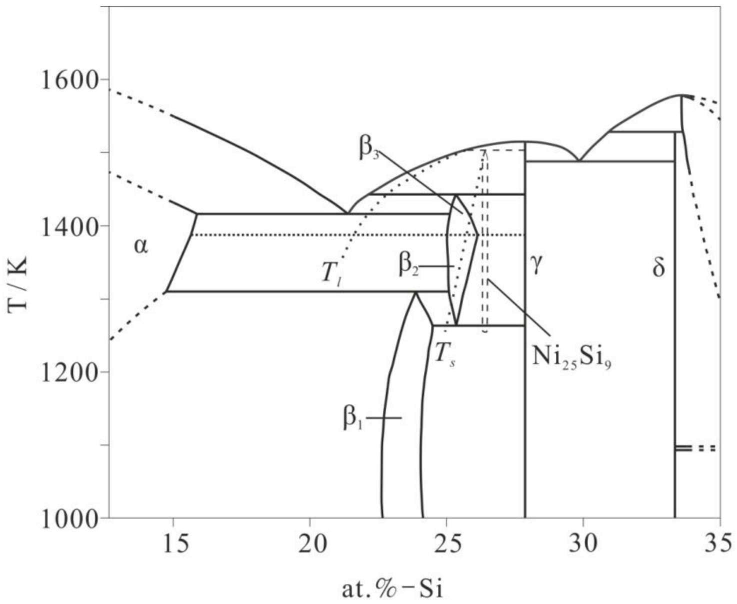

Figure 6.1: Ni-rich portion of the Ni-Si phase diagram with the metastable $Ni_{25}Si_9$ phase field included [17]. Dotted lines T_l and T_s are metastable extensions of liquidus and solidus lines of the $Ni_{25}Si_9$ phase.

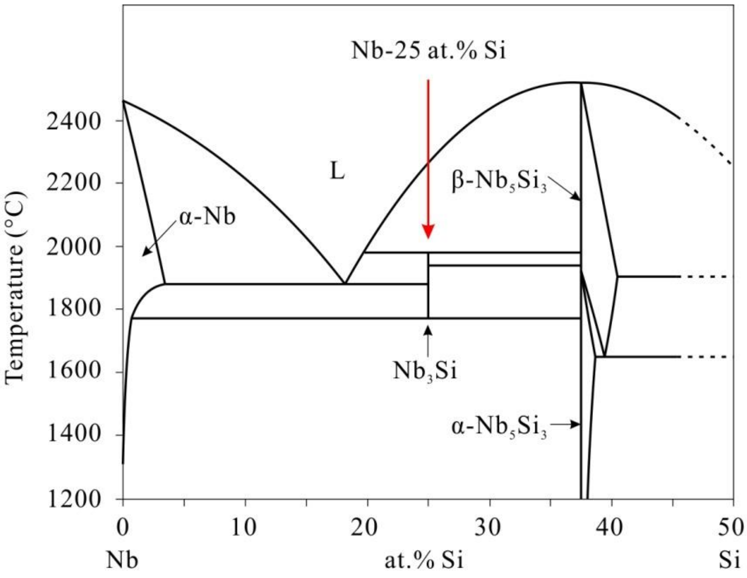

Figure 6.2: The Nb-rich part of the Nb-Si binary phase diagram [101]

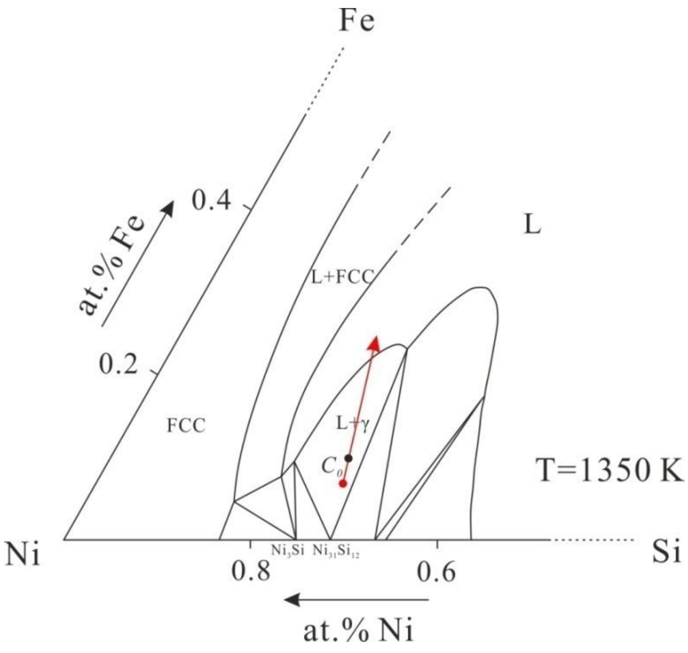

Figure 6.3: Ni-Fe-Si ternary phase diagram calculated by MTDATA software (T=1350 K). The black and red dots denote the composition of $Ni_{64.7}Fe_{10}Si_{25.3}$ and corresponding γ-$Ni_{31}Si_{12}$ (I_1) phases. The red arrow denotes the general trend of the change in composition of the remaining liquid. [88]

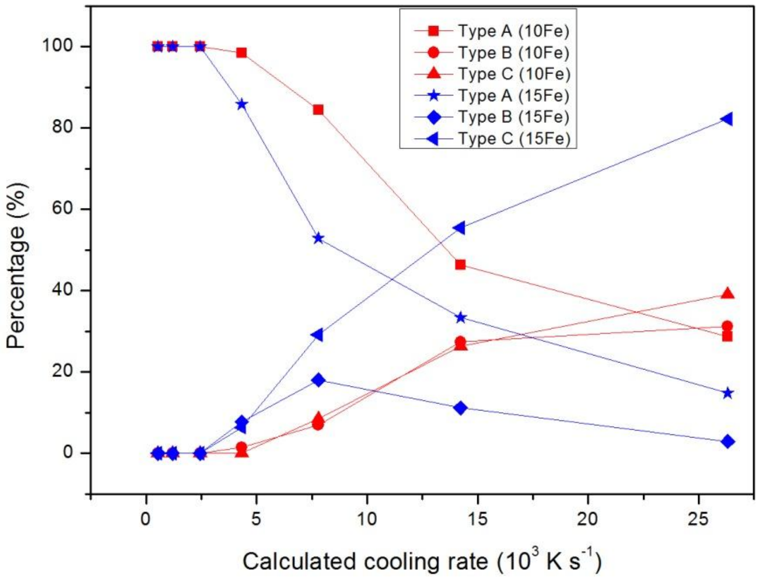

Figure 6.4: The percentage of the different types of particles (A, B and C) at different cooling rates. Type A and type C particles represented the entire regular structure I and the entire anomalous structure III, respectively, while type B particles presented the mixed structure of I, II and III. 10Fe and 15Fe in the diagram denote the $Ni_{64.7}Fe_{10}Si_{25.3}$ and $Ni_{59.7}Fe_{15}Si_{25.3}$ alloys.

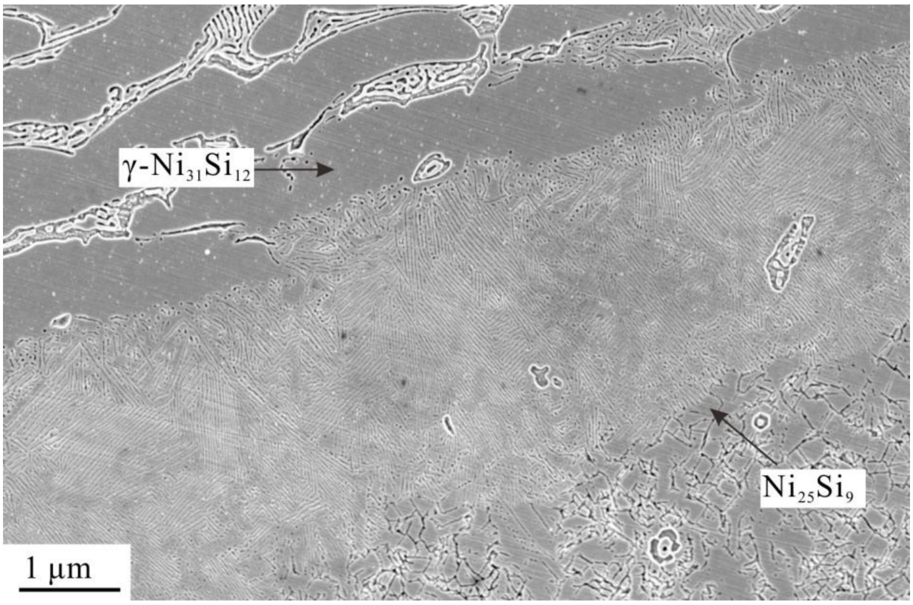

Figure 6.5: SEM image of the $Ni_{59.7}Fe_{15}Si_{25.3}$ particles showing the refined lamellar structure develops on the surface of the γ-$Ni_{31}Si_{12}$ and $Ni_{25}Si_{9}$ phases.

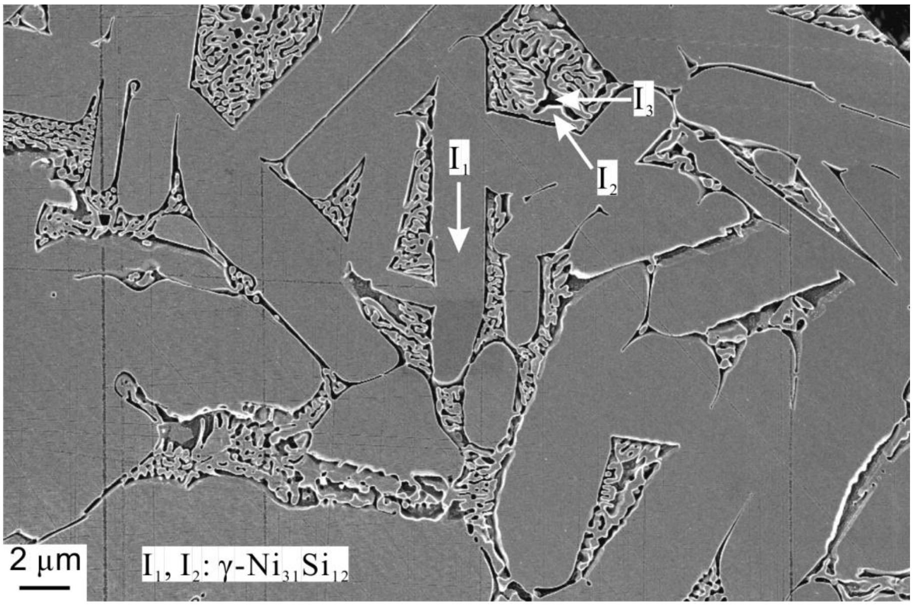

Figure 6.6: SEM image showing the regular structure in the $Ni_{64.7}Fe_{10}Si_{25.3}$ particles

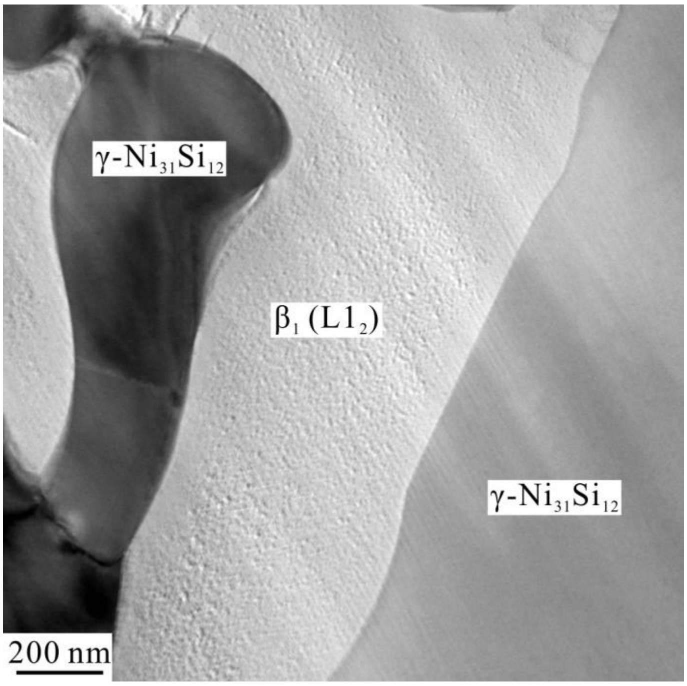

Figure 6.7: TEM high-resolution image of the eutectic structure of the $Ni_{64.7}Fe_{10}Si_{25.3}$ particle, consisting of the single phases γ-$Ni_{31}Si_{12}$ and $\beta_1(L1_2)$.

7 Conclusions

1. The Ni-25.3 at.% Si samples produced in the arc-melting furnace and drop tube show the same phase constitution of β_1-Ni_3Si, γ-$Ni_{31}Si_{12}$ and $Ni_{25}Si_9$. The difference is that β_1-Ni_3Si formed as the dominant phase in the arc-melted sample, while the dominant phase in the drop tube samples is the metastable phase $Ni_{25}Si_9$.
2. The observed regular lamellar structure consists of $Ni_{25}Si_9$ and β_1-Ni_3Si, the width of these being around 200 nm and 20 nm respectively. The fine scale of the microstructure would be indicative of very low diffusivity in the liquid.
3. The regular and anomalous eutectic structures indicate that there is a novel, metastable eutectic reaction between the $Ni_{25}Si_9$ and β_1-Ni_3Si phases in the Ni-Si binary phase diagram.
4. At high undercooling the particles appear to be able to bypass the newly identified eutectic and form a near single phase $Ni_{25}Si_9$ structure (heteroclite structure). The fraction of the particles with entire heteroclite structure increases from 13.91 % (300-500 μm) to 40.1% (75-106 μm).
5. The metastable phase $Ni_{25}Si_9$ decomposes to stable phases, β_1-Ni_3Si and γ-$Ni_{31}Si_{12}$, with the onset transformation temperature being around 491 ℃ at the heating rate of 10 K min^{-1}.
6. The arc-melted Ni-Fe-Si alloys show the typical lamellar structure morphology, comprising the alternating lamellae of the single-phase γ-$Ni_{31}Si_{12}$ and the eutectic/eutectoid structural layer.
7. For the Ni-Fe-Si drop tube samples, only γ-$Ni_{31}Si_{12}$ and β_1 phases formed at low cooling rates ($< 2.44 \times 10^3$ K s^{-1}), while at high cooling rates ($>2.44 \times 10^3$ K s^{-1}), the additional metastable phase, $Ni_{25}Si_9$, formed. It indicates that there is an extended $Ni_{25}Si_9$ stability field in the Ni-Fe-Si phase diagram.
8. The substitution of Fe for Ni can occur with a small amount of alloyed Fe (< 15 at.% in present work).
9. There are three typical microstructures with increasing cooling rate, regular structure, fine lamellar structure and anomalous structure. The lamellar structure is the intermediate but not the necessary state of the transition from the regular structure to anomalous structure.

10. Fe appears to stabilise the $L1_2$ phase as a γ-β_1 eutectic is observed rather than a α-γ eutectic predicted by the ternary phase diagram. Meanwhile, it is also different from that of Ni-25.3 at.% Si, where it is very difficult to obtain β_1 from the liquid.

8 Future work

Although this study has already revealed some interesting results, there are still some unclear points, which would benefit for further study:

1. Further studies on Ni-25.3 at.% Si at high cooling rates would be useful to reveal the remaining questions raised in this work. The first question is the origin of the eutectic reaction of the $Ni_{25}Si_9$ and β_1-Ni_3Si phases. Due to the impossibility of direct investigation of undercooling and solidification on the falling droplets, more studies on its microstructure would be useful to understand the mechanism of the formation of the nano-scale regular and anomalous eutectic structures. Secondly, further studies on the structures of $Ni_{25}Si_9$/$Ni_{74}Si_{26}$ are necessary. Neutron diffraction was performed on the Ni-Si particles, but the analysis was not possible due to the scarcity of information on the crystal structures. In the present work, they are treated as the same metastable category. Thirdly, the experimental results of Ni-25.at% Si and Nb-25at.% Si alloys indicate that the direct formation of the β_1-Ni_3Si and Nb_3Si phases, which appears to be suppressed at low cooling rates, becomes accessible at high cooling rates. However, the origin of this behaviour presented at different cooling rates is still not fully settled.
2. Additional investigation on the Ni-rich portion of the Ni-Fe-Si phase diagram would be useful. Firstly, although the formation of the metastable phase $Ni_{25}Si_9$ has been observed, its stability field in the metastable phase diagram is still unclear. Secondly, thermodynamic properties of the metastable $Ni_{25}Si_9$ phase needs to be studied, including the phase transformation temperature and the corresponding equilibrium stable phases. Thirdly, it is still controversial about the phase that constitutes the eutectic structure with γ-$Ni_{31}Si_{12}$.

9 Reference

[1] Sukidi, N., et al. The oxidation of Ni_3Si-base alloys. Materials Science and Engineering: A. 1995, 191, pp.223-231.

[2] Milenkovic, S. and Caram, R. Effect of the growth parameters on the Ni-Ni_3Si eutectic microstructure. *Journal of Crystal Growth*. 2002, **237**, pp.95-100.

[3] Cui, C., et al. Microstructure and properties of Ni-Ni_3Si composites by directional solidification. *Physica B: Condensed Matter*. 2012, **407**(17), pp.3566-3569.

[4] Fleischer, R.L. High-strength, high-temperature intermetallic compounds. *Journal of Materials Science*. 1987, **22**(7), pp.2281-2288.

[5] Schulson, E.M. et al. The strength and ductility of Ni_3Si. *Acta Metallurgica et Materialia*. 1990, **38**(2), pp.207-213.

[6] Stoloff, N.S. et al. Emerging applications of intermetallics. *Intermetallics*. 2000, **8**(9), pp.1313-1320.

[7] Takasugi, T. et al. Environmental effect on mechanical properties of recrystallized $L1_2$-type $Ni_3(Si,Ti)$ intermetallics. *Journal of Materials Science*. 1991, **26**(5), pp.1179-1186.

[8] Ward-Close, C.M. et al. Intermetallic-matrix composites-a review. *Intermetallics*. 1996, **4**(3), pp.217-229.

[9] Yang, J.M. The mechanical behavior of in-situ NiAl-refractory metal composites. *JOM*. 1997, **49**(8), pp.40-43.

[10] Herlach, D.M. Non-equilibrium solidification of undercooled metallic melts. *Materials Science and Engineering: R: Reports*. 1994, **12**(4), pp.177-272.

[11] Schulson, E.M. and Barker, D.R. A brittle to ductile transition in NiAl of a critical grain size. *Scripta Metallurgica*. 1983, **17**(4), pp.519-522.

[12] Kaneno, Y. et al. Effects of Grain Size and Temperature on Environmental Embrittlement of $Ni_3(Si, Ti)$ Alloy. *Materials Transactions*. 2001, **42**(3), pp.418-421.

[13] Cahn, R.W. et al. The order-disorder transformation in Ni_3Al and $Ni_3Al \cdot Fe$ alloys-I. Determination of the transition temperatures and their relation to ductility. *Acta Metallurgica*. 1987, **35**(11), pp.2737-2751.

[14] Cahn, R.W. et al. The order-disorder transformation in Ni_3Al and $Ni_3Al \cdot Fe$ alloys-II. Phase transformations and microstructures. *Acta Metallurgica*. 1987, **35**(11), pp.2753-2764.

[15] Ahmad, R. et al. The formation of regular αNi-$\gamma(Ni_{31}Si_{12})$ eutectic structures from undercooled Ni–25 at.% Si melts. *Intermetallics*. 2012, **22**, pp.55-61.

[16] Cochrane, R.F. et al. Dendrite growth velocities in undercooled $Ni \cdot Si$ alloys. *Materials Science and Engineering: A*. 1991, **133,** pp.698-701.

[17] Leonhardt, M. et al. Metastable phase formation in undercooled eutectic $Ni_{78.6}Si_{21.4}$ melts. *Materials Science and Engineering: A*. 1999, **271**(1), pp.31-37.

[18] Lu, Y. et al. Amorphous formation in an undercooled binary Ni-Si alloy under slow cooling rate. *Journal of Materials Science & Technology*. 2009, **25**(3), pp.370.

[19] Fisher, K. and Kurz, W. *Fundamentals of solidification*. Switzerland: Trans Tech Publications, 1986.

[20] Himuro, Y. et al. Stability of ordered $L1_2$ phase in Ni_3Fe-Ni_3X (X: Si and Al) pseudobinary alloys. *Intermetallics*. 2004, **12**(6), pp.635-643.

[21] Himuro, Y. et al. Phase equilibria and γ'-L1$_2$ phase stability in the Ni-rich portion of Ni-Fe-Si and Ni-Fe-Al systems. *Intermetallics*. 2005, **13**(6), pp. 20-630.

[22] Cullity, B.D. and Stock, S.R. *Elements of X-ray Diffraction*. 3rd ed. Upper Saddle River, NJ: Prentice-Hall, 2001.

[23] Porter, D.A. and Easterling, K.E. *Phase transformations in metals and alloys*. 3rd ed. London: CRC press, 1992.

[24] Jackson, C.L. and McKenna, G.B. The melting behavior of organic materials confined in porous solids. *The Journal of Chemical Physics*. 1990, **93**, pp. 9002.

[25] Stefanescu, D.M., *Science and engineering of casting solidification*. 2nd ed. London: Springer, 2008.

[26] Laudise, R.A. et al. Crystal Growth. *Annual Review of Materials Science*, 1971. **1**(1): p.253-288.

[27] Aziz, M.J. Model for solute redistribution during rapid solidification. *Journal of Applied Physics*. 1982, **53**(2), pp.1158-1168.

[28] Jackson, K.A. and Hunt, J.D. Lamellar and rod eutectic growth. *AIME Met Soc Trans*. 1966, **236**, pp.1129-1142.

[29] Seetharaman, V. and Trivedi, R. Eutectic growth: Selection of interlamellar spacings. *Metallurgical Transactions A*. 1988, **19**(12), pp.2955-2964.

[30] Trivedi, R. et al. Theory of eutectic growth under rapid solidification conditions. *Acta Metallurgica*. 1987, **35**(4), pp.971-980.

[31] Bei, H. et al. Directional solidification and microstructures of near-eutectic Cr–Cr$_3$Si alloys. *Acta Materialia*. 2003, **51**(20), pp.6241-6252.

[32] Caram, R. and Milenkovic, S. Microstructure of Ni-Ni$_3$Si eutectic alloy produced by directional solidification. *Journal of Crystal Growth*. 1999, **198**, pp.844-849.

[33] Liu, X.R. et al. Microstructure evolution and solidification kinetics of undercooled Co-Ge eutectic alloys. *Scripta Materialia*. 2002, **46**(1), pp.13-18.

[34] Xing, L.Q. et al. Solidification of undercooled Ni-32.5 wt% Sn eutectic alloy. *Journal of Materials Science*. 1993, **28**(10), pp.2733-2737.

[35] Kattamis, T.Z. and Flemings, M.C. Structure of undercooled Ni-Sn eutectic. *Metallurgical and Materials Transactions B*. 1970, **1**(5), pp.1449-1451.

[36] Kerr, H.W. et al. On equilibrium and non-equilibrium peritectic transformations. *Acta Metallurgica*. 1974, **22**(6), pp.677-686.

[37] StJohn, D.H. The peritectic reaction. *Acta Metallurgica et Materialia*. 1990, **38**(4), pp.631-636.

[38] Gokhale, A.A. et al. Grain refinement in castings and welds. *TMS-AIME, Warrendale*. 1983, **223**.

[39] Flemings, M.C. Solidification processing. *Metallurgical Transactions*. 1974, **5**(10), pp.2121-2134.

[40] Horvay, G. The tension field created by a spherical nucleus freezing into its less dense undercooled melt. *International Journal of Heat and Mass Transfer*. 1965, **8**(2), pp.195-243.

[41] Schwarz, M. et al. Physical mechanism of grain refinement in solidification of undercooled melts. *Physical Review Letters*. 1994, **73**(10), pp.1380.

[42] Herlach, D.M. Metastable materials solidified from undercooled melts. *Journal of Physics: Condensed Matter*. 2001, **13**(34), pp.7737.

[43] Karma, A. Model of grain refinement in solidification of undercooled melts. *International Journal of Non-Equilibrium Processing*. 1998, **11**(2), pp.201-233.

[44] Mullis, A.M. and Cochrane, R.F. On the Karma model for spontaneous grain refinement at high solid fractions. *International Journal of Non-equilibrium Processing*. 2000, **11**(3), pp.283-297.

[45] Biswas, K. et al. Disorder trapping and grain refinement during solidification of undercooled Fe-18 at% Ge melts. *Philosophical Magazine*. 2007, **87**(25), pp.3817-3837.

[46] Dragnevski, K.I. et al. The mechanism for spontaneous grain refinement in undercooled pure Cu melts. *Materials Science and Engineering: A*. 2004, **375**, pp.479-484.

[47] Mullis, A.M. and Cochrane, R.F. Grain refinement and the stability of dendrites growing into undercooled pure metals and alloys. *Journal of Applied Physics*. 1997, **82**(8), pp.3783-3790.

[48] Mullis, A.M. and Cochrane, R.F. A phase field model for spontaneous grain refinement in deeply undercooled metallic melts. *Acta materialia*. 2001, **49**(12), pp.2205-2214.

[49] Dragnevski, K. et al. Experimental evidence for dendrite tip splitting in deeply undercooled, ultrahigh purity Cu. *Physical Review Letters*. 2002, **89**(21), pp.215502.

[50] Herlach, D.M. et al. Phase seeding in the solidification of an undercooled melt. *Materials Science and Engineering: A*. 1991, **133**, pp.795-798.

[51] Shechtman, D. et al. Metallic phase with long-range orientational order and no translational symmetry. *Physical Review Letters*. 1984, **53**(20), pp.1951-1953.

[52] Ohashi, W. and Spaepen, F. Stable Ga-Mg-Zn quasi-periodic crystals with pentagonal dodecahedral solidification morphology. *Nature*. 1987, **330,** pp.555-556.

[53] Tsai, A.P. et al. Stable icosahedral Al-Pd-Mn and Al-Pd-Re alloys. *Materials Transactions, JIM*. 1990, **31**, pp.98-103.

[54] Tsai, A.P. et al. A stable quasicrystal in Al-Cu-Fe system. *Japanese Journal of Applied Physics*. 1987, **26,** pp.L1505-L1507.

[55] Telford, M. The case for bulk metallic glass. *Materials Today*. 2004, **7**(3), pp.36-43.

[56] Zhang, B. et al. “Soft” bulk metallic glasses based on cerium. *Applied Physics Letters*. 2004, **85**(1), pp.61-63.

[57] Klement, W. et al. Non-crystalline structure in solidified gold–silicon alloys. *Nature*. 1960, **187**, pp. 869-870.

[58] Chen, H.S. and Turnbull, D. Thermal evidence of a glass transition in gold-silicon-germanium alloy. *Applied Physics Letters*. 1967, **10**(10), pp.284-286.

[59] Chen, H.S. and Turnbull, D. Evidence of a glass-liquid transition in a gold-germanium-silicon alloy. *The Journal of Chemical Physics*. 1968, **48**, pp.2560.

[60] Chen, H.S. and Turnbull, D. Formation, stability and structure of palladium-silicon based alloy glasses. *Acta Metallurgica*. 1969, **17**(8), pp.1021-1031.

[61] Drehman, A.J. et al. Bulk formation of a metallic glass: $Pd_{40}Ni_{40}P_{20}$. *Applied Physics Letters*. 1982, **41**, pp.716.

[62] Kui, H.W. et al. Formation of bulk metallic glass by fluxing. *Applied Physics Letters*. 1984, **45**, pp.615.

[63] Inoue, A. et al. Bulky La-Al-TM (TM= Transition Metal) amorphous alloys with high tensile strength produced by a high-pressure die casting method. *Materials Transactions, JIM*. 1993, **34**(4), pp.351-358.

[64] Inoue, A. et al. Al-La-Ni amorphous alloys with a wide supercooled liquid region. *Materials Transactions, JIM*. 1989, **30**(12), pp.965-972.

[65] Lu, Z.P. et al. Glass formation in la-based La-Al-Ni-Cu-(Co) alloys by Bridgman solidification and their glass forming ability. *Acta Materialia*. 1999, **47**(7), pp.2215-2224.

[66] Inoue, A. et al. Preparation of 16 mm diameter rod of amorphous $Zr_{65}Al_{7.5}Ni_{10}Cu_{17.5}$ alloy. *Materials Transactions, JIM*. 1993, **34**, pp.1234-1234.

[67] Peker, A. and Johnson, W.L. A highly processable metallic glass: $Zr_{41.2}Ti_{13.8}Cu_{12.5}Ni_{10.0}Be_{22.5}$. *Applied Physics Letters*. 1993, **63**, pp.2342.

[68] Lin, X.H. et al. Effect of oxygen impurity on crystallization of an undercooled bulk glass forming Zr-Ti-Cu-Ni-Al alloy. *Materials Transactions, JIM*. 1997, **38,** pp.473-477.

[69] Nishiyama, N. and Inoue, A. Glass-forming ability of $Pd_{42.5}Cu_{30}Ni_{7.5}P_{20}$ alloy with a low critical cooling rate of 0.067 K/s. *Applied Physics Letters*. 2002, **80,** pp.568-570.

[70] Duwez, P. et al. Amorphous phase in palladium-silicon alloys. *Journal of Applied Physics*. 1965, **36**(7), pp.2267-2269.

[71] Yao K.F. and Fang, R. Pd–Si binary bulk metallic glass prepared at low cooling rate. *Chinese Physics Letters*. 2005, **22**(6), pp.1481.

[72] Schwarz, R.B. et al. The synthesis of amorphous Ni · Ti alloy powders by mechanical alloying. *Journal of Non-Crystalline Solids*. 1985, **76**(2), pp.281-302.

[73] Li, H. et al. Study on the crystallization process of Ni · P amorphous alloy. *Applied Surface Science*. 1998, **125**(1), pp.115-119.

[74] Davis, L.A. and Yeow, Y.T. Flow and fracture of a Ni-Fe metallic glass. *Journal of Materials Science*. 1980, **15**(1), pp.230-236.

[75] Li, H. et al. XPS studies on surface electronic characteristics of Ni-B and Ni-P amorphous alloy and its correlation to their catalytic properties. *Applied Surface Science*. 1999, **152**(1), pp.25-34.

[76] Liu, X.J. et al. Ordered clusters and free volume in a Zr-Ni metallic glass. *Applied Physics Letters*. 2008, **93**(1), pp.011911-011911-3.

[77] Xu, D. et al. Bulk metallic glass formation in binary Cu-rich alloy series-$Cu_{100-x}Zr_x$(x= 34, 36, 38.2, 40 at.%) and mechanical properties of bulk $Cu_{64}Zr_{36}$ glass. *Acta Materialia*. 2004, **52**(9), pp.2621-2624.

[78] Luborsky, F. et al. Formation and magnetic properties of Fe-B-Si amorphous alloys. *Magnetics, IEEE Transactions on*. 1979, **15**(4), pp.1146-1149.

[79] Yao, K.F. and Zhang, C.Q. Fe-based bulk metallic glass with high plasticity. *Applied Physics Letters*. 2007, **90**(6), pp.061901-061901-3.

[80] Inoue, A. et al. Fe-and Co-based bulk glassy alloys with ultrahigh strength of over 4000MPa. *Intermetallics*. 2006, **14**(8), pp.936-944.

[81] Poon, S.J. et al. Glass formability of ferrous-and aluminum-based structural metallic alloys. *Journal of Non-Crystalline Solids*. 2003, **317**(1), pp. 1-9.

[82] Lu, Z.P. et al. Structural amorphous steels. *Physical Review Letters*. 2004, **92**(24), pp.245503.

[83] Bei, H. et al. A review of directionally solidified intermetallic composites for high-temperature structural applications. *Journal of Materials Science*. 2004, **39**(12), pp.3975-3984.

[84] Massalski, T.B. et al., *Binary alloy phase diagrams*. Metals Park, Ohio: American Society for Metals, 1986.

[85] Ellner, M. et al. Einige strukturelle untersuchungen in der mischung $NiSi_N$. *Journal of the Less Common Metals*. 1979, **66**(2), pp.163-173.

[86] Çadırlı, E. et al. Characterization of rapidly solidified Ni-Si and Co-Al eutectic alloys in drop tube. *Journal of Non-Crystalline Solids*. 2010, **356**(9), pp.461-466.

[87] Dutra, A.T. et al. Microstructure and metastable phase formation in a rapidly solidified Ni-Si eutectic alloy using a melt-spinning technique. *Journal of Alloys and Compounds*. 2004, **381**(1), pp.72-76.

[88] MTDATA is licensed by the National Physical Laboratory, UK.

[89] Nash, P. and Nash, A. The Ni-Si (Nickel-Silicon) system. *Bulletin of Alloy Phase Diagrams*. 1987, **8**(1), pp.6-14.

[90] Çadırlı, E. et al. Microstructural, mechanical, electrical and thermal characterization of arc-melted Ni-Si and Co-Si alloys. *Journal of Non-Crystalline Solids*. 2010, **356**(33), pp.1735-1741.

[91] Karaköse, E. and Keskin, M. Microstructure evolution and mechanical properties of intermetallic Ni-xSi (x= 5, 10, 15, 20) alloys. *Journal of Alloys and Compounds*. 2012, **528**, pp.63-69.

[92] Dutra, A.T. et al. Microstructure and mechanical behavior of in situ Ni-Ni_3Si composite. *Journal of Alloys and Compounds*. 2007, **432**(1), pp.167-171.

[93] Liu, F. et al. Competitions incorporated in rapid solidification of the bulk undercooled eutectic $Ni_{78.6}Si_{21.4}$ alloy. *Journal of Materials Research*. 2007, **22**(10), pp.2953-2963.

[94] Lu, Y. et al. Microstructure and hardness of undercooled $Ni_{78.6}Si_{21.4}$ eutectic alloy. *Journal of Alloys and Compounds*. 2010, **490**(1), pp.L1-L4.

[95] Lu, Y. et al. Grain refinement in solidification of highly undercooled eutectic Ni–Si alloy. *Materials Letters*. 2007, **61**(4), pp.987-990.

[96] Goetzinger, R. et al. Mechanism of formation of the anomalous eutectic structure in rapidly solidified Ni-Si, Co-Sb and Ni-Al-Ti alloys. *Acta Materialia*. 1998, **46**(5), pp.1647-1655.

[97] Lu, Y. et al. Composite growth in highly undercooled $Ni_{70.2}Si_{29.8}$ eutectic alloy. *Applied Physics Letters*. 2006, **89,** pp.241902.

[98] Lu, Y. et al. The formation of quasiregular microstructure in highly undercooled $Ni_{70.2}Si_{29.8}$ eutectic alloy. *Journal of Applied Physics*. 2008, **104**(1), pp.013535-013535-5.

[99] Fredriksson, H. and Nylen, T. Mechanism of peritectic reactions and transformations. *Metal Science*. 1982, **16**(6), pp.283-294.

[100] Barker, N.J.W. and Hellawell, A. The Peritectic Reaction in the System Pb-Bi. *Metal Science*. 1974, **8**(1), pp.353-356.

[101] Bertero, G.A. et al. Containerless processing and rapid solidification of Nb-Si alloys of hypereutectic composition. *Metallurgical Transactions A*. 1991, **22**(11), pp.2723-2732.

[102] Bendersky, L. et al. Microstructural characterization of rapidly solidified Nb-Si alloys. *Materials Science and Engineering*. 1987, **89**, pp.151-159.

[103] Himuro, Y. et al. Effect of ausaging on the morphology of martensite in an Fe-25% Ni-7.5% Si alloy. *Le Journal de Physique IV*. 2001, **11**(PR8), pp.205-210.

[104] Ikeda, O. et al. Phase equilibria in the Fe-rich portion of the Fe-Ni-Si system. *Journal of Alloys and Compounds*. 1998, **268**(1), pp.130-136.

[105] Ackerbauer, S. et al. The constitution of the ternary system Fe-Ni-Si. *Intermetallics*. 2009, **17**(6), pp.414-420.

[106] Oya, Y. and Suzuki, T. The Nickel-rich portion of the Ni-Si phase diagram. *Z. Metallkd*. 1983, **74**(1), pp.21-24.

[107] Goodhew, P.J. et al. *Electron microscopy and analysis*. 3rd ed. London: Taylor & Francis, 2001.

[108] Reed, S.J.B. *Electron microprobe analysis and scanning electron microscopy in geology*. Cambridge: Cambridge University Press, 2005.

[109] Rietveld, H.M. The crystal structure of some alkaline earth metal uranates of the type M3UO6. *Acta Crystallographica*. 1966, **20**(4), pp.508-513.

[110] Rietveld, H.M. Line profiles of neutron powder-diffraction peaks for structure refinement. *Acta Crystallographica*. 1967, **22**(1), pp.151-152.

[111] Larson, A.C. and Von Dreele, R.B. General Structure Analysis System (GSAS); *Los Alamos National Laboratory Report LAUR*. 2004, pp.86-748.

[112] Rodr ǵuez-Carvajal, J. Recent advances in magnetic structure determination by neutron powder diffraction. *Physica B: Condensed Matter*. 1993, **192**(1), pp.55-69.

[113] McCusker, L.B. et al. Rietveld refinement guidelines. *Journal of Applied Crystallography*. 1999, **32**(1), pp.36-50.

[114] Fultz, B. and Howe, J.M. *Transmission electron microscopy and diffractometry of materials*. 3rd ed. New York: Springer, 2012.

[115] Williams, D.B. and Carter, C.B., *The Transmission Electron Microscope*. New York: Springer, 1996.

[116] Mackenzie, R.C., *Differential thermal analysis*. London and New York: Academic Press, 1970.

[117] Champness, P.E. *Electron diffraction in the transmission electron microscope.* Oxford: BIOS Scientific publishers Ltd, 2001.

[118] Dodd, J.W. et al. *Thermal methods.* New York: Wiley, 1987.

[119] Rappaz, M. Modelling of microstructure formation in solidification processes. *International Materials Reviews*. 1989, **34**(1), pp.93-124.

[120] Bird, R.B. et al. *Transport phenomena*. New York: wiley, 1960.

[121] Coker, A.K. *Ludwig's applied process design for chemical and petrochemical plants*. 4th ed. Burlington: Elsevier, 2007.

[122] Cole, W.A. and Wakeham, W.A. The viscosity of nitrogen, oxygen, and their binary mixtures in the limit of zero density. *Journal of Physical and Chemical Reference Data*. 1985, **14**(1), pp.209-226.

[123] Latto, B. and Saunders, M.W. Viscosity of nitrogen gas at low temperatures up to high pressures: a new appraisal. *The Canadian Journal of Chemical Engineering*. 1972, **50**(6), pp.765-770.

[124] Smith, J.M. and Van Ness, H.C. *Introduction to chemical engineering thermodynamics*. 3rd ed. New York: McGraw-Hill, 1975.

[125] Gale, W.F. and Totemeier, T.C. *Smithells metals reference book*. 8th ed. Oxford: Butterworth-Heinemann, 2003.

[126] Rocha, O.L. et al. Heat flow parameters affecting dendrite spacings during unsteady-state solidification of Sn-Pb and Al-Cu alloys. *Metallurgical and Materials Transactions A*. 2003, **34**(4), pp.995-1006.

[127] Bouchard, D. and Kirkaldy, J.S. Prediction of dendrite arm spacings in unsteady-and steady-state heat flow of unidirectionally solidified binary alloys. *Metallurgical and Materials Transactions B*. 1997, **28**(4), pp.651-663.

[128] Kasperovich, G. et al. Microsegregation during Solidification of an Al-Cu Binary Alloy at Largely Different Cooling Rates (0.01 to 20,000 K/s): Modeling and Experimental Study. *Metallurgical and Materials Transactions A*. 2008, **39**(5), pp.1183-1191.

[129] Pandey, O.P. et al. Nonequilibrium solidification of undercooled melt of Ag-Cu alloy entrained in the primary phase. *Metallurgical and Materials Transactions A*. 1994, **25**(11), pp.2518-2523.

[130] Herlach, D.M. et al. Containerless processing in the study of metallic melts and their solidification. *International Materials Reviews*. 1993, **38**(6), pp.273-347.

[131] Ridley, N. A review of the data on the interlamellar spacing of pearlite. *Metallurgical Transactions A*. 1984, **15**(6), pp.1019-1036.

[132] Clopet, C.R. et al. The origin of anomalous eutectic structures in undercooled Ag-Cu alloy. *Acta Materialia*. 2013, **61**(18), pp.6894-6902.

[133] Wei, B. et al. High undercooling and rapid solidification of Ni-32.5% Sn eutectic alloy. *Acta Metallurgica et Materialia*. 1991, **39**(6), pp.1249-1258.

[134] Li, J.F. et al. Structural evidence for the transition from coupled to decoupled growth in the solidification of undercooled Ni-Sn eutectic melt. Metallurgical and Materials Transactions A. 2007, 38(8), pp.1806-1816.

10 Appendix

The phases involved in this project are α-Ni solid solution, β phases, γ-$Ni_{31}Si_{12}$ and metastable $Ni_{25}Si_9$ and $Ni_{74}Si_{26}$ phases. The data of $Ni_{74}Si_{26}$ are from the reference [85], while the data of the rest phases can be obtained from the XRD diffraction database, including the cell parameters and XRD diffraction peak list, as listed in **Table 10.1**.

Table 10.1: The standard XRD intensity data of the phases involved in present work

Phase	H	k	l	d(Å)	2Theta (degree)	I(%)
Ni	1	1	1	2.0348	44.489	100
04-001-2619	2	0	0	1.7622	51.841	42.3
Cubic	2	2	0	1.2461	76.365	16.5
Fm-3m, 225	3	1	1	1.0626	92.924	14.7
a=b=c=3.5244 Å	2	2	2	1.0174	98.423	4
α=β=γ=90°	4	0	0	0.8811	121.912	1.7
	3	3	1	0.8086	144.59	5.5
β_1-Ni_3Si	1	0	0	3.505	25.391	7.8
04-001-3377	1	1	0	2.4784	36.216	5.7
Cubic	1	1	1	2.0236	44.749	100
Pm-3m, 221	2	0	0	1.7525	52.15	42.5
a=b=c=3.5050 Å	2	1	0	1.5675	58.868	1.7
α=β=γ=90°	2	1	1	1.4309	65.14	1
	2	2	0	1.2392	76.868	17.1
	3	0	0	1.1683	82.498	0.4
	3	1	0	1.1084	88.049	0.2
	3	1	1	1.0568	93.588	15.6
	2	2	2	1.0118	99.161	4.3
	3	2	0	0.9721	104.822	0.1
	3	2	1	0.9368	110.625	0.2
	4	0	0	0.8762	123.077	1.9
	4	1	0	0.8501	129.951	0.1
	4	1	1	0.8261	137.641	0.1
	3	3	1	0.8041	146.657	6.1
$Ni_{25}Si_9$	0	0	1	9.618	9.187	0.1
04-007-3362	1	0	0	5.8006	15.262	0.1
Hexagonal	1	0	1	4.9672	17.843	0.2
P-3, 147	0	0	2	4.809	18.435	0.1
a=b=6.6980 Å	1	0	2	3.7022	24.018	0.7
c=9.6180 Å	1	1	0	3.349	26.595	0.1
α=β=90 °	0	0	3	3.206	27.805	2.1
γ=120°	1	1	-1	3.1628	28.192	3.8
	2	0	0	2.9003	30.804	0.1
	1	0	3	2.806	31.867	0.4
	2	0	1	2.7768	32.211	1.4

	1	1	-2	2.7482	32.555	9.8
	2	0	2	2.4836	36.137	6.7
	0	0	4	2.4045	37.369	0.1
	1	1	-3	2.3159	38.855	3
	1	0	4	2.2212	40.583	6.5
	2	1	0	2.1924	41.14	12.9
	0	2	3	2.1508	41.973	49.2
	2	1	-1	2.1376	42.244	53.4
	1	2	-2	1.9949	45.428	18.4
	1	1	-4	1.9532	46.454	100
	3	0	0	1.9336	46.953	77.3
	0	0	5	1.9236	47.212	2.7
	3	0	1	1.8956	47.953	0.9
	2	0	4	1.8511	49.181	5.3
	0	1	5	1.8258	49.909	8.2
	1	2	-3	1.8097	50.384	22.1
	2	2	0	1.6745	54.777	0.6
	1	1	-5	1.668	55.008	1.8
	0	3	3	1.6557	55.452	0.9
	2	2	-1	1.6497	55.671	1.9
	2	1	-4	1.6201	56.779	4.7
	3	1	0	1.6088	57.215	0.5
	0	2	5	1.603	57.441	2.9
	3	1	-1	1.5868	58.083	7.6
	2	2	-2	1.5814	58.3	0.9
	0	1	6	1.5451	59.807	1.7
	1	3	-2	1.5257	60.647	1.7
	0	3	4	1.5068	61.49	0.6
	2	2	-3	1.4842	62.53	0.4
	4	0	0	1.4502	64.169	1.2
	1	2	5	1.4459	64.383	0.5
	1	3	-3	1.4379	64.784	0.8
	0	4	1	1.434	64.982	0.4
	0	2	6	1.403	66.602	0.6
	0	4	2	1.3884	67.395	0.9
	2	2	-4	1.3741	68.193	7
	0	3	5	1.3637	68.785	0.1
	1	3	4	1.3371	70.353	3.6
	2	3	0	1.3308	70.736	0.2
	4	0	3	1.3213	71.322	1.7
	3	2	-1	1.3182	71.515	3.7
	2	1	-6	1.294	73.066	0.8
	2	3	2	1.2826	73.822	2.2
	1	1	-7	1.2712	74.596	0.4
	1	4	0	1.2658	74.969	3.3
	2	2	-5	1.263	75.164	0.6
	1	4	-1	1.255	75.727	1.1
	4	0	4	1.2418	76.677	1
	3	1	5	1.2341	77.244	6.3

	2	3	-3	1.2291	77.617	9.8
	1	4	-2	1.2241	77.994	0.6
	0	0	8	1.2022	79.694	1.1
	4	1	-3	1.1772	81.741	1.4
	3	2	-4	1.1643	82.844	6.8
	5	0	0	1.1601	83.21	0.6
	0	4	5	1.158	83.395	3.9
	0	5	1	1.1518	83.946	0.7
	3	1	-6	1.1355	85.434	1.1
	1	1	-8	1.1316	85.799	7.6
	0	5	2	1.1278	86.159	0.4
	4	1	-4	1.1201	86.898	3.1
	3	3	0	1.1163	87.268	1.7
	2	0	8	1.1106	87.83	0.3
	3	3	1	1.1089	87.999	1
	2	4	0	1.0962	89.288	1.4
	2	3	-5	1.0944	89.474	0.9
	5	0	3	1.0909	89.839	2.7
	4	2	-1	1.0892	90.018	2.1
	3	3	-2	1.0874	90.208	0.5
	0	4	6	1.0754	91.498	1.2
	4	2	-2	1.0688	92.227	1
	2	2	-7	1.0622	92.97	0.2
	4	1	-5	1.0574	93.519	2.6
	3	3	-3	1.0542	93.89	1.8
	1	3	-7	1.0448	94.999	1.9
	5	1	0	1.0418	95.36	0.7
	4	2	-3	1.0373	95.907	0.9
	5	1	-1	1.0358	96.091	1.6
	2	3	-6	1.0239	97.583	0.8
	0	3	8	1.021	97.956	0.4
	1	5	-2	1.0182	98.319	1.3
	3	3	-4	1.0125	99.068	0.5
	0	2	9	1.0028	100.376	0.1
	4	0	7	0.9974	101.123	0.8
	4	1	-6	0.9934	101.686	0.4
	5	1	3	0.9908	102.056	1.5
	2	2	-8	0.9766	104.139	2.8
	6	0	0	0.9668	105.642	0.6
	3	3	-5	0.9655	105.846	0.1
	1	3	-8	0.963	106.24	0.8
	6	0	1	0.9619	106.415	0.3
	2	1	-9	0.9606	106.623	0.8
	2	3	-7	0.9559	107.382	1.5
	4	3	0	0.9536	107.759	0.3
	4	2	-5	0.9524	107.957	0.6
	3	4	-1	0.949	108.524	0.3
$Ni_{74}Si_{26}$[85]	0	0	3	9.618	9.187	nbt
Hexagonal	1	0	1	5.687	15.57	nbt

a=b=6.6980 Å c=28.8550 Å α=β=90 ° γ=120° Intensity[11] sss =5% ss =10% s =20% m- =40% m =50% m+ =60% st =80% sst =100%	0	1	2	5.382	16.458	nbt
	0	0	6	4.809	18.434	nbt
	1	0	4	4.52	19.623	nbt
	0	1	5	4.091	21.705	nbt
	1	0	7	3.36	26.506	nbt
	1	1	0	3.349	26.595	ss
	0	0	9	3.206	27.804	s
	1	1	3	3.163	28.193	s
	0	1	8	3.063	29.131	nbt
	0	2	1	2.885	30.963	ss
	2	0	2	2.843	31.436	ss
	1	1	6	2.748	32.554	m
	0	2	4	2.691	33.268	nbt
	2	0	5	2.591	34.585	nbt
	1	0	10	2.583	34.694	s
	0	0	12	2.405	37.368	sss
	0	1	11	2.39	37.602	sss
	0	2	7	2.372	37.9	m-
	1	1	9	2.316	38.854	s
	2	0	8	2.26	39.852	m
	2	1	1	2.186	41.263	s
	1	2	2	2.617	41.633	m+
	2	1	4	2.098	43.088	m
	1	0	13	2.073	43.626	ss
	1	2	5	2.049	44.153	nbt
	0	2	10	2.046	44.243	st
	1	1	12	1.953	46.453	sst
	2	0	11	1.945	46.649	nbt
	0	1	14	1.942	46.735	s
	2	1	7	1.936	46.9	nbt
	0	3	0	1.933	46.955	sst
	0	0	15	1.924	47.211	s
	0	3	3	1.896	47.952	nbt
	1	2	8	1.873	48.556	m-
	0	3	6	1.794	50.857	nbt
	0	2	13	1.763	51.826	nbt
	2	1	10	1.746	52.368	m
	1	0	16	1.722	53.141	s
	1	2	11	1.682	54.504	s
	2	0	14	1.682	54.58	nbt
	2	2	0	1.674	54.777	nbt
	1	1	15	1.668	55.006	s
	0	3	9	1.656	55.45	nbt
	2	2	3	1.65	55.671	ss
	0	1	17	1.629	56.44	s
	1	3	1	1.606	57.311	nbt
	0	0	18	1.603	57.439	s

---

[11] The intensities are obtained in comparison to the incomplete XRD card.

	3	1	2	1.599	57.602	s
	2	2	6	1.581	58.301	ss
	1	3	4	1.57	58.755	s
	2	1	13	1.56	59.187	nbt
	3	1	6	1.55	60.647	nbt
	0	3	12	1.507	61.489	sss
	1	2	14	1.502	61.722	sss
	1	3	7	1.499	61.858	nbt
	2	2	9	1.484	62.528	ss
	1	0	19	1.469	63.244	nbt
	3	1	8	1.469	63.239	sss
	2	0	17	1.465	63.448	nbt
	4	0	1	1.448	64.262	nbt
	1	1	18	1.446	64.381	nbt
	0	4	2	1.443	64.533	ss
	4	0	4	1.422	65.614	nbt
	0	4	5	1.406	66.418	ss
	1	3	10	1.405	66.486	-
	0	1	20	1.4	66.758	nbt
	2	1	16	1.393	67.155	nbt
	0	0	21	1.374	68.196	m
	2	2	12	1.374	68.19	-
	3	1	11	1.371	68.344	nbt
	4	0	7	1.368	68.54	nbt
	0	3	15	1.364	68.784	nbt
	0	2	19	1.345	69.856	nbt
	0	4	8	1.345	69.851	ss
	1	2	17	1.342	70.05	nbt
$Ni_{31}Si_{12}$	0	0	1	12.28	7.193	0.1
	0	0	2	6.14	14.414	0.2
04-006-9133	1	0	0	5.7831	15.309	0.1
Hexagonal	1	0	1	5.2319	16.933	0.3
P321, 150	1	0	2	4.2098	21.087	0.1
a=b=6.6777 Å	0	0	3	4.0933	21.694	0.2
c=12.2800 Å	0	1	3	3.3388	26.678	2.9
α=β=90 °	1	1	1	3.2219	27.665	2.3
γ=120°	0	0	4	3.07	29.063	0.7
	1	1	2	2.9332	30.45	5.6
	2	0	0	2.8915	30.9	0.7
	0	2	1	2.8146	31.767	0.6
	0	1	4	2.7116	33.007	1.2
	2	0	2	2.616	34.25	9.9
	1	1	3	2.5873	34.642	8.5
	0	0	5	2.456	36.557	1.3
	2	0	3	2.3617	38.072	0.1
	1	0	5	2.2599	39.858	3.3
	2	1	0	2.1858	41.27	5.8
	1	2	1	2.152	41.948	28.8
	0	2	4	2.1049	42.933	25.4

	1	2	2	2.0592	43.935	8.4
	0	0	6	2.0467	44.217	2.7
	1	1	5	1.9784	45.829	100
	3	0	0	1.9277	47.106	93.6
	0	3	1	1.9044	47.718	0.6
	2	0	5	1.8719	48.599	6.9
	3	0	2	1.8392	49.521	0.3
	2	1	4	1.7806	51.266	12.6
	0	0	7	1.7543	52.092	0.1
	1	1	6	1.7449	52.394	4.4
	0	1	7	1.6788	54.625	0.1
	0	2	6	1.6705	54.919	1.8
	2	2	1	1.6542	55.506	0.9
	2	1	5	1.6328	56.298	5
	2	2	2	1.6109	57.133	0.5
	3	1	0	1.6039	57.406	0.7
	1	3	1	1.5904	57.939	3.6
	3	1	2	1.5519	59.519	0.3
	2	2	3	1.5458	59.778	1.3
	0	0	8	1.535	60.242	0.9
	0	3	5	1.5164	61.059	0.5
	2	0	7	1.4998	61.808	0.1
	1	2	6	1.4934	62.102	0.4
	0	1	8	1.4836	62.559	0.8
	2	2	4	1.4666	63.367	0.3
	4	0	0	1.4458	64.388	0.5
	4	0	1	1.4358	64.891	0.1
	1	3	4	1.4216	65.62	0.6
	0	4	2	1.4073	66.372	0.7
	0	3	6	1.4033	66.586	0.6
	1	1	8	1.3947	67.051	0.1
	2	2	5	1.3807	67.822	9.9
	1	2	7	1.3681	68.533	1.1
	0	4	3	1.3632	68.814	0.1
	0	2	8	1.3558	69.243	0.5
	1	3	5	1.3429	70.005	0.5
	1	0	9	1.3267	70.987	0.2
	2	3	1	1.319	71.465	3.2
	4	0	4	1.308	72.16	1.5
	2	3	2	1.2968	72.883	1.1
	2	2	6	1.2936	73.092	1.6
	3	1	6	1.2624	75.206	3.6
	4	1	1	1.2554	75.699	1.3
	4	0	5	1.2459	76.38	0.1
	4	1	2	1.2361	77.096	0.6
	0	0	10	1.228	77.699	3.4
	3	2	4	1.2179	78.467	6.6
	2	2	7	1.2094	79.126	0.1
	1	4	3	1.206	79.393	0.5

	1	0	10	1.2012	79.774	1.8
	3	1	7	1.1837	81.197	0.1
	0	4	6	1.1809	81.43	1.9
	2	3	5	1.1673	82.584	3
	2	1	9	1.1574	83.448	2.5
	1	1	10	1.1525	83.883	1.7
	0	5	2	1.1366	85.332	0.1
	2	2	8	1.1303	85.922	0.9
	4	1	5	1.1225	86.666	6
	2	3	6	1.113	87.592	4.3
	3	1	8	1.109	87.989	0.7
	3	3	2	1.0951	89.402	0.1
	4	2	0	1.0929	89.63	0.6
	4	2	1	1.0886	90.081	1.6
	5	0	4	1.0824	90.74	1.7
	4	2	2	1.076	91.433	0.8
	4	1	6	1.0742	91.63	3
	2	1	10	1.0706	92.027	2.1
	2	3	7	1.0582	93.427	0.4
	2	2	9	1.0565	93.623	0.1
	0	4	8	1.0524	94.1	0.8
	0	5	5	1.0463	94.82	1.3
	1	3	9	1.0387	95.736	0.8
	3	0	10	1.0357	96.103	5.5
	2	4	4	1.0296	96.862	0.7
	1	5	2	1.0241	97.558	0.5
	3	3	5	1.0137	98.909	0.2
	0	5	6	1.007	99.804	0.8
	3	2	8	1.0038	100.239	0.3
	2	4	5	0.9985	100.97	0.1
	1	2	11	0.9942	101.573	0.5
	4	0	9	0.9923	101.842	0.1
	2	2	10	0.9892	102.285	0.6
	5	1	4	0.9839	103.055	1.4
	1	1	12	0.9777	103.974	0.1
	1	3	10	0.975	104.381	0.8
	0	5	7	0.9656	105.83	0.1
	2	4	6	0.9638	106.114	1.4
	0	6	1	0.9609	106.575	0.1
	1	5	5	0.9566	107.268	0.6
	3	2	9	0.9512	108.157	0.9
	4	3	1	0.9479	108.709	0.3
	4	3	2	0.9398	110.098	0.1
	6	0	3	0.9382	110.378	0.1
β_2-Ni_3Si	-2	0	1	3.48	25.577	60.0
00-032-0699	2	0	0	2.614	34.277	10.0
Monoclinic	0	2	1	2.446	36.712	60.0
a=6.9700 Å	-3	1	1	2.122	42.57	40.0
b=6.2500 Å	-3	1	2	2.075	43.583	40.0

c=5.0700 Å α=90 ° β=131.26 ° γ=90°	2	2	0	2.011	45.045	100.0
	-2	2	2	1.964	46.184	80.0
	1	2	1	1.915	47.437	80.0
	-4	0	2	1.741	52.52	100.0
	-2	0	3	1.655	55.477	10.0
	2	3	0	1.629	56.441	20.0
	0	4	0	1.564	59.013	40.0
	2	2	1	1.492	62.167	20.0
	-4	2	1	1.429	65.238	40.0
	-5	0	2	1.376	68.085	40.0
	1	4	1	1.312	71.906	10.0
	-5	2	2	1.262	75.234	10.0
	-3	1	4	1.233	77.326	100.0
	-1	5	1	1.214	78.768	20.0
	-5	0	4	1.201	79.79	10.0
	-2	0	4	1.18	81.506	20.0
	-4	2	4	1.17	82.352	20.0
	-6	0	3	1.161	83.132	20.0
	-6	0	2	1.122	86.714	40.0
	4	3	0	1.108	88.089	40.0
β_3-Ni_3Si 00-032-0700 Monoclinic a=7.0400 Å b=6.2600 Å c=5.0800 Å α=90 ° β=131.16 ° γ=90°	1	1	0	4.01	22.15	20.0
	0	2	0	3.15	28.309	60.0
	-2	0	2	2.542	35.279	60.0
	-3	0	1	2.273	39.619	60.0
	-1	1	2	2.207	40.855	20.0
	-3	1	1	2.138	42.236	100.0
	2	2	0	2.024	44.74	100.0
	-2	2	2	1.971	46.011	100.0
	0	0	2	1.915	47.437	20.0
	-4	0	2	1.759	51.942	80.0
	0	4	0	1.567	58.888	60.0
	-3	2	0	1.545	59.812	40.0
	-2	2	3	1.459	63.736	60.0
	-4	2	3	1.403	66.602	40.0
	-5	1	2	1.365	68.71	60.0
	-5	1	3	1.34	70.178	20.0
	1	4	1	1.316	71.653	80.0
	-4	3	1	1.283	73.796	60.0
	-5	2	3	1.257	75.586	60.0
	-3	1	4	1.231	77.475	20.0
	4	2	0	1.22	78.306	60.0
	-4	2	4	1.173	82.096	20.0
	-5	3	3	1.142	84.834	20.0
	2	5	0	1.131	85.856	40.0
	3	3	1	1.109	87.989	20.0
	-6	2	3	1.101	88.796	40.0